

Investigation of nanocrystalline zinc oxide and zinc oxide/copper oxide composites for use in a continuous flow biosensor

Lu Cao

A thesis submitted in partial fulfilment of the requirements of the University of
the West of England, Bristol
for the degree of Doctor of Philosophy

Faculty of Environment and Technology, University of the West of England, Bristol

January 2022

Abstract

There are an increasing number of applications for point-of-care biosensing technologies that are able to monitor biochemical levels over a period, rather than as a measurement at a single time point. As with all point-of-care devices, cost and appropriate sensitivity for measurement in the clinical range of the target analyte are very important factors.

In the study described in this thesis, impedimetric, affinity-based non-faradaic biosensors, which incorporate nanoparticles have been investigated to progress towards devices that are suitable for such point-of-care applications. To keep fabrication costs low, a simple colloidal dispersion technique, incorporating sonication was used to create sensor surfaces of zinc oxide (ZnO) and zinc oxide / copper oxide (CuO) nanoparticles. The nanoparticles acted to enhance the signals and thus increase the sensitivity. Using the nanoparticles, two sensor structures were evaluated; the first was formed by dropping the nanoparticle colloidal suspensions on to polyethylene terephthalate (PET) substrates and the second was created by facilitating the absorption of the nanoparticle colloidal suspensions in to nitrocellulose membranes.

Results of the analysis of the sensor structures, performed using scanning electron microscopy, Raman spectroscopy and electrical analysis, are presented. In order to evaluate the biosensing properties, C-Reactive Protein (CRP) was used as a model analyte. The progression from a 2D nanoparticle surface (on PET substrates) to 3D nanoparticle surface (nanoparticle impregnated membranes) resulted in a significant increase in the sensitivity. For example, the limit of detection improved from 0.4 ng/mL for the ZnO/CuO (1:2) nano-surfaces to 16 pg/mL for the ZnO/CuO (1:2) nanoparticle membrane. Altering the ratio of ZnO to CuO within the suspension used to make the sensors structures, also resulted in variation in the sensitivity.

This thesis also reports a flow assay based on ZnO and ZnO/CuO nanoparticle impregnated membranes, using impedance measurement with both planar and interdigitated electrodes. These new paper-based flow systems showed high sensitivity and wide detection ranges over approximately a 2 hour testing period (where samples were added at fixed time intervals).

Using CRP as the analyte, the dynamic range of the biosensor was demonstrated to encompass 10 pg/mL to 366,660 pg/mL on 4 mm gap planar electrode and 1 pg/mL to 3,166 pg/mL on interdigitated electrode , with a calculated limit of detection of < 5 pg/mL for both nano-ZnO and nano-ZnO/CuO membranes. This technique, which combines the benefits of nanoparticle technology, impedimetric measurement and flow immunoassays, offers great potential for the development of real-time, low-cost, point-of-care biosensing devices.

Contents

Abstract.....	i
Contents.....	iii
List of Figures	vii
List of Tables	x
Abbreviations.....	xi
Acknowledgments.....	xiii
Chapter 1 Introduction.....	1
1.1 Thesis Statement.....	2
1.2 Biosensor Components	3
1.3 Bioreceptors.....	5
1.3.1 Various Receptors	5
1.3.2 Antibody-Based Biosensors.....	6
1.3.3 Antibody Immobilisation.....	7
1.4 Substrates	11
1.4.1 Solid Support Matrices.....	11
1.4.2 3D Porous Membranes	12
1.5 Transducers.....	14
1.5.1 Electrical Biosensors	14
1.5.2 Optical Technologies.....	15
1.5.3 Mechanical Biosensors.....	16
1.5.4 Electrochemical Biosensors	17
1.5.5 Impedimetric Biosensors	18
1.5.6 Comparison of Biosensors	20
1.6 Flow Systems.....	23
1.7 Zinc Oxide and Copper Oxide Nanoparticles	26
1.7.1 ZnO Nanoparticles.....	26
1.7.2 CuO Nanoparticles	27
1.7.3 Fabrication of ZnO and CuO Nanostructures.....	27
1.7.4 Sonication.....	30
1.8 Summary	32
Chapter 2 Impedimetric Biosensors.....	33
2.1 Faradaic and Non-Faradaic Processes.....	34

2.2 Principles of Impedimetric Biosensors.....	38
2.2.1 Electrical Double Layer.....	38
2.2.2 Debye Length	40
2.2.3 Data Analysis.....	42
2.3 Equivalent Circuit Modelling of Impedimetric Biosensors.....	43
2.3.1 Electrochemical Impedance Measurement	43
2.3.2 Randles Model	44
2.3.3 Equivalent Electrical Circuit of the 1% ZnO Nanoparticle Biosensor	45
2.3.4 Experimental Impedance Measurement Set-up and Results	48
2.4 Summary	51
Chapter 3 Zinc Oxide Based Bio-surfaces	52
3.1 Introduction	53
3.1.1 ZnO Nano-surfaces Fabrication.....	53
3.1.2 CRP Clinical Range.....	53
3.1.3 Antibody Densities and Concentrations	54
3.1.4 Antigen Experimental Range and Timings	58
3.2 Materials and Methods.....	60
3.2.1 Nano-surfaces Preparation	60
3.2.2 Characterisation of Nano-surfaces	60
3.2.3 CRP Sensor Fabrication and CRP Assay.....	61
3.2.4 Statistical Analysis.....	63
3.3 Results and Discussion	64
3.3.1 Validation of Nano-surfaces Fabrication.....	64
3.3.2 Characterisation of Surface.....	65
3.3.3 Raman Spectroscopy Analysis of the Surfaces.....	67
3.3.4 Calibration Curve Comparison of the Three ZnO Nano-surfaces with CRP Immobilised	69
3.3.5 Comparisons of Non-Specific Binding	73
3.4 Summary	75
Chapter 4 Copper Oxide-Enhanced Composite Nano-surface Biosensor	76
4.1 Introduction	77
4.2 Materials and Methods.....	79
4.2.1 Nano-surfaces Preparation	79
4.2.2 Characterisation of Nano-surfaces	80
4.2.3 Surface Uptake of Antibody	80
4.2.4 CRP Sensor Fabrication and CRP Assay.....	81
4.2.5 Statistical Analysis.....	82

4.3 Results and Discussion	84
4.3.1 Morphological Study	84
4.3.2 Raman Spectroscopy Analysis of the Nano-surfaces	89
4.3.3 Antibody Capture on ZnO/CuO Nano-surfaces.....	91
4.3.4 Detection of CRP on Different ZnO/CuO Composite Nano-surfaces	92
4.3.5 Calibration Curve Comparisons of Different Nano-surfaces with Capture Antibody	96
4.4 Summary	99
Chapter 5 Nanoparticle-Based 3D Membrane for Impedimetric Biosensor Applications	100
5.1 Introduction	101
5.2 Materials and Methods.....	103
5.2.1 Membrane Preparation	103
5.2.2 Characterisation of Membranes	103
5.2.3 CRP Sensor Fabrication and CRP Assay.....	104
5.2.4 Statistical Analysis	106
5.3 Results and Discussion	108
5.3.1 Characterisation of Membrane.....	108
5.3.2 EDS Results.....	110
5.3.3 Calibration Curves Using Different Nano-membranes with Capture Antibody.....	112
5.4 Summary	120
Chapter 6 Nano-membrane Based Biosensors for Detection of C-Reactive Protein by Flow- Based Methodology	122
6.1 Introduction	123
6.1.1 Background	123
6.1.2 Affinity.....	124
6.1.3 Design Considerations and Flow Rate.....	125
6.2 Materials and Methods.....	127
6.2.1 Nanoparticles-Based Flow Test Strip Fabrication	127
6.2.2 CRP Sensor Fabrication and CRP Assay.....	132
6.2.3 Valuation of Flow-Based Test Strip and CRP Assay.....	133
6.2.4 Statistical Analysis	135
6.2.5 Modelling the Response	135
6.2.6 Validation of Flow Rate	137
6.3. Results and Discussion	138
6.3.1 Characterisation of Membrane.....	138
6.3.2 Calibration Curves	138
6.3.3 Responses of Bare Nitrocellulose Membranes and PBS.....	141

6.3.4 Results by Flow-Based Methodology	144
6.3.5 Flow Rate.....	147
6.4 Summary	151
Chapter 7 Conclusion.....	153
7.1 Key Findings	153
7.2 Suggestions for Future Work	157
7.2.1 Targets.....	157
7.2.2 Fabrication and Design.....	157
7.2.3 Antibody Immobilisation.....	158
7.2.4 Electrical Impedance Spectroscopy	158
7.2.5 Future Applications	159
References	160
Appendix A Chapter 4 Supplementary Information	175
Appendix B Chapter 5 Supplementary Information	181
Appendix C Chapter 6 Supplementary Information	196
Appendix D Copyright Permissions	203

List of Figures

Figure 1. 1 The principle of a biosensor (transducer mechanism adapted by [4–6])	4
Figure 1. 2 Structure of IgG and IgG immobilized in a random fashion on a surface (Adapted from [30])	8
Figure 1. 3 Schematic presentation of immobilization capture antibody (a) Random immobilization on 2D surface. (b) Random immobilization on a 3D membrane. (Adapted from [35])	12
Figure 1. 4 Typical configuration of a LFIA strip [66].	23
Figure 2. 1 A diagram of the charge distribution at ZnO surface adapted from [1].	38
Figure 2. 2 Randles model redrawn from [42,112].	44
Figure 2. 3 Equivalent circuit model for the ZnO nanoparticle biosensor [117].	46
Figure 2. 4 The equivalent circuit associated with C60 arrangement [117].	48
Figure 3. 1 Schematic illustration of biosensor fabrication and sensing: The ZnO sensing area was defined using tape (a); then the antibody was added to the ZnO surface (b); and dried at 4 °C overnight (c); different concentrations of antigen were prepared (d); and added to the immobilized antibody on the ZnO surface (e); the impedance was measured on a blank surface (f) and a surface subjected to the assay protocol (g).....	62
Figure 3. 2 Impedance spectra (n=24) of three different concentrations of ZnO nano-powders (blue: 5%, red: 1%, lime green: 0.5%) on PET substrates.....	64
Figure 3. 3 SEM images for ZnO nano-surfaces on PET via suspensions at different concentrations (g/100 mL) of ZnO nano-crystals: (a) 5% ZnO; (b) 1% ZnO; (c) 0.5% ZnO.	66
Figure 3. 4 Plots of grayscale profiles along a horizontal line within images (mag ×2000) for nano-surfaces made by three different concentrations of ZnO suspensions: 0.5%, 1% and 5%.....	67
Figure 3. 5 Raman spectra of bare PET (blue line) and PET covered by 1% ZnO nanocrystals (green line) at room temperature. Conditions of recording Raman Spectrum of bare PET: time acquisition 30s, wavelength 785 nm. Conditions of recording Raman Spectrum of nano-ZnO on PET: time acquisition 50s, wavelength 785 nm.	68
Figure 3. 6 Raman spectra of ZnO nano-surface on PET (blue line) and ZnO with capture antibody on PET (green line). Conditions of recording ZnO with capture antibody on PET: time acquisition 150s, laser wavelength 785 nm.	69
Figure 3. 7 Impedance values from 1% ZnO nano-sensors, with 100 ng capture antibody with increasing concentrations of antigen: 0 - 15 ng/mL for 5, 10 and 15 minute incubation time.	70
Figure 3. 8 Cole-Cole plots for the CRP dose response (n=1) of each of three different concentrations of nano-surfaces with 100 ng antibodies loading at D-shape electrode representing the capacitance of the system calculated from impedance data (a) 0.5% (b) 1% (c) 5%.	71
Figure 3. 9 Impedance change in response to increasing concentrations of antigen on 0.5% and 1% ZnO nano-surfaces (n=3) with 100 ng capture antibody.	72
Figure 3. 10 Comparison of anti-CRP loading 1% ZnO nano-surface (n=3) at the frequency of 138 Hz for the detection of 5 ng/mL CRP.	74
Figure 4. 1 The cross-section illustration of biosensor.	82
Figure 4. 2 SEM images of nano-surfaces: (a) 1% pure ZnO (b) 1% ZnO and CuO suspensions with the ratio of 1:2 (c) 1:1 (d) 2:1.	85

Figure 4. 3 AFM 3D images of 3 μm by 3 μm area of the nano-surfaces: (a) 1% pure ZnO; (b) 1% pure CuO; (c) 1% ZnO and CuO suspensions with the ratio of 1:2.....	86
Figure 4. 4 A simple numerical calculation: (a) Schematic representation of ZnO film, where the diameter $d=1.5 \text{ cm}$ estimated by the formed ZnO film and (b) SEM image of cross-section of ZnO film which presented as estimated ZnO thickness (c) Histogram of Thickness of ZnO nano-surface on PET substrate using R with the average height $h=4.00 \mu\text{m}$, data measured using ImageJ.	88
Figure 4. 5 Raman spectra: (a) Raman spectra of pure ZnO (green line) and ZnO/CuO composite (blue line) nano-surfaces at room temperature. Conditions of recording the Raman Spectrum of the ZnO nano-surface: time acquisition 50s, wavelength 785 nm. Conditions of recording the Raman Spectrum of mixed ZnO/CuO nano-surface: time acquisition 300s, wavelength 785 nm; (b) The inset shows a magnified view of the 100-800 cm^{-1} section of the Raman spectra of ZnO/CuO composite (blue line) nano-surfaces; (c) The inset shows a magnified view of the 280-620 cm^{-1} section of the Raman spectra Raman spectra of pure CuO nano-surfaces was tested at room temperature. Conditions of recording the Raman Spectrum of the CuO nano-surface: time acquisition 150s, wavelength 785 nm.....	90
Figure 4. 6 EIS data: (a) Impedance spectroscopy of 1% ZnO/CuO (1:2) of 200 ng dry antibody, adding PBS and 1 ng/mL CRP for 10 minutes with magnified impedance - 10 to 1000 Hz (b) and phase - 10 to 1000 Hz (c).	93
Figure 4. 7 Comparisons of anti-CRP loading (100 ng and 200 ng) on different surfaces for the detection of 1 ng/mL CRP (n=3) with standard error bars. (Exception: pure 1% ZnO nano-surfaces with 200 ng capture antibody (n=4)).	94
Figure 4. 8 Phase change response versus antigen (CRP) concentration for sonicated ZnO/CuO of 1:2 (n=3) (red) and pure ZnO nano-surfaces (n=4) (blue) with 200 ng capture antibody measured at the frequency of 138 Hz, – standard error bars are shown.	97
Figure 5. 1 Illustration of the ZnO nanoparticle nitrocellulose membrane sandwiched between two coverslips positioned above the electrodes.	105
Figure 5. 2 Scanning electron micrographs of the nitrocellulose membrane cross-section: (a) whole cross-section at 1,000 \times magnification; (b) upper layer of nano-ZnO/nitrocellulose membrane (with small pore structures) at 30,000 \times magnification; (c) middle layer of nano-ZnO/nitrocellulose membrane (with bigger and loose pore structures) at 30,000 \times magnification; (d) lower layer of nano-ZnO/nitrocellulose membrane (with biggest pore structures) at 30,000 \times magnification.....	108
Figure 5. 3 Scanning electron micrographs of nano-ZnO nitrocellulose membrane cross-section at 80,000 \times magnification: (a) upper layer; (b) middle layer; (c) lower layer. Scanning electron micrographs of nano-ZnO/CuO nitrocellulose membrane cross-section at 80,000 \times magnification: (d) upper layer; (e) middle layer; (f) lower layer.....	109
Figure 5. 4 SEM/EDS spectrum/mapping showing the distribution of Zn on the lower layer cross-section of the nano-ZnO membrane: (a) SEM image; (b) EDS spectrum and (c) EDS mapping of the elements of Zn.	111
Figure 5. 5 EDS spectrum/mapping on the lower layer cross-section of the nano-ZnO/CuO membrane: (a) EDS spectrum and (b) EDS mapping of the elements: O, C, Au, Cu, Zn and Al.....	112
Figure 5. 6 Impedance amplitude/kOhms ($Z/\text{k}\Omega$) and phase change/degree ($\phi/^\circ$) on nano-ZnO nitrocellulose membranes (n=3) and nano-ZnO/CuO nitrocellulose membranes (n=3) after a 10 minute incubation time with increasing concentrations of CRP, measured at a frequency of 100 Hz.	114
Figure 5. 7 Impedance phase change/degree ($\Delta\phi/^\circ$) response to seven concentrations of antigen (CRP) on the six different types of membrane. For the 3 nano-ZnO membranes (n=3): with 200 ng capture antibody and without sonication (red), without capture antibody and with sonication (yellow) and with 200 ng capture antibody and with sonication (green). For the 3 nano-ZnO/CuO membrane (n=3): with	

200 ng capture antibody and without sonication (light blue) and without capture antibody but with sonication (dark blue), with 200 ng capture antibody and with sonication (pink purple). 115

Figure 5. 8 Phase change/degree ($\Delta\phi/^\circ$) response versus antigen (CRP) concentration for sonicated nano-ZnO nitrocellulose membranes (blue) and nano-ZnO/CuO nitrocellulose membranes (red) with capture antibody (n=3) measured at the frequency of 100 Hz, – standard error bars are shown. .. 117

Figure 6. 1 The drawings of electrode design: (a,b) the design of planer electrode and (c,d) the interdigitated comb electrode. (a,c) the drawings of electrodes and (b,d) designed sensing area with coverslip as insulating material between nitrocellulose membranes and electrodes as non-direct contact. The liquid molecules (not scaled) shows the flow direction. 128

Figure 6. 2 Illustration of flow-based system: (a) Schematic diagram of strip by flow-based methodology; Illustration of flow-based system composed by components: glass fibre, nitrocellulose and cellulose fibre; (b) The photo of the flow-based biosensor system with angle shaped by two overlapped cover slips on electrodes and 3D printing model (seen Figure 6.3), and the degree was analysed by image J; (c) Dimensions of width and length of components arrangement with angle formed by two overlapped cover slips. 129

Figure 6. 3 3D printing design and assembly: (a) Drawing of 3D printed model design of sensor holder; (b) Photo of 3D printed structure; (The distance of the dots was designed to be the same width as sample pad and absorbent pad and was used to fix the pads of the strip. The electrode board was embedded above the sunken square to create the flow assembly almost at same horizontal level.) (c) Photo of complete flow system: materials (sample pad, nitrocellulose membrane and absorbent pad) alignment with angle formed by two overlapped cover slips on interdigitated electrode with flow rate calculation marks. 131

Figure 6. 4 Impedance change (Z/kOhms) on different nano-membranes on two separate electrodes: (a) nano-ZnO nitrocellulose membranes (n=3) and (b) nano-ZnO/CuO nitrocellulose membranes (n=3) on 4 mm gap planar electrode. (c) nano-ZnO nitrocellulose membranes (n=4) and (d) nano-ZnO/CuO nitrocellulose membranes (n=3) on interdigitated electrode after a 9 minute fluidic time with accumulative concentrations of CRP, measured at a frequency of 100 Hz. 139

Figure 6. 5 Impedance change/kOhms on blank nitrocellulose membranes with 200 ng antibody capture on two separate electrodes: (a) blank nitrocellulose membranes (n=3) on 4 mm gap planar electrode; (b) blank nitrocellulose membranes (n=3) on interdigitated electrode after a 9 minute fluidic time with accumulative concentrations of CRP, measured at a frequency of 100 Hz. 142

Figure 6. 6 Impedance change (Z/kOhms) Comparisons of nano-ZnO/CuO membranes (with 200 ng antibody capture) on two separate electrodes with addition of CRP concentrations (black) vs. pbs buffer only (red) with standard error bars: (a) nano-ZnO/CuO nitrocellulose membranes (n=3) on 4 mm gap planar electrode and (b) nano-ZnO/CuO nitrocellulose membranes (n=3) on interdigitated electrode after a 9 minute fluidic time with accumulative concentrations of CRP, measured at a frequency of 100 Hz. 143

Figure 6. 7 Experimental results (red points), and modelled data, plotted versus time for (a) nano-ZnO on planar electrode; (b) nano-ZnO on interdigitated electrode; (c) nano-ZnO/CuO membranes on planar electrode and (d) nano-ZnO/CuO membranes on interdigitated electrode. 144

Figure 6. 8 Average flow rate (Black lines show regression fits with data points measured) on the planar electrode for CRP concentrations 10 - 166,660 pg/mL (Nitrocellulose membranes with 200 ng antibodies: (a) blue: blank; (b) green: ZnO; (c) red: ZnO/CuO). 148

Figure 6. 9 Average flow rate (Black lines show regression fits with data points measured) on the interdigitated electrode with increasing concentrations of CRP, 1 - 3,166 pg/mL. (Nitrocellulose membranes with 200 ng antibodies: (a) blue: blank; (b) green: ZnO; (c) red: ZnO/CuO). 149

List of Tables

Table 1. 1 A small selection of biosensors illustrating different types and performance	21
Table 2. 1 Comparisons of faradaic and non-faradaic biosensors	36
Table 3. 1 Comparisons of antibodies captured	55
Table 3. 2 Comparisons of antigen/target detection ranges on different biosensors	58
Table 3. 3 Data analysis on impedance values on each set of ZnO nano-surfaces at fixed frequency	65
Table 4. 1 Image surface area comparisons of nano-surfaces, analysed by NanoScope Analysis software.	87
Table 4. 2 Absorbance values associated with anti-mouse Ig-HRP on various nano-surfaces after washing. (n=2).....	92
Table 5. 1 The significant differences in the membrane treatment analyzed by a Wilcoxon rank sum test among four different nano-particles/nitrocellulose membranes with antibody immobilised. ..	116
Table 5. 2 Limits of detection of the phase change calibration curve for non-sonicated and sonicated ZnO and ZnO/CuO membranes.....	118
Table 6. 1 limits of detection on 4 different sensing flow assembly	140
Table 6. 2 Comparison of affinity and ELISA results on both nano-ZnO membranes and nano-ZnO/CuO membranes	145
Table 7. 1 Summary of different types of nano-surfaces/nano-membranes	155

Abbreviations

2D	two dimensional
3D	three dimensional
Ab	antibody
AC	alternating current
AFM	atomic force microscopy
Ag	silver
AgCl	silver chloride
AuNP-DP	gold-labelled detecting probes
BNP	brain natriuretic peptide
CDRs	complementarity-determining regions
cTnT/cTnI	cardiac troponins
CuO	copper oxide
CNTFET	carbon nanotube field effect transistor
CRP	C-reactive protein
CV	cyclic voltammetric
CVD	chemical vapour deposition
DSP	dithiobis (succinimidyl propionate)
EDL	electrical double layer
EDS	energy dispersive X-ray microanalysis
EGFR	epidermal growth factor receptor
EIS	electrochemical impedance spectroscopy
ELISA	enzyme-linked immunosorbent assay
ESEM	emission scanning electron microscope
EtG	ethyl glucuronide
ETD	Everhart-Thornley detector
FET	effect transistor biosensor
Fab	fragment antigen binding
Fc	fragment crystallisable
FNs	fluorescent nanospheres
FTO	fluorinated-tin oxide
GOx	glucose oxidase
GSED	gaseous secondary electron detector
HEMTs	high electron mobility transistors
HIV	human immunodeficiency Virus-1
IED	interdigitated microelectrode
IEP	high isoelectric point
IHP	inner Helmholtz plane
IgG	immunoglobulin G
ITO	indium tin oxide
LFIA	lateral flow immunoassays
LOD	limit of detection
MoS ₂	molybdenum disulphide

NC	nitrocellulose
NHS	N-hydroxysuccinimide
OHP	outer Helmholtz plane
OPN	osteopontin
PBS	phosphate-buffered saline
PCB	printed circuit board
PCL	polycaprolactone
PET	polyethylene terephthalate
PVD	physical vapour deposition
QCM	quartz-crystal-microbalance
QD	quantum dot
RBC	red blood cell
RF	radio frequency
RIFS	reflectometric interference spectroscopy
SAM	self-assembled monolayers
SCC	squamous cell carcinoma
SCL	space charge layer
SELEX	Systemic Evolution of Ligand by Exponential enrichment
SEM	scanning electron microscopy
SiN	silicon nitride
SNR	signal-to-noise ratio
SSA	specific surface area
SWCNTs	single walled carbon nanotubes
TMS	trimethylsilylchloride
TiO ₂	titanium dioxide
Urs	urease enzyme
ZnO	zinc oxide

Acknowledgments

My PhD project would have been impossible without the support from a UWE studentship. During the time of my PhD, I learned to be open-minded and creative. With a slow maturation process, I challenge myself to explore my research independently, with some guidance. The research process helped me to learn how to research things new, design experiments, sort out problems and how to present information clearly.

I would like to express my deep gratitude to Prof. Janice Kiely and Prof. Richard Luxton for their supervision. They brought me in the field of biosensors. Their academic and professional experience also taught me how to become a good researcher. During the years of their supervision, I could keep learning and making progress step by step. Each step of growth is visible. I also thanks to Martina Piano for her supervision and contribution in lab. She helps me be familiar with the experimental environment faster. I also thank David Patton for assisting me to get perfect images by electron microscopy and Energy dispersive X-ray microanalysis. And I also thank Dr Timothy Cox for his support with the Atomic Force Microscopy and Raman Spectroscopy.

I would like to thank all the technicians and staff in HAS and FET faculties for their wonderful and academic help. Without the help of them, it would be impossible to get my experiments done. I have been in a very harmonious team with skilful and kind academics. Team work is also very important, and I feel I have enhanced my skills in working with people.

From the heart, I won't finish my PhD thesis without the support from my parents and friends. They are all right behind me. Although my family is very far from me, I can feel the warmth and trust from them. I also want say thank you to myself for being brave, giving me strength to remain here and persist in difficult times.

I have never thought the year 2020 would totally change my life. Covid-19 has become a big challenge for human beings worldwide. Lifestyle has changed, but we must keep going in life. Be brave and positive, we will succeed.

Chapter 1

Introduction

The development of new analytical approaches that can be applied at point-of-care or point-of-test and allow monitoring of variations in biochemical levels over time is in increasing demand across healthcare, environmental and other fields. Biosensors that can provide continuous information about changing levels of biologically important molecules within our bodies have vast potential in terms of management of chronic conditions, as well as screening and aiding personalised healthcare. Continuous monitoring can provide instant feedback on important biochemical changes and can permit prediction and learning, offering superior performance compared with a single measurement that may miss a pathologically important transient or deliver an erroneous result caused by noise or natural fluctuation.

In the healthcare sector, continuous monitoring of diabetes patients' glucose levels in blood or interstitial fluid is becoming common. However, the enzyme-based electrochemical sensing technique that is used is not readily applicable to monitoring many clinically important (or other) targets. Affinity-based sensors are much more flexible in terms of their range of possible targets, but the vast majority of these on the market or under development in research laboratories focus on single time point measurement. This is generally because the sensor surface becomes saturated with the target molecule and therefore preventing measurement over a prolonged period.

This PhD project addressed some of the limitations associated with existing technology to progress towards an inexpensive, continuous monitoring sensor system, adaptable to a wide range of analytes. This chapter defines the hypothesis and objectives of the research project presented in this thesis. Relevant background information is cited to provide explanations for the direction of the investigation and to demonstrate the novelty of the approach.

1.1 Thesis Statement

The hypothesis that was tested in this research project was: Nano-particle metal oxide semiconductor materials can be integrated within a porous structure to create a sensitive, rapid immunoassay biosensor for measurement of biological target by flow-based methodology.

To test this hypothesis four objectives were defined to provide incremental development of the biosensor and to evaluate the elements of the device, using C-reactive protein (CRP) as the model analyte.

(a) To develop an impedance-based biosensor, comprising a ZnO nano-surface, fabricated using a simple ultrasonic colloidal-dispersion fabrication methodology.

(b) To evaluate the benefits of adding CuO to ZnO to enhance the sensitivity of the 2D nano-surface biosensor.

(c) To demonstrate that a 3D nano-structured biosensor can be fabricated by infusing ZnO and CuO nanoparticles in to a porous membrane.

(d) To evaluate a flow based immuno–biosensor using ZnO/CuO nanoparticle porous structure for detection of CRP in real-time over a period of hours by flow-based methodology.

1.2 Biosensor Components

Biosensors are bioanalytical devices which integrate technologies and techniques from multiple disciplines, such as physics, engineering, chemistry and biology, to deliver readable output signals in response to specific chemical species [1]. The basic concept involves the combination of a biological recognition element and a physicochemical transducer, with biosensors being applicable broadly, for detection, measurement and monitoring purposes in the healthcare, food safety, public health, environmental and security fields. Biosensors are commonly used as point-of-test or point-of-care devices because they can be portable, simple, easy to use, cost-effective and disposable. The majority of biosensors on the market and under development in research laboratories are focussed on the healthcare sector, where they are used to detect physiological analytes or biomarkers, i.e. biochemicals indicative of a disease or physiological conditions. In these applications, to make them effective point-of-care tools for the early detection and monitoring of disease, biosensors must be adapted to measure real biological samples, e.g. blood serum and plasma, urine and saliva and have sensitivities and selectivities within appropriate clinical ranges, whilst delivering the benefits of rapid response, low cost and simplicity of use [2].

Figure 1.1 illustrates the basic elements of a biosensor. A biosensor utilises a biological recognition element, such as antibody, nucleic acid, enzyme and aptamer, immobilised on to a sensing surface. Sensing surfaces can have a variety of different forms, depending on the type of biosensor, including planar, membrane and nanofilms. The sensing surface is linked to, or forms part of, a transducer, which converts a chemical interaction on the sensing surface to a physical output in electrical or optical form. When the biological recognition element interacts with a specific target, such as antigen or DNA sequence, on the sensing surface an output signal which is proportional to the concentration of the target in the sample is produced. Various factors are used for validation of biosensor such as sensitivity, selectivity, reproducibility, stability and linearity [3]. The various components of a biosensor are described below.

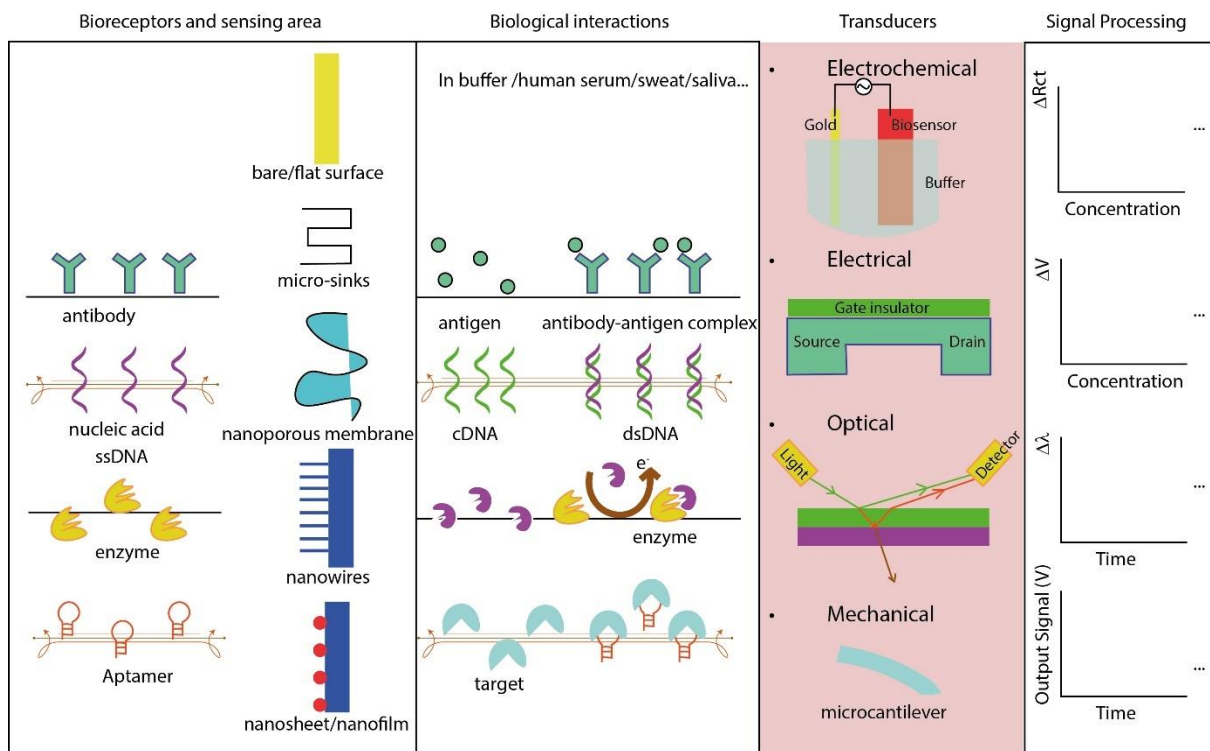


Figure 1. 1 The principle of a biosensor (transducer mechanism adapted by [4–6])

1.3 Bioreceptors

1.3.1 Various Receptors

The choice of a bioreceptor for a biosensor is dependent on the analyte (or biomarker) to be detected and the transducer employed. Biosensor types can be classified according to bioreceptor interactions, i.e. enzymes/substrates, antibody/antigen, nucleic acids/DNA, protein receptors/ligands, cellular structures/cells, or biomimetic materials.

The working principle for enzyme-based biosensors is linked to their capability to specifically detect their target and to catalyse its transformation. There are many examples of enzyme-based biosensors in the literature [4,7–10]. For example, Mozaffari *et al.* immobilised urease enzyme on to a sputtered nano-zinc oxide thin film on a conductive fluorinated tin oxide layer, for urea detection by the measurement of the electrochemical potential across the film [4]. This demonstrated the main advantages of enzyme-based biosensors, i.e. that the biosensor can be inexpensive and provide a rapid result. The main disadvantage of this type of biosensors is that the possible targets are restricted.

Yew *et al.* utilised polycaprolactone (PCL) electrospin-coated test strip to fabricate a nucleic acid-based lateral flow assay [11]. The PCL nanofibers on nitrocellulose membrane improved the sensitivity of lateral flow assay detection for nucleic acid [11]. A second example is provided by Cao *et al.* [12]. This research team developed a sensitive DNA sensor based on a Schottky-contacted ZnO nanowire device for detection of the human immunodeficiency virus 1 gene. The piezoelectric effect was used to measure the performance of the DNA sensor by testing its output current under different target cDNA concentrations [12]. Electrochemistry results showed inverse relationship between the output current and the human immunodeficiency virus 1 gene [12]. Compared with other sensors nucleic acid sensors have the ability to detect sequences of DNA and therefore ideally suited to detection of virus/bacteria.

Aptamers are oligonucleotide or peptide molecules that bind to a specific target molecule. Chu *et al.* demonstrated an aptamer-immobilized AlGaN/GaN high electron mobility transistors that can be used to directly detect proteins with high sensitivity [13]. The operation of this sensors was based on the principle that the protein binding induced gate

voltage drop causing local charge density re-distribution in the gate electrode area which lead to subsequent changes in the charge density on the active channel [13]. An aptamer-functionalized molybdenum disulphide (MoS_2) nanosheet based biosensor was developed for detection of thrombin through the impedance changes of interactions between immobilized aptamer on the electrode surface and thrombin in the electrolyte [14]. Aptamers are adaptable to many applications and advantages including that they are small in size, chemically stability and cost effectiveness. Most aptamers are obtained through a combinatorial biology technique called SELEX (Systemic Evolution of Ligand by Exponential enrichment) [5,15]. A major limitation associated with their use is the lack of high-quality aptamers for clinically important targets.

1.3.2 Antibody-Based Biosensors

Antibody-based biosensors (immunosensors) remain the most adaptable devices, capable of detection of a wide range of analytes and thus being well-suited to varied applications. Their operation is based on an immunochemical reaction between an antigen and an antibody, resulting in a biosensor with high specificity and rapid recognition of the target analyte. There are thousands of examples in the literature. For example, measurement of cardiac troponins (cTnT and cTnI), which are tissue-specific expression markers for coronary heart disease, was performed by Shanmugam *et al.* [16] using a blood circulation diagnostic test, delivering a sensitivity of 1 pg/mL. Osteopontin (OPN), a biomarker of a prostate cancer, was measured using an antibody-based biosensor based on single-walled carbon nanotubes at a sensitivity of 0.3 pg/mL [17]. Similarly, cortisol, a generic biomarker for stress, secreted in sweat, was detected by ultra-sensitive and highly specific electrical double layer modulated biosensor [18]. Other examples of antibody-based biosensors include those for the detection of epidermal growth factor receptor (EGFR) [19], brain natriuretic peptide [20] and insulin [21].

Antibody-based sensors can be categorised as those requiring a label and those that are label-free. Syahir *et al.* [22] summarised a range of label-based biosensor detection methods that are commonly utilised i.e. fluorescently labelled probes [23], chemiluminescent labelling [24] and nanoparticles labelling [25]. Although the kinetics of biomolecular binding to the labels need to be considered, the benefit is the enhanced sensitivity that can be achieved by indirect

measurement of the label rather than the analyte. In contrast, label-free biosensors take advantage directly of properties of the analyte, for example molecular weight (such as microcantilevers [26], quartz-crystal-microbalance [27]) and refractive index (such as surface plasmon resonance [28]) to sense dynamic change [22]. The main advantage of label-free biosensors is that the interactions between biological recognitions are directly detected. Thus, the conjugation of a label to an assay component for the biosensor can be omitted along with any secondary label activation step.

The positive attributes of adaptability and simplicity, together with high sensitivity and selectivity, as shown from the examples above, are the key reasons for the selection of an antibody as the bioreceptor in this research study.

1.3.3 Antibody Immobilisation

A key consideration in the development of an antibody-based biosensor platform is the orientation of the antibody relative to the sensing substrate, as this greatly affects the performance of the biosensor in terms of its sensitivity and selectivity. Welch *et al.* reviewed the orientation and characterisation of immobilised antibody and concluded that the orientation of surface immobilised capture antibody played an important role in immunology [29]. This importance is related to the antibody structure. **Figure 1.2** shows a diagram of immunoglobulin G (IgG) which is an antibody most commonly used in biosensors. The IgG molecule consists of two light chains and two heavy chains which are joined by di-sulphide bonds to form a Y-shaped molecule. The regions which bind to an antigen are found at the ends of the “Y” in the Fab (fragment antigen binding) part of the molecule. The binding site is unique for a given antigen whereas the Fc (fragment crystallisable) part of the molecule is constant and is involved in antibody recognition on cell surfaces. Antigen recognition and binding is through the interaction of six Complementarity-Determining Regions (CDRs), 3 on the light chain and 3 on the heavy chain which make up the antigen binding site. There are two antigen binding sites on each IgG molecules and are responsible for the specific Ab-antigen interactions.

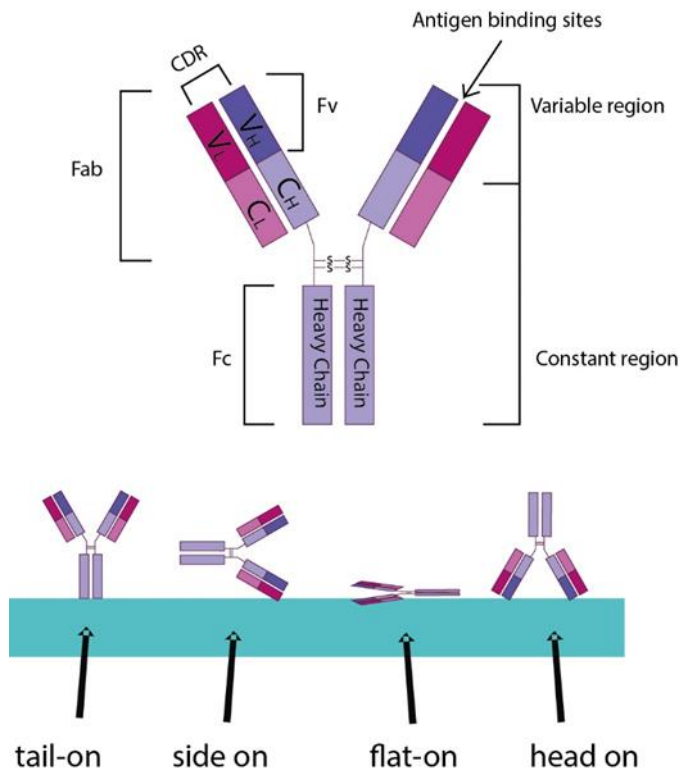


Figure 1. 2 Structure of IgG and IgG immobilized in a random fashion on a surface (Adapted from [30])

Given that the two antigen binding sites are at the terminal ends of the “Y” it is important that the antibody is immobilised on the surface in a way that the antigen binding sites are exposed and available for binding with the antigen. There are two main approaches to antibody immobilisation, one is to chemically couple the antibody to the sensor surface through the creation of covalent bonds; the other approach is to physically absorb the antibody to the sensor surface through the non-covalent bonds. The formation of covalent bonds requires a 1 or more sequential chemical reactions that modify the protein structure of the antibody. There are many chemistries described such as 11–Mercaptoundeconoic acid (MUA) [31], bis(sulfosuccinimidyl) suberate (BS3) [27] and self-assembled monolayers (SAM) of thiol molecules [32] but the N-Ethyl-N’-(3-dimethylamino-propyl) carbodiimide hydrochloride (EDC)/N-hydroxysuccinimide (NHS) chemistry is commonly used [26,33,34]. Covalent binding attaches the antibody permanently to the sensor surface allowing vigorous washing procedures to be used in the assay but the chemical reaction may “attack” the antigen binding sites and reduce the ability of the antibody to bind to the antigen. Non-

covalent attachment on the other hand does not modify the antibody structure as the attachment to the sensor surface is via , electrostatic, hydrophobic and physical interaction through van der Waals forces [30]. With both approaches for immobilising the antibody molecule, the orientation of the molecule on the surface is not controlled. **Figure 1.2** shows the immobilized IgG in four exemplary molecular orientations: tail-on (Fc attached to the surface), side-on (one Fc and one Fab attached to the surface), flat-on (all three fragments attached to the surface) or head-on (both Fab's attached to the surface) [30]. This results in a loss of potential antigen binding sites for the antigen on the sensor surface. Trilling *et al.* presented several immobilization methods: non-covalent and covalent surface attachment, yielding oriented or random coupled Abs [30].

In order to ensure that there is a maximum number of antigen binding sites available on the sensor surface the antibody should be attached via the Fc part of the molecule. This can be achieved in a number of ways, including formation of covalent bonds using a chemistry that only cross-links the Fc terminal amino acids [29], and the use of a second biological molecule on the sensor surface that binds with the antibody via the Fc such as protein G or streptavidin. The issue here is that the antibody capture molecule has to be first attached to the sensor surface as described above. The use of self-assembled monolayers has been described to give a uniformly charged surface to electrostatically bind capture molecules such as Protein A [27] and Protein G [29].

Controlling antibody orientation is a method commonly used to increase the sensitivity in immunological biosensors [35]. There are both advantages and disadvantages of such an approach. Choi *et al.* [28] immobilized anti-CRP on a surface, aligning the orientation of bound anti-CRP to expose the Fab's via protein A, for use in reflectometric interference spectroscopy. The sensitivity of CRP detection was enhanced, compared with the direct immobilisation of antibody without the use of protein A [28]. Ghisellini *et al.* found a 30% higher IgG coverage with an oriented antibody, constructed using the protein A layer, as compared with the randomly oriented one [36].

But in some circumstances not all the intermediate antibody binding molecules will be active and result in capture of antibody molecules, resulting in a lower density of antibody, although orientated correctly (the quantity of adsorbed antibodies per area unit decreases) [35]. The

other major disadvantage of this method of antibody alignment is that the size of antibody capture linker pushes the antibody/antigen interaction further from the sensor surface and potentially beyond the electrical double layer region [15]. Further discussion of this will be provided in Chapter 2.

For applications detecting changes in electrical properties on the sensor surface it is important to ensure that the antibody/antigen interaction is as close to the sensor surface as possible. Despite the loss of some antigen binding sites a simple adsorption of antibody to the sensor surface, immobilised through the formation of non-covalent bonds, has proved successful in generation sensitive biosensors. In one paper, where random immobilisation was used, the exposure of Fab structure maintained good conformation and binding ability [35]. Justino *et al.* fabricated carbon nanotube field effect transistor (CNTFET) devices, which showed linear detection range of 10^{-4} - 10^2 $\mu\text{g/mL}$ for CRP with 1 μg anti-CRP antibodies immobilised on CNTFET surface by non-covalent adsorption [37].

Non-covalent immobilization can result in loss of the antibody from the sensor surface if the binding strength is not strong or if there are extreme changes in pH during the assay [8]. However, these disadvantages have not been realised with ZnO due to the high isoelectric point of 9.5. For example, Penicillinase enzyme was immobilised to ZnO using a simple physical adsorption method [8]. The result showed a good reproducibility and selective biosensor for the quick monitoring penicillin [8]. In another example, positively charged ZnO nanowires with biocompatible nature and larger surface area, were used to bind to Glucose oxidase through electrostatic attraction [38]. In another study, Shen *et al.* demonstrated that EGFR antibody bound to ZnO nanorods were more stable and reproducible than assays using the antibody not on a ZnO surface [19]. The device showed a larger current increment due to the binding of the antibody to Hs68 when immobilised on ZnO nanorods [19].

The approach taken in this study was to use a simple adsorption method to immobilise antibody on the ZnO and ZnO/CuO surfaces as strong electrostatic interactions hold the antibody firmly in place on the surface. Also, the antibody/antigen interaction occurs very close to the sensor surface. It was decided that the simplicity of this approach outweighed the potential advantages of a complex immobilisation protocol to capture antibody on the surface via the Fc region through an additional layer on the sensor surface.

1.4 Substrates

1.4.1 Solid Support Matrices

Biosensor behaviour is strongly influenced by the substrate (sensing surface) geometry. Important attributes of a sensor surface are that it should be biocompatible and the chemical constituents of the material should not interfere with the attached protein. Glass substrates are commonly used as they fulfil these criteria. In addition, they possess other advantages, such as being optically transparent, having good binding properties through charges on the surface, being suitable for high processing temperatures and being inherently versatile [39]. Glass substrates are commonly used for optical biosensors. For example, ZnO nanorods were used in conjunction with FITC-labelled protective antigen affinity peptide on glass substrate for detection of a protective antigen (PA₈₃) of anthrax, using optical ultraviolet emission images with a digital camera [40]. Similarly, the thiol-based cross-linker molecule dithiobis (succinimidyl propionate) (DSP) was incubated on a ZnO coated glass slide for 90 minutes [41]. Fluorescence imaging was used to quantify the fluorescence of Rhodamine 123 in order to determine how well DSP is bound to the ZnO surface [41]. A key weakness of glass is that it is rigid and fragile, compared to other plastic and flexible materials.

Selvam *et al.* compared the performance of both rigid glass and flexible polyimide substrates with deposited gold and zinc oxide electrodes as electrochemical sensors and found that both electrodes demonstrated stable and consistent impedance trends for quantification of ethyl glucuronide (EtG) [42]. Polyethylene terephthalate (PET) is an example of a flexible substrate that is commonly used. Ahmad *et al.* [43,44] utilised hydrothermal growth at low temperatures, using drop seeding on to a PET substrates to produce ZnO nanostructures. Pradhan *et al.* utilised Au-coated PET substrate for an enzymatic glucose biosensor. This author identified that there were commercial advantages associated with the use of this substrate, specifically the lower cost and improved portability due to the light weight and flexibility [38]. For these reasons, flexible plastics, such as PET, polyimide, polyester are frequently utilised as wearable flexible biosensors, for example using inkjet printing to create a temporary 'tattoo' [45].

1.4.2 3D Porous Membranes

Wang *et al.* schematically presented the capacity for antibody immobilization on 3D matrix compared with a conventional 2D surface, as shown in **Figure 1.3** [35]. It confirmed the greater quantity of effective antibodies per unit area sharply increases from 2D to 3D immobilisation [35].

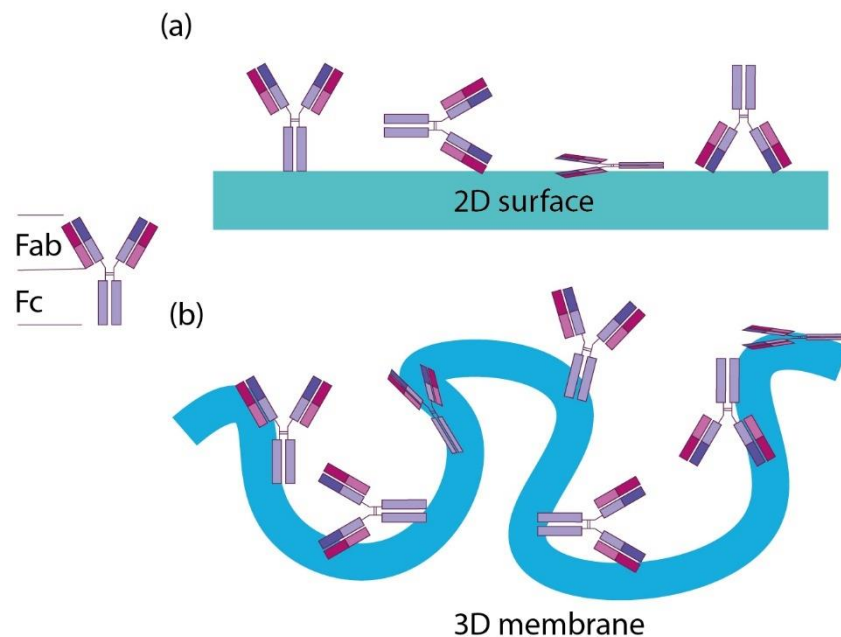


Figure 1. 3 Schematic presentation of immobilization capture antibody (a) Random immobilization on 2D surface. (b) Random immobilization on a 3D membrane. (Adapted from [35])

The physical properties of a nitrocellulose membrane, particularly the pore size, is an important element of a lateral flow system, which affects the performance of the test [46]. A key benefit of performing an immunoassay on a nitrocellulose membrane is that pre-prepared antibodies can be simply dispense on to the membrane to perform the assay to form the test and control lines [46]. Currently, there are many journal articles which describe utilising membranes in colorimetric [46], fluorometric [47,48], and electrochemical [16,49] biosensing systems. In addition to ease of use, three-dimensional substrates/membranes also offer increased surface area for antibody binding so reducing the problem of steric hindrance that may prevent antigen capture [29]. Within the micropore/nanopores a phenomenon known

as 'macromolecular crowding' can be observed. Here, due to volume exclusion, the accessible free space and availability of the sample fluid become limited and this can have a profound effect on the properties of the confined biomolecules. Macromolecular crowding has been shown to increase the stability of biomolecules [50]. Nanoporous materials can also enhance charge screening through nanoconfinement, which affects electron transfer kinetics inside the nanopores [18]. The mass transport within the pores reduces the diffusion time and enhances the detection capability by higher surface to volume ratio [50]. The nanoporous membrane is also selective associated with pore size which reduces background noise from interfering molecules [50].

1.5 Transducers

Antibody-based biosensors can commonly be classified into the following groups: (1) Electrical biosensor, e.g. field effect transistors and capacitive sensors [37]; (2) Optical biosensors, e.g. based on fluorescence [46] and interference spectroscopy [28]; (3) Mechanical biosensors e.g. microcantilevers and surface acoustic wave devices [26]; and (4) Electrochemical sensors, e.g. based on potentiometry [51] and electrochemical impedance spectroscopy [52]. Examples of each type are provided below.

1.5.1 Electrical Biosensors

One of the main advantages of electrical detection methodologies is their capability of being easily integrated within standard electronic microfabrication formats, as well as requiring very small analytical volumes. One example is the field-effect transistor biosensor (bio-FET), which comprises 2 electrodes (the source and drain) integrated with a conducting material as well as the third electrode (the gate). When charged molecules (analyte) bind to bioreceptors on the gate, a change in the charge distribution of the underlying semiconductor material occurs, altering the conductance between the source and the drain and hence the output. Adaptation of the gate surface can enhance the properties of the bio-FET [5].

Justino *et al.* presented results for carbon nanotube field-effect transistor (CNTFET) biosensor [37]. In a CNTFET biosensor, an array of carbon nanotubes is used as the channel material instead of bulk silicon as in the traditional FET structure. The electrical mechanism associated with the biosensor operation was that the amine groups of the antibodies reduced the number of holes in the nanotubes, which consequently reduced the drain current [37]. The advantage of this label-free sensing methodology was that a lower limit of detection at 10^{-4} $\mu\text{g/mL}$ and a broad detection range linear detection range of 10^{-4} - 10^2 $\mu\text{g/mL}$ for CRP [37]. Compared with conventional FET biosensors, Chu *et al.* demonstrated an antibody and an aptamer-immobilized AlGaIn/GaN high electron mobility transistors (HEMTs) for directly detecting various proteins including CRP in both buffer and human serum in 5 minutes with high sensitivity around 0.36 mg/mL [13]. The sensors are based on the principle that the protein binding induces a gate voltage drop, causing local charge density re-distribution in the

gate electrode area which leads to subsequent changes in the charge density on the active channel [13].

Although bio-FETs offer excellent sensitivity and the potential for inexpensive mass manufacture of devices, the key challenges relate to the practical implementation of the devices particularly the integration with microfluidic systems for real sample. However, the new advancements in microfluidics are set to overcome these issues in the future.

1.5.2 Optical Technologies

Biosensors utilising optical transducers are common both in the research laboratories and as commercial products. In optical biosensors, the transduction process induces a change in optical properties, such as the absorption, transmission, reflection, or refraction in response to the chemical change caused by the biological interaction. Optical biosensors have been fabricated where an optical label is utilised to indicate binding in an immunoassay. Wu *et al.* [46] fabricated a fluorescence biosensor based on quantum dot (QD) labels and a lateral flow test strip for CRP detection. The QD fluorescence signal was measured on the test line and control line after 3 minutes, the output being captured under a 365 nm UV light. The ratio of quantum dots to antibodies was a key point for optimising biosensor performance. This QD-based lateral flow immunoassay offered a broad detection range from 0.5 to 1000 ng/mL with a 99.9% correlation coefficient [46]. Sensitivity has been further improved through the use of fluorescent nanospheres (FNs). One FN contains a number of quantum dots, has a 380-fold higher luminescence compared with one QD [48]. An immunofluorescent nanosphere (IFN)-based lateral flow assay strip has been shown to be more sensitive than conventional Au-based lateral flow test strip for CRP detection, with a limit of 27.8 pM. Results were generated within 20 minutes, with fluorescence intensity and bioactivity of fluorescent nanospheres remaining stable for 6 months [48]. Another label-based approach involves the use of coloured nanoparticles. Cai *et al.* [47] developed a rapid immunoassay based on Nile-red doped nanoparticles/CRP monoclonal antibody conjugate. This immunochromatography technique based on carboxyl polystyrene nanoparticle is simple and fast (3 minutes) with a detection limit of 0.091 mg/L, and provides quantitative analysis in the range of 0.1 - 160 mg/L. The advantage of label-based biosensors is that they can be utilised for a wider range of

biomarkers and can deliver could sensitivity [47]. The disadvantage is that the addition of a label adds complexity to the measurement process.

By contrast, reflectometric interference spectroscopy (RIfS), another type of optical biosensor, is label-free. The principle of operation is that when an analyte is applied to the sensing surface, there is red-shift in the wavelength due to the increase of optical thickness [28]. The difference in wavelength before and after the adsorption is used as an index of analyte binding. Choi *et al.* adapted of this technique for a continuous flow CRP biosensor in which anti-CRP was immobilised on a silicon nitride-coated chip using protein A to ensure aligned orientation, for the RIfs sensing [28]. This provided an alternative to the more commonly used surface plasmon resonance sensors [53]. In general, label-free optical biosensors show promise regarding detection and measurement of targets in real complex samples, avoiding or limiting the sample preparation phase.

1.5.3 Mechanical Biosensors

Mechanical biosensors measure force, displacement or mass changes associated with a biological interaction on the sensing surface. Among mechanical biosensors, piezoelectric approaches have become the most established techniques, as compared with other techniques such as surface acoustic wave and micro-cantilevers. One example of a combination of these approaches is reported by Yen *et al.* [26]. This research team produced a piezoresistive microcantilever biosensor that was composed of several layers, i.e. a structural insulation layer of nitride and oxide, a piezoresistive polysilicon layer, an insulation layer of nitride, a gold layer for surface reactions, and a passivation layer of nitride [26]. The induced change in surface stress, caused by deflection of the cantilever due to immobilised antibody molecules binding with the target, was measured [26]. A response curve to CRP concentrations in the range from 1 µg/mL to 200 µg/mL had a linear range between 10 to 110 µg/mL [26]. This technique also demonstrated the saturation of responses beyond 100 µg/mL [26]. The advantage of this technique was that the microcantilever could be modified to be able to detect CRP by designing surface area for exposure of immobilised antibody. In the laboratory, cantilever biosensors demonstrate very high sensitivity, fast response time, and they also benefit from ease of miniaturization for the development of point-of-care sensors.

The disadvantage is that the response of microcantilever was extremely sensitive to temperature change and other factors.

Another example of a mechanical biosensor is the quartz-crystal-microbalance (QCM) biosensor. These devices determine the mass change on a sensor surface due biological interaction by measuring the change in frequency of a quartz crystal resonator. Kentaro *et al.* developed a wireless QCM biosensor for detection of CRP with a mass-amplified biomarker in the form of a bio-nanocapsules [27]. Each nanocapsule captured about 60 IgG molecules [27]. The resonance frequency decreased significantly for the resonator chip exposed to CRP when they were injecting anti-CRP antibodies [27]. The detection limit is lower than 10 pg/mL [27]. Compared with optical techniques, QCM is more sensitive to water-associated adsorbed protein [27]. But there are few disadvantages, such as long detection time with low-throughput measurement [27].

1.5.4 Electrochemical Biosensors

Electrochemical biosensors are generally based on an enzyme-catalysed oxidation/reduction reaction that produces or consumes electrons. Analytical techniques used for measurement of the electron transfer or charge distribution include are potentiometric, capacitive and impedimetric methods. One of the key benefits of enzyme-based reactions is that the sensor can provide a rapid and reliable result with good performance [54]. The use of multiple tests over period of time to show change in analyte concentration, results in assay variability and high reagent consumption. This is reduced by continuous flow measurements. Zhang *et al.* developed a continuous monitoring method for the dynamic methylation process and obtained more objective and precise information in less time and lower reagent consumption [55].

More recently researchers have utilised nanomaterials to improve standard electrochemical biosensor performance. For example, Ibupoto *et al.* [51] fabricated a disposable antibody-immobilized zinc oxide (ZnO) nanotube based potentiometric biosensor. ZnO nanotubes, with the high isoelectric point (IEP) value, about 9.5, showed a strong affinity for low IEP protein molecules which promoted the binding of proteins and provided a high electron transfer [51].

The electrochemical assay of antibody immobilized ZnO nanotube based sensor electrode showed a linear logarithmic response from 0.01 ng/mL to 1000 ng/mL with good regression coefficient, approximately 0.99, with a result produced in less than 10s once the analyte was added [51]. Batra *et al.* also found that ZnO thin film with large surface area for effective loading of cholesterol oxidase (ChOx) [56]. The prepared bioelectrode ChOx/ZnO/Pt/Si is highly sensitive to the detection of cholesterol over a wide concentration range, 0.12 - 12.93 mM for 5 second response time [56]. It showed the antibody immobilized ZnO nanotubes revealed the good linearity and fast response time.

The electrochemical biosensor normally converts the detected analyte into an electrical signal that can be measured. The biosensor has the advantages of high sensitivity with fast response time by direct transduction of electrons. The electrodes can also be modified and improved with combination of carbon-based or non-carbon-based nanomaterials. However, the traditional electrochemical biosensors are limited on types of analyte due to electrical properties. And they are quite strict under biocompatible environment especially ionic strength with optimum temperature and pH.

1.5.5 Impedimetric Biosensors

Electrochemical impedance spectroscopy (EIS) is commonly applied for monitoring the changes in the capacitances of an electrochemical biosensor or the charge transfer resistance (R_{CT}) when biomolecules bind to the bioreceptors on the sensing surface. Bryan *et al.* [52] presented a sensitive and reusable electrochemical impedimetric biosensor for the detection of CRP in blood serum. EIS spectra were collected across the 0.05 Hz to 10 kHz frequency range. It was found that charge transfer resistance increased linearly with logarithmic CRP concentrations in the range 0.5 - 50 nM [52]. Nanomaterials have also been shown to improve electrochemical impedimetric biosensor performance. Yagati *et al.* [57] developed an impedimetric biosensor based on an indium tin oxide (ITO) electrode array, functionalised with a reduced graphene oxide-nanoparticle hybrid, for the detection of CRP. A calibration curve was plotted based on the change of impedance at 10 Hz across the 10^{-1} ng/mL to 10^4 ng/mL range [57]. The biosensors of both of these authors [52,57] were faradaic using redox couple ferro/ferricyanide ($[\text{Fe}(\text{CN})_6]^{3-/4-}$) to ensure a significant change in charge transfer

resistance following binding of CRP. More details about comparisons of faradaic and non-faradaic EIS is provided in the next chapter, section 2.1.

Impedance spectroscopy can also be used to interrogate non-faradaic biosensors. For direct non-faradaic analyte detection, capacitance changes are measured in the absence of faradaic currents following a biological interaction on the sensing surface [58]. No redox probe is required for non-faradaic sensors, some of which are referred to as capacitive sensors [59]. The principle of operation of this sensor is that changes in dielectric properties and charge distribution caused by the formation of antibody-antigen complexes on the sensing surface give rise to variations in impedance [60]. Qureshi *et al.* [60] fabricated a multianalyte capacitive immunosensor based on a gold interdigitated electrode capacitor. Dielectric constant values were calculated in the frequency range from 50 to 173 MHz by analysing the differences relative to the control results. The biosensor proved capable of detection of CRP in the range of 25 pg/mL to 25 ng/mL [60].

There are a number of advantages of impedimetric-biosensors compared with other devices, including low cost, low power and high sensitivity with minimal hardware demand [61]. Similarly to other label-free biosensors, less sample preparation is necessary compared with labelled approaches and for non-faradaic biosensors this benefit is enhanced by the lack of requirement for a redox probe [41]. Similarly to other electrochemical sensors, impedance responses can be utilised to dynamically monitor analyte concentrations [62]. A further advantage of capacitive sensors is that a sensor surface can be easily decoupled from the sensor itself, thus providing the potential for inexpensive measurement with disposable sensor surfaces (rather than sensors). It is for these reasons that a non-faradaic impedimetric approach was used in this research study.

1.5.6 Comparison of Biosensors

Traditionally, immunoassay technologies, such as enzyme-linked immunosorbent assay (ELISA), have been used for measurement of diagnostic biomarkers. ELISA is a traditional well-plate-based test with antibodies by enzyme-labelled bound to a plastic well to measure added antigen bound to the antibodies. Although ELISA is the most utilised method for detection of biomarkers, there are several drawbacks to this method which prevents its use as a rapid diagnostic and which are a driver for the development of biosensor technologies. Firstly the method is expensive and time-consuming [63]. Secondly, the method generally requires specialised laboratory procedures, such as the need for use of labels, detection times of several hours and large volumes of reagents [63,64]. Nowadays, the ELISA technique has been used as a comparison with other point-of-care devices for early diagnostics and there are numerous examples in the literature. For example, Malkoc *et al.* compared their label-free EIS system with ELISA measurements, illustrating comparable performance, but demonstrating the benefit of the EIS approach in terms of portability and ease of use [21].

Table 1.1 compares a limited number of biosensors illustrating a number of transduction methods, bioreceptors and antibody immobilisation methods. Key important comparative features are incubation and/or analysis time and sensitivity plus limit of detection. Although it must be noted that in most cases the total sample preparation time was not provided, so there is some difficulty in obtaining true comparison. However, from the table it can be seen that short response time is possible with impedimetric sensors, particularly from the sensor developed by Mozaffari *et al.* [4]. The table also shows that both covalent and non-covalent immobilisation techniques are commonly used with both techniques delivering biosensors with good performance parameters. The use of nanocrystalline-based membrane or nanoparticles has consistently enhanced the sensitivity of biosensors, e.g. [17]. Even relatively simple techniques, such as immunochromatography, has benefited from the use of carboxyl polystyrene nanoparticle delivering results relatively rapidly with high sensitivity across a broad range [51]. Nanostructured metal oxide semiconducting films have also shown to offer good performance, for example, biosensors using ZnO surfaces demonstrating sensitivities about 4 times higher than devices fabricated from planar gold [16]. Combining non-faradaic

impedimetric sensing with the benefits of nanosurfaces has delivered very high sensitivity and presumably rapid measurement time [13].

Table 1. 1 A small selection of biosensors illustrating different types and performance

Biosensors / Transducer	Biological recognition element	Sensing surface/ Layer	Antigen/ Tested range	Incubation time / Time for analysis	Sensitivity / Detection limit	Refs
Electrochemical biosensor	Antibody to cardiac troponin-T (cTnT) (Covalent attachment using crosslinking molecule)	Planar gold, nanotextured ZnO and nanostructured ZnO	1, 10 and 100 ng/mL cTnT in PBS and HS buffer	15 minute incubation time (No analysis time reported)	1 pg/mL for cTnT in HS on nano-ZnO electrodes	[16]
Electrical biosensor Indium–Gallium–Zinc–Oxide thin film transistor	Antibody to (epidermal growth factor receptor) EGFR (Non-covalent conjugation with ZnO nanorods on the micro-sink)	Indium–Gallium–Zinc–Oxide thin film transistor on the glass substrate and an extended sensing pad	0.1 ng/mL EGFR in the total protein solution of extracted from Squamous cell carcinoma (SCC)	8 minute preparation time (No analysis time provided)	Selectively detects 36.2 fM of EGFR in the total protein solution of 0.1 ng/mL extracted from SCC	[19]
Electrochemical biosensor Flexible nanoporous membrane EIS biosensor	Antibody to α - cortisol (Covalent immobilisation by Dithiobis [Succinimidyl Propionate] (DSP) linker)	ZnO deposited on nanoporous polyamide substrate	1 pg/mL to 100 ng/mL cortisol hormone	15 minute incubation time	1 pg/mL cortisol in synthetic sweat and 1 ng/mL in human sweat	[18]
Electrochemical biosensor Non-Faradaic Impedimetric Sensor	Antibody to brain natriuretic peptide (BNP) (Covalent immobilisation by DSP linker)	The printed circuit board (PCB) sensor with interdigitated electrodes interfaced with nanoporous alumina membrane	1 fg/mL to 100 ng/mL brain natriuretic peptide (BNP)	15 minute incubation time	10 fg/mL	[20]
Electrochemical biosensor EIS	Antibody to insulin (Covalent self-assembled linker onto the electrode surface)	Gold disk working electrode, silver/ silver chloride reference and platinum counter	0 pM to 1500 pM target insulin within the physiological insulin range	N.A.	2.26 pM	[21]
Electrical biosensor A label-free, highly sensitive and transparent immunosensor	Antibody to osteopontin (OPN) (Covalent immobilisation on the single walled carbon nanotubes (SWCNTs))	carboxyl group functionalized SWCNTs deposited between two gold/ indium tin oxide electrodes on a glass substrate	1pg/mL to 1mg/mL in PBS	60 minute incubation time / less than 1 minute detection time	0.3 pg/mL	[17]

Electrical biosensor AlGaN/GaN high electron mobility transistor (HEMTs)	Aptamer (ssDNA) to Human Immunodeficiency Virus-1 Reverse Transcriptase (HIV-1 RT) (Covalent immobilisation on gold gate electrode opening via S-Au self-assembly)	EDL AlGaN/GaN HEMTs are designed as a separated gate electrode from the active channel of the HEMTs	Measured concentrations are 1 fM, 10 fM, 100 fM, 1 pM and 10 pM.	5 minute incubation time	N.A.	[13]
Electrochemical biosensor Impedimetric biosensor	Aptamer (ssDNA) to thrombin (Covalent conjugation with molybdenum disulphide (MoS ₂) nanosheet via thiol moiety)	MoS ₂ nanosheets on a silicon substrate with platinum electrodes	2.67 pM–267 pM in PBS 53 pM–854 pM in diluted human serum	15 minute incubation time	267 fM in PBS/ 53 pM in human serum	[14]
Electrochemical biosensor Impedimetric biosensor	Urease enzyme (Urs) to urea (Non-covalent immobilisation by electrostatic adsorption)	Sputtered Nano-ZnO thin film on conductive fluorinated-tin oxide (FTO) layer FTO/Nano-ZnO/Urs -serving as sensing electrode	Linear range of 0.83–23.24 mM	Short response time of less than 4 seconds	0.40 mM for urea and sensitivity of 0.637 kΩ per mM	[4]
Optical biosensor A nucleic acid-based lateral flow assay	Synthetic target oligonucleotide (Non-covalently bound to the gold-labelled detecting probes (AuNP-DP) at the test lines)	lateral flow test strips with electrospun polycaprolactone (PCL) fibres on the nitrocellulose membrane	Tested range 5 nM -0.1 nM.	N.A.	0.5 nM	[11]
Optical biosensor Lateral flow immunoassay with optical labels	Antibody to C-reactive protein CRP (Covalent immobilisation on carboxylic groups on the surface of the red fluorescent nanoparticles)	Antibody-antigen complexes were captured on the nitrocellulose membrane	Analysed range 0.1–160 mg/L.	3 minute detection process	0.091 mg/L	[47]
Optical biosensor Reflectometric interference spectroscopy (Rifs)	Antibody to C-reactive protein CRP (Covalent immobilization via protein A on a silicon nitride)	The silicon nitride-coated silicon substrate (SiN chip) treated with trimethylsilylchloride (TMS), followed by UV-irradiation to generate silanols	0.01 to 10 µg/mL	UV-light was irradiated for 15 minutes/ 5 minute stabilisation time	N.A.	[28]
Electrochemical biosensor Potentiometric biosensor	Antibody to CRP (Covalent immobilisation on ZnO nanotubes mixed with solution of glutaraldehyde)	ZnO nanotubes-based sensor electrodes	0.01 ng/mL to 1000 ng/mL	Less than 10 second response time	0.001 ng/mL	[51]
Electrical biosensor Schottky-contact ZnO nanowire biosensor	ssDNA to human immunodeficiency virus 1 (HIV1) gene (Non-covalent immobilisation by electrostatic adsorption)	ZnO nanowires on a polyethylene terephthalate substrate	1×10^{-10} and 1×10^{-7} M	N.A.	N.A.	[12]

1.6 Flow Systems

The first lateral flow tests presented qualitative results based on the presence or absence of a signal line and then test design has progressed toward semi-quantitative and quantitative assays and the integration of hand-held readers [65]. Traditional lateral flow immunoassays (LFIA) are designed to provide a cost effective, simple, rapid and portable means of testing of analytes. Gold nanoparticles (AuNP) are commonly used as reporters. The idea behind the LFIA is that a sample (liquid) containing the target analyte moves within the various compartments of the strip with no application of external forces by capillary action. This leads to the interaction between the analyte and the molecules within the strip. Conventionally a lateral flow strip consists of sample pad, conjugate pad and absorbent pad as well as nitrocellulose membrane with test line and control line, as seen from **Figure 1.4** [66].

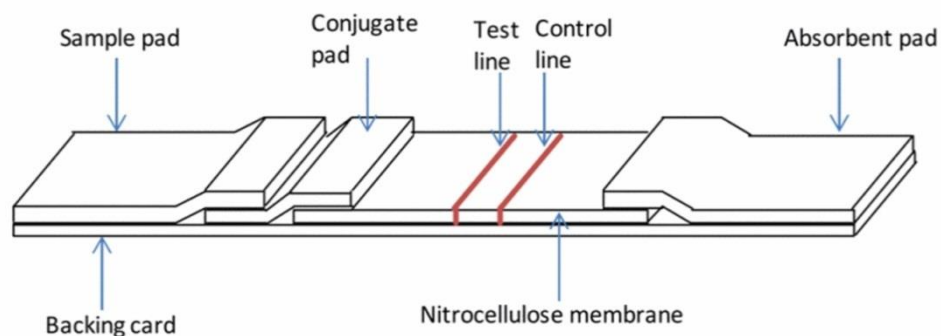


Figure 1. 4 Typical configuration of a LFIA strip [66].

The analyte-detector antibody complex and free analyte target flow through the membrane by capillary force in LFIA system and bind to a line of antibody immobilised within nitrocellulose membrane capturing the reporter agents and forming a visible line in the nitrocellulose. The formation of the line is dependent on the affinity of the antibody/antigen interactions along with other factors such as those associated with capillary flow. These also include practical issues, for example, if adsorption occurs at the point of dispensing, the buffer may actually spread further than the capture reagent. This is because the rate at which the capture reagent adsorbs in to the nitrocellulose could cause the applied reagent spread into

a wider line. To overcome this problem, the reagent can be dispensed at a higher concentration in a low volume to apply the same mass. Li *et al.* recognised [67] this phenomenon and found, as expected, that red blood cell (RBC) flow rate was significantly slower than the plasma and was strongly affected by the addition of calcium (Ca^{2+}) ions. Consequently, travel time could be used to determine the relative viscosity of sample fluids. Research is also reported on methods for improved measurement of the test and control lines. For example, analysis of the image taken by a commercial smartphone, with an attached microlens and 3D-printed chip-phone interface, of a gold nanoparticle-based colorimetric LFIA has been used to quantify the levels of CRP in a sample [63].

The application of lateral flow assay type technologies has broadened with development of paper-based biosensors. Many of these are simple adaptations of the LFIA. For example, Oh *et al.* [68] introduced an additional antigen line in sandwich AuNP-conjugate-antigen conventional LFIA which interacted with CRP antibody solution in nitrocellulose membrane. However, many variations of the standard LFIA format are reported. For example, Hegener *et al.* presented a paper-based diagnostic device which consisted of a sample pad, a porous membrane, and a wicking pad [69]. The aim was to distinguish anticoagulation patients taking vitamin K antagonists, so that anticoagulant dose could be adjusted appropriately [69]. Yew *et al.* utilised polycaprolactone (PCL) electrospin-coated test strips to create a nucleic acid-based lateral flow assay [11]. The PCL nanofibers on nitrocellulose membrane improved the sensitivity of LFIA detection for nucleic acid with the limit of detection (LOD) of 0.5 nM [11].

Within healthcare there is an unmet need for point-of-care, continuous, dynamic, non-invasive monitoring of biochemical markers to understand health conditions [62]. Flow systems offer this capability. One solution is the development of lab-on-chip systems that incorporate microfluidic channels to move reagents and the sample to a sensor chamber [70]. This approach is complex and expensive contrary to the paper fluidic systems. Carrell *et al.* advocated the integration of sensing, such as electrochemical sensors, with lateral flow systems to improve detection limits and increase diagnostic practicality [71]. Kinnamon *et al.* developed a portable electronic device to demonstrate the feasibility and translatability of a real time cortisol biosensor into an economical and compact form factor for eventual wearable integration [49]. The efficacy of the device was established using both a lab

potentiostat and developed miniaturised electronics by performing measurements to demonstrate a dose response in continuous dosing studies [49].

The key advantages of paper-based biosensors for flow assays remain their low cost and ease of use. Therefore, techniques to adapt and improve these should not impact greatly on these features. An additional benefit of a flow system is that it is well suited to continuous monitoring of an analyte. In the research work presented in this thesis a flow system is developed which retains the advantages of the technique whilst creating a biosensor with increased sensitivity utilising the nanoporous membrane for enhanced biomolecule capture.

1.7 Zinc Oxide and Copper Oxide Nanoparticles

Section 1.5.6 evidences that nanoparticles can play a crucial role in improving the performance of antibody-based biosensors. Semiconductor oxide nanoparticle-based layers need low temperature and short or easy annealing process to convert a precursor and to form sensing surfaces [39]. Furthermore, metal oxide nanostructured affinity based biosensors can be downsized with high sensitivity and selectivity due to nano-scale dimensions and increased surface area for biomolecular binding [16].

1.7.1 ZnO Nanoparticles

From a structural perspective, zinc oxide crystallizes in two main forms, hexagonal wurtzite and cubic zinc blende. The wurtzite structure is most stable at ambient conditions and thus most common. ZnO wurtzite nanostructures are composed of Zn^{2+} and O^{2-} ions which are stacked alternatively along the c-axis [1]. Because of the presence of zinc interstitials and oxygen vacancies, ZnO is intrinsically a n-type semiconductor material [1]. ZnO can produce a piezoelectric effect once it is strained due to the non-centrosymmetric crystal structure [72]. The Fermi level, E_F , is defined by the condition of charge neutrality including free-carriers (holes in p-type semiconductors and electrons in n-type semiconductors) concentrations in valence and conduction band [73]. The band gap (E_g) is determined by the differences of the top valence band and the lowest conduction band [73]. ZnO has a wide band gap at 3.37 eV, which allows for an ability to sustain large electrical field [18].

When an electrolyte interfaces with a ZnO nano-surface (semiconducting material), polarization of charges in sensing surface occurs and a complementing charge layer is formed in the fluid [42]. This electrical double layer is described in more detail in Chapter 2. At physiologically relevant pH values, as ZnO has high isoelectric point (IEP), at approximately 9.5, it has a positively charged functionalised surface. This facilitates electrostatic immobilisation of negatively charged biomolecules, as generally they have a lower IEP [1]. ZnO nanostructures have other advantages, for example their high surface to volume ratio which results in improved sensitivity. Also, their biocompatibility and non-toxicity allows the biomolecules to retain activity while immobilised on the surface. In addition, ZnO material

and methods of nanoparticle fabrication are low cost. This combination of properties makes ZnO nanoparticles particularly suitable for biosensing applications.

1.7.2 CuO Nanoparticles

CuO is a semiconductor with a relatively narrow band gap of 1 eV - 1.57 eV and is defined as p-type with copper vacancies acting as acceptors for hole conduction [74]. CuO material is frequently added to ZnO structures forming the p-CuO/n-ZnO junctions with electron-hole recombination. The higher resistance of ZnO/CuO layers indicates the formation of a p-n junction which are depleted of electrons from ZnO layer more effectively than oxygen adsorption [75]. Todorova-Balvay *et al.* [76] researched the immobilisation of human antibodies for metal-ion affinity chromatography and found that the affinity of IgG(s) for Cu is larger than Zn. The mixture CuO nanoparticles with ZnO also increased the signal response of the biosensor. Widiarti *et al.* [77] found that the addition of CuO decreased the band gap energy of the composite which enhanced the conductivity of the material, as the electrons can be easily excited from the valence band to the conduction band. They also demonstrated that this enhanced antibacterial activity. Compared with ZnO nanostructures, biosensors fabricated by ZnO/CuO composite have been shown to be more sensitive [75].

1.7.3 Fabrication of ZnO and CuO Nanostructures

A number of methods have been used to synthesize ZnO and ZnO/CuO films and other types of nanostructures on substrates for biosensors, such as ZnO micro-pompons [78], nanowires [79], nanorods [19,80,81], nanofibres [82] and nanotubes [83,84]. Vapour deposition techniques are the frequently preferred techniques for production of thin films and other highly regular structures, because they result in films with high purity, reproducible properties, and smoothness. Physical vapour deposition (PVD) [85] describes a variety of vacuum deposition techniques. The basis of the process involves converting a material from a solid/liquid to a vapour phase and then back to a thin film on a substrate.

The most common PVD processes are sputtering and evaporation. One example is radio frequency (RF) magnetron sputtering system [4]. Sputtering is the process whereby atoms or molecules of a material are ejected from a target by the bombardment of high-energy particles. RF magnetron sputtering method is a high-rate vacuum coating technique which can be precisely controlled. It can also be utilised for functionalising terminated sites on thin film. Magnetron sputtering is recognised as the most scalable technique with low crystalline inequality [73]. The pulsed laser deposition [86] is a second PVD technique which uses a high-power laser to create the vapour rather than being based on the RF power under background gases with suitable growth pressure. In a similar way to RF magnetron sputtering, laser deposition requires consideration of a number of key factors that may influence the quality of deposition during the process, such as background gas, growth pressure, substrate temperature, laser energy density, target to substrate distance and the pulse repetition rate. For example, thin films of ZnO/CuO composites of thickness of 120 nm have been deposited onto a glass substrate using the pulsed laser deposition technique at an oxygen pressure of 100 mT with substrate temperature of 300 °C [86]. Compared with PVD, which, in general, utilises a vapour condensed on substrates without chemical reaction, in typical chemical vapour deposition (CVD), the substrate is exposed to one or more volatile precursors, which react or decompose on the substrate surface to produce the desired deposit [87]. The key disadvantages of these vapour deposition techniques are the high cost of equipment and operating processes.

By comparison the wet chemical bath method, followed by calcination, is one of the most common techniques for synthesising ZnO nanostructures for biosensors because it is relatively simple and requires inexpensive equipment. The disadvantage is that the ZnO nanostructures fabricated based on wet chemical method are highly dependent on the fabrication protocol and quite unique, for example ZnO micro-pompons [78] and waxberry-like ZnO microstructures [88].

Other techniques are utilised to produce specific ZnO and ZnO/CuO structures. For example, electrospinning is a simple and versatile technique for fabrication of ZnO nanowires and nanofibers. This method uses electric force to draw charged threads from solutions up to fibre to create fibres of hundreds of nanometers. Zhao *et al.* [89] created single mesoporous ZnO

nanofibres on substrate electrodes by electrospinning and subsequent annealing process which exhibited good biosensing performance, stability and high electrical communication efficiency [89]. The key advantage of this technique is that electrospun nanowires are relatively easily to fabricate with low cost for large-scale fabrication of nanowires. The disadvantage includes the use of organic solvent. Hydrothermal synthesis includes the various techniques of crystallizing substances from high-temperature aqueous solutions at high vapour pressures method [79,90]. Sanguino used a hydrothermal process to produce a high density of ZnO structures deposited on Au microelectrodes, however, the lack of deposition time caused the uneven coverage of the electrode [91].

The examples listed below are the main important fabrication methods contributed to experimental methodologies in this thesis. Drop casting method is a quick and easy method for fabrication of ZnO nanostructures in a large scale at low cost [92]. It involves dropping a solution on to a surface and allowing the solvent to evaporate to leave the required solid film. Anusha *et al.* [92] fabricated enzymatic glucose biosensor with ZnO porous nanostructure by simple drop casting technique. The ZnO nanoparticles formed in the surface range from 30 to 50 nm which exhibited good biosensor properties with high sensitivity ($62.14 \mu\text{A}\text{mM}^{-1} \text{cm}^{-2}$), and the detection limit of the biosensors was estimated for the electrode ZnO/Pt/CS/GOx at $16.6 \mu\text{M}$ glucose [92]. The disadvantage is that it is difficult to obtain a uniform coating and to control the thickness. However, the technique is quick, simple and inexpensive. Instead of dropping sol on glass substrate [92], Yang *et al.* utilised ZnO sonicated suspension to drop on glassy carbon electrodes to develop the hydrogen peroxide biosensors [93]. The as-prepared ZnO nanostructures were synthesised by citric acid assisted annealing process. The precursor made by mixing the solution of 0.16 M citric acid ($\text{C}_6\text{H}_8\text{O}_7 \cdot \text{H}_2\text{O}$) in ethanol and 1.8 M zinc acetate ($\text{Zn}(\text{CH}_3\text{COO})_2 \cdot 2\text{H}_2\text{O}$) in distilled water. The precursor was stirred at $80 \text{ }^\circ\text{C}$ for 9 h followed by calcination at $400 \text{ }^\circ\text{C}$ for 2 h to obtain the ZnO nanopowders [93]. The suspension of as-prepared ZnO nanostructures were dispersed in ethanol by ultrasonication for 1 h. $5 \mu\text{L}$ of complex, which consisted of multiple fork-like ZnO nanostructures in suspension, was dropped onto the surface of glassy carbon electrode and dried at room temperature [93]. These methods were relatively simple to perform, and the key factor was the control of the precursor which may influence the shapes of ZnO nanostructures.

The drop cast and calcination method suffers from problems associated with aggregation of particles when they are in the form of a dry powder due to electrostatic charges. The sol made using precursors also needs to be carefully prepared to ensure a homogeneous suspension. In this research study, a new approach has been developed in which a nanoparticle homogeneous suspension is utilised in a drop cast process. A key element of this is using sonication to obtain a homogeneous solution.

1.7.4 Sonication

Sonication is a common, efficient and convenient way for dispersing nanoparticles in a fluid. Ultrasound helps in the dispersion of powders with the aim of fragmenting large agglomerates and to avoid subsequent aggregation. Generally, commercial ZnO powders consist of both strongly and weakly bonded aggregates. Chung *et al.* [94] compared the characteristics of ZnO nanoparticles in water prepared via ultrasonic dispersion using a probe and a bath. In an ultrasonic system, the transducer transfers energy into the fluid in the form of pressure waves to collapse agglomerates with the released pressure resulting in an increase in temperature in the surrounding fluid. The results of the experiments found that a probe immersed in a suspension was more effective than bath immersion to produce fine ZnO nanoparticles in water [94].

Ultrasound has been utilised to enhance the fabrication of ZnO nanostructures in combination with a number of techniques. Chen *et al.* [95] applied an ultrasound-assisted method to grow ZnO nanorods via the reaction between zinc acetate dehydrate ($\text{Zn}(\text{CH}_3\text{COO})_2 \cdot 2\text{H}_2\text{O}$) and sodium hydroxide (NaOH) in the ionic liquid 1-Butyl-3-methyl imidazole six hexafluorophosphoric acid salts ([BMIM][PF₆]) aqueous solution. By comparing images it was found that very few active sites could produce nuclei to obtain flower-like structures without ultrasound. They summarised that ionic liquids such as [BMIM][PF₆] played the dual role of diffusion controller and anisotropic growth director while ultrasound was an active site trigger [95]. Lee *et al.* [96] utilised the sonication technique by immersing nanopillar array film within aqueous solution (0.01 M zinc acetate dehydrate

($\text{Zn}(\text{CH}_3\text{COO})_2 \cdot 2\text{H}_2\text{O}$) and 1.57 M ammonia water ($\text{NH}_3 \cdot 2\text{H}_2\text{O}$) within 5 minutes to fabricate ZnO nanoparticles coated film without a significant surface damage [96].

It is also common to use ultrasonic techniques for dispersions of other metal oxide nanomaterials. One very relevant method of producing electrodes was described by Zhang *et al.* [97] to produce titanium dioxide (TiO_2)-modified carbon paste electrodes. Titanium dioxide hollow microsphere colloid powder was sonicated in buffer to produce a well-dispersed colloidal solution [97]. Then the well-dispersed solution was dropped on to a surface and dried in air [97]. This technique had the benefits of being simple, low-cost and could be carried out at room temperature.

In summary, ultrasound is an effective technique to produce homogenous suspension of ZnO particles and the drop-and-dry method can be used to produce inexpensive nanoparticle films in a process that is simple without the need for expensive equipment, harsh chemicals or extreme temperatures pressure. Due to these benefits, in this research work these techniques have been combined and adapted to fabricate ZnO and ZnO/CuO films and 3D sensor structures.

1.8 Summary

This chapter has described the components of a biosensor and for each element various systems/methods presented in the literature have been identified, to provide a comparison and to highlight the benefits of the approach adopted in this research study. The key findings from this literature survey were used to inform the aims and objectives (section 1.1) and are as follows. Antibody-based impedimetric biosensors can offer high specificity and sensitivity, as well as being adaptable for detection of a wide range of analytes. ZnO/CuO nanoparticle biosensors showed enhanced performance (sensitivity and limit of detection) relative to sensors without nanostructures. Ultrasonic processing of the nanomaterials can result in enhanced performance and non-covalent antibody immobilisation could be used to effectively bind antibody on ZnO or ZnO/CuO. 3D porous membranes have been utilised to create flow-based biosensors. The challenge of the research study presented in this thesis is to combine and adapt the techniques identified in the literature to incrementally develop a sensitive, rapid immunoassay biosensor using nano-particle metal oxide semiconductor materials which are integrated within a porous structure for measurement of biological target by flow-based methodology.

To deliver the research study objectives, this thesis is structured as follows. Chapter 2 explains the principle of non-faradaic impedance spectroscopy. The Debye length and circuit modelling were described and discussed. Chapters 3 and 4 focus on the development of a ZnO (Chapter 3) and ZnO/CuO (Chapter 4) nano-surface for detection of CRP on a 2D surface. The evaluation of ZnO and ZnO/CuO composite nano-surfaces was based on the signal change measured by impedance spectroscopy for detection of CRP. The biosensors were compared by using the signal change resulting from CRP binding to antibody on the biosensor surface. The addition of CuO to ZnO, in Chapter 4 investigated the enhancement of the sensitivity of the biosensor for the detection of CRP.

To investigate the development of a 3D structured biosensor a nitrocellulose membrane was substituted as the biosensor substrate. Chapters 5 focused on the development of 3D ZnO/CuO nano-membranes for the detection of CRP in a porous structure. Chapter 6 then investigated how the porous structure could be used by flow-based methodology to measure binding of the target analyte to antibody on nano-crystalline surface.

Chapter 2

Impedimetric Biosensors

In impedimetric measurement, the resistive and capacitive properties of a system are determined, via the application of a sinusoidal AC excitation signal. In impedance spectroscopy, an impedance spectrum is obtained by varying the frequency of the input voltage signal over a defined range in order that the resistive and capacitive elements of the system can be determined from the real and imaginary parts of the current responses. Impedance measurement/spectroscopy is used to detect immunological binding events, such as antibody/antigen binding occurring on the sensing surface of a biosensor. In this PhD project impedance spectroscopy/measurement was used in this way, providing a measurement of the binding on the sensor surfaces, and thus quantifying the analyte delivered to the zinc oxide and zinc oxide/copper oxide biosensors.

This chapter presents the basic terms and concepts associated with impedimetric biosensors. The categories of faradaic and non-faradaic are described and examples from the literature of biosensors in both these classes are presented. This chapter also provides brief details of relevant physical principles, e.g. electrical double layer. The methods of analysing impedance spectroscopy data are also discussed.

Finally, in this chapter a simple electrical circuit model for the biosensors studied in this PhD project is presented. The model builds on the Randles model [20], adapting for the unique properties associated with the non-faradaic sensors studied in this work. In addition, the measurement instrument is modelled to decouple the output features associated with the biosensor and instrument. The aim is to enhance understanding of the biosensor operation and thus aid future biosensor development.

2.1 Faradaic and Non-Faradaic Processes

Electrochemical processes can be categorised into two types. (1) Faradaic – in which charges (e.g. electrons) are transferred across a solid-solution interface. In biosensors, this electron transfer is caused by oxidation or reduction reactions. (2) Non-faradaic – in which no charge-transfer reactions occur. Although charge does not cross the interface, external currents can be measured which are associated with movement of electrolyte ions, reorientation of solvent dipoles, adsorption/desorption, etc. at the electrode-electrolyte interface [98]. Both faradaic and non-faradaic processes can simultaneously occur when electrode reactions take place and impedimetric biosensors which are defined as faradaic, often exhibit both processes. In fact, impedance spectroscopy can be used to decouple the faradaic and non-faradaic processes across an electrode-electrolyte interface. Affinity binding in the presence of redox active species is detected through changes in faradaic charge transfer across the electrode-electrolyte interface, whereas non-faradaic impedance spectroscopy leverages changes in interfacial capacitance to determine targeted biomolecule binding events [99].

Commonly, faradaic electrochemical biosensors use a conventional three-electrode system in the presence of a redox probe, for example ferricyanide ($[\text{Fe}(\text{CN})_6]^{3-/4-}$) [4]. In this arrangement, the redox probe is alternately oxidized and reduced by the transfer of an electron to and from the electrode, with the charge transfer resistance correlating with the quantity of target analyte [58]. By comparison, for non-faradaic biosensors, no redox probe is required [59]. In the absence of faradaic currents, capacitance effects dominate and vary in accordance with the biological recognition events [58]. Consequently, some non-faradaic biosensors are referred to as capacitive sensors, with the electronic and ionic charges staying in or at the electrode where there is no redox reaction [100]. The main motivation for selecting the non-faradaic approach is that less complex sample preparation processes can be employed [59]. This is particularly relevant for point-of-care applications.

A number of examples of impedimetric biosensors, mostly zinc oxide based structures, are listed in **Table 2.1**. The key conclusions from the publications in this table are:

1. Non-faradaic biosensors can be effectively used for label-free detection of antigens, such as troponin-T [101], cortisol [18], pp65-antigen [59] and thrombin [14].

2. Impedimetric biosensors are commonly used for enzymeless detection for example using antibody/antigen interactions [50].
3. The interfacial behaviour of faradaic and non-faradaic impedance spectroscopy biosensors can be described by Randles equivalent circuit [4,21]. For faradaic biosensors, the charge transfer resistance (R_{ct}) can be extracted from the Nyquist plot and the change of R_{ct} , is dependent on the binding of the target and used to determine the concentration of an analyte [102].
4. One form of non-faradaic biosensor is a capacitive biosensor with the change in capacitance being dominant [91].
5. A fixed frequency is frequently used for plotting dose response for non-faradaic biosensors. Low frequencies are usually selected. The frequency of 100 Hz is often chosen due to significant change in impedance between the different doses of antigen [50,101].
6. Non-Faradaic mode of operation allows detection without need of a reference electrode (which is required in Faradaic mode) because no DC potential is required. Instead, by charging and discharging the double-layer capacitance, it is possible to assess the dielectric changes due to the binding of the target analyte to the sensor surface/conductive substrate. This makes the technique amenable to miniaturization.

Table 2. 1 Comparisons of faradaic and non-faradaic biosensors

Sensors	Faradaic or non-faradaic	Principle	Detection sensitivity	Data analysis	Refs
An impedimetric sensor fabricated on a printed circuit board (PCB) chip	Non-faradaic	Nanoporous alumina with pore diameter of 200nm and pore depth of 250 nm was used as the signal amplifying medium	10 fg/mL cardiac biomarker, brain natriuretic	Nyquist plots	[103]
An impedimetric sensor fabricated on nanotextured zinc oxide thin films sputter deposited on printed circuit boards (PCB)	Non-faradaic	Due to the oxygen vacancies in the ZnO thin film; The double layer capacitance directly corresponds to protein binding effects on the sensor surface	Limit of detection of troponin-T - 10 fg/mL and 100 fg/mL in PBS and human serum	Nyquist plot	[101]
FTO/Nano-ZnO/Urs biosensor based on uniform sputtered Nano-ZnO thin film on the conductive fluorinated-tin oxide (FTO) layer	Faradaic	Sensor was immobilized urease enzyme (Urs) for urea detection; The corresponding current was measured by varying potential across the film	Sensitivity for urea detection within 0.83–23.24 mM and limit of detection as 0.40 mM	I–V curves showing with increasing urea concentration	[4]
Capacitive biosensor was built from two copper IDE with a width and spacing of 50 μm which were covered with an insulating layer of parylene	Non-faradaic	Insulating layer helped prevent Faradaic currents; capacitance changes were measured in a liquid environment	N.A.	Capacitance (C) and phase shift variation were measured	[91]
Flexible nanoporous tunable electrical double layer biosensors	Non-faradaic	The double layer capacitance enhanced at the liquid-semiconductor interfaces due to formation of biomolecular complexes	High sensitivity of detection of 1 pg/mL or 2.75 pmol cortisol in synthetic sweat and 1 ng/mL in human sweat	Imaginary impedance was measured for cortisol concentration in human sweat	[18]
A nanotextured surface on flexographic printed zinc oxide thin film	Non-faradaic	N.A.	Limit of detection of 5 pg/mL of the pp65-antigen HCMV protein	The change in capacitance and phase were measured from	[59]
Zinc Oxide based flexible bioelectronics	Non-faradaic	Using non-faradaic electron-ionic charge transfer, cyclic voltammogram indicated a significant enhancement of the oxidation current for glucose concentration	Reliable limit of detection (LOD) of 0.1 mg/dL glucose in human sweat	Nyquist spectra with decreasing glucose concentration	[50]

Proposed impedance spectroscopy Using interdigitated Microelectrodes	Faradaic	An aggregation-free faradaic EIS (f-EIS) technique was proposed to achieve the high detection sensitivity of amyloid beta ($A\beta$)	The sensitivity of the proposed f-EIS sensor was enhanced approximately 7.40-fold and 10.93-fold compared to the f-EIS sensor and the non-faradaic sensor, respectively.	Impedance spectrum and phase were measured, overall % impedance changes were compared	[102]
Detection of Insulin Using Electrochemical Impedance Spectroscopy	Faradaic	The imaginary impedance was correlated to insulin concentration on a gold disk electrode with insulin antibody immobilized	The lower limit of detection was found to be 2.64 μ M and dynamic range from 50 μ M to 1500 μ M.	Correlation of charge transfer resistance to target concentration	[21]
An aptamer-functionalized molybdenum disulphide (MoS_2) nanosheet based biosensor	Non-faradaic	Thrombin in human serum was detected through the impedance changes of interactions between immobilized aptamer on the electrode surface and thrombin in the electrolyte.	A high sensitivity ranging from 267 fM to 267 μ M in PBS buffer, and a limit of detection of 53 μ M for thrombin in 1% human serum samples	Change in impedance (ΔZ_{mod}) for the calibration dose response with thrombin	[14]

2.2 Principles of Impedimetric Biosensors

2.2.1 Electrical Double Layer

When a conductor/semiconductor is brought in to contact with an ionic liquid, an electrical double layer (EDL) is formed at the liquid-semiconductor interface. In biosensors, the capacitance change of the EDL relates to the concentration of bio-molecular binding at or near to the interface [18]. A diagram showing the creation of an EDL in an example scenario is shown in **Figure 2.1**. There is an EDL formed when a buffer solution containing C-Reactive Protein (CRP) is brought in to contact with an anti-CRP antibody-loaded ZnO nano-surface electrode. In the diagram, the distribution of positive and negative ions on the surface is depicted. In the Helmholtz model, charges are distributed at the surface of the two interfaces and the opposite signs of the charges form a double layer which can be modelled as a capacitor. The structure is sub-divided into four planes, i.e., the space charge layer (SCL), inner Helmholtz plane (IHP), the outer Helmholtz plane (OHP) and the diffuse layer. In **Figure 2.1**, the position of the interface between these layers (illustrated by the black line) fluctuates across the surface because of the roughness of the ZnO surface.

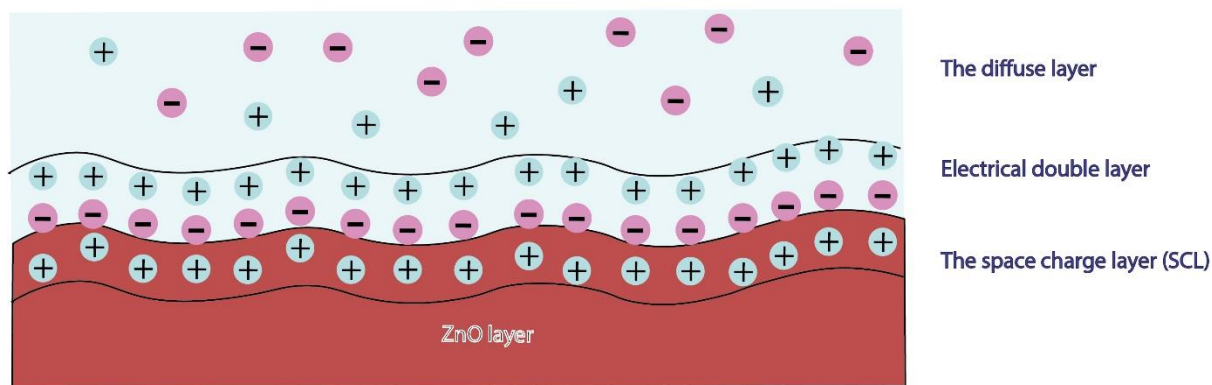


Figure 2. 1 A diagram of the charge distribution at ZnO surface adapted from [1].

For zinc oxide, an n-type semiconductor electrode, on contact with an electrolyte, electrons will be transferred from the electrode into the solution. There is thus a positive charge associated with the space charge layer which has a thickness of several nanometres [1]. The isoelectric point of ZnO is ~ 9.5 , consequently the space charge layer is within the solid ZnO semiconductor with positive charges [1]. The Helmholtz double layer is considered to be

formed by two planar sheets of charges. The inner one is due to the ions in solution adsorbed at the surface of the solid and the outer Helmholtz plane (OHP) is due to the ions of opposite sign attracted by adsorbed ions, via Coulomb force. Finally, the diffuse layer is the region beyond the OHP, where there is an excess of free ions of one sign, which are free to move in the fluid rather than being firmly anchored. The electric potential decays exponentially towards zero in the diffuse layer [14]. Beyond Debye length, counterions' screening effect predominates and the charge detection is reduced [18].

For impedance spectroscopy, characterisation of the electrode-electrolyte system interface requires information relating to conductivity, dielectric constants and capacitance [41]. The dielectric changes to different concentrations of protein marker targets can be compared due to charge accumulation in the protein layer and the electrodes [60]. Larger concentrations of target antigen result in greater changes in the relative dielectric permittivity within the electrical double layer, which for a non-faradaic response contributes to the increase in interfacial capacitance. The dielectric constant depends on the frequency of alternating electric field and also the chemical structure and the imperfections (defects) of the sensor surface material, as well as the temperature and pressure [104]. The surface charge of density consists of the bound charge and the free charge. The free charge portion produces the electric field, while the bound charge portion produces polarisation [104]. Not only dielectric constant and compact layer thickness, but the size of electrodes and the concentration of the supporting electrolyte varies electrical double layer capacitance [105].

The bulk solution resistance provides a value for the conductivity of the solution due to the ionic concentrations and the mobility of positive and negative ions [106]. Other factors that influence the resistance are the contact area between the solution and electrodes due to the length/width of electrode and substrates and the separation between the electrodes [106].

A number of researchers have examined the EDL associated with ZnO biosensors in some detail. Munje *et al.* [18] depicted the double layer at the liquid-semiconductor interface and demonstrated that the EDL capacitance changed actively with the concentration of bio-molecular binding. They utilised a ZnO thin film as an active region in contact with liquid, in order to amplify the EDL formed at the liquid-semiconductor interface [18]. Shanmugam *et al.* [107] explained the electrochemical characterisation of ZnO nanoelectrode/electrolyte

interface when an EDL formed. Without combining with biological molecules, the ions at electrode surface formed Inner Helmholtz plane (IHP) and the ionic gradient distribution extending in to electrolyte is the outer Helmholtz plane (OHP). When DSP linker conjugated to electrode surface, it resulted in a change in potential drop between IHP and OHP which changed the capacitance of the EDL. When alpha-cTnT antibody was immobilised, it moved OHP further away from nanoelectrode. When antigen (cTnT) bound to antibody, it further perturbed charge distributions in EDL, which was monitored as a change of electrical double layer capacitance [107].

2.2.2 Debye Length

The Debye length is a measure of a charge carrier's net electrostatic effect within a solution. It defines the characteristic distance at which a charged molecule is shielded such that the resulting electric potential decreases in magnitude by 1/e [108]. The Debye length is proportional to reciprocal of the ionic strength defined by equation (2.1) [108]. Ionic strength is the function of all concentration in solution defined by equation (2.2) [109].

$$\lambda = \frac{1}{\kappa} = \left[\frac{\varepsilon k T}{e^2 \sum_i C_i Z_i^2} \right]^{\frac{1}{2}} \quad (2.1)$$

$$I = \frac{1}{2} \sum_{i=1}^n C_i Z_i^2 \quad (2.2)$$

ε is the permittivity, k ($=1.381 \times 10^{-23} \text{ JK}^{-1}$) is the Boltzmann constant, T (K) is the absolute temperature, e ($=1.6021 \times 10^{-19} \text{ C}$) is the elementary charge [110]. In equation (2.1) and (2.2), C_i is the molar concentration (M) and Z_i is the charge number of the ion.

$$\delta = \left[\frac{\varepsilon k T}{e^2 N_a 2C} \right]^{\frac{1}{2}} \quad (2.3)$$

For a 1:1 electrolyte, e.g. sodium chloride (NaCl), the ionic strength is equal to the concentration. The Debye length, δ , can be simplified as equation (2.3) [14]. In this case, $Z_i=1$. In equation (2.3), C is the molar concentration and N_a is the Avogadro number [110].

In this PhD study, the buffer of phosphate-buffered saline (PBS) concentration (0.01 M), contained 0.137 M of the sodium chloride (NaCl) ions, 0.003 M of potassium chloride (KCl) ions, 0.008 M disodium hydrogen phosphate (Na_2HPO_4) ions, and 0.0015 M potassium dihydrogen phosphate (KH_2PO_4) ions, giving a final pH of 7.4. The ionic strength of the buffer solution 0.01 M is calculated to be 0.1655 M.

In equation (2.1) and (2.3), e is the charge of electron and ϵ is the permittivity ($\epsilon = \epsilon_r \epsilon_0$). The relative permittivity, ϵ_r of PBS is 80 [111] and ϵ_r is between 2 to 5 for CRP biomolecules [112]. T is the temperature with the unit of K. Room temperature of 293.15 K is assumed. Consequently, the calculated Debye length at the CRP concentrations is 0.67 - 1.06 and 1.50 - 2.37 nm in 2.5 \times and 0.5 \times PBS electrolyte. However, the Debye length in this thesis is more complicated because nanoparticle-based sensing area is rough and non-uniform.

CRP is a 115-kDa acute phase protein, which is naturally unglycosylated and is a stable pentamer formed by 5 non-covalently linked protomers [53,113]. The molecular weight and the estimated scale of CRP on the basis of the protein data bank¹ is 116 kDa, $10 \times 10 \times 4$ nm [114]. The anti-CRP antibody isotype is polyclonal IgG. The IgG size is 151 kDa, $16 \times 5 \times 5$ nm [114].

Analyte size and net charge must be considered when designing the biosensor through charge modulation within the EDL when measuring non-faradaic changes [14]. Most commonly, the Debye length is matched to or larger than the size of the binding biomolecules [14]. However, some authors have recognised that measurement can still be performed beyond the Debye length where there is still an electric potential gradient. Palazzo *et al.* [108] developed a bio-electrolyte-gated organic field-effect transistor sensor to successfully detect binding events occurring at distances that are 3 times the Debye length value from the transistor gate. In this PhD project, this principle was utilised, measuring the antibody/antigen interaction beyond a distance of the Debye length from the nanoparticle/solution interface.

¹ <http://www.rcsb.org/pdb/home/home.do>

2.2.3 Data Analysis

The impedance spectrum of a biosensor, which is a function of frequency, can be presented as a Nyquist or a Bode plot. For a Nyquist plot, the real and imaginary components of impedance are plotted on the x and y axes. There are many examples of this format of data presentation in the literature. For example, Jacobs *et al.* [101] compared the performance of the anti-troponin-T capture antibody immobilised sputter deposited ZnO films with or without oxygen based on Nyquist plots corresponding to frequencies from 1 Hz to 1MHz in a impedimetric immunoassay. However, a single frequency of 100 Hz was selected to create a calibration curve using the modulus impedance values. Also, Selvam *et al.* [103] also used Nyquist plot to measure the impedance over the frequency range from 100 mHz to 1 MHz. This author also concluded that changes to the double layer capacitance are most significant at lower frequencies, less than 1 KHz. Finally, Munje *et al.* [18] developed ZnO surface functionalized with DSP linker and α -cortisol antibody biosensor. Nyquist plots were used to represent the impedance output in the range 1 Hz to 1 KHz. The authors derived the double layer capacitance from the imaginary component of the impedance, concluding that a lower imaginary component means higher double layer capacitance [18].

To examine the performance of impedimetric biosensors other authors have utilised Bode plots, where the magnitude and phase are plotted separately, each as a function of frequency. For example, Munje *et al.* [50] fabricated a flexible electrochemical biosensor for label-free detection of glucose in human sweat. The magnitude of the impedance variations was analysed over the frequency from 1 Hz to 10 MHz. They found that at the frequency of 50 - 100 Hz, the signal-to-noise ratio (SNR) was highest [50].

The majority of studies on impedimetric biosensors in the literature use the impedance spectrum to identify the optimum frequency (or frequency range) at which the analysis should be performed. Consistently researchers have found that low frequencies, below approximately 1 kHz, are the optimum. This approach has also been used in this work, explanations for the frequencies selected are given in subsequent chapters.

2.3 Equivalent Circuit Modelling of Impedimetric Biosensors

2.3.1 Electrochemical Impedance Measurement

For impedance measurements most commonly, a sine wave, $V(t) = V_0 \sin(\omega t)$, which varies periodically with an angular frequency, $\omega = 2\pi f$, rad/s, (where f is the frequency) is used. The current response $I(t)$ to the applied voltage $V(t)$ is also the sine wave, but $I(t)$ is shifted over the time interval (Δt) (or phase shift, $\phi = 2\pi f(\Delta t)$), relative to $V(t)$ because of capacitance and/or inductance components of the impedance, Z . Generally, it is assumed that there are no changes in impedance value during the observation time interval and therefore, time dependence is not included in the mathematical expression of impedance [61]. The impedance, Z , can therefore be written as:

$$Z(t) = \frac{V(t)}{I(t)} = \frac{V_0 \sin(2\pi f t)}{I_0 \sin(2\pi f t + \phi)} = \frac{1}{Y} \quad (2.4)$$

V_0 and I_0 are the maximum voltage and current signals respectively and Y is the complex admittance.

The total impedance can be calculated from the components within a circuit, for example the equivalent circuit model described in next section 2.3.2. The capacitive reactance of a capacitor is given by the following equation, where j denotes the imaginary component.

$$X_c = -\frac{1}{j\omega C} \quad (2.5)$$

The total impedance of a circuit comprising solely of resistive and capacitive elements can be calculated as follows. The magnitude (modulus) of the impedance, $|Z|$ can be calculated as follows.

$$Z = R + jX_c; |Z| = \sqrt{R^2 + X_c^2} \quad (2.6)$$

The phase angle ϕ , as defined above can be calculated from the following equation.

$$\phi = \arctan \left[\frac{X_c}{R} \right] \quad (2.7)$$

Selvam *et al.* [42] compared the phase plots of the impedance measured over a range of frequency from 1 Hz to 10 MHz. They found a 60 degree phase lag which indicated the capacitive nature of the sensor response [42].

2.3.2 Randles Model

The Randles equivalent circuit is commonly used for modelling the performance of impedimetric biosensors. This aids in the understanding of the mechanism of charge transfer and effects of the biomolecular interactions for quantification of target biomarker concentration [1]. The circuit schematic of the Randles model is shown in **Figure 2.2**. In this equivalent circuit, R_s represent the resistance of the solution (mainly electrolyte) and C_d is the constant phase that models the behaviour of the electrical double layer at the interface of electrode-electrolyte [15]. The total current through the electrode/solution interface is considered as the sum of the current from faradaic processes, i_f , and from the double-layer charging, i_c [112]. This is often simplified to the electrical double layer capacitance. R_{ct} represents the faradaic impedance charge transfer resistance, and the Warburg impedance Z_w due to diffusion of the chemical reactants in solution [15,101]. These two elements represent the impedance of a faradaic reaction and therefore are not included in the Randles model for a non-faradaic impedimetric biosensor.

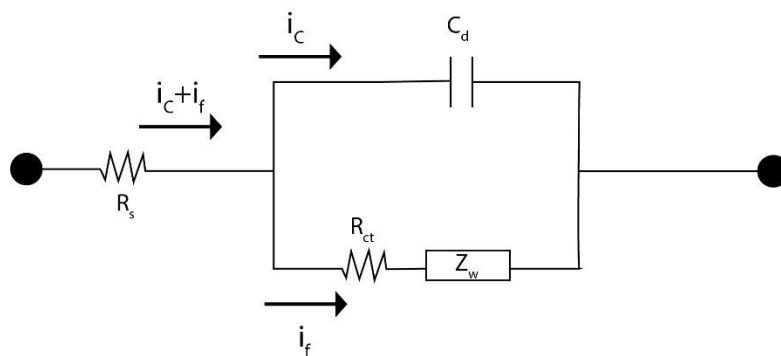


Figure 2. 2 Randles model redrawn from [42,112].

In various publications in the literature, this basic model has been adapted to relate more closely to the biosensor under study. Other factors have been included in these models to

represent properties such as electrochemical cell's geometry, electrode track resistance; electrode's substrate material permittivity; electrolyte solution permittivity and other system parasitic elements, all of which affects the total impedance response of the biosensor [106,115]. The electrical double layer element C_{dl} may sometimes also be expanded to show the contribution of the individual immunoassay elements, such as a linker molecule, capture-antibody and target antigen [116].

Associated with this study, a model has been created for the ZnO biosensor using the following approach. Estimated parameters gave baseline approximations for the expected impedances of the sensor physical structure and were validated by experimental measurement. To find the model parameters that resulted in the best agreement between a model's impedance spectrum and a measured spectrum, a non-linear least squares fitting algorithm was used. Finally, the dominance of each component of the sensor system on measurement stability was analysed [117].

2.3.3 Equivalent Electrical Circuit of the 1% ZnO Nanoparticle Biosensor

Building on the Randles model, an equivalent electrical circuit model has been developed for the 1% ZnO nanoparticles-based impedimetric biosensor studied in this PhD work for coplanar electrode configuration. The biosensor structure comprises the following layers (a) coplanar copper electrodes on a pcb substrate, (b) a polyethylene terephthalate (PET), (c) a ZnO nanoparticle layer and (d) antibody on the ZnO surface in contact with buffer solution (See Chapter 3 for details of biosensor construction). Finally, C-Reactive Protein (CRP) has been used as a model antigen to allow assessment and comparison of performance. The resistive/capacitive circuits, representing the constituent components of the biosensor, were included to build up the complete circuit model at the frequency of 100 kHz, as shown in **Figure 2.3**. Further, information on the model is provided in the publication by Eveness, Cao *et al.* [117].

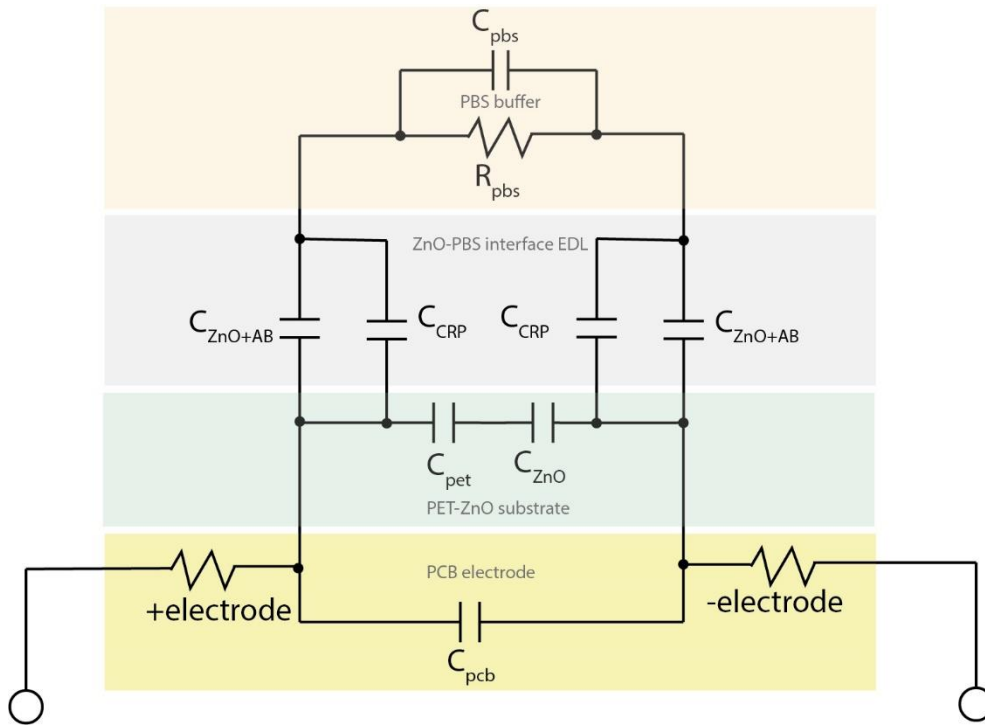


Figure 2. 3 Equivalent circuit model for the ZnO nanoparticle biosensor [117].

For modelling purposes a symmetrical system is assumed. The model includes the key elements of the Randles model for a non-Faradaic biosensor including the capacitance of the electrical double layer (C_{ZnO+AB} , C_{CRP}) plus the resistance of the solution (R_{pbs}) and the capacitance C_{pbs} . Additional elements that are specific to the biosensor studied in this PhD are also incorporated in the overall circuit model. These include the resistance of the copper electrodes (this is a very small value but included in the model to illustrate each electrode node) and the C_{pcb} is the capacitance associated with the two co-planar electrodes on the printed circuit board (PCB) dielectric substrate. An equivalent capacitance of the PET substrate (C_{pet}) is included in series with the ZnO intrinsic capacitance (C_{ZnO}). The resistance value R for PET is extremely high, of the order of $10^6 \Omega$ (due to its high resistivity), and as a parallel open-circuit component would have negligible effect on the response of the model within the frequency bandwidth we are operating. Finally a parallel capacitance representing the effect of the antigen binding is included as a separate component from the electrical double layer capacitance component. This is a common representation in the literature [61].

Consequently, the total interfacial capacitance is the accumulative effect of the ZnO nanoparticles, antigen and antibodies and can be written as:

$$C_{total} = C_{ZnO+AB} + C_{CRP} \quad (2.8)$$

The model assumes sensor electrical parameter symmetry for both electrodes. The model was created by analysis of the real and imaginary parts of the measured impedance of the constituent layers of the biosensor, i.e. PCB, PET, ZnO nanoparticles, antibody functionalised ZnO in contact with PBS and finally, CRP antigen [117]. The capacitive reactance (imaginary) was the dominant component used to construct a model from the measured impedance data. The resistive (real) component of impedance magnitude was found to be negligible contribution to the impedance magnitude and was omitted from the resultant equivalent circuit model. The model shows that the capacitive effects are dominant. Consequently, the biosensor could be referred to as a capacitive biosensor. The model's response was validated by comparing the modelled impedance to that of the measured impedance spectra and simulated using Analog Devices LTspice® circuit simulator software as shown in the paper by Eveness, Cao *et al.* [117]. Estimated parameters gave baseline approximations for the expected impedances of the sensor physical structure and have been validated by experimental measurement. This is further investigated where analysis of the dominance of each component of the sensor system on measurement stability is tested [117].

When the antigen binds to the ZnO surface through capture by the receptor antibody, the measured decrease in the absolute impedance value due to increase in the overall negative charge with increasing CRP loading, which is demonstrated in Chapter 3. The equivalent electrical circuit model developed demonstrates a capacitive sensing system, with quantified changes to the capacitance of the EDL formed at the zinc oxide semiconductor-PBS interface. Larger concentrations of target antigen in a sample will result in a greater amount of molecular interaction at the EDL, resulting in greater changes in the relative dielectric permittivity at the electrical double layer, which for a non-faradaic response contributes to the increase in interfacial capacitance, presented as a parallel capacitance connected to the ZnO-Antibody interfacial capacitance.

2.3.4 Experimental Impedance Measurement Set-up and Results

For each of the studies described in this thesis, the co-planar electrode was connected to a Cypher Instruments C60 Impedance-Amplitude-Phase Analyser (Cypher Instruments Ltd) configured to impedance-mode measurement, via a 0.5 m 50 Ohm impedance coax cable. The equivalent circuit associated with this arrangement is depicted in **Figure 2.4**. The output impedance parameters provided are obtained from the manufacturer's specification. The C60 generates a sine wave voltage excitation at 2 Vpp. Although 2 V ac is relatively high, most of the voltage will fall on the dielectric and hence the voltage on the electrochemical double layer is much smaller. The signal voltage across the sensor and the current flowing through the sensor is measured by the C60 to determine the impedance.

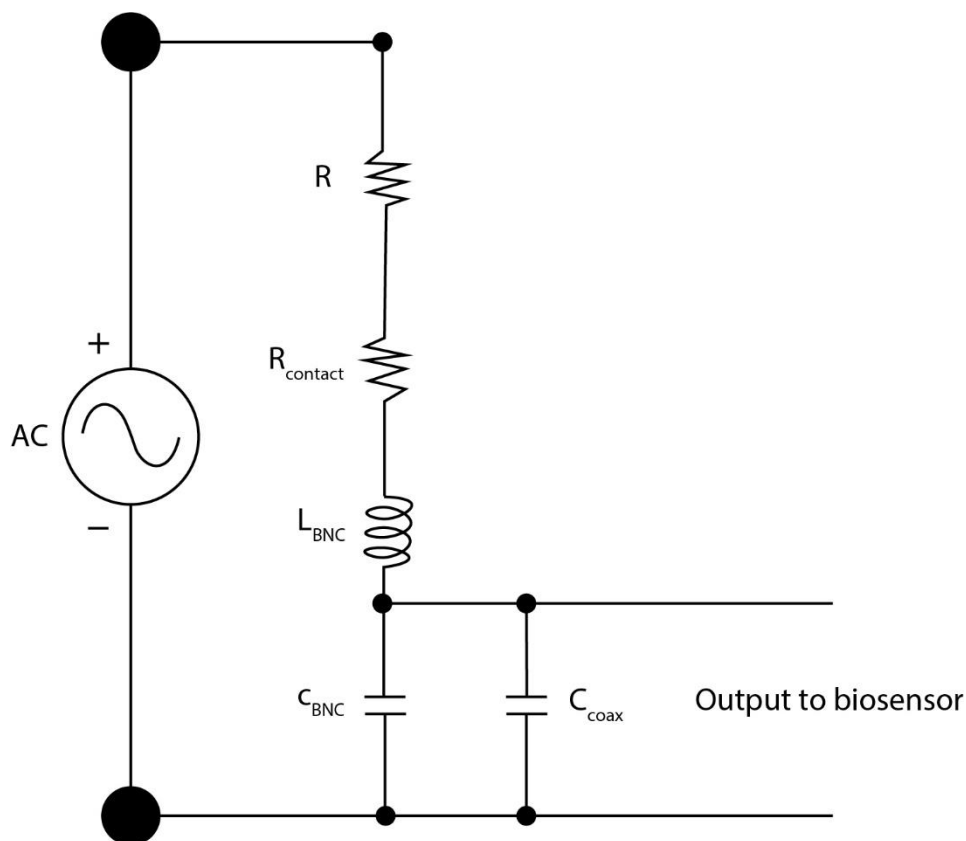


Figure 2. 4 The equivalent circuit associated with C60 arrangement [117].

From the manufacturer's specification, there is an upper boundary of measurement defined by the internal noise of the C60 and is equal to 455 k Ω , measured at open circuit. As shown

in **Figure 2.4**, the lower impedance boundary is set by the output resistance $R_{contact}$ (BNC contact resistance) and inductance L_{BNC} (23 nH). This is normally a 10 m Ω resistive boundary at low frequencies [117]. The output capacitance of the C60 (C_{BNC}) is 3 pF. The co-planar electrode was connected to the C60 impedance measurement BNC connector by BNC 50 Ω coaxial cable. The coax cable capacitance C_{coax} is 104.5 pF. The correlation between impedance value and increasing concentrations of CRP was demonstrated in Chapter 3, which shows impedance decreasing for increase in CRP loading. **Table 2.1** shows corresponding calculated capacitance for 1 ng/mL and 10 ng/mL of CRP. The capacitance for the antibody captured ZnO-ionic buffer interface to be in order several pico-Farads (3.7 pF) and is therefore dominant over the series connected ionic bulk buffer solution capacitance.

Table 2.1 Modelled impedance values (at 100 kHz) representing each physical component of the sensor and the electrochemical quantities of the interfacial impedance: PBS buffer solution and the lower and upper concentrations of CRP [117].

Sensor system component	Equivalent circuit element reference	Estimated electrical value	Model's fitted capacitance (Farads)
Coax	C_{coax}	100 pF	104.5 pF
Bare PCB electrode	C_{pcb}	3.0 pF	4.2 pF
PET substrate	C_{pet}	2.0 pF	2.0 pF
1% Nano-structured ZnO substrate	C_{ZnO}	-	0.15 pF
Bulk PBS	R_{pbs}	200 Ω	calculated
	C_{pbs}	12.4 pF	calculated
ZnO-PBS Interface EDL	C_{ZnO+AB}	-	7.4 pF (3.7 pF total)
1 ng/mL CRP	C_{CRP}	-	3 pF (1.5 pF total)
10 ng/mL CRP		-	3.8 pF (1.9 pF total)

Modelling the measurement system parameters allows for the decoupling of the equivalent circuit parameters (and thus the elements of the output signal) of the biosensor from the impedance measurement instrument.

There are two different electrodes used in this thesis, one is planar electrode and the other interdigitated electrode. Hugo *et al.* presented that a finite element analysis of the coplanar electrode layout investigated the influence of the geometrical parameters on the output signal with lower peak amplitude at the increase of the interelectrode distance [118]. The side by side planar electrode produces a non-homogeneous electric field, which resulted the impedance is very dependent on the vertical position [118]. Hugo *et al.* concluded that the standard planar or facing electrode configuration enables to measure cell/particle position and correct data [118]. The measurement imaginary parts of impedance were similar with the varied distance between two microelectrodes (120, 300 and 800 μm) [119]. The interdigitated electrode designed increases the overall capacitance due to increased surface area [120].

2.4 Summary

In this chapter, faradaic and non-faradaic impedimetric biosensors have been compared. For non-faradaic impedimetric biosensor, measurement of the change of capacitance in electrical double layer due electrical charge accumulation, which influenced by ionic strength and can be measured even beyond Debye length.

The equivalent circuit model specific to the biosensors studied in this PhD has been presented. It is based on the non-faradaic representation of the Randles model and shows the capacitances and resistances associated with the constituent elements of the biosensor. The equivalent circuit model helps evaluate the dominance of each of the physical and biochemical equivalent electrical parameters for non-faradaic impedimetric biosensing measurement. The impedance behaviours of biochemical binding of CRP could be analysed using EIS to quantify the concentration of CRP in a capacitive non-faradaic sensing system. An equivalent circuit model of the instrumentation used to measure the real and imaginary components of the impedance of the system has been included. This allows for the decoupling of the measurement features associated with instrument from that of the biosensor. The limitations of the instrumentation have been mentioned.

In order to investigate the relationship between impedance responses of surface interface and CRP concentration, the following Chapters 3 and 4 describe the fabrication of ZnO and ZnO/CuO nano-surfaces, via colloidal dispersion using sonication, for CRP detection. The background study assists design the experiments for detection of CRP on ZnO/CuO based nano-surfaces or membranes.

Chapter 3

Zinc Oxide Based Bio-surfaces

The first experimental chapter investigates zinc oxide (ZnO) based nano-surfaces applicable for non-faradaic impedimetric biosensor on planar electrode. C-reactive protein (CRP) was used as the model analyte to evaluate the sensor performance. The thesis reports a non-faradaic impedimetric biosensor formed from antibody coated ZnO nano-crystals which has been prepared using a rapid and inexpensive fabrication method which utilises colloidal dispersion enhanced by using sonication. This technique was used to prepare highly ordered and uniform nano-crystalline sensor surfaces on polyethylene terephthalate (PET) using 0.5%, 1% and 5% concentrations (g/100 mL) of zinc oxide nano-crystal suspensions. In order to achieve sensing areas, anti-CRP antibodies were immobilised on sensing area without a washing step. Different concentrations of ZnO nano-surfaces are compared and discussed. Changes in impedance values, at a frequency of 138 Hz, were used to establish dose dependent responses for CRP antigen. It will be followed by the discussion on possibility of measuring electrical double layer capacitance based on semiconductor-liquid double layer non-direct contact with electrode. This chapter provides the underlying principles for the rest of the chapters and demonstrates the investigation of a capacitively dominant impedance test.

The work presented in this chapter has been mostly published in Cao *et al.* [121]. I contributed to the research design and carried out all experimentation including nano-surfaces preparation and fabrication, surface characterisation, immunology assay and impedance test. I also processed the experimental data, discussed the results, and wrote the initial draft of the manuscript.

3.1 Introduction

3.1.1 ZnO Nano-surfaces Fabrication

In Chapter 1, the advantages of ZnO nanoparticles due to low-cost, biocompatibility, ability to absorb proteins and semiconductor properties were highlighted. Different methods for fabrication of ZnO nano-structures were also compared. The technique of colloidal dispersion of ZnO nanoparticles shows both disadvantages and advantages. The disadvantage of ZnO nano-crystals is that the crystals easily aggregate. During the process of growth, Park *et al.* [40] found that several ZnO crystallites of about 5-10 nm agglomerated and formed a horizontal hexagonal platelet, which was a different output compared with other published results. Through a comparison of different concentrations (1%, 3%, 5% and 7%) of ZnO dispersions either in water or methanol to make the surface of ZnO-polyester composite textile materials, Rimbu [122] demonstrated that the larger concentration leads to agglomerations and a diminished coating quality. In order to mitigate the problem of aggregation, the process of sonication can be used. For example, in order to fabricate an ultrasensitive biosensor for DNA detection, Liu *et al.* employed sonication to achieve water-soluble ZnO/Au nanocomposites [123]. The advantage of the colloidal dispersion techniques is that ZnO nanocrystals of defined shape and size can be purchased ensuring that well characterised films can be created.

In this chapter, preliminary results are presented of a biosensor that is fabricated using a colloidal dispersion technique, incorporating sonication, to create a ZnO nanocrystal surface. The advantage of this technique is that biosensor surfaces, with controlled compositions and nanostructures, could be created at low cost with standard laboratory equipment; the technique also being suitable for large scale synthesis. Non-faradaic impedance spectroscopy was used to interrogate the biosensor surface to create a compact biosensor.

3.1.2 CRP Clinical Range

In order to prove the functionality of the ZnO nano-crystal biosensor, C-reactive protein (CRP) was selected as the model antigen. CRP is a biomarker that, when elevated from a concentration of 1 mg/L to a level of, or above, 3 mg/L, indicates an infection or other active

inflammatory process. CRP is synthesised in the liver and released in response to inflammatory changes. It is regulated by interleukin-6, interleukin-1 β and tumour necrosis factor- α [124] and is thought to be a key biomarker of systemic inflammation [125].

CRP has been shown as a biomarker of various health outcomes, such as cardiovascular disease [126], obesity [127], diabetes [128], cerebrovascular disease [129], chronic kidney disease [130], cancer [131]. The clinical range of CRP is levels of hsCRP of <1, 1 to <3, and >3 mg/L have been suggested to define low, moderate, and high-risk groups for cardiovascular events [132].

3.1.3 Antibody Densities and Concentrations

Antibody density affects the efficiency of antigen/antibody binding on the surface; this is why it is important to test and determine the appropriate antibody density after immobilisation [60,112]. In **Table 3.1**, there are some examples of antibody immobilisation details in antibody concentrations as well as sensing area sizes. Initially, the capacitance/dielectric properties using a large number of capacitors were tested after immobilizing appropriate amounts of antibodies on a given area of gold interdigitated (GID) electrodes. It was found that the immobilization of pure antibodies for detection of single target antigen often yielded low signal-to-noise ratio, and this method was suitable for concentrations over ng/mL levels [60]. The high antibody concentration may cause signal saturation, for example, at 5 $\mu\text{g/mL}$ for anti-CRP and 1 $\mu\text{g/mL}$ for anti-MPO, impedance reached saturation with the diatom membrane and the saturation doses for alumina were 1 $\mu\text{g/mL}$ for anti-CRP as well as for anti-MPO [133]. Due to the maximum antibody density, 3.77 ng/mm² [112], obtained if the antibodies are modelled as a homogeneous sphere. The optimised antibody amounts based on defined sensing area (10 mm \times 4 mm) will be 150.8 ng of antibody by roughly calculation.

Table 3. 1 Comparisons of antibodies captured

Biosensors	Sensing area	Antibodies volumes and concentrations in solution	Total amounts immobilised	Incubation time and storage time	Refs
Label-free capacitive using gold interdigitated capacitor arrays	3 mm × 3 mm dimension of each GID on capacitor surface	20 µl of 100 µg/mL of anti-CRP antibodies in PBS	2000 ng of anti-CRP antibodies	1 hour	[60]
Nanoporous alumina membrane-based biosensor using EIS	N.A.	10 µl of 5 µg/mL of anti-CRP antibodies in 0.15 M PBS	50 ng of anti-CRP antibodies	N.A.	[133]
Reflectometric interference spectroscopy-based biosensor	Silicon nitride (SiN) chips (L 9 mm × W 9 mm × H 0.725 mm)	50 µL of 50 µg/mL of anti-CRP antibodies in 10 mM acetate buffer	2500 ng of anti-CRP antibodies	Injected on the sensor surface at a flow rate of 10 µL·min ⁻¹	[28]
Non-faradaic impedimetric sensor	Lateral diameter 13 mm of nanoporous alumina membrane	150 µL of (10 ng/mL to 1 µg/mL) 10 ng/mL and 750 ng/mL of anti-brain natriuretic peptide (BNP) antibodies in 0.15 M PBS	1.5 and 112.5 ng of anti-BNP antibodies	150 µL of 10 ng/mL of anti-BNP at 15 minutes and 750 ng/mL of anti-BNP at 30 minutes	[103]
A three-line lateral flow assay strip for	A piece of NC membrane (0.25 × 30 cm ²) was used	Immobilize 1 mg/mL antibodies in distinct zones by using a dispenser. The concentrated AuNP-antibody	N.A.	N.A.	[68]

		conjugate (12 mL) was incubated on the conjugation pad humid chamber (25%) (0.75 × 0.38 cm ²)			
A carbon nanofiber based biosensor using Cyclic voltammetry (CV) and electrochemical impedance spectroscopy (EIS)	A 4-inch silicon (100) wafer with 500 nm thermal oxide layer consists of 30 devices (or chips). Each device contains nine identical micro pads (electrodes), each with a surface area of 40,000 μm ² , arranged in 3 × 3 array format	50 μL of anti-CRP (20 μM) solution in PBS (10 mM)	20 μM is 2400 ng/ul, so with 120,000 ng anti-CRP	Incubated at room temperature for 1 hour	[134]
A reduced graphene oxide-nanoparticle hybrid impedimetric sensor	ITO-coated electrode arrays on glass surfaces (7.5 × 2.5 cm) composed of eight working (sensing) disk electrodes (r = 250 μm)	20 μL of anti-CRP (10 μg/mL) solution in PBS (10 mM)	200 ng of anti-CRP	Kept in a humid chamber for 2 h	[57]
A glucose biosensor in sweat using Zinc Oxide based flexible	Four arrays each contained five capacitors on	3-5 μl of 10 μg/mL α-glucose	20-50 ng α-glucose oxidase antibody	15 minutes	[50]

bioelectronics via non-faradaic EIS	a SiO ₂ chip with a 3 mm × 3 mm dimension of	oxidase antibody			
A Paper-Based Microfluidic Immunoassay with Smartphone (CRP-Chip)	Round 7 mm diameter absorbent pad and conjugate pad	0.1 μL of anti-CRP antibody (200 ng/μL) on the nitrocellulose membrane	20 ng anti-CRP	N.A.	[63]
A portable cortisol biosensor using non-faradaic EIS	The sensing region of the sensor is 3 mm × 6 mm in area allowing for ~2.5 μL of total volume to saturate the sensing region.	MoS ₂ nanosheet was functionalized with 5 μL of 100 ug/mL alpha-cortisol antibody in pH values 2, 4, 6, and 8 of synthetic sweat	500 ng alpha-cortisol antibody	Incubated for 15 minutes	[49]
A hook effect-free immunochromatographic assay (HEF-ICA)	NC membrane 30 × 2.5 cm ²	10 μL of anti-CRP monoclonal antibody (1 mg/mL) was added to a mixture of 1 mL of 20 nm AuNP colloid (1 OD) and 100 μL of borate buffer (0.1 M)	10 μg	At room temperature for 30 minutes	[25]
Carbon nanotubes based disposable immunosensors on field effect transistors	Defined electrode has a 1.5 mm width, and a 1000 mm length	A droplet of 1 mL stock solution of anti-CRP (1 g/L) in PBS	1 mg	Stored overnight at 4 °C	[37]

3.1.4 Antigen Experimental Range and Timings

The optimised detection range is associated with antibody concentration to optimise the high efficiency of the binding of antigen/antibody. In **Table 3.2**, it can be concluded that the incubation time is commonly at 15 minutes.

Table 3. 2 Comparisons of antigen/target detection ranges on different biosensors

Biosensors	Antigen/Target detection range and separate concentrations	Incubation time	Refs
Label-free capacitive using gold interdigitated capacitor arrays	25 pg/mL to 25 ng/mL of CRP in buffer (0, 25, 250, 500, 1000, 25000 pg /mL)	1 hour incubation time	[60]
Nanoporous alumina membrane-based biosensor using EIS	1 pg/mL to 1 µg/mL of CRP in 0.15 M PBS The 0 dose, 0.001, 0.01, 0.1, 1, 10, 100, 1000 ng/mL	15 minute incubation time	[133]
Reflectometric interference spectroscopy-based biosensor	0.01, 0.1, 1.0, and 10 µg/mL of CRP dissolved in 10 mM 4-(2-hydroxyethyl)-1-piperazineethanesulfonic acid (pH 7.4) buffer containing 10 mM CaCl ₂ and 0.001% Tween 20	The CRP injection (50 µL) was flow rate of 20 µL·min ⁻¹ ; Baseline came to be stable within 5 minutes of injection.	[28]
Non-faradaic impedimetric sensor	1 fg/mL to 1 µg/mL of BNP in 0.15 M PBS	15 minute incubation time	[103]
A three-line lateral flow assay strip for	CRP (1 ng/mL to 500 µg/mL) and pegylated-CRP were used as test antigens. Pegylated-CRP was mixed with methoxy polyethylene glycol succinate N-hydroxysuccinimide (NHS-PEG) (1% in 10 mM PBS) and 1 mg/mL CRP	Incubated the mixture for 1 h, after which they dialyzed the mixture for 24 h in PBS; Required assay time at 10 minutes	[68]

A carbon nanofiber based biosensor using Cyclic voltammetry (CV) and electrochemical impedance spectroscopy (EIS)	From 50 ng/mL to 5 µg/mL of CRP in PBS (10 mM)	1 hour incubation time	[134]
A reduced graphene oxide-nanoparticle hybrid impedimetric sensor	0.1 ng/mL - 10,000 ng/mL of CRP in human serum. (control, 0.1, 1, 10, 100, 500, 1000, 5000 and 10,000 ng/mL)	N.A.	[57]
A glucose biosensor in sweat using Zinc Oxide based flexible bioelectronics via non-faradaic EIS	A increasing doses of glucose concentrations from 0.01 to 100 mg/dL (0.01, 0.1, 1, 10, 100, 200 mg/dL in sweat)	15 minute incubation time	[50]
A Paper-Based Microfluidic Immunoassay with Smartphone (CRP-Chip)	0–2 µg/mL CRP in standard, plasma and serum (0, 0.5, 1.0, 1.5, 2.0 µg/mL)	A single CRP-Chip can perform the test in triplicate on a single chip within 15 minutes.	[63]
A portable cortisol biosensor using non-faradaic EIS	Four cortisol concentration regimes (0.5, 5, 50, and 500 ng/mL) in pH 4 and pH 8 synthetic sweat	Added at a rate of 3 µL per 7 minutes for continuous 3 hours (7 minute incubation time)	[49]
A hook effect-free immunochromatographic assay (HEF-ICA)	CRP was diluted with CRP-free serum from 0.01 µg·mL ⁻¹ to 500 µg·mL ⁻¹	15 minute incubation time	[25]
Carbon nanotubes based disposable immunosensors on field effect transistors	Between 0.1 ng/mL to 100 µg/mL CRP in PBS (0.1 ng/mL, 1 ng/mL, 10 ng/mL, 0.1 µg/mL, 1 µg/mL, 10 µg/mL, 100 µg/mL)	15 minute incubation time at room temperature	[37]

3.2 Materials and Methods

Zinc oxide nanopowders (ZnO, 99.9+%, 80 - 200 nm) were purchased from US Research Nanomaterials Inc. The biological molecules including monoclonal mouse anti-human C-reactive protein (4C28 Mab: C6) and human C-reactive protein (CRP) (8C72) were purchased from HyTest Ltd. Phosphate Buffered Saline (PBS, pH 7.3 ± 0.2 at 25 °C) was purchased from OXOID Microbiology products. The PBS buffer was diluted to 0.025 M adjusting the pH to 7.40.

3.2.1 Nano-surfaces Preparation

Accurately weighed quantities of ZnO nano-crystals were added to double deionized water to make a range of concentrations (g/100 mL) of ZnO suspensions: 0.5%, 1% and 5%. Chung *et al.* observed ZnO in the liquid dispersed by ultrasonic horn is effective in terms of the size reduction rate, the minimum achievable size, and sedimentation rates with the horn system consumed 48 W during operation [94]. The ZnO suspensions were stirred for one hour and then 1.5 mL aliquots were ultra-sonicated for 7 periods of 20 seconds, at 4 minute intervals using an exponential microprobe (Soniprep 150) at 30 watts. The intervals between the sonication aimed to cool down the heat due to sonication power. The 7 periods of 20 seconds aimed to have enough accumulated sonication time to form a colloidal suspension. The use of small aliquots enables the efficient dispersion of the nanoparticles without wastage. 200 μ L ZnO suspensions dropped onto clean PET surface. Subsequently, the 24 samples for each concentration (g/100 mL) in a batch were dried in oven at 65 °C for 80 minutes and cooled to room temperature and stored in a dry atmosphere with silica gel for up to 2 days.

3.2.2 Characterisation of Nano-surfaces

The morphology of ZnO nano-surface was analysed by scanning electron microscopy (SEM). The samples were coated with a thin layer of Au prior to analysis. A grayscale profile of each image was created using ImageJ software. Grayscale values along a horizontal line comprising 966 points, were used to produce a 'Roughness Index'. A grayscale value (0 - 255) is a single number that represents the brightness of the pixel. The light areas indicate charge on the surface in the SEM with higher points reflecting electrons and accumulating charge more

easily. This means that “deeper” areas do not reflect or accumulate charge as readily and consequently have lower values. Consequently, The Roughness Index was defined as the summation of absolute changes in grayscale values between each two adjacent points. Consequently, the Roughness Index gives an indication of surface area; a larger index means a larger surface area. Grayscale value plots derived from the images of SEM results were plotted by placing a horizontal line across the image using ImageJ software.

Raman spectroscopy was used to distinguish the chemical compositions of the ZnO nanocrystal surfaces. A XploRA Raman spectrometer from Horiba, equipped with a confocal microscope was used. The Raman signals were collected in a range of 0 -3500 cm^{-1} using a 785 nm red laser excitation. The laser beam was focused on the sample using objective magnification of 50 \times .

3.2.3 CRP Sensor Fabrication and CRP Assay

The sensing area (10 mm \times 4 mm) of ZnO nanoparticles was defined by tapes (**Figure 3.1a**). Subsequently, 40 μL (100 ng) antibody (MAb isotypes: C6) was added to the surface (**Figure 3.1a**). Ibupoto *et al.* [8] prepared the immobilised enzyme penicillinase on electrodes with grown ZnO nanorods by a cross linker for 20 minutes and kept them at 4 $^{\circ}\text{C}$ for about 16 hours. In this chapter, the biosensor was then dried in a desiccator with silica gel at 4 $^{\circ}\text{C}$ overnight for 18 hours (**Figure 3.1c**) without wash.

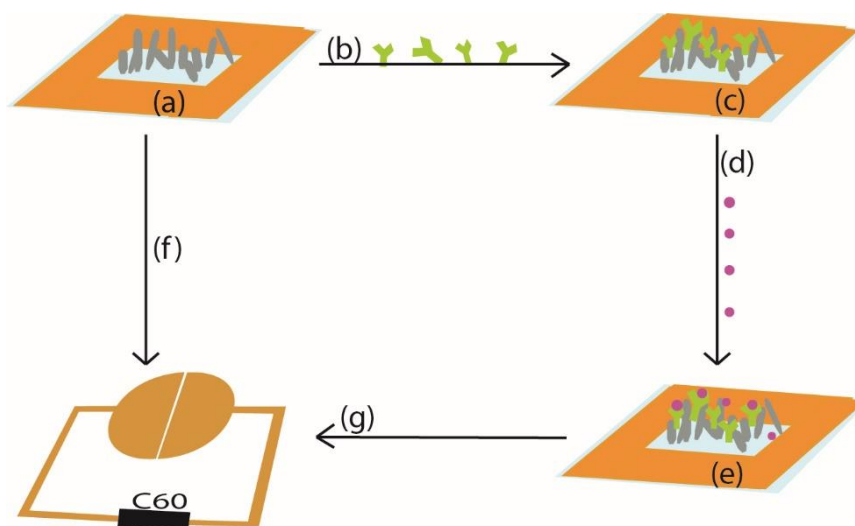


Figure 3. 1 Schematic illustration of biosensor fabrication and sensing: The ZnO sensing area was defined using tape (a); then the antibody was added to the ZnO surface (b); and dried at 4 °C overnight (c); different concentrations of antigen were prepared (d); and added to the immobilized antibody on the ZnO surface (e); the impedance was measured on a blank surface (f) and a surface subjected to the assay protocol (g).

A Cypher Instruments C60 Impedance-Amplitude-Phase Analyser was used to measure the impedance of the nano-crystal surfaces (**Figure 3.1f**). The frequency was scanned from 10 Hz to 4 MHz at a voltage of 2 Vpp and a DC offset of 0.9 mV, with 300 test points. The impedance plots were analysed by Cypher Graph V1.21.0, Impedance Amplitude and Phase Analyser graphing application software. Impedance spectra of ZnO nano-surfaces were acquired on 24 independent measurements at each of the three concentrations (g/100 mL) of ZnO used to prepare the surface.

CRP was prepared at a range of concentrations: 0 (PBS only), 1, 2.5, 5, 10, and 15 ng/mL (**Figure 3.1d**). 75 μ L of each concentration of antigen was added to the biosensor (**Figure 3.1e**) without wash. Following set incubation times, the impedance was measured (**Figure 3.1g**) without wash. Impedance measurements were also made at each stage of the assay process, namely: (1) On the nano-crystal surfaces with dry antibody; (2) Instantly, after adding 75 μ L of different concentrations of antigen and (3) at 5 minute intervals until 30 minute incubation time had passed. In order to plot logarithmic concentrations of CRP, the measurement of PBS buffer only with no CRP (control), was defined as 0.1 ng/mL CRP (rather than 0 ng/mL). The difference in impedance was derived by subtracting the impedance value of control for the

blank from each impedance measurement of the CRP assay at the various concentrations. The calibration curve was plotted based on impedance change versus logarithmic concentrations of detection CRP.

3.2.4 Statistical Analysis

Statistical tests were performed on impedance results of each different concentrations (g/100 mL) 0.5%, 1%, 5% ZnO nano-surface using Minitab. The %CV = (Standard Deviation/Mean*100) was used to compare variation and demonstrate reproducibility within groups. A 2-Sample t-test for between group comparisons was used to prove significant differences, a p value of <0.05 was considered significant.

A 4-parameter linear-log logistic curve of impedance changes in 0.5% and 1% ZnO nano-surface, with the error bars, was created using R.

In order to evaluate the capacitance of the system, a complex capacitance was defined as [135]:

$$C^* = -\frac{z''}{\omega|Z|^2} - j \frac{z'}{\omega|Z|^2} = C' + jC'' \quad (3.1)$$

Where C' corresponds to the real part of the capacitance and C'' corresponds to the imaginary part of the capacitance. Z' and Z'' are the real and imaginary components of the measured impedance, respectively, and $\omega=2\pi f$ is the angular frequency of the measurement. From the capacitance data, Cole-Cole capacitance plots can be obtained [135].

3.3 Results and Discussion

3.3.1 Validation of Nano-surfaces Fabrication

Impedance spectroscopy of the three ZnO nano-surfaces (from concentrations of ZnO nano-crystals suspensions of 5%, 1% and 0.5%) are shown in **Figure 3.2**. The results were plotted based on average impedance value of 24 samples for each concentration. These measurements were made on different sensors over a series of days. **Figure 3.2** shows that the average impedance values decreases as the concentrations of ZnO suspension decreases. This is due to the high loading of zinc oxide in the 5% sample causing the maximum perturbation of the electromagnetic field of the impedance sensor, due to the increased positive charge associated with the ZnO crystals.

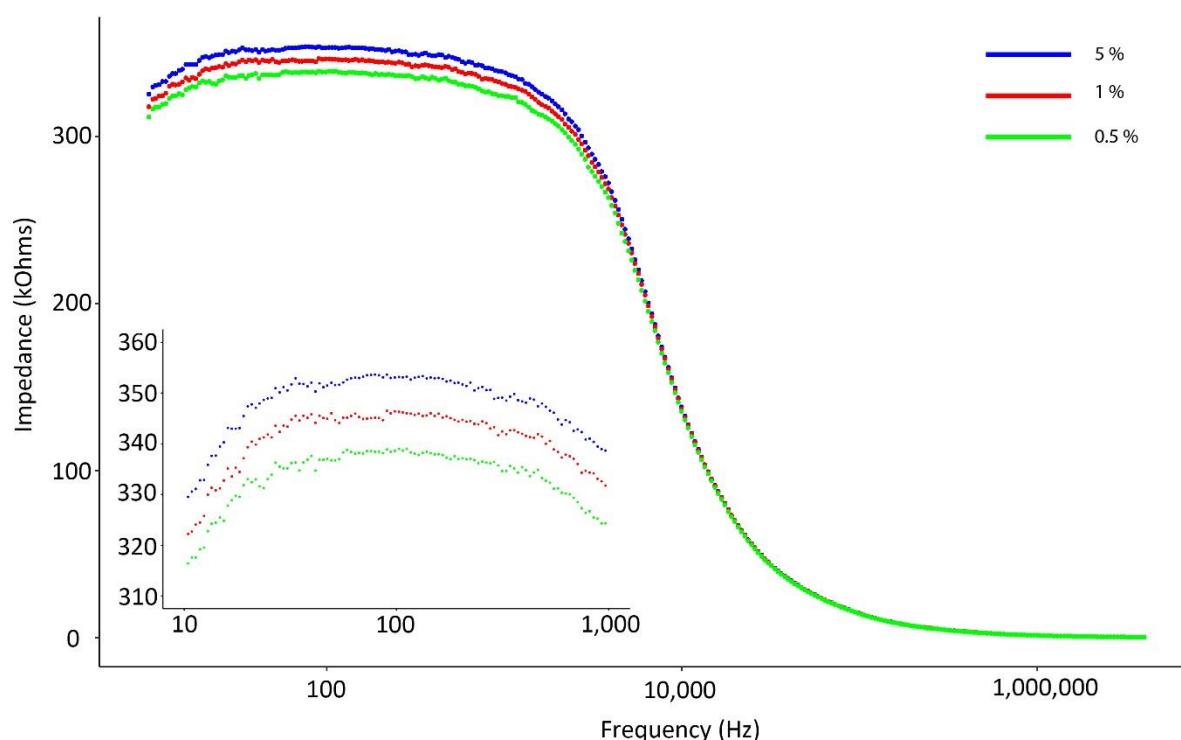


Figure 3. 2 Impedance spectra (n=24) of three different concentrations of ZnO nano-powders (blue: 5%, red: 1%, lime green: 0.5%) on PET substrates.

The greatest difference between the impedance values of the nano-surfaces at different concentrations of ZnO occurred at a frequency of 138 Hz. This frequency was similar to

frequencies used in the literature. For example, Jacobs *et al.* [101] found that the most significant changes occurred around 100 Hz, when adding various concentrations of the protein troponin-T on to a ZnO surface. Jacobs reported that this was due to the fact that the electrical double layer is greater at low frequencies below 1000 Hz [101]. A statistical analysis of the impedance values taken at a frequency of 138 Hz are shown in **Table 3.3**. The %CVs demonstrate that the fabrication process is reliable as the 24 measurements were performed on individual sensor surfaces. Although all surfaces were highly reproducible, the highest concentration of ZnO nano-crystals resulted in the highest reproducibility. At all concentrations, there was a highly significant difference between the impedance of bare PET material and the impedance of the PET with ZnO ($p < 0.001$).

Table 3. 3 Data analysis on impedance values on each set of ZnO nano-surfaces at fixed frequency

Different concentrations of ZnO suspensions dropped on PET	N	Mean	StDev	CV (%)
5 %	24	352870	2453	0.70
1 %	24	345567	4117	1.19
0.5 %	24	338387	5633	1.66

3.3.2 Characterisation of Surface

From the SEM images, **Figure 3.3(a)**, 5% ZnO suspension, shows a surface with a more complete covering of ZnO compared with **Figure 3.3(b)**, 1% ZnO suspension. This observation was as expected owing to the larger mass of ZnO applied. **Figure 3.3(c)** shows that the surface of 0.5% ZnO nano-crystals on PET is significantly different from the 1% and 5%, with abnormal sharp, platelet-like shapes. It is postulated that the relative absorption of ultrasound energy is greater by the crystals when there is a lower mass of ZnO material (0.5% ZnO), resulting in the fracture of the ZnO crystals forming the observed sharp platelets. It suggests that the size of composites could be due to the sonication-induced aggregation [123]. In other words, the lower concentrations of ZnO suspension are subject to larger shear forces which may fracture

the existing nanocrystal structures and subsequent agglomerate results in the formation of the other ZnO nano-structures observed.

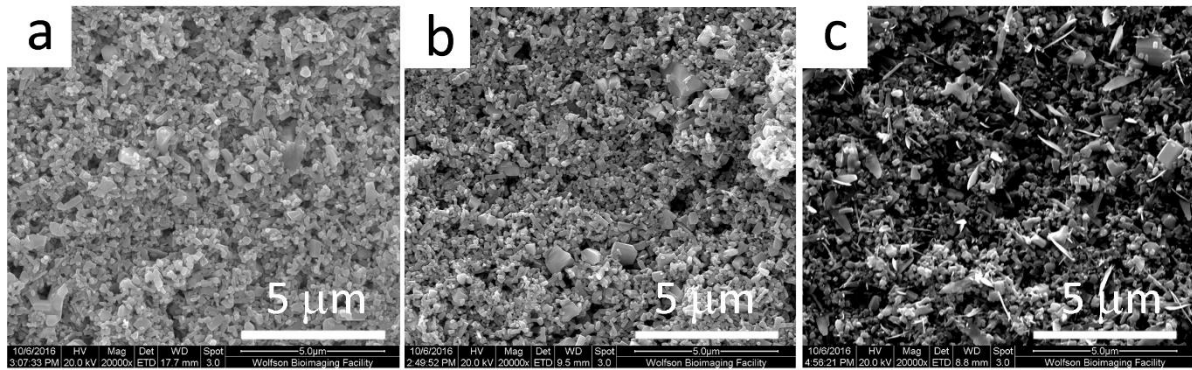


Figure 3. 3 SEM images for ZnO nano-surfaces on PET via suspensions at different concentrations (g/100 mL) of ZnO nano-crystals: (a) 5% ZnO; (b) 1% ZnO; (c) 0.5% ZnO.

From **Figure 3.4** it is clear that even though the surface is covered with dense nanoparticles, there are still many voids resulting in a porous surface. The lower values of grayscale represent darker areas on the image where the substrate is revealed and the higher grayscale values represent the lighter areas with a maximum grayscale value of 255. The profile plot of 5% ZnO shows a narrowest range of grayscale values compared with 1% and 0.5%, indicating that the surface of 5% is smoother than the others, with less deep holes and peaks across the nano-surface, reflecting the high density of ZnO nanocrystals present. This demonstrates that the colloidal dispersion technique and drop method provides uniformed ZnO films with 5% ZnO. In comparison, the 1% ZnO nano-surface gave full coverage of ZnO but with a rougher surface, whereas the 0.5% nano-surface showed many areas where the grayscale value was zero, indicating deep pits, revealing the underlying PET. The roughness index of the 0.5% ZnO nano-surface was calculated to be 8097, the 1% ZnO nano-surface was 10718 and 5% ZnO nano-surface was 2310. The results indicates that 1% ZnO nano-surface has the largest surface area; the 0.5% ZnO nano-surface had a relatively large surface area but there was incomplete coverage of the PET substrate whereas the 5% nano-surface is the least rough, with the smallest surface area.

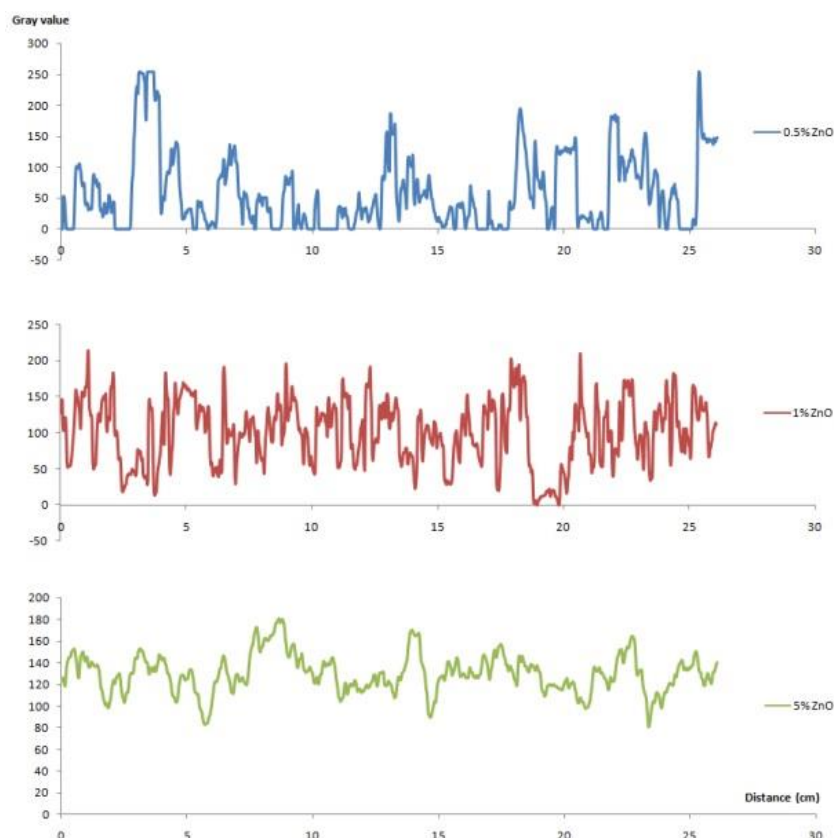


Figure 3. 4 Plots of grayscale profiles along a horizontal line within images (mag $\times 2000$) for nano-surfaces made by three different concentrations of ZnO suspensions: 0.5%, 1% and 5%.

3.3.3 Raman Spectroscopy Analysis of the Surfaces

Figure 3.5 shows the Raman spectra of bare PET (blue line) and PET covered with 1% ZnO nanocrystals (green line). There was a strong correlation with a Raman spectrum of pure PET [136], two strong, characteristic bands were observed at 1723 cm^{-1} and 1610 cm^{-1} which corresponded to C=O stretching and benzene ring structures. The band at 854 cm^{-1} corresponded to the ester C(O)O bending mode [136]. ZnO possesses C_{6v}^4 symmetry ($P6_3mc$) space group; there are eight sets of optical phonons at Γ point of Brillouin zone: $\Gamma=A_1+2B_1+E_1+2E_2$, with A_1 , E_1 and $2E_2$ modes are Raman active [137–139]. Published Raman spectra of ZnO nanorods [138,140], indicate significant bands at 438 cm^{-1} and 1050 cm^{-1} and a few weak bands at 330 , 379 , 535 and 585 cm^{-1} . The strong peak at 438 cm^{-1} indicate high E_2 mode, which represents ZnO wurtzite hexagonal spectrum [139]. The Raman spectrum of the ZnO surface shown in **Figure 3.5**, shows that the bands associated with the PET are attenuated due to being covered by ZnO, additional bands are seen at 324 , 435 , 532 , 582 and

1050 with the significant bands at 324, 435 and 1050 cm^{-1} . These results strongly indicate the ZnO nano crystals cover the surface. A Raman peak at 324 cm^{-1} represents a highly crystalline structure in the ZnO nanomaterials, while peaks at 584 and 673 cm^{-1} represent disordered material and impurities which assigned to the E_{1L} and A_1 phonon modes [139]. Comparing the intensity of two peaks at 324 cm^{-1} and 582 cm^{-1} , the peak at 435 cm^{-1} was far greater, indicating that the nano-surface with ZnO crystals was highly ordered and uniform.

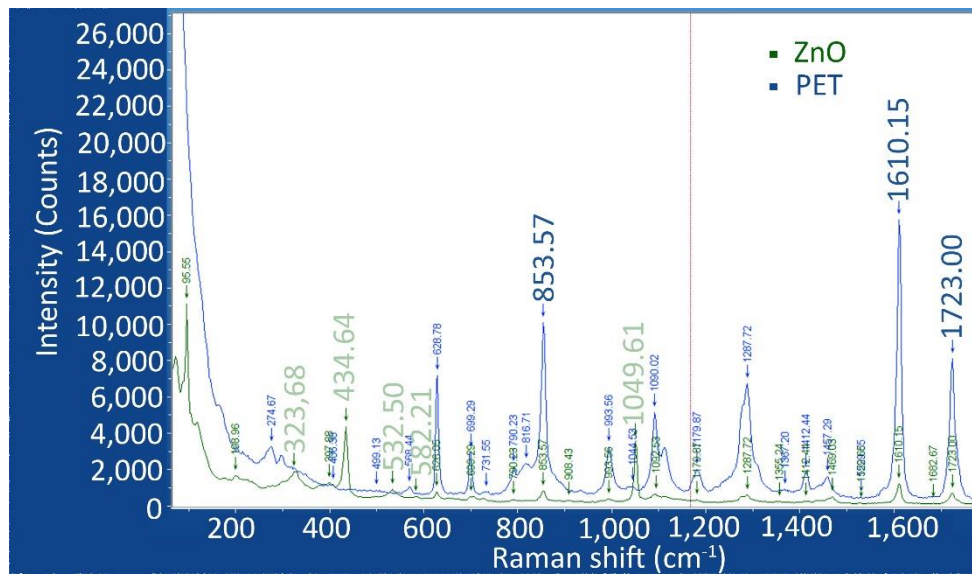


Figure 3. 5 Raman spectra of bare PET (blue line) and PET covered by 1% ZnO nanocrystals (green line) at room temperature. Conditions of recording Raman Spectrum of bare PET: time acquisition 30s, wavelength 785 nm. Conditions of recording Raman Spectrum of nano-ZnO on PET: time acquisition 50s, wavelength 785 nm.

Figure 3.6 shows the Raman spectra of 1% ZnO with capture antibody (green line) and ZnO without the capture antibody molecule (blue line). The main goal is to identify antibody on the surface of the ZnO through the spectra derived from antibody. The anti-Human C-reactive protein, used in this study is an IgG2a isotype. Bands associated with antibody were observed at 2937, 2576, 2211, 1125, 999 and 914 cm^{-1} , providing strong evidence that antibody is on the surface because of the ZnO nanocrystals. Kengne-Momo [141] reports that IgG will give bands at 914 cm^{-1} (CH_2 deformation (ρCH_2); 2937 cm^{-1} (C–H stretching ($\nu\text{C–H}$) of aliphatic chains). Both of these bands are evident in **Figure 3.6**. In addition, the backbone skeletal $\nu\text{C–C}$ vibration bands were observed in the region of 999 to 1125 cm^{-1} .

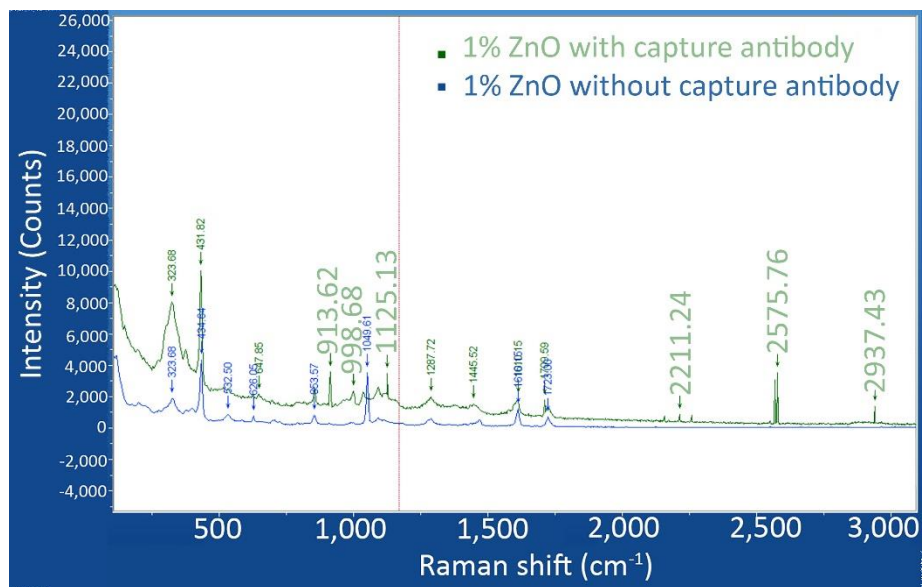


Figure 3. 6 Raman spectra of ZnO nano-surface on PET (blue line) and ZnO with capture antibody on PET (green line). Conditions of recording ZnO with capture antibody on PET: time acquisition 150s, laser wavelength 785 nm.

3.3.4 Calibration Curve Comparison of the Three ZnO Nano-surfaces with CRP Immobilised

To examine the effect of varying the incubation period, measurements were performed on 1% ZnO nano-surfaces prepared with antibody and incubated for 5, 10, 15 minutes. **Figure 3.7** shows the plots were similar indicating that beyond 5 minutes the incubation time does not greatly influence the result, which suggests that binding of CRP to the antibody occurs rapidly.

The instability of impedance values at 15 minutes is due to ZnO nanoparticles degradation in buffer solution [142,143]. The dose dependent response of absolute impedance for each incubation time shows decreasing impedance with increasing CRP loading. The manufacturers technical specification state that the CRP was produced from a human source, which is assumed to be pentameric. This can be explained by the fact that in this experimental set-up the ZnO is positively charge, whereas the CRP is dominated by negative charge (the calculated isoelectric point of CRP pentamer is ~ 5.3 [144]). Impedance spectroscopy provides a measurement of the capacitance of an electrical double layer formed when a semiconducting material interacts with liquid electrolytes [18]. Consequently, when binding to the ZnO occurs, through capture by the antibody on the surface, there is a decrease in the overall positive charge with increasing CRP loading and a decrease in the absolute impedance value. This observation concurs with the literature where it is reported that, for non-faradaic biosensors, changes in the surface dielectric and charge distribution are induced when a protein target binds to the receptor, previously attached in the electrode, displacing water and ions from the surface [61].

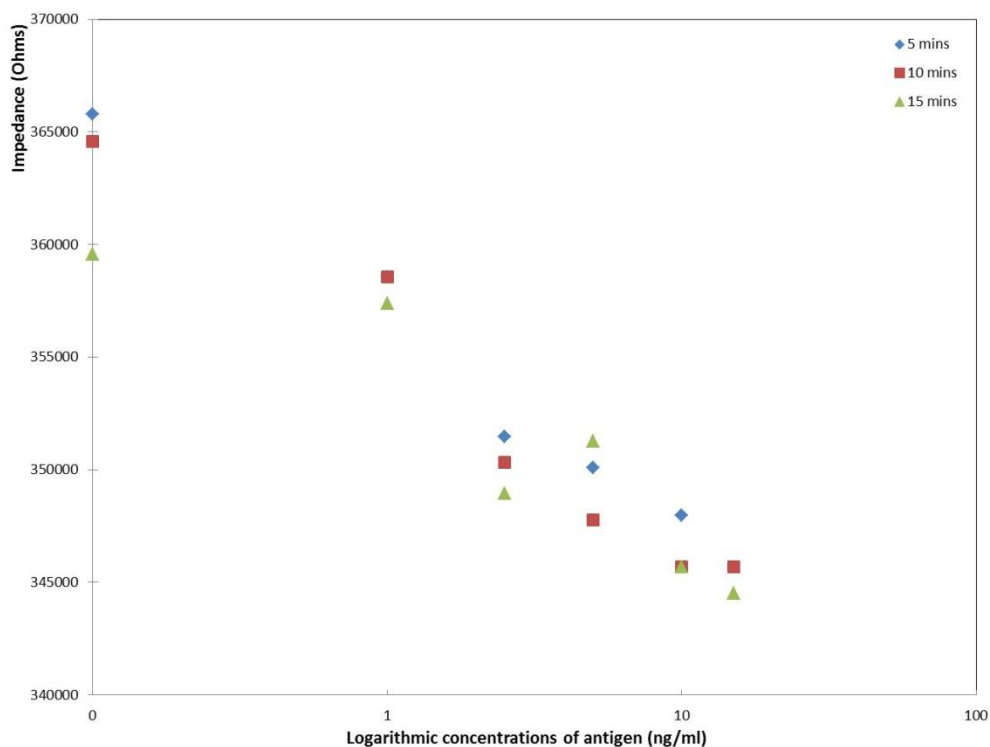


Figure 3. 7 Impedance values from 1% ZnO nano-sensors, with 100 ng capture antibody with increasing concentrations of antigen: 0 - 15 ng/mL for 5, 10 and 15 minute incubation time.

The three different nano-surfaces were compared by measuring impedance changes with 100 ng capture antibody by adding different concentrations of CRP from 0 to 15 ng/mL at 138 Hz with 10 minute incubation time. **Figure 3.8** depicts Cole-Cole plots with dose response of CRP on three different nano-surfaces 0.5%, 1% and 5%. **Figure 3.8(b)** shows the most obvious capacitive shift with the concentrations of CRP on 1% ZnO nano-surface. **Figure 3.9** also demonstrates the change impedance with increasing concentrations of CRP.

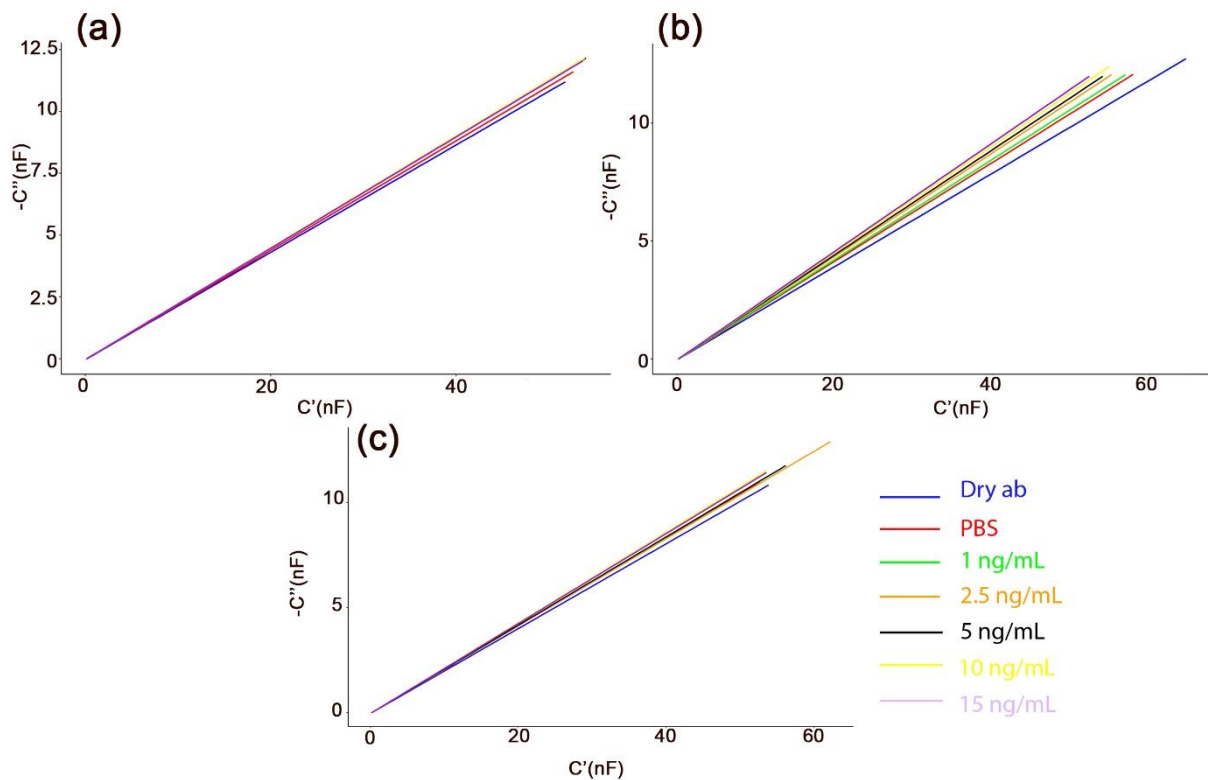


Figure 3. 8 Cole-Cole plots for the CRP dose response ($n=1$) of each of three different concentrations of nano-surfaces with 100 ng antibodies loading at D-shape electrode representing the capacitance of the system calculated from impedance data (a) 0.5% (b) 1% (c) 5%.

These experimental conditions were used because, as described above, reproducible differences between each type of samples were evident at 138 Hz. In addition, from **Figure 3.7**, the absolute impedance behaviours have shown to perform reliably within a 10 minute incubation time. The modulus of the impedance differences (impedance value minus the blank) were employed to plot a calibration curve as shown in **Figure 3.9**. The impedance

difference plot shows increasing values of the modulus of the impedance difference with increasing concentrations of CRP for the 0.5% and 1% ZnO nano-surfaces.

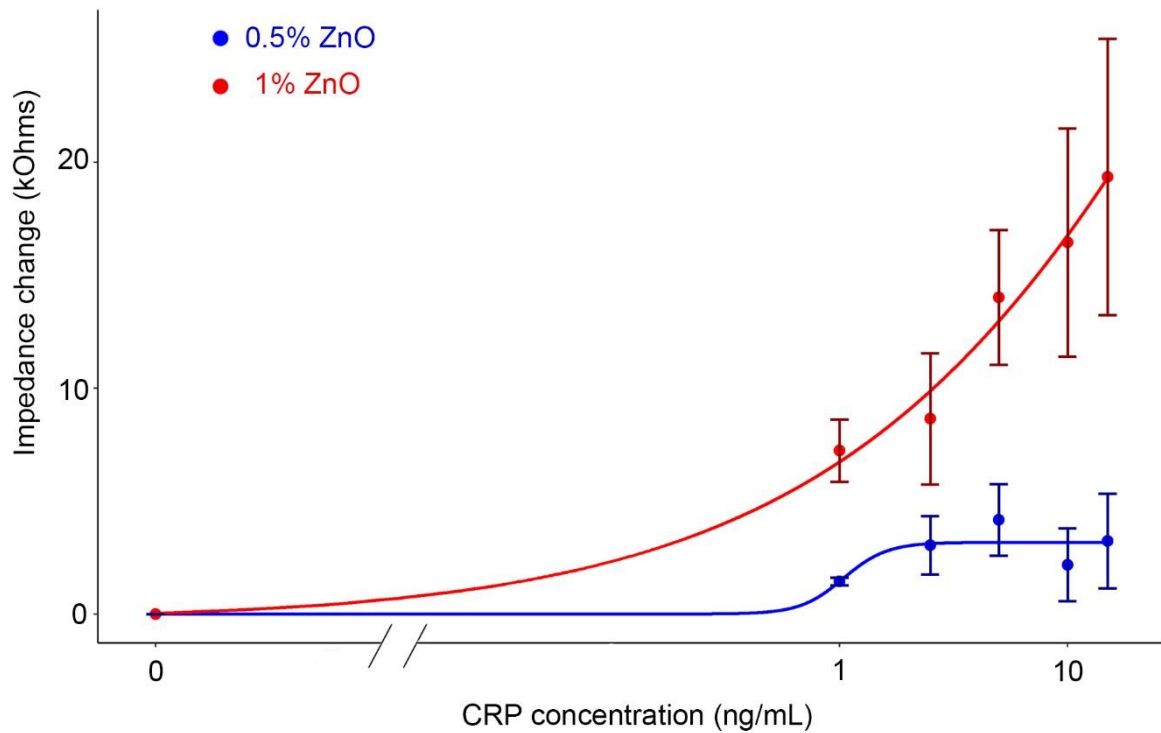


Figure 3.9 Impedance change in response to increasing concentrations of antigen on 0.5% and 1% ZnO nano-surfaces ($n=3$) with 100 ng capture antibody.

Figure 3.9 shows 4-parameter linear-log logistic curves, with the error bars, was created using R. **Figure 3.9** also shows that biosensors prepared with 1% ZnO gave the significant higher output for each concentration of CRP compared with 0.5%. The performance of the biosensors is related to the availability of antibody on the surface to bind CRP when added to the surface. Increasing concentrations of antigen binds to a fixed amount of antibody in a dose dependent manner defined by the binding affinity. It is speculated that there is increased charge accumulation due to the bound antigen on the surface compared with the antigen in solution. This acted as a parallel capacitor to the modelling circuit, which increased the capacitance and reduced the impedance values. In addition, there will be an increased amount of isolated antigen flowing freely in solution, resulting in a decrease in the charge carriers and hence resistance of the solution. However, it will influence the sensitivity of the

sensing surfaces due to non-specific bindings in the solution with loose uncaptured antibodies. Surfaces fabricated using 1% ZnO showed the highest roughness Index implying it has the greatest surface area on which the anti-CRP antibody were captured. **Figure 3.9** plots the impedance change against concentrations of CRP. The slope was calculated to represent the sensitivity. The calibration curve using 1% shows high sensitivity with an average enhancement of 5 times a greater signal compared with 0.5% ZnO. The biosensor based on 1% ZnO nano-surface has the potential to be developed into a rapid, inexpensive and sensitive diagnostic test for CRP. The low sensitivity of 0.5% ZnO nano-surface is likely to be due to the fact that using 0.5% ZnO the PET surface is not fully covered and that the ZnO exists as “islands” of nanocrystals in a modified form due to the ultrasonication. Because of the thickness of flatter 5% ZnO nano-surface, it was easy to break during the process of protein immobilization. The impedance tests were unstable with big error bars excluded in **Figure 3.9**. As presented in Chapter 2, the C60 impedance analyser reaches a maximum impedance of 450 kOhms boundary at low frequencies. This results in background noise due to instability, which resulted in experimental impedance changes with big error bars.

3.3.5 Comparisons of Non-Specific Binding

Impedance comparisons of anti-CRP loading (0 ng, 100 ng and 200 ng) with 5 ng/mL CRP on 1% ZnO nano-surfaces are shown in **Figure 3.10**. The results show that 200 ng loading of antibody gave a response two times greater signal than that of 100 ng antibody loading signal when the control (0 ng) was taken into consideration. **Figure 3.10** also showed the weakest signal on 1% ZnO nano-surface with 0 ng capture antibody when 5 ng/mL CRP was added. As predicted, the figure shows that the signal generated is associated with the interaction between anti-CRP antibodies and CRP which was greater when there was a greater number of binding sites provided through the capture antibodies.

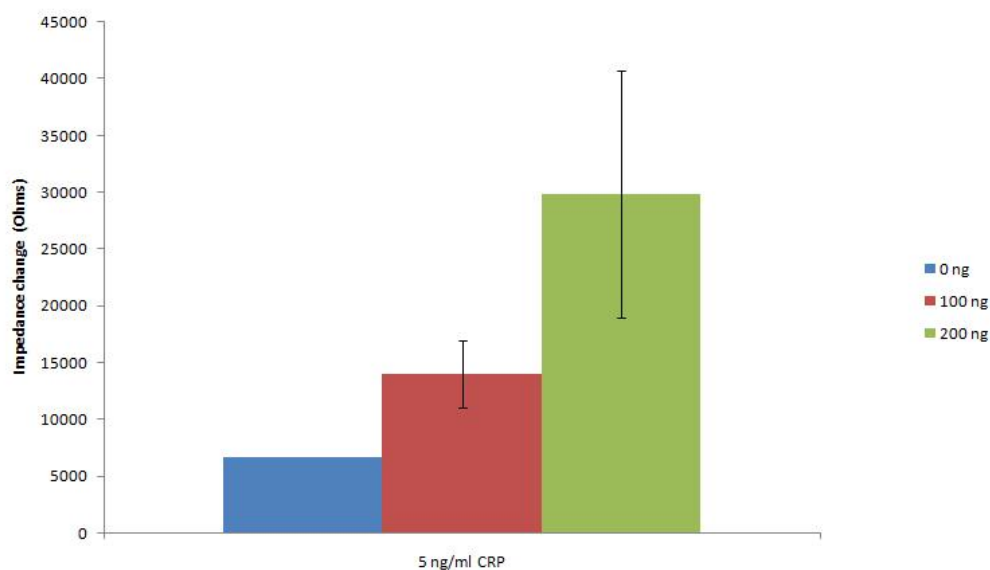


Figure 3. 10 Comparison of anti-CRP loading 1% ZnO nano-surface (n=3) at the frequency of 138 Hz for the detection of 5 ng/mL CRP.

The response that was seen in the absence of antibody represents the non-specific binding of CRP on the ZnO nano-surface. Assaifan *et al.* utilised PBS solution to replace the antigen solution on their ZnO biosensor to show a zero result without binding of antigen to antibody [59]. They concluded that the charge accumulation caused by the binding of antibody and antigen is the main factor in impedance change and not due to the changes of the testing solution or the EIS test itself [59].

3.4 Summary

This chapter shows that zinc oxide nano-surfaces can be created simply and at low cost using a new colloidal dispersion technique, incorporating sonication. ZnO nano-surfaces showed the potential to develop a nano-crystalline based biosensor. The high isoelectric point is important for electrostatic attraction to biological molecules. The fabrication of ZnO nano-surfaces is low-cost and results in enhanced behaviour of the biosensor, whilst being highly stable. Raman spectra of the surface indicated the ZnO crystal surfaces was highly ordered and uniform. Impedance analysis confirmed that the ZnO surfaces were highly reproducible, individual measurements being taken across many days. SEM analysis illustrated differences in the surfaces when three different ZnO suspension concentrations were applied. The highest concentration studied (5% ZnO) showed the smoothest surface whereas the lowest concentration (0.5%) showed incomplete coverage of the substrate. 1% ZnO demonstrated full coverage of the surface and the largest surface area which was quantified by a roughness index. After addition of the antibody to the ZnO surface, Raman spectroscopy confirmed that there was coverage of ZnO surface with the IgG antibody.

At a fixed frequency of 138 Hz, a dose dependent response was observed from 0.1 ng/mL to 15 ng/mL CRP for all 3 concentrations of ZnO (5%, 1% and 0.5%). The calibration curve using 1% shows high sensitivity with an average enhancement of 5 times a greater signal compared with 0.5% ZnO. 1% ZnO nano-surface showed the best results with the highest sensitivity of the 3 plots. This may be explained by the fact that the 1% ZnO nano-surface has the highest roughness index of the 3 concentrations, calculated from **Figure 3.4**, and hence the largest surface area for binding. In contrast, the 0.5% ZnO nano-surface shows incomplete coverage, high variability of particle size and shape and also the lowest sensitivity. Interestingly, during biosensor preparation, the 1% ZnO nano-surface was more stable than 5% during the process of protein immobilisation. Finally, the method for fabrication of ZnO nano-surface via colloidal dispersion coupled with ultra-sonication is simple and inexpensive and therefore suitable for future application as the basis of disposable biosensors.

The next chapter builds on this work to develop ZnO/CuO nanosurfaces. The signal outputs are analysed to explore the effect of CuO within a nano-structured surface of a biosensor.

Chapter 4

Copper Oxide-Enhanced Composite Nano-surface Biosensor

Following on from the previous chapter, the 1% zinc oxide (ZnO) nano-surface shows good behaviour being stable and enhancing sensitivity for detecting C-Reactive Protein (CRP). The second experimental chapter investigates the improvement in performance when copper oxide (CuO) nanoparticles are mixed with ZnO nanoparticles to develop non-faradaic impedimetric biosensor. In order to achieve sensing areas, anti-CRP antibodies were also immobilised on ZnO/CuO nanoparticle surface in a technique that includes no wash step. To demonstrate the enhancement of copper oxide (CuO) mixture with ZnO nanoparticles, different combinations of CuO and ZnO colloidal suspensions are used to fabricate nano-surfaces. The surfaces were characterised and compared using techniques including measurement of the phase changes using impedance spectroscopy. This chapter provides the evidence, which is then built on in the remaining chapters, to demonstrate the enhanced sensitivity achieved using a combination of ZnO and CuO nanoparticles.

The work presented in this chapter has been mostly published in Cao *et al.* [145]. I contributed to the research design and carried out the experimentation including nano-surfaces preparation and fabrication, surface characterisation, immunology assay and impedance test. I also processed the experimental data and discussed the results, wrote the initial draft of the manuscript.

4.1 Introduction

The previous experimental chapter has proven the validity of using ZnO nano-surface as a biosensing area for detection of CRP by non-faradaic process. This experimental chapter presented here investigated mixtures of ZnO and CuO nanoparticles to fabricate nanocrystal surfaces for the immobilisation of anti-CRP antibodies. An enzyme labelled antibody was used to assess protein uptake on the nano-surfaces. The fabrication of the nano-surfaces used a simple and inexpensive colloidal dispersion technique. ZnO nanocrystals were deposited on PET, coated with anti-CRP antibodies and then sandwiched between two glass coverslips for the detection of CRP. The bottom glass slip is to provide support for the sensor. The upper glass slip is to seal the biosensor without liquid evaporation. The binding of CRP to the antibody on the biosensor surface was detected and quantified using impedance spectroscopy. Fabrication of the ZnO/CuO nano-surfaces was straight forward, with a process that is compatible with large scale manufacture.

Enhancement of material properties have been demonstrated by incorporating other materials or elements within a ZnO matrix. For example, the implantation of iron oxide (Fe_3O_4) in ZnO nanosheets decreases the charge transfer resistance and also ensures that the nanosheets are photostable and reusable, and thus suitable for application as photocatalysts [146]. In order to enhance the electrocatalytic properties of a modified electrode, carbon xerogel-zinc oxide composites were synthesized by the sol-gel method, contributing to good material conductivity [147].

The addition of CuO to ZnO has been shown to improve sensitivity by enhancing the redox property and electron transfer. ZnO surfaces have been created by an electro-spinning method followed by hydrothermal treatment, with CuO subsequently being added by a wet method [75]. These 'CuO-decorated ZnO hierarchical nanostructures' were employed to enhance the performance of a hydrogen sulphide (H_2S) gas-sensor. Furthermore, a novel free-standing ZnO-CuO composite film, which was fabricated by a modified hydrothermal method, in order to remove the need for a substrate [148], formed the basis for a gas sensor which showed a good improvement in response for sensing carbon monoxide (CO) gas compared with pure ZnO nanowires [148]. Finally, a ZnO-CuO composite matrix was fabricated on an indium tin oxide coated corning glass substrate by pulsed laser deposition [86]. The inclusion

of CuO resulted in excellent redox properties, and consequently, in the absence of any external mediator, good oxidation and reduction peaks were visible on a cyclic voltammogram. The improvement in properties in these composite nanoparticles has been related to the decrease in the band gap energy. In fact, it has been shown that the higher the concentration of CuO in a ZnO-CuO composite, the smaller the band gap [77].

However, for all of these examples plus others in the literature, the formation of ZnO/CuO composite nanoparticles/nano-surfaces requires complex processes, typically involving high temperature and long time periods. For example, ZnO nanowires have been grown by thermal evaporation and CuO films have been synthesized by thermal oxidation (at 400 °C for 12 hours in 80 % oxygen/20% argon atmosphere); the Cu films initially being produced by a radio frequency sputtering technique [149]. Methods described for fabricating CuO/ZnO nanocomposites are also complex. For example, Widiartiet *et al.* [77] added copper(II) sulphate pentahydrate ($\text{CuSO}_4 \cdot 2\text{H}_2\text{O}$) to citric acid stirring until homogenous and the precursor solution made by ethylene glycol mixed with $\text{Zn}(\text{CH}_3\text{COO})_2 \cdot 2\text{H}_2\text{O}$, deionized water and citric acid by vigorous stirring for an hour. The solution was added by NaOH drop by drop stirring for one hour and kept for 48 hours for aging. The gel was washed and dried in oven to constant weight and then calcined at 500 °C for 4 hours [77].

4.2 Materials and Methods

4.2.1 Nano-surfaces Preparation

Preliminary experiments were carried out to find the optimised combinations of nano-surfaces. The nanoparticles-based surfaces were produced using 1:1 volume ratio of 1% or 5% concentrations (g/100 mL) of nano-ZnO and CuO suspensions shown in Appendix **Figure S4.1**. The 5% CuO sensors were not stable during the process of antibody immobilisation. **Figure S4.2**, Appendix A, shows a number of sensors that had been prepared using 5% CuO. In all cases the nanoparticles fractured and broke away from the surfaces. The lower concentration of 0.5% ZnO nano-surfaces gave uneven nanoparticles distribution. Although ZnO nanoparticles had the ability to smooth the surface, too much nanoparticles created cause the break easily. So the optimised concentration of using ZnO and CuO is 1%.

To create both 1% ZnO and 1% CuO suspensions, 0.15 g ZnO nanoparticles (ZnO, 99.9+%, 80 - 200 nm) was added to 15 mL double deionized water and 0.1 g CuO nanoparticles (CuO, 99.5+%, width 10 - 30 nm, Length: 200 - 800 nm) was added to 10 mL double deionized water. The suspensions of both 1% ZnO and 1% CuO were stirred at room temperature for 1 hour. Five different nano-surfaces were produced using 1% ZnO and 1% CuO by volume ratio as follows: 0% CuO (ZnO only), 33% CuO (2:1 ZnO/CuO via volume ratio), 50% CuO (1:1 ZnO/CuO), 67% (1:2 ZnO/CuO) and 100% CuO (CuO only). The methods were the same as Chapter 3, then 1.5 mL aliquots of each preparation (prepared by volume ratios) were ultra-sonicated for 7 periods of 20 seconds, at 4 minute intervals using an exponential microprobe (Soniprep 150) at 30 watts. Small volumes of nanoparticle suspension were well dispersed using sonicated probe. The intervals between the sonication aimed to cool down the heat due to sonication power. The 7 periods of 20 seconds aimed to have enough accumulated sonication time to form a colloidal suspension. 200 μ L of each suspension were dropped on to clean PET substrates (20 mm x 20 mm) separately to make ZnO/CuO nano-surfaces. Subsequently, the 12 samples for each different nano-surfaces were dried in an oven at 65 °C for 80 minutes and cooled down to room temperature, then stored in a dry atmosphere with silica gel for up to 2 days [121]. The samples can be kept for years for Raman, SEM tested after production in dry atmosphere. For impedance test, the samples behave stable in a year based on phase analysis comparison shown in Appendix **Table S4.1**.

4.2.2 Characterisation of Nano-surfaces

The morphology of pure ZnO and mixed ZnO/CuO composite nano-surfaces were analysed by the Quanta 200 Scanning Electron Microscope | Thermo Fisher Scientific. The samples were coated with a thin layer of Au prior to analysis. SEM picture of CuO only could not be obtained, as the CuO is highly conductive and there was a risk that the nanoparticles would contaminate the SEM.

Atomic Force Microscopy (AFM) was used to examine the topology of the different nano-surfaces using Bruker Innova Atomic Force Microscope with an antimony (n) doped silicon tip. Each AFM image was analysed using the NanoScope Analysis software. Image surface areas were compared within a 3 μm by 3 μm scan area. Calculation of the total surface area and mean roughness (R_a) within the scanned region provided a method of comparing the roughness of the various nano-surfaces.

Raman spectroscopy was used to analyse the chemical compositions of the pure 1% ZnO and mixed 1% ZnO/CuO (1:2) nano-surfaces. An XploRA Raman spectrometer from Horiba, equipped with a confocal microscope, was used. The Raman signals were collected in a range of 0 - 3500 cm^{-1} using a 785 nm red laser excitation. The laser beam was focused on the sample using objective magnification of 50 \times .

4.2.3 Surface Uptake of Antibody

Due to the maximum antibody density, 3.77 ng/mm^2 [112], i.e. a sphere with the same molecular weight as the antibody but with an homogeneous distribution of mass, that has a radius of 3.6 nm and a molecular weight of 150 kDa, the optimised antibody amounts based on my defined sensing area (10 mm \times 4 mm) will be 150.8 ng of antibody by roughly calculation. The maximum volume (75 μL) can contain on the nano-surface (experimental experience). The calculated 2.5 $\text{ng}/\mu\text{L}$ concentration of anti-mouse Ig-HRP was diluted in PBS.

To understand how ZnO and CuO capture protein on their surfaces an antibody-enzyme conjugate was used in place of the anti-CRP. Here, 75 μL anti-mouse Ig-HRP (2.5 $\text{ng}/\mu\text{L}$) from Bio-Rad Antibodies Inc. was dropped on each surface within the sensing area and dried in a

desiccator with silica gel at 4 °C overnight for 18 hours, same as biosensor CRP assay in next section 4.2.4. Anti-HRP stock solution was stored and diluted in 0.05 M PBS [56] with pH 7.40. The 75 µL volume of anti-mouse Ig-HRP is the maximum amount can be covered on the surface in order to fully react. Following a thorough wash, to remove unbound protein, with 0.05 M PBS, 40 µL 3,3',5,5'-Tetramethylbenzidine (TMB) was added on the surface for 10 minutes after which 50 µL stop 3,3',5,5'-Tetramethylbenzidine solution was added. The colour intensity of each test was read at 450 nm using a microplate reader (EZ Read 400). The relative amounts of surface bound antibody were defined by the optical density of the tests of the different sensor surfaces.

Data were presented with one blank sample on each nano-surface, without anti-mouse Ig-HRP, as a control and two test samples (with antibody) on each nano-surface.

4.2.4 CRP Sensor Fabrication and CRP Assay

The sensing area (10 mm × 4 mm) of each ZnO/CuO nano-surface on PET was defined by tape. Subsequently, 40 µL (100 ng or 200 ng) of monoclonal mouse anti-human C-reactive protein from HyTest Ltd (Turku, Finland) was added to the surface. Anti-CRP antibodies were stored and diluted in 0.025 M PBS with pH 7.40. The biosensor was then dried in a desiccator with silica gel at 4 °C overnight for 18 hours. The nano-surface biosensors were then aligned above a pair of D-shape electrodes to perform impedance measurements.

A Cypher Instruments C60 Impedance-Amplitude-Phase Analyser was used to measure the impedance of the nano-crystal surfaces. The frequency was scanned from 10 Hz to 4 MHz at a voltage of 2 Vpp with a DC offset of 0.9 mV, with 300 test points. The impedance plots were analysed by Cypher Graph V1.21.0, Impedance Amplitude and Phase Analyser graphing application software. Impedance spectra of the ZnO/CuO nano-surfaces were acquired in triplicate for each of the following types of surface: 1% ZnO and 1:1, 1:2 and 2:1 volume ratio of 1% ZnO and 1% CuO suspensions.

The impedance amplitude and phase were measured after 10 minute incubation time following the addition of 40 µL of different concentrations of human C-reactive protein (CRP) from HyTest Ltd and sealing the sensing region to form a chamber using cover slip. The specific

concentrations of CRP were as follows: 0, 1, 5, 10 and 100 ng/mL diluted in 0.025 M PBS with pH 7.40.

The cross-section of one of the biosensors (ZnO only) is illustrated in **Figure 4.1**. This shows the sensing area with ZnO nanocrystals, on PET and dry anti-CRP antibodies for the detection of CRP sandwiched between two coverslips.

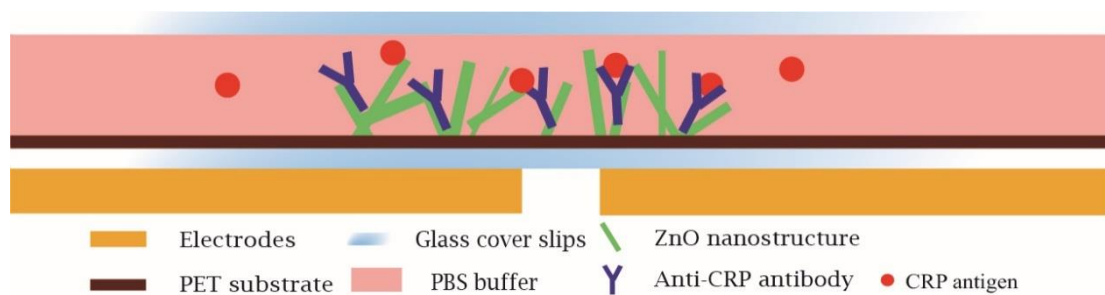


Figure 4. 1 The cross-section illustration of biosensor.

The sensor response was plotted using readings taken at a frequency of 138 Hz, for the reason described in section 3.3.1. Impedance values were compared with both 100 ng and 200 ng anti-CRP capture antibody. The phase change was defined as the difference of the phase value after adding CRP, after 10 minute incubation, and the control. Only CRP in buffer was added to the surfaces, no non-specific proteins were in the system. The changes of phase only show the difference of antibody-antigen bindings when adding various concentrations of CRP. In order to plot logarithmic concentrations of CRP, the measurement of PBS buffer only with no CRP (control), was defined as 0.1 ng/mL CRP (rather than 0 ng/mL). The calibration curve was plotted based on phase change versus logarithmic concentrations of CRP.

4.2.5 Statistical Analysis

Calculation of thickness of ZnO nano-film was using ImageJ software with 20 measurements collected and histogram distribution was plotted by R software.

A Kruskal-Wallis test was used to analyse the phase change with the ratio of CuO/ZnO and level of significance was defined as $p \leq 0.05$. A Kruskal-Wallis test was used to analyse the absorbance values and data of phase change, level of significance was defined as $p \leq 0.05$.

A 4-parameter linear-log logistic curve, with the error bars, was created using R. The estimated limit of detection (LoD) was defined as the intercept on the y axis of the calibration curve, plus 3 times the standard deviation of the blank and calculated using R. The mean value and Standard deviation of the "intercept" at the working zero found using the 4-parameter logistic curve.

The %CV = $(\text{Standard Deviation}/\text{Mean} * 100)$ was used to compare variation and demonstrate reproducibility within groups.

4.3 Results and Discussion

4.3.1 Morphological Study

Figure 4.2 shows SEM images of nano-surfaces of 1% ZnO and different combinations of 1% ZnO and 1% CuO suspension after ultra-sonication with the ratio of 2:1, 1:1 and 1:2 ZnO/CuO. (**Figure S4.3** shows other magnifications of nano-surfaces of 1% ZnO and different combinations of 1% ZnO and 1% CuO suspension after ultra-sonication with the ratio of 2:1, 1:1 and 1:2 ZnO/CuO.) It was found that the surfaces appeared uniform at magnification of 10,000× and 20,000×. SEM images were taken and selected at specific area but representative as a whole surface characterisation. **Figure 4.2(a)** clearly shows the columnar wurtzite structure of ZnO nanoparticles with a number of voids within this structure. **Figure 4.2(b-d)** show the effects of adding increasing amounts of CuO nanoparticle flakes (marked by triangle frame) to the nano-surface (67% CuO, 50% CuO and 33% CuO respectively). It can be seen that the CuO plates pack into the spaces within the ZnO structure (marked by rectangle frame) having the effect of creating a smoother and less “pitted” surface.

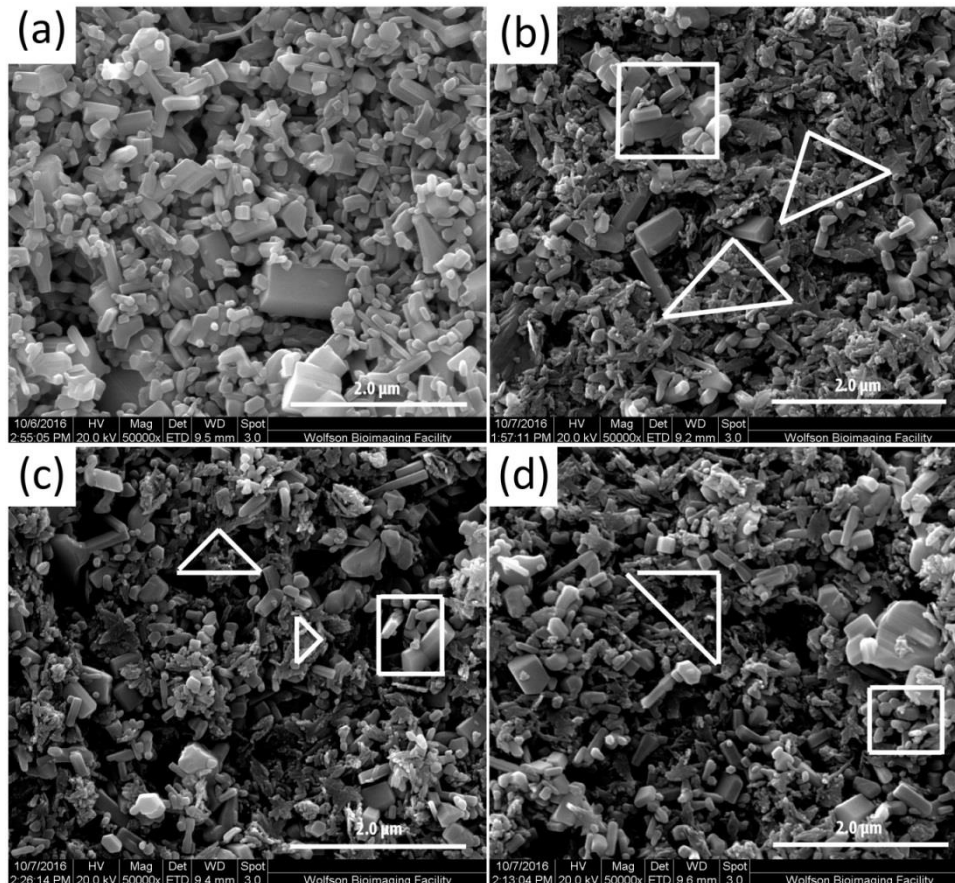


Figure 4.2 SEM images of nano-surfaces: (a) 1% pure ZnO (b) 1% ZnO and CuO suspensions with the ratio of 1:2 (c) 1:1 (d) 2:1.

Figure 4.3 shows 3D surface model AFM images (areas of 3 μm by 3 μm) of pure ZnO and CuO as well as a mixed ZnO/CuO nano-surface. **Figure S4.4** shows 3D surface model AFM images (areas of 1 μm by 1 μm) of pure ZnO as well as a mixed ZnO/CuO nano-surface. **Figure S4.5** shows 3D surface model AFM images (areas of 10 μm by 10 μm) of pure ZnO and CuO as well as a mixed ZnO/CuO nano-surface. The reason for choosing the scan area of 3 μm by 3 μm is that **Figure S4.4** shows AFM images (areas of 1 μm by 1 μm) cannot provide the whole scale of the surface, and **Figure S4.5** AFM images (areas of 10 μm by 10 μm) cannot distinguish the surface characteristics more in details. Therefore, the scan area of 3 μm by 3 μm was a balance to compare the surface characteristics.

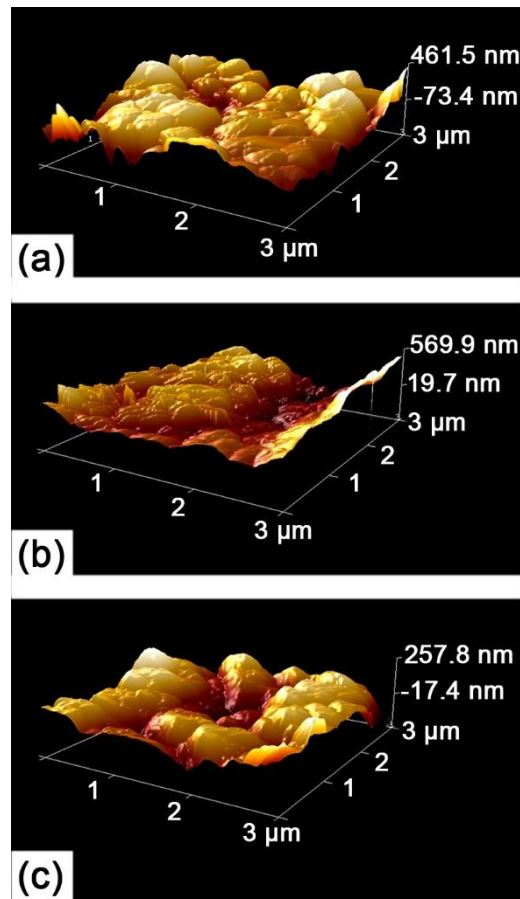


Figure 4.3 AFM 3D images of 3 μm by 3 μm area of the nano-surfaces: (a) 1% pure ZnO; (b) 1% pure CuO; (c) 1% ZnO and CuO suspensions with the ratio of 1:2.

The images demonstrate that the CuO nanoparticles are distributed evenly across the ZnO nano-surfaces for the mixed ZnO/CuO surface of **Figure 4.3(c)**. Consequently, the smaller CuO nanoparticles tend to smooth the surface of the mixed nanostructure relative to the ZnO nano-surface. **Table 4.1** shows both surface area (μm^2) and mean roughness (R_a) of nano-surfaces. R_a gives a good general description of the height variations among the nano-surfaces. From **Table 4.1**, the ZnO nano-surface shows largest surface area. Although CuO nanoparticles are smaller than ZnO nanoparticles they exist as flake like structures with a very high surface area, reflected in the large roughness measured. Interestingly, the mixed nano-surface had both the smallest surface area and roughness. Inspection of the SEM images suggests that the CuO nanoparticles fill deep voids between ZnO nanoparticles and that the CuO nanocrystals appear to lay flat on the ZnO nanocrystal. This is probably due to the fact

that ZnO (n-type) and CuO (p-type) nanoparticles have opposite charges resulting in attraction between the two materials.

Table 4. 1 Image surface area comparisons of nano-surfaces, analysed by NanoScope Analysis software.

Different types of mixed nano-surfaces	Image surface area (μm^2) of 3 μm scan size	Mean Roughness (R_a) (nm)
1% ZnO	14.6	109
1% CuO	14.1	120
1% ZnO: 1% CuO (1:2)	10.3	65.7

A simple numerical calculation was applied to quantitatively explore the correlation between the deposited 1% ZnO suspension and the nano-surface formed. As the first approximation, the ZnO film volume is equal to $V = \frac{1}{4}\pi d^2 h$ (where d and h are shown in **Figure 4.4**). This volume is associated with the volume of drop of 200 μl 1% ZnO suspension. So the mass for each film surface made by ZnO nanoparticles was M=2 mg. The details of the ZnO nanoparticles specific surface area (SSA) is $s=4.8 - 6.8 \text{ m}^2/\text{g}$ (information provided by the manufacturer). For the AFM capture zone in scan range x^2 , **Table 4.1** shows the average of ZnO height as mean roughness, $R_a=109 \text{ nm}$. As a second approximation, the AFM detection volume was calculated by $v = x^2 \cdot R_a$. (It was assumed that the ZnO nanoparticles were distributed among the film evenly.) Using the values explained above the value of the surface area of nanoparticles, S_{AFM} , could be determined by the following equation in equation (4.1) to calculate the approximated surface area on AFM detection volume.

$$S_{AFM} = M \cdot s \cdot \frac{4x^2 R_a}{\pi d^2 h} \quad (4.1)$$

This quantitative analysis, produced values of $S_{AFM}=13.32 - 18.88 \mu\text{m}^2$. This matched the results analysed by software at $14.6 \mu\text{m}^2$, providing further evidence that the ZnO nanoparticles were evenly distributed with uniform shapes and sizes. It also demonstrates that there was little loss of nanoparticles during the fabrication of ZnO nano-surface.

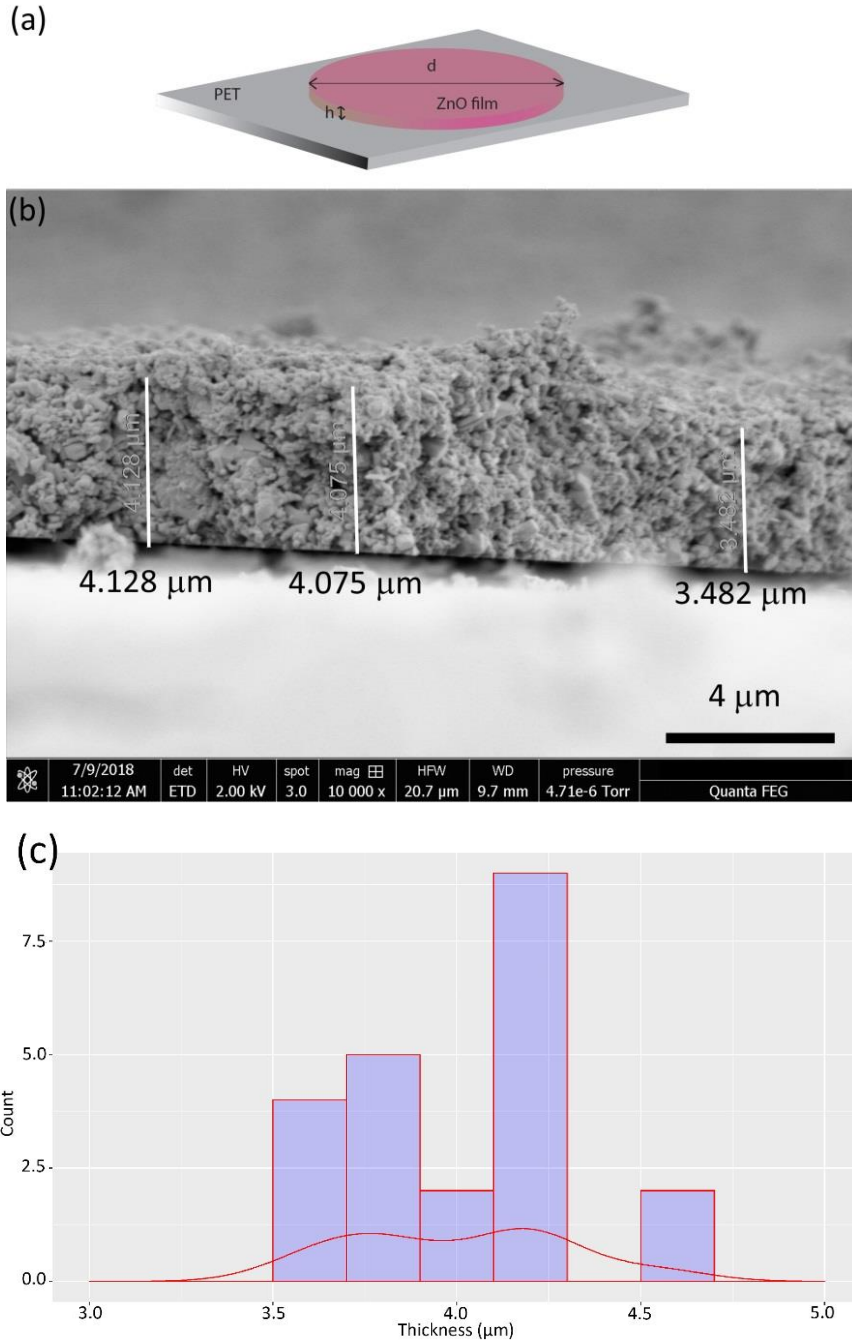


Figure 4. 4 A simple numerical calculation: (a) Schematic representation of ZnO film, where the diameter $d=1.5$ cm estimated by the formed ZnO film and (b) SEM image of cross-section of ZnO film which presented as estimated ZnO thickness (c) Histogram of Thickness of ZnO nano-surface on PET substrate using R with the average height $h=4.00$ μm , data measured using ImageJ.

4.3.2 Raman Spectroscopy Analysis of the Nano-surfaces

Figure 4.5a (green) shows bands at 90, 324, 435, 532, 582 and 1050 cm^{-1} . This strongly indicates that the ZnO nanocrystals cover the surface of the PET. 90 and 435 cm^{-1} prove the presence of the phonon modes E_2 (low) and E_2 (high) of ZnO wurtzite phase [86]. From the magnified region (**Figure 4.5b**) of ZnO/CuO composite spectra, it is shown that there are two obvious peaks at 270 - 340 cm^{-1} and 580 - 630 cm^{-1} . CuO belongs to C_{2h}^6 space group with nine one-centre optical phonon modes with symmetries, $4A_u+5B_u+A_g+2B_g$; only three A_g+2B_g modes are Raman active [150–152]. Rashad *et al.* showed three Raman peaks at 282, 330, and 616 cm^{-1} on pure CuO nanoparticles with 10 nm \pm 2 nm particle size measured in TEM images [150]. **Figure 4.5c** reveals two bands at 290 and 340 cm^{-1} which represents A_g and B_g symmetry respectively [74]. The other band is distinguished at about 590 cm^{-1} representing B_g symmetry in the Raman Spectrum [74]. Wang *et al.* found an additional two peaks on the Raman spectra of ZnO/CuO composite at 286 and 627 cm^{-1} representing crystalline CuO [148]. Batra *et al.* [86] also observed the onset of well-defined phonon peaks at 216 cm^{-1} and 625 cm^{-1} which were attributed to A_g and B_g modes according to the vibrations of oxygen atoms in the CuO matrix. Therefore, the results of Raman spectroscopy in this study prove the formation of ZnO/CuO composite nano-surface due to the coexistence of Raman modes of ZnO and CuO.

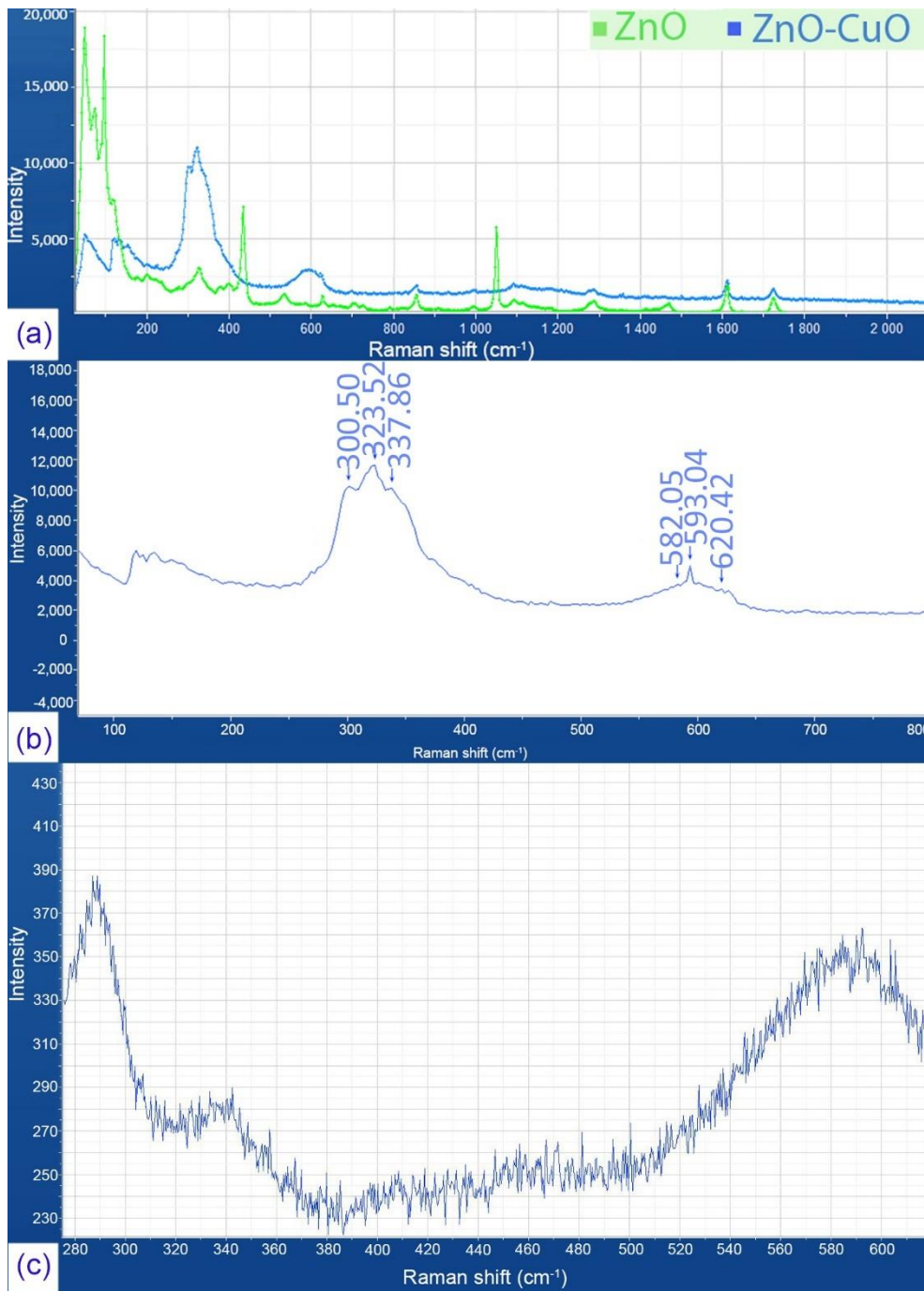


Figure 4.5 Raman spectra: (a) Raman spectra of pure ZnO (green line) and ZnO/CuO composite (blue line) nano-surfaces at room temperature. Conditions of recording the Raman Spectrum of the ZnO nano-surface: time acquisition 50s, wavelength 785 nm. Conditions of recording the Raman Spectrum of mixed ZnO/CuO nano-surface: time acquisition 300s, wavelength 785 nm; (b) The inset shows a magnified view of the 100-800 cm⁻¹ section of the Raman spectra of ZnO/CuO composite (blue line) nano-surfaces; (c) The inset shows a magnified view of the 280-620 cm⁻¹ section of the Raman spectra Raman spectra of pure CuO nano-surfaces was tested at room temperature. Conditions of recording the Raman Spectrum of the CuO nano-surface: time acquisition 150s, wavelength 785 nm.

4.3.3 Antibody Capture on ZnO/CuO Nano-surfaces

To understand the uptake of protein on the ZnO and CuO nano-surfaces and mixtures, a fixed amount of antibody, tagged with an enzyme, was added to the different nano-surfaces and detected through the generation of a coloured product by the enzyme tag. The colour generated gave a direct indication to the amount of antibody on the surfaces. The absorbance values of the coloured product are given in **Table 4.2**, the controls all had absorbance values less than 0.06, which are significant less than absorbance values obtained when antibody was present ($p=0.002$). There was no significant difference between the amount of antibody bound to ZnO or CuO, but some variability was seen with mixtures of ZnO and CuO. The results indicated that 1:1 ratio of ZnO/CuO had less antibody binding than the pure metal oxides and the 2:1 mixture demonstrated greater binding of antibody. Although absorbance values associated with the 1:2 ZnO/CuO surface was higher than both pure ZnO and CuO and higher than the 1:1 mixture, statistical significance was not obtained. Proteins have multiple positive and negative charges on the surface and immobilisation to the nanocrystal surface is largely due to electrostatic interactions. Pure ZnO and CuO interact with proteins only through negative charges or only positive charges, respectively. Whereas mixtures of ZnO and CuO will interact with proteins through both positive and negative charges on the surface immobilising greater numbers of protein molecules as seen with the 2:1 and 1:2 mixtures. The fact that the 1:1 mixture showed significantly less binding than the pure metal oxide surfaces could be a result of the ZnO and CuO cancelling out some charges thereby reducing the numbers of charges available for interacting with protein molecules. Although there were differences in the physical surface area between the pure metal oxides and the mixtures this was not reflected in the amount of protein that bound to the surfaces. This could be due to the fact that the amount of antibody-enzyme complex did not saturate all the binding sites available on the surfaces.

Table 4. 2 Absorbance values associated with anti-mouse Ig-HRP on various nano-surfaces after washing. (n=2)

ZnO/CuO Nano-Surfaces	Average Absorbance	95% Confidence Interval
CuO	0.579	0.5692 - 0.5888
1:2 ZnO/CuO	0.5955	0.42204 - 0.76896
1:1 ZnO/CuO	0.416	0.38268 - 0.44932
2:1 ZnO/CuO	0.656	0.65208 - 0.65992
ZnO	0.5545	0.51432 - 0.59468

4.3.4 Detection of CRP on Different ZnO/CuO Composite Nano-surfaces

The isoelectronic point (pI) of ZnO (9.5) and CuO (8.7-10.3) means that the nano-surfaces are positively charged at the pH of the buffer system. Anti-CRP binds strongly through electrostatic interactions to the surface.

The buffer solution containing CRP, placed on the biosensor contains salt ions and has a pH 7.40. CRP is dominated by negative charge (pI of CRP is ~5.45). At a fixed frequency of 138 Hz, the increased accumulation of negative charges of antigen binding to antibody on the nano-surfaces causes a decrease in impedance as shown in **Figure 4.6(a)**. **Figure 4.6(b)** shows that the impedance of nano-surfaces decreased when PBS buffer and 1 ng/mL CRP was incubated for 10 minutes on a 1% ZnO/CuO (1:2) nano-surface, relative to the spectra obtained from 200 ng dry anti-CRP antibody.

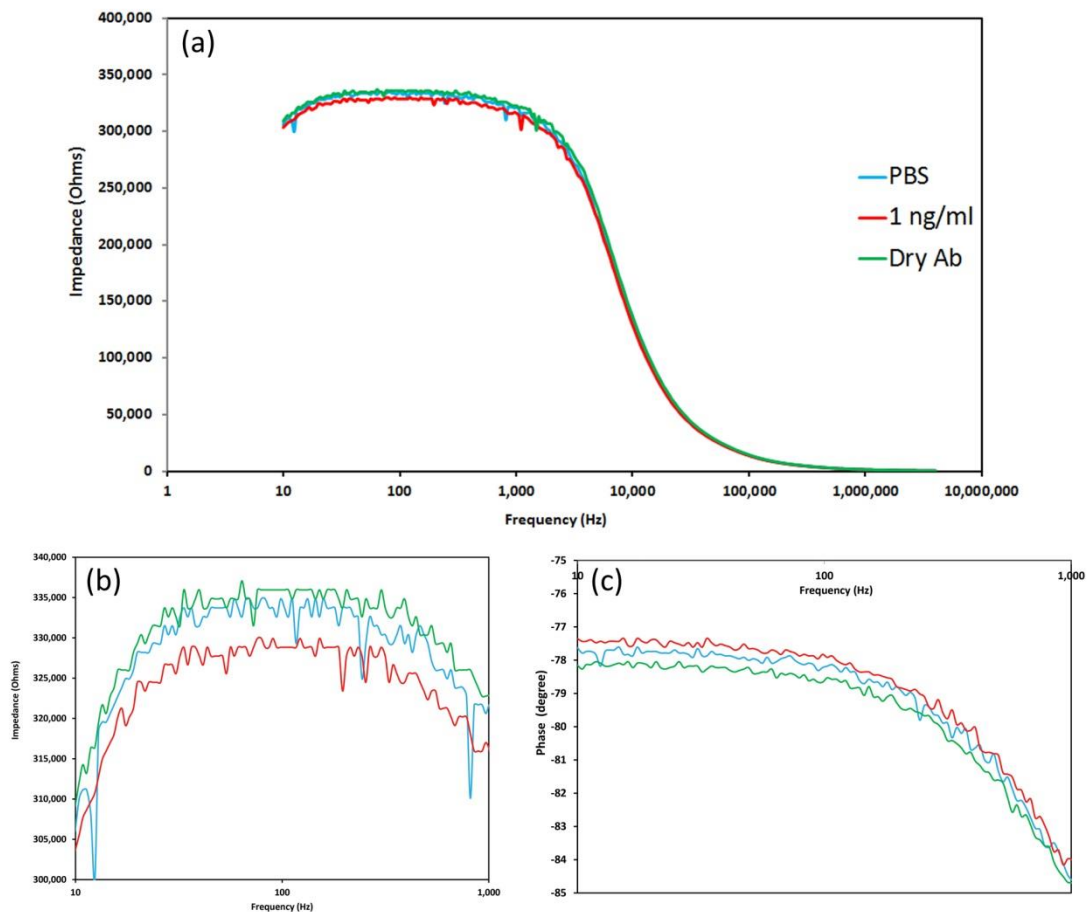


Figure 4. 6 EIS data: (a) Impedance spectroscopy of 1% ZnO/CuO (1:2) of 200 ng dry antibody, adding PBS and 1 ng/mL CRP for 10 minutes with magnified impedance - 10 to 1000 Hz (b) and phase - 10 to 1000 Hz (c).

This figure also shows the large changes in impedance are at low frequencies due to the electrical double layer as described in section 3.3.1. The phase angle value in **Figure 4.6(c)** also decreased when adding CRP (1 ng/mL) onto the surface. Consequently, when binding to antibodies on the ZnO/CuO nano-surfaces, there is an increase in the overall negative charge with increasing CRP loading and a decrease in the absolute impedance and phase value.

Figure 4.7 shows the phase change for 1, 10 and 100 ng/mL of CRP respectively, together with standard error bars. **Figure S4.6** in Appendix shows the impedance change for 1, 10 and 100 ng/mL of CRP respectively, together with standard error bars.

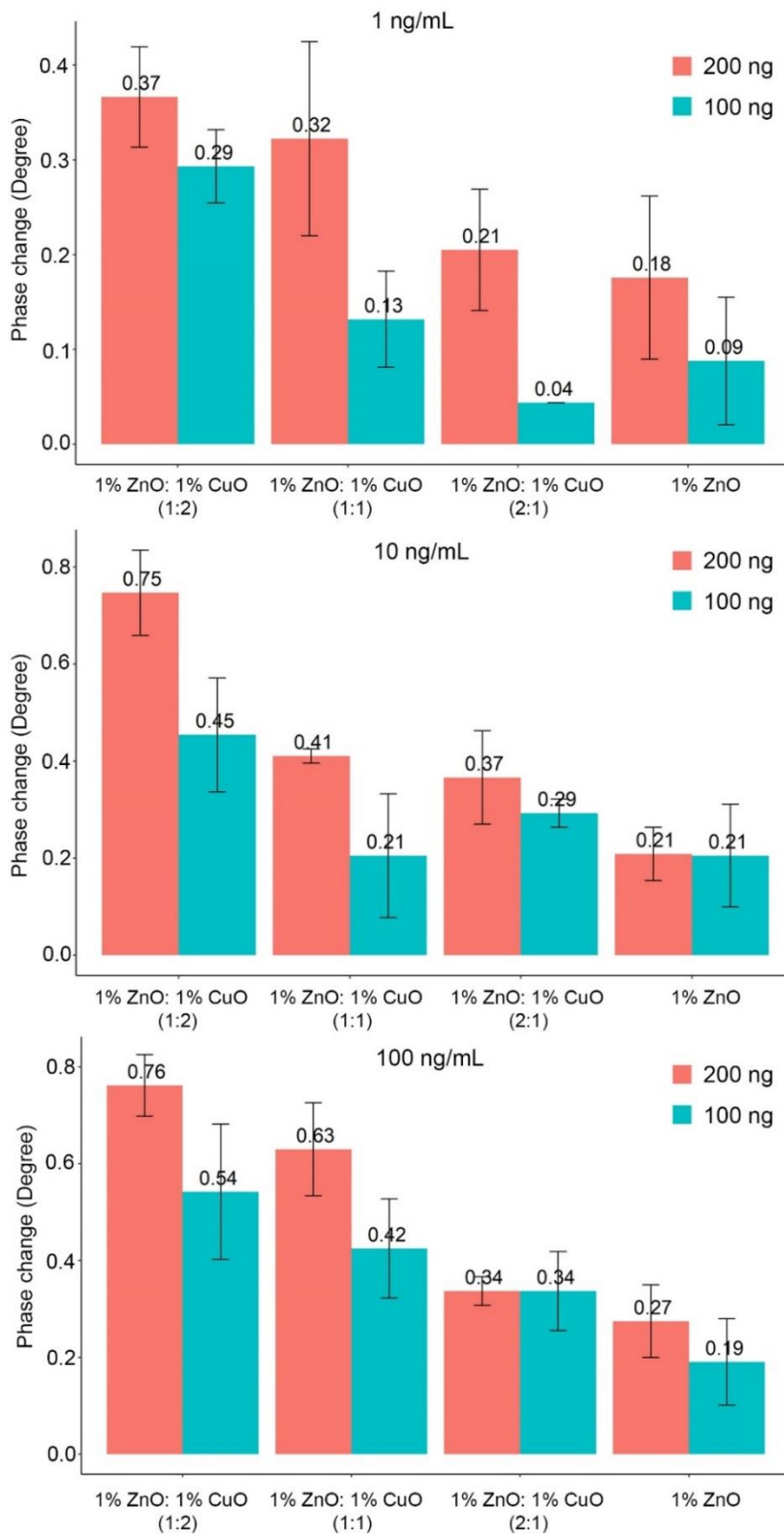


Figure 4. 7 Comparisons of anti-CRP loading (100 ng and 200 ng) on different surfaces for the detection of 1 ng/mL CRP (n=3) with standard error bars. (Exception: pure 1% ZnO nano-surfaces with 200 ng capture antibody (n=4)).

Figure 4.7 compared with **Figure S4.6** shows the better effect of adding increasing amounts of CRP to the sensor surface coated with anti-CRP with loadings of 100 ng and 200 ng, for biosensors fabricated from a pure ZnO nano-surface and from ZnO/CuO nano-surfaces with volume ratios of 1:1, 1:2 and 2:1 of ZnO:CuO. There were no results for pure CuO nano-surfaces or surface with higher ratios of CuO because the surfaces were fragile and easily broke away from the underlying substrate. **Figure S4.2** shows the break of flatter 5% CuO nano-surfaces during the process of protein immobilization, the same as 1% CuO.

From these results it can be seen that the biosensors fabricated using 200 ng antibody generated larger output signals compared with the biosensors fabricated using 100 ng antibody. This is an expected observation as there are more binding sites available for antigen capture resulting in greater protein loading on the surface and thus a greater signal generation with 200 ng of antibody.

Interestingly, **Figure 4.7** illustrates that increasing the relative amount of CuO in the nano-surface increases the signal output for all concentrations of CRP. Across all concentrations of CRP, 67% CuO (1:2 ZnO/CuO) gave the greatest change in output signal, whereas the sensors with no CuO gave the smallest responses. The effect of increasing the CuO content of the sensors was statistically significant at higher CRP concentrations for the sensors fabricated with 200 ng antibody, $p=0.055$ for 100 ng/mL CRP and $p=0.059$ for 10 ng/mL CRP. For 1 ng/mL CRP concentration for the sensors fabricated with 200 ng antibody, there was not a significant effect of the CuO content, $p=0.288$. The effect of increasing the CuO content of the sensors was not showing statistically significant at higher CRP concentrations for the sensors fabricated with 100 ng antibody, $p=0.329$ for 100 ng/mL CRP and $p=0.326$ for 10 ng/mL CRP. For 1 ng/mL CRP concentration for the sensors fabricated with 100 ng antibody, there was a significant effect of the CuO content, $p=0.032$. This is likely to be due to the small changes in signal with less background of antibody.

The explanation for the improvement in the output with increased CuO could relate to an increase in the efficiency of charge accumulation on the nano-surface as a result of CRP binding to the antibody and a decrease in the resistance to the transient currents within the ZnO-CuO composite. *Batra et al.* [86] demonstrated that ZnO-CuO composites have better conductivity than ZnO only, which is attributed to the low band gap energy of CuO (1.2 eV)

and the participation of holes within the semi-conductor structure. The higher resistance of ZnO-CuO sensor indicates the formation of a p-n junction depleting electrons from ZnO layer more effectively [75]. Wang *et al.* [148] compared ZnO-CuO composite nanotube sensor with a ZnO sensor; the response of both increased with increasing of gas concentrations. The initial resistance of ZnO-CuO composite at 300 °C showed higher resistance because of the high resistance of CuO phase in the composite [148]. They also found that the sensitivity of ZnO-CuO composite is over three times greater than ZnO with both faster response and recovery times because p-type CuO forms a heterocontact interface with the ZnO [148]. The phase change is based on the relative charge accumulation on different nano-surfaces. Greater levels of CuO will increase the resistance and the sensitivity to charge accumulation. In all cases but one, increasing the concentration of CRP added to the biosensors resulted in an increase in output signal, the maximum output occurring for 1:2 ZnO/CuO at 100 ng/mL CRP with an antibody loading of 200 ng.

4.3.5 Calibration Curve Comparisons of Different Nano-surfaces with Capture Antibody

Figure 4.8 shows a comparison of the sensor response using biosensors fabricated with 1:2 ZnO/CuO and biosensors fabricated with no CuO, each coated with 200 ng anti-CRP. (The 1:2 ratio was selected as this offered the maximum impedance output value for each CRP concentration in **Figure 4.7**.) **Figure 4.8** shows 4-parameter linear-log logistic curves, with the error bars. It shows that the biosensor fabricated using ZnO/CuO showed a three-fold increase in signal at the higher concentrations of CRP compared with the pure ZnO nano-surface. Although the ZnO only biosensor gave an increasing signal with increasing CRP concentration this was not significant.

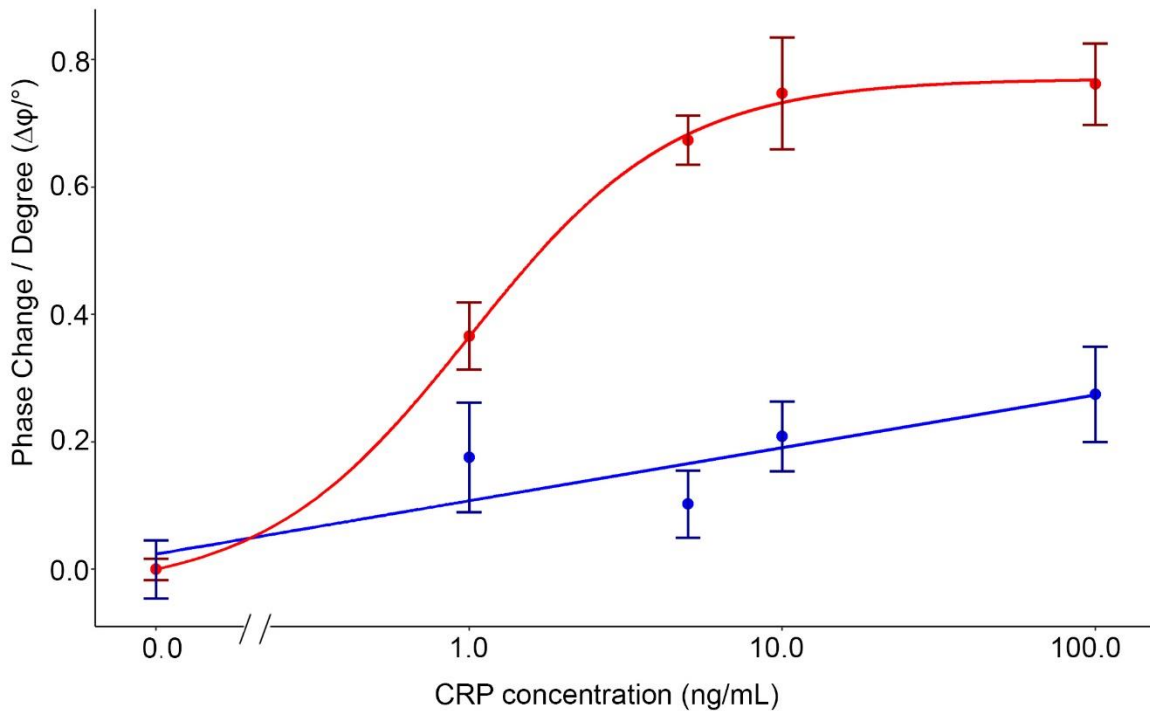


Figure 4. 8 Phase change response versus antigen (CRP) concentration for sonicated ZnO/CuO of 1:2 (n=3) (red) and pure ZnO nano-surfaces (n=4) (blue) with 200 ng capture antibody measured at the frequency of 138 Hz, – standard error bars are shown.

The 4-parameter logistic curve of sonicated ZnO/CuO of 1:2 nano-surfaces shows that above 10 ng/mL CRP the biosensor becomes saturated with no significant difference seen in the signal generated for 10 and 100 ng/mL CRP. In addition, there was a significant difference between the control and 1 ng/mL ($p < 0.05$). The limit of detection (LOD) for 1% ZnO nano-surfaces with 200 ng anti-CRP was 3.3 ng/mL, while for 1% ZnO/CuO (1:2) nano-surfaces with 200 ng anti-CRP it was 0.4 ng/mL. It shows high sensitivity response on phase change of 1% ZnO/CuO (1:2) nano-surfaces with 200 ng anti-CRP. The %CV was used to compare the groups of phase change of 1% ZnO nano-surfaces and 1% ZnO/CuO (1:2) nano-surfaces with 200 ng anti-CRP. 1% ZnO/CuO (1:2) nano-surfaces shows the average of %CV on each concentration of CRP with 10.1% compared with 1% ZnO nano-surfaces with 37.1%. It shows the coefficient of variation of phase responses on 1% ZnO/CuO (1:2) nano-surfaces are just on biological variation.

The results above demonstrated that the ZnO/CuO nano-surfaces are more sensitive with higher concentrations of CuO. It is known that mixtures of ZnO and CuO have higher resistivity compare to ZnO due to the formation of P-N junctions where the CuO and ZnO crystals are adjacent. Referring to Chapter 2 section 2.3.2, the equivalent circuit of a non-faradaic impedance network shows a resistor-capacitor circuit. At mid frequencies, such as those used in this study, a resistance increase will result in higher impedance output. This may result in an increase of the sensitivity with the addition of CuO nanoparticles.

The limit of detection for nano-crystalline based biosensing nano-surfaces was compared with other ZnO biosensors for the detection of CRP described in the literature. Wang *et al.* [153] described a ZnO biosensor for CRP, which had a detection limit of 100 ng/mL, using a quartz crystal microbalance and Ibupoto *et al.* [51] described the use of ZnO nanorods to measure CRP using a potentiometric technique which was able to detect 10 ng/mL CRP. Finally, Borse and Srivastava described a lateral flow technology using quantum dots as the detection technology which gave a detection limit of 300 ng/mL for CRP [154]. The results presented in this chapter demonstrate the nano-surfaces with ZnO and with CuO all show the ability for the sensitive detection of CRP.

4.4 Summary

ZnO/CuO composite nano-surfaces were fabricated using a colloidal dispersion technique, incorporating sonication. SEM images and AFM 3D surfaces indicated that the nano-surfaces were modified when increasing amounts of CuO were added to form ZnO/CuO nano-surfaces. The results illustrated that the smaller CuO nanoparticle flakes filled the large voids in the ZnO surface and also align themselves flat against the ZnO surface area due to electrostatic attraction, thereby reducing the overall surface area.

Although there was not a significance difference in the antibody loading on the 1:2 ZnO/CuO compared with the ZnO only nano-surface, there was a significantly higher signal produced from the biosensor fabricated with 1:2 ZnO/CuO compared with the biosensor fabricated with ZnO only. Compared with ZnO nano-surfaces, ZnO/CuO nano-surfaces are more sensitive with higher resistance which results the increase of output signal. This suggests that the electrical interaction between ZnO and CuO nano-structures plays an important part in the generation of the enhanced signal.

Using an antibody loading of 200 ng and the 1:2 ZnO/CuO nano-surface, 1 ng/mL CRP was easily detected in 10 minutes, with the potential that sub-ng/mL concentrations could be detected with a calculated limit of detection of 0.4 ng/mL, which could potentially be lower following further optimisation of the biosensor. In addition to enhanced sensitivity, the biosensor is easily fabricated and provides a rapid result, making it well suited to the development of point-of-care devices for the healthcare sector.

The next chapter will describe the transformation of the ZnO/CuO composite nano-surface to a ZnO/CuO composite 3D membrane, in order to benefit from the advantages of lateral flow assay. This will make the biosensor even more suitable for point-of-care diagnosis. In this work, impedance phase change will again be measured using the non-faradaic impedance spectroscopy in which ZnO nano-membrane and 1:2 ZnO/CuO nano-membrane will be compared.

Chapter 5

Nanoparticle-Based 3D Membrane for Impedimetric Biosensor Applications

In the third experimental chapter nanoparticle-based membranes, prepared with sonication and without sonication, and their application to biosensing technology are presented. In order to compare the sensitivity of nano-membranes, CRP was used as the model target, allowing differences in the performance of the nanocrystal structures in the 3D matrix to be analysed. To demonstrate the capacitive change due to combination of mixture of antibody and antigen, nano-membranes with and without antibody capture are compared using impedance spectroscopy. A discussion of the benefits of sonication is presented by comparing limits of detection. The work presented in this chapter is aimed at single-use biosensing applications.

The work presented in this chapter has been mostly published in Cao *et al.* [155]. I contributed to the research design and carried out all the experimentation including nano-membranes preparation and fabrication, surface characterisation, immunology assay and impedance test. I also processed the experimental data, discussed the results, and wrote the initial draft of the manuscript.

5.1 Introduction

In this chapter the fabrication and evaluation of nano-ZnO and nano-ZnO/CuO nitrocellulose membrane biosensors, formed using a colloidal sonication technique is presented. The biosensors are label-free and non-faradaic, i.e. there is no charge transfer between the biomolecule complex and the sensor electrodes. The membranes were analysed using scanning electron microscopy (SEM) and energy-dispersive spectroscopy (EDS) analysis and performance of the biosensors was characterised by the measurement of CRP using impedance spectroscopy. For non-faradaic impedimetric biosensors, at the liquid-semiconductor interfaces, the electrical double layer forms a large interfacial capacitance with high density of charge accumulation [18]. This capacitance changes actively with the concentration of biomolecular binding [18] and in this work, excellent limits of detection for the biosensor are demonstrated.

Three-dimensional membranes are widely used in biosensing. Recently their utilisation alongside ZnO nanoparticles has been reported. For example, Al-Hinai *et al.* grew ZnO nanorods on the top surface of a poly(ether sulfone) membrane on a flat glass plate to form a biosensor [156]. Selvam *et al.* utilized gold and ZnO electrodes integrated on flexible polyimide compared with glass as electrochemical sensors to perform detection and continuous monitoring of EtG from human sweat in a wearable configuration using chemiresistive mechanism of detection via impedance change on the sensor surface with assay immobilization steps. [42]. In the case of ZnO electrodes on the glass and flexible substrates, Selvam *et al.* observed a high levels of sensitivity with detection limits of 0.0001 µg/L and 0.001 µg/L respectively [42].

Munje *et al.* developed a flexible biosensor, including a ZnO thin film active region by deposition of nanoparticles on to a nanoporous polyamide membrane [50]. This was compared with planar glass substrates associated with glucose and cortisol detection in synthetic sweat [50]. The research team found ~3.5 fold increase in capacitance for ZnO thin film on nanoporous substrate is compared to the ZnO thin film on planar glass substrate for baseline to 100 mg/dL concentration at 100 Hz frequency [50]. For cortisol immunoassay, they observed ~15 times increase in capacitance for ZnO thin film on nanoporous substrate compared to the ZnO thin film on planar glass substrate for baseline to 100 ng/mL

concentration at 1 Hz frequency [50]. This indicates that an increased capacitance is observed for nanoporous substrates over planar glass substrates, with the electrical double layer formed at the liquid-semiconductor interface being amplified in the presence of the nanoporous substrate with an associated enhancement in charge storage [18].

There have been no previous reports of impregnating a porous membrane with ZnO (or CuO) to form the active layer of a biosensor, as described in this paper. Nitrocellulose membrane also helps to build a systematic biosensor by flow-based technology which will be mentioned in the next experimental chapter.

5.2 Materials and Methods

5.2.1 Membrane Preparation

Fabrication process for the 1% nano-ZnO nitrocellulose membranes: 0.6 g ZnO nanoparticles (ZnO, 99.9+%, 80 - 200 nm from US Research Nanomaterials Inc.) were added to 60 mL double-distilled water. A 1% (w/v) ZnO suspension was stirred for 1 h at room temperature. Nitrocellulose blotting membranes (Sartorius) with 0.45 μm pore size were cut using a Biodot guillotine to form a 15 mm \times 15 mm square. The 40 samples of nano-membranes were immersed in the ZnO colloidal suspension and sonicated for 15 minutes in a sonication bath (Langford Ultrasonics) with a power of 300 W at 40 Hz. Another 40 samples of nano-membranes were immersed for 15 minutes without sonication for comparison. Finally, all the membranes were rinsed in deionised water 3 times and dried in sealed box with silica gel before being used for the immobilisation of antibody.

Fabrication process for the 1% nano-ZnO/CuO nitrocellulose membranes: In the process 0.2 g ZnO nanoparticles and 0.4 g CuO nanoparticles (CuO, 99.5+%, width 10 - 30 nm, Length: 200 - 800 nm from US Research Nanomaterials Inc.) were added to 60 mL double deionized water. 1% ZnO (w/v) was mixed with 1% CuO (w/v) nanopowders in water for 1 h to give 1:2 (v/v)/(wt%:wt%) ZnO/CuO colloidal suspension. The 40 samples of nano-membranes were then soaked in the ZnO/CuO suspension and subjected to sonication for 15 minutes as described above; another 40 samples of nano-membranes immersed for 15 minutes were without sonication for comparison. Finally, all the membranes were rinsed using deionised water 3 times and dried in atmosphere with silica gel before being coated with antibody.

5.2.2 Characterisation of Membranes

The cross-section of a nanoparticle nitrocellulose membrane was prepared using a double edge razor blade and examined using a FEI Quanta 650 field emission scanning electron microscope (ESEM) with Everhart-Thornley Detector (ETD). The morphology of cross-sections of untreated nitrocellulose membranes, a nano-ZnO nitrocellulose membrane and a nano-ZnO/CuO nitrocellulose membrane, were analysed. To perform the SEM analysis, samples were mounted on an aluminium stub and coated with a thin layer of Au using an Emscope

SC500 Gold sputter coating unit prior to analysis. For the ZnO/CuO nitrocellulose membrane, a Gaseous Secondary Electron Detector (GSED), with a high pressure at 3 Torr, was also used in the SEM.

EDS (Oxford Instruments AZtec EDS) was used to analyse the chemical compositions of the sonicated nano-ZnO and nano-ZnO/CuO nitrocellulose membranes.

5.2.3 CRP Sensor Fabrication and CRP Assay

To prepare the membranes for the assays, 40 μL (200 ng) of monoclonal mouse anti-human C-reactive protein (4C28, from HyTest Ltd, Turku, Finland) was diluted in 5 mM phosphate buffered saline (PBS) at pH 7.4 (OXOID Microbiology products). The capture antibody was immobilised on to the nitrocellulose membranes (from the upper side to lower side) until it was fully wet. For IgG, the approximate loading capacity is 1 $\mu\text{g}/\text{cm}^2$, and the binding capacity is 11.250 - 4.5 μg (Nitrocellulose blotting membranes with 15 mm \times 15 mm) [65]. Therefore, for 3D membrane, the protein binding capacity is not an issue. The anti-CRP antibody was readily immobilised in the membrane through electrostatic interaction as the ZnO nanostructures distributed within the nitrocellulose membrane were positively charged (as the pH of the buffer was 7.4 and the isoelectric point of ZnO and CuO is around 9.5 [157,158]), whereas the anti-CRP antibody used in this study is predominantly negatively charged. The membranes were then dried in a desiccator with silica gel at 4 $^{\circ}\text{C}$ overnight for 18 h. Anti-CRP antibody is immobilised on membrane not only through electrostatic interaction [159], but also other physical absorption processes, such as hydrophobic interactions and van der Waal's forces, forming non-covalent interactions. Wang *et al.* schematically presented the capacity of antibody immobilization on 3D matrix compared with a conventional 2D surface, to illustrate that it is much higher, shown in section 1.4.2 **Figure 1.3** [35]. This work confirmed that the quantity of effective antibodies sharply increases from 2D to 3D immobilisation [35].

After the overnight incubation, the nano-particle nitrocellulose membranes were repeatedly (4 times) immersed in 5 mM PBS and then blocked with 1% (w/v) skimmed milk for 30 s.

Human C-reactive protein (CRP) (8C72, from HyTest Ltd, Turku, Finland) was diluted in 5 mM PBS. The PBS buffer molar concentration is decreased compared with previous two experimental chapters because ions in solution can interfere with electrostatic interactions between the membrane and the capture reagents. The Debye length is increased with reduced lower concentration of PBS buffer as well. Then, 40 μ l of CRP at different concentrations were placed on the membranes to facilitate a slow liquid absorption in to the membrane until it was fully wet. The specific concentrations of CRP were as follows: 0 (PBS only), 0.1, 0.5, 1, 5, 10, 15 ng/mL.

During the impedance testing, the membranes were laid on a glass coverslip (from Deltalab, 22 mm \times 22 mm and 0.13 - 0.16 mm thick), and positioned on a 23 mm diameter D-shape electrode pair with 1 mm gap, with the lower layer and hence the highest density of nanoparticles closest to the electrode. (The gradated porosity and associated variation in nanoparticle density are described in section 5.3.1). A second coverslip was placed on top of the membrane to prevent evaporation during the measurement. The schematic diagram of the arrangement is shown in **Figure 5.1**. The impedance amplitude and phase angle were measured and analysed after 10 minutes incubation time with the added CRP. The impedance values were recorded at each concentration of antigen, with 3 replicates of the nanoparticles/nitrocellulose membranes, measured from 10 Hz to 4 MHz.

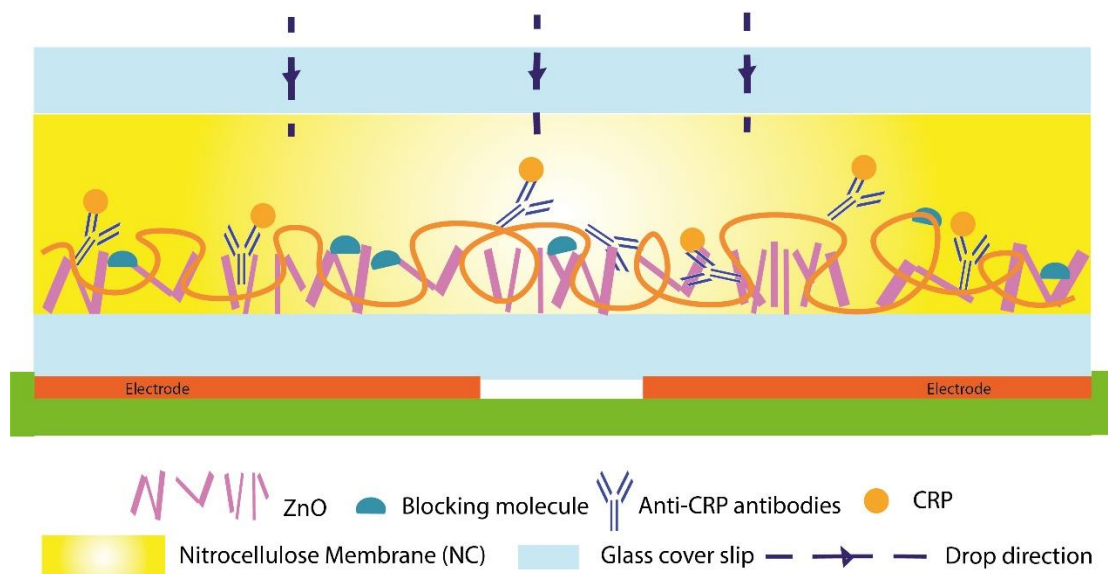


Figure 5. 1 Illustration of the ZnO nanoparticle nitrocellulose membrane sandwiched between two coverslips positioned above the electrodes.

A Cypher Instruments C60 Impedance-Amplitude-Phase Analyser was used to measure the impedance change of the nano-particles nitrocellulose membranes associated with antibody/antigen interactions. The frequency was scanned from 10 Hz to 4 MHz, with 300 test points, at an AC peak-to-peak voltage of 2 V with a DC offset of 0.9 mV. The impedance plots were analysed by Cypher Graph V1.21.0, Impedance Amplitude and Phase Analyser graphing application software. The change of impedance amplitude and phase angle was evaluated as function of antigen (CRP) concentration in the buffer. Rather than correlate the overall impedance to different concentrations of CRP, a single frequency is determined to give the maximum relative changes and a stable reading [20]. As mentioned in previous chapters, 138 Hz was chosen for nano-surfaces for plotting calibration curves. For nitrocellulose membranes, the sensor responses were taken at a frequency of 100 Hz, which results in better behaviour and fit to the calibration curves. The slight shift of frequency chosen is due to varieties of substrates. Phase changes with ZnO and ZnO/CuO (1:2) nanoparticle nitrocellulose membrane were compared with or without sonication. The phase change was defined as the difference of the impedance phase value of the biosensor after 10 minute incubation with CRP and the phase angle of the control. Results were plotted using a logarithmic scale on the x-axis.

5.2.4 Statistical Analysis

The ZnO and ZnO/CuO nanoparticles as well as membrane voids' sizes are measured by ImageJ software. Numbers of n=10 for voids and n=20 for nanoparticles were selected to measure the average size.

A 4-parameter linear-log logistic curve, with the error bars, was created using R. The estimated limit of detection (LoD) was defined as the mean of the intercept on the y axis of the calibration curve, plus 3 times the standard deviation of the intercept and calculated using R. The mean value and standard deviation of the "intercept" at the working zero found using the 4-parameter logistic curve.

The coefficient of variation %CV = (Standard Deviation/Mean*100) was used to demonstrate reproducibility for each membrane type.

A Wilcoxon rank sum test was used to analyse the differences in phase changes between ZnO and ZnO/CuO (1:2) nano-membranes with and without sonication at each concentration, the level of significance was defined as $p \leq 0.05$. Analysis was performed using R.

5.3 Results and Discussion

5.3.1 Characterisation of Membrane

The nitrocellulose membranes used in this study showed gradated porosity (**Figure 5.2**) and, as seen in the scanning electron micrograph of **Figure 5.2(a)**, can be divided into three layers. The upper layer has the smallest pore sizes and structures shown in **Figure 5.2(b)**, whereas the lower layer has a loose pore structure between the white support matrix as shown in **Figure 5.2(d)**. The horizontal lines visible in the white fillers indicate the cutting direction of the nitrocellulose membrane. The nitrocellulose membrane is manufactured by casting the nitrocellulose in solvents, which causes the significant asymmetry in the porous structures due to the evaporation of solvent [160].

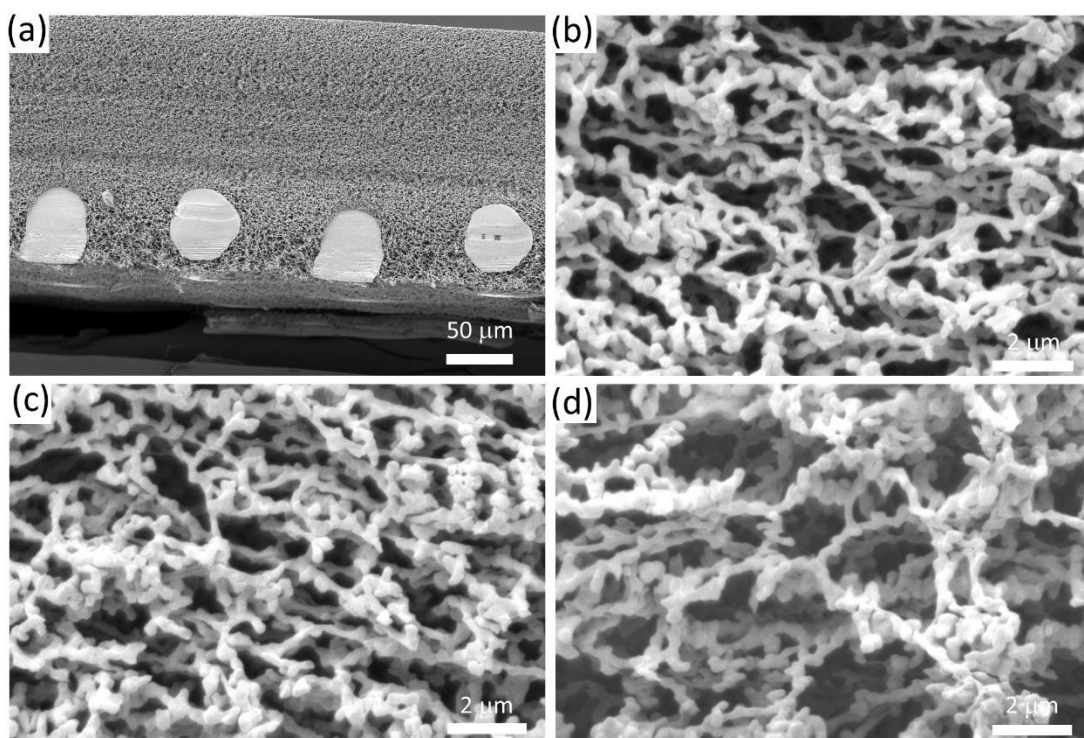


Figure 5. 2 Scanning electron micrographs of the nitrocellulose membrane cross-section: (a) whole cross-section at 1,000× magnification; (b) upper layer of nano-ZnO/nitrocellulose membrane (with small pore structures) at 30,000× magnification; (c) middle layer of nano-ZnO/nitrocellulose membrane (with bigger and loose pore structures) at 30,000× magnification; (d) lower layer of nano-ZnO/nitrocellulose membrane (with biggest pore structures) at 30,000× magnification.

During the fabrication of the nano-particle nitrocellulose membranes, the membranes were incubated in nano-particle colloidal suspensions. **Figures 5.3(a) to 5.3(c)** show scanning electron micrographs of the three layers of the nitrocellulose membrane. A smaller number of nanoparticles entered the upper structure due to the lower porosity, as seen in **Figure 5.2(a)**. The nanoparticles easily entered the lower layer of the membrane as seen in **Figure 5.2(c)** by the force of sonication and then diffused into the middle layer, as shown in **Figure 5.2(b)**. **Figure 5.3(c)** clearly shows a high number of the columnar wurtzite structures of the ZnO nanoparticles at average diameter of 142 nm ($n=20$) (measured from **Figure S5.1** in the lower layer of the nitrocellulose membrane).

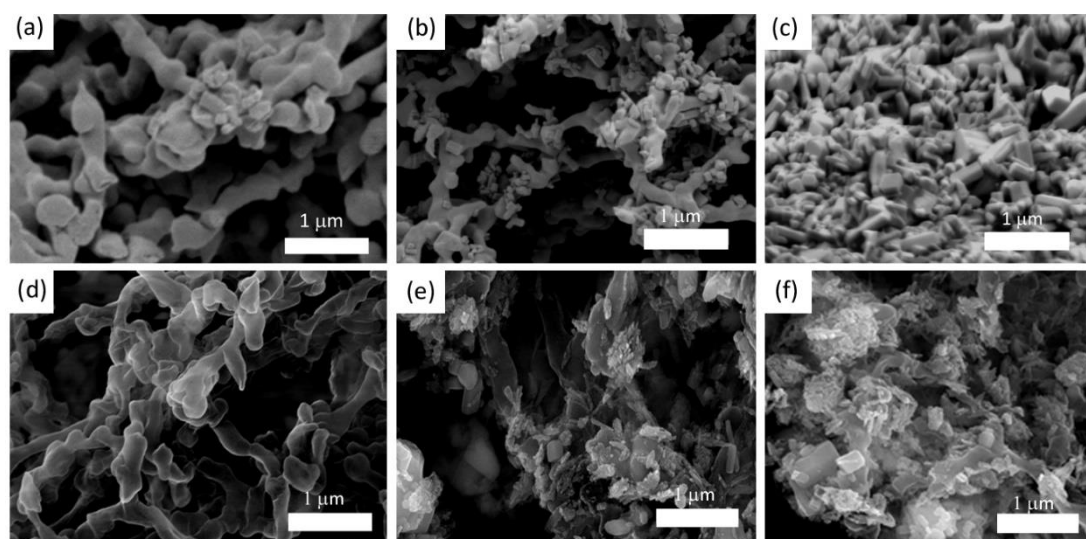


Figure 5. 3 Scanning electron micrographs of nano-ZnO nitrocellulose membrane cross-section at 80,000× magnification: (a) upper layer; (b) middle layer; (c) lower layer. Scanning electron micrographs of nano-ZnO/CuO nitrocellulose membrane cross-section at 80,000× magnification: (d) upper layer; (e) middle layer; (f) lower layer.

Imaging of the conductive nano-ZnO/CuO nitrocellulose membrane was performed using a Gaseous Secondary Electron Detector, as the CuO particles became charged under normal SEM conditions (seen as lighter areas at nano-crystal margins), and are shown in **Figures 5.3(d) to 5.3(f)**. As with the ZnO membranes, **Figures 5.3(d) to 5.3(f)** show an increasing number of ZnO and CuO nanoparticles distributed within the membrane, with the highest density of the

CuO nanoparticle (at average of diameter of 30 nm (n=20) and length of 260 nm (n=20), as shown in **Figures** S5.2 and S5.3) flakes and columnar wurtzite structure of ZnO in the lower layer of the nano-ZnO/CuO membrane. **Figure** 5.3 also reveals that the ZnO/CuO nanostructures formed a larger size of voids compared with ZnO, which is beneficial for the antibody capture. The voids in the ZnO/CuO nanostructures in nitrocellulose membrane had an average size of 536 nm (n=10) (measured from micrograms shown in **Figure** S5.4) compared with average 188 nm (n=10) for the ZnO nanostructures (measured from **Figure** S5.5.) It can be seen that the mixture composite ZnO/CuO nanoparticles has larger average particle diameter than pure ZnO nanoparticles. This observation concurs with results provided by Chatkaewsueb *et al* [161].

The Appendix shows how representative images were chosen from SEM work to include in the main part of the thesis (**Figures** S5.6 to S5.9).

5.3.2 EDS Results

From the scanning electron micrographs, both ZnO and CuO nanoparticles were observed to be densest in the lower layer of the membrane, so the EDS analysis was performed on the lower layer. The result of atomic composition analysis by EDS on the cross-section of the nano-ZnO and nano-ZnO/CuO nitrocellulose membrane is shown in **Figure** 5.4 and **Figure** 5.5. The following elements were detected: C, (Cu,) O, Zn and Au. **Figure** 5.4 shows the results for zinc; 5(a) is the SEM image, 5(b) is the EDS spectrum and in **Figure** 5.4(c) the yellow areas show the regions where the Zinc is concentrated. **Figure** 5.5 shows the results of the EDS analysis on the ZnO/CuO membrane. The distribution of the 6 elements within the lower layer of the nitrocellulose membrane is shown in **Figure** 5.5(b). The intensity of the coloured areas highlights the element location and loading within the matrix. The nanoparticle density was greatest between the fibres of the support matrix of the membrane, which also had the largest pore size within the layer. A small amount of Al was detected at the edge of the membrane, from the SEM stub. Referring to **Figure** 5.5(a), the carbon originates from the nitrocellulose and Au from the sputtered layer used in the sample preparation. The grayscale intensity of the zinc and copper in **Figure** 5.5(a), had a ratio of Zn to Cu 1:2.08, corresponding

to 1:2 ratio of ZnO/CuO in the original nanoparticle colloid suspension. This confirmed that the fabrication methodology resulted in proportional absorption in to the membrane of the ZnO and CuO nanoparticles.

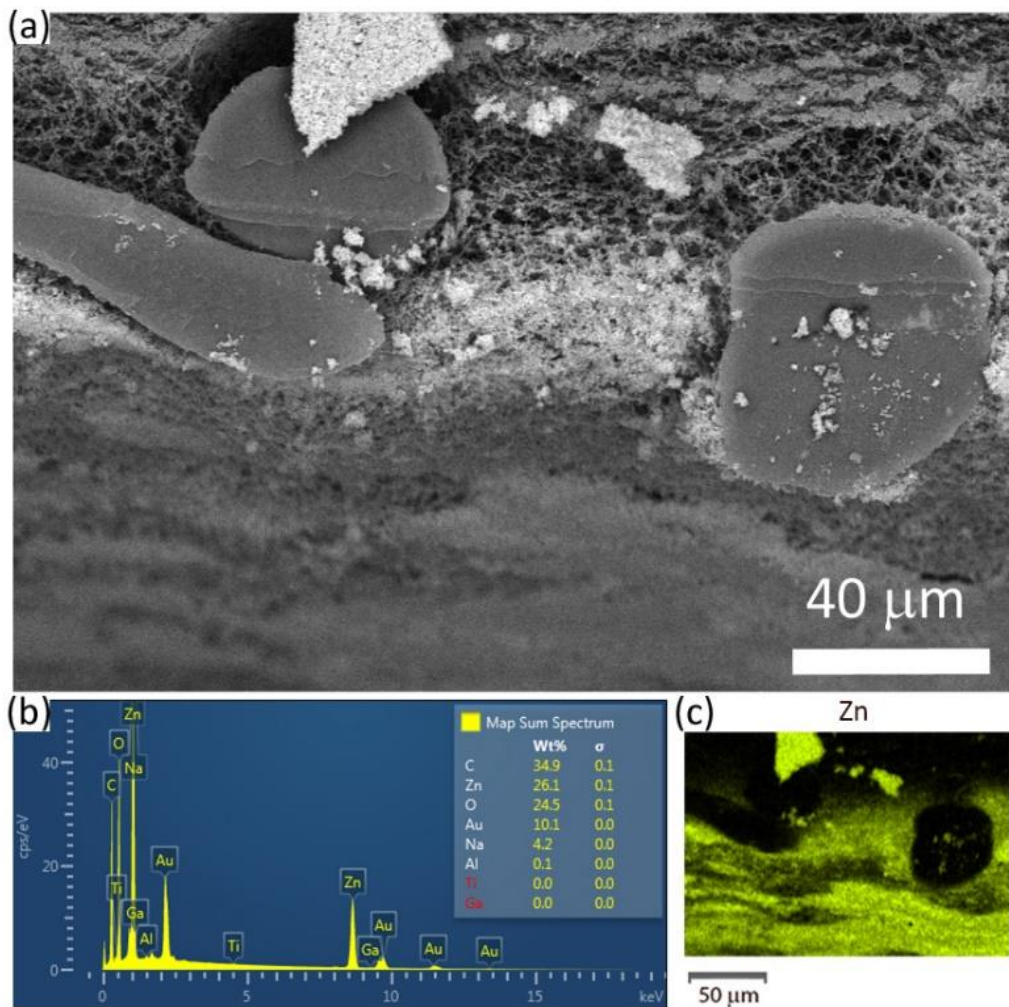


Figure 5. 4 SEM/EDS spectrum/mapping showing the distribution of Zn on the lower layer cross-section of the nano-ZnO membrane: (a) SEM image; (b) EDS spectrum and (c) EDS mapping of the elements of Zn.

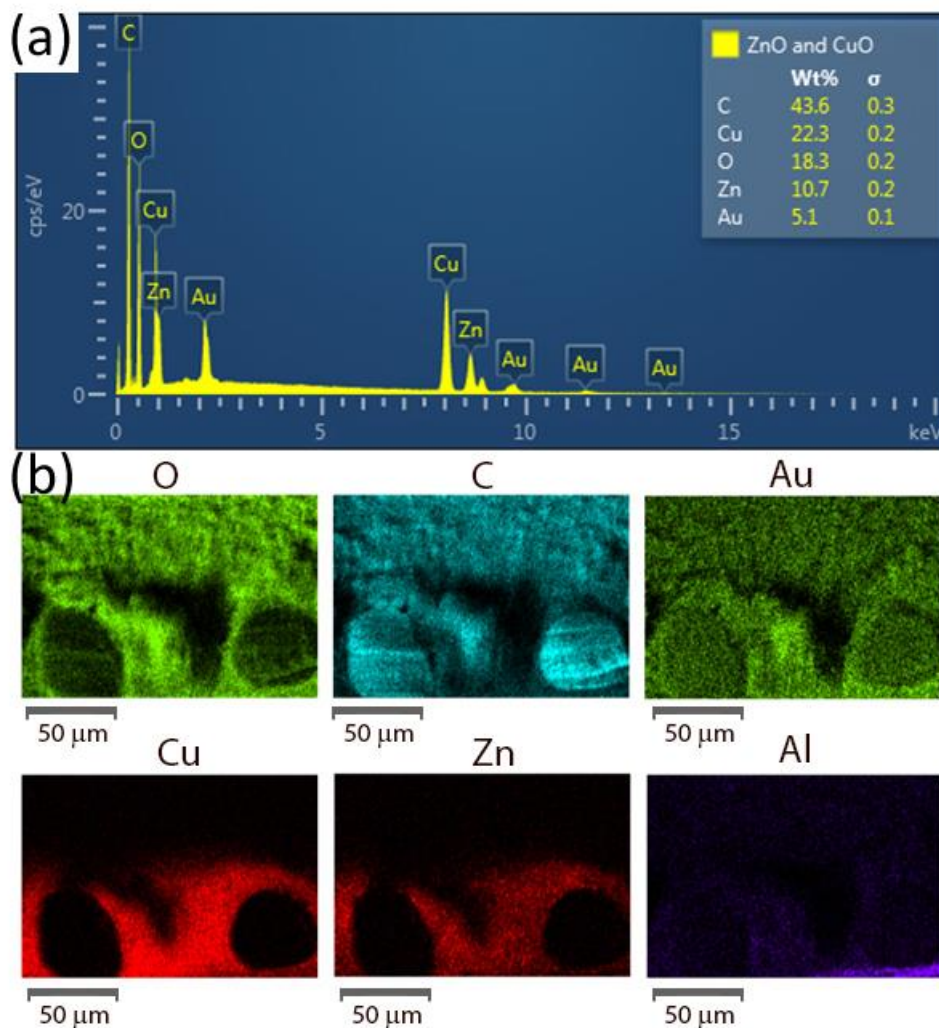


Figure 5.5 EDS spectrum/mapping on the lower layer cross-section of the nano-ZnO/CuO membrane: (a) EDS spectrum and (b) EDS mapping of the elements: O, C, Au, Cu, Zn and Al.

5.3.3 Calibration Curves Using Different Nano-membranes with Capture Antibody

Figures 5.3(d) to 5.3(f) and Figure 5.5(b) evidence that the ZnO/CuO nanoparticles are distributed within the porous membrane following sonication. The cross-section of the biosensor developed in this study is schematically depicted in **Figure 5.1**. This shows the sensing nanoparticle nitrocellulose membrane with antibody coating, which is sandwiched between two glass cover slips and positioned above two electrodes. The electrodes face the lower layer of the membrane, which was loaded with nanoparticles for capturing biological molecules. Impedance spectroscopy was used to quantify binding of CRP to the antibody on

the nano-ZnO/CuO membranes, with and without sonication, and the nano-ZnO membranes, with and without sonication, for these non-faradaic biosensors.

The impedance was recorded for CRP concentrations between 0 and 15 ng/mL, with 3 replicate nano-ZnO and ZnO/CuO membranes with or without sonication and with or without antibody immobilised, over the frequency range 10 Hz to 4 MHz (bode plots are shown in the Appendix **Figure S5.10-5.11**). In this study the most significant changes were observed below 1 kHz, around 100 Hz. This observation concurred with other published work. Selvam *et al.* measured the impedance of their non-faradaic biosensor over the frequency range 100 Hz to 1 MHz and found the changes to the double layer capacitance were most significant at frequencies less than 1 kHz [20]. Kinnamon *et al.* selected 100 Hz for their calibration dose response, as this maximised the percentage change in impedance relative to the baseline measurement, performed post-antibody functionalization [49].

Figure 5.6 shows the impedance amplitude and phase values measured on both the nano-ZnO membranes and the nano-ZnO/CuO membranes with different concentrations of CRP after a 10 minute incubation at 100 Hz, the mean of 3 replicates. For both the nano-ZnO membranes and the nano-ZnO/CuO membranes, the impedance decreases with CRP concentration. As both ZnO and CuO are semiconducting materials, an electrical double layer is formed when they interact with the liquid electrolytes, resulting in charge accumulation at the interface region. When binding of the CRP molecules (~116 kDa) to the antibodies occurs adjacent to this interface, the double layer capacitance is enhanced, resulting in the observed change in the impedance. Note that in **Figure 5.6C**, the error bars of impedance response on nano-ZnO/CuO membranes look large compared with the other plots. This is due to the fact that the range of the impedance change is small, thus the scale is magnifying the error bars. From **Figure 5.6**, the lines of best fit have lower residuals for the phase angle compared with the amplitude of the impedance. Consequently, subsequent calibration curves were plotted using the change in the absolute phase relative to the PBS control using a logarithmic scale on the x-axis.

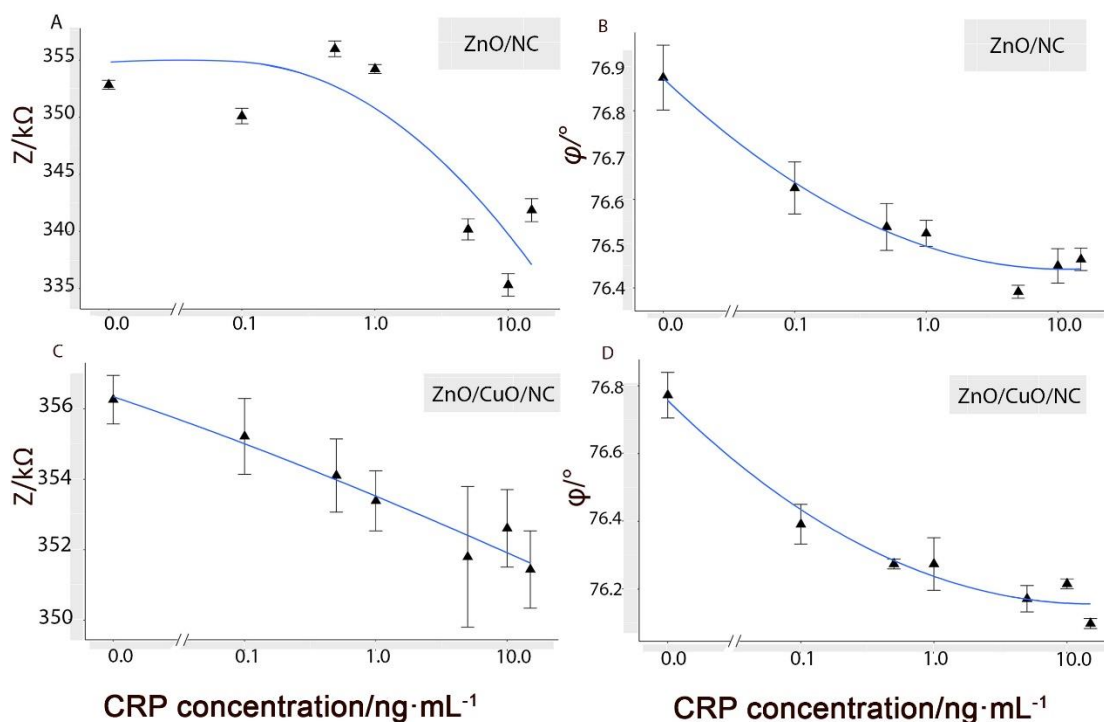


Figure 5.6 Impedance amplitude/kOhms ($Z/k\Omega$) and phase change/degree ($\phi/^\circ$) on nano-ZnO nitrocellulose membranes ($n=3$) and nano-ZnO/CuO nitrocellulose membranes ($n=3$) after a 10 minute incubation time with increasing concentrations of CRP, measured at a frequency of 100 Hz.

Figure 5.7 shows the phase change for six different nano-particle/nitrocellulose membranes at a frequency of 100 Hz. In **Figure 5.7**, the average phase change of samples fabricated without the sonication stage (the red bar represents nano-ZnO membrane and the light blue bar represents nano-ZnO/CuO membrane) is lower compared with the phase change for samples prepared with sonication (the green bar represents nano-ZnO membrane and the pink purple bar represents nano-ZnO/CuO membrane). The phase change for nano-ZnO/CuO membrane after sonication approximately doubles compared with no sonication, whereas for the nano-ZnO membrane there is an approximate 3-fold increase. This indicates that the sonication has a greater effect on ZnO nano-particles than on the ZnO/CuO mixture in terms of signal enhancement. These results demonstrate the importance of the sonication process in the fabrication of the biosensor. However, despite this, the ZnO/CuO membranes remain superior in terms of the amplitude of the signals relative to the control. The sonication had a

highly significant effect on the signal generated from the membranes ($p < 0.0005$ by Kruskal-Wallis chi-squared test).

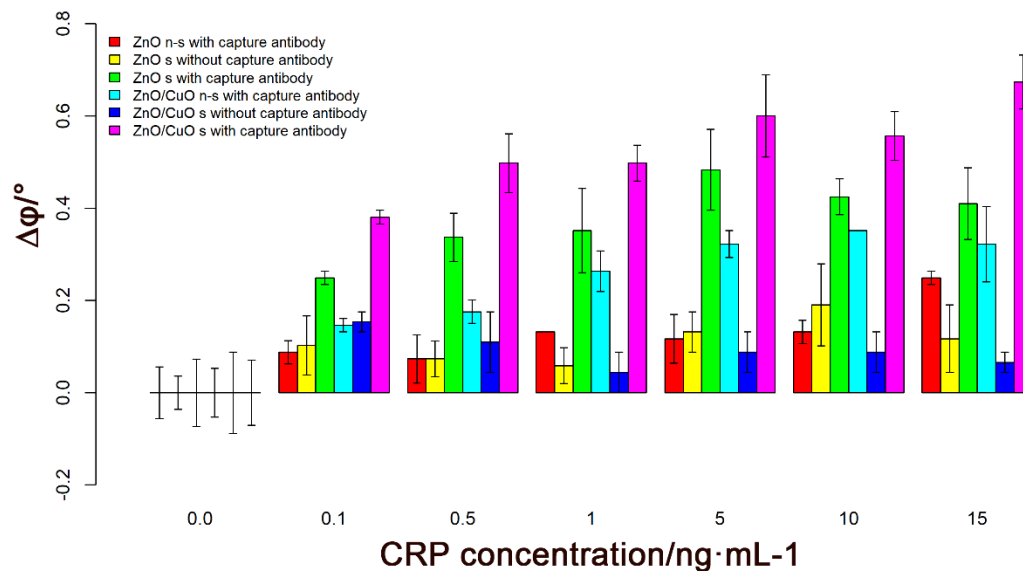


Figure 5.7 Impedance phase change/degree ($\Delta\phi/^\circ$) response to seven concentrations of antigen (CRP) on the six different types of membrane. For the 3 nano-ZnO membranes ($n=3$): with 200 ng capture antibody and without sonication (red), without capture antibody and with sonication (yellow) and with 200 ng capture antibody and with sonication (green). For the 3 nano-ZnO/CuO membrane ($n=3$): with 200 ng capture antibody and without sonication (light blue) and without capture antibody but with sonication (dark blue), with 200 ng capture antibody and with sonication (pink purple).

Table 5.1 shows pairwise comparisons, using a Wilcoxon rank sum test, on four types of membranes with antibody immobilised. The phase responses of the nitrocellulose membranes show a significant difference between sonicated and non-sonicated membranes for both the nano-ZnO and ZnO/CuO membranes ($p < 0.05$).

Table 5. 1 The significant differences in the membrane treatment analyzed by a Wilcoxon rank sum test among four different nano-particles/nitrocellulose membranes with antibody immobilised.

A Wilcoxon rank sum test	ZnO-ns	ZnO/CuO-ns	ZnO/CuO-s
ZnO/CuO-ns	0.019	-	-
ZnO/CuO-s	0.013	0.013	-
ZnO-s	0.013	0.054	0.024

Figure 5.7 also shows the phase change for both nano-ZnO membrane and nano-ZnO/CuO membrane biosensors without capture antibody, but blocked with skimmed milk. The results were significantly lower than those obtained with the membranes containing antibody. Unsurprisingly the composition of the membranes was not statistically significant with respect to the biosensors with no capture antibody ($p=0.565$). This control did show a slight increase in signal output with increasing concentrations of CRP, which can be attributed to non-specific binding of CRP to proteins on the surface.

With antibody in the membranes, for both the nano-ZnO membrane and the nano-ZnO/CuO membrane, dose response relationships were evident from **Figure 5.7**. This indicates that the charge interactions of antigen binding with antibody resulted in significantly larger output signals. It is speculated that there is increased charge accumulation due to the bound antigen on the surface compared with the non-specific binding of CRP.

The coefficient of variation (CV) was used to compare the variability of the data from ZnO with that from the ZnO/CuO membranes, with 200 ng anti-CRP. The average CV of the phase response at each concentration of CRP for the nano-ZnO/CuO (1:2) membrane is 9.6% compared with 15.6% for the nano-ZnO membrane, i.e. the ZnO/CuO membrane has better reproducibility. The ZnO/CuO membrane and ZnO membrane without sonication show CVs of 12.6% and 28.5% respectively. This demonstrates that the sonication stage of the fabrication process improved the reproducibility of nanoparticle membranes and the sonication process

gave significantly higher results; for ZnO sonicated vs non-sonicated $p=0.035$ and for ZnO/CuO $p=0.025$.

The 4-parameter logistic curve fits of the phase change data for both nano-ZnO and nano-ZnO/CuO membranes with sonication are shown in **Figure 5.8**. It can be seen that the dose response curve with nano-ZnO membrane appears to become saturated at CRP concentrations above approximately 5 ng/mL, while with nano-ZnO/CuO membrane appears to saturate at approximately 15 ng/mL. The addition of CuO enabled an average enhancement of 1.4 times a greater signal across the range of 0.1 to 15 ng/mL. One explanation of this difference is the enhanced effect of nano-confinement in the ZnO/CuO membrane biosensor. This occurs when binding molecules are matched in size to the voids in the nanoparticle structure, resulting in charge screening due to the electric field distribution inside the structure [50]. **Figure 5.3** shows that the ZnO/CuO membranes have a closer packed structure with smaller voids, due to the smaller size of the CuO nanoparticles.

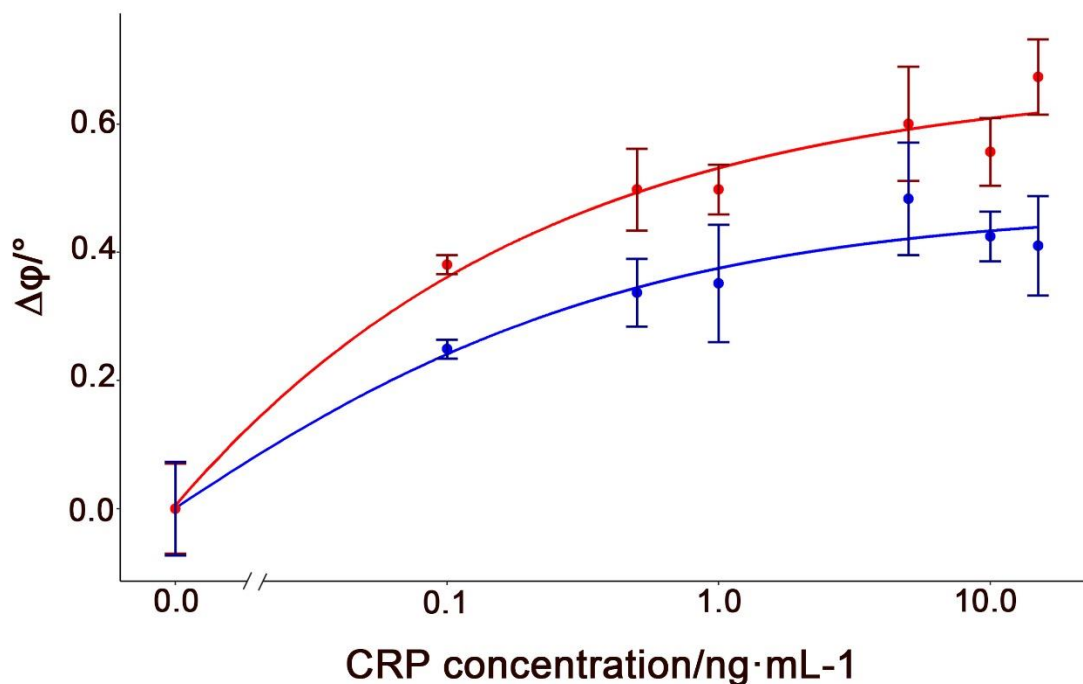


Figure 5. 8 Phase change/degree ($\Delta\phi/^\circ$) response versus antigen (CRP) concentration for sonicated nano-ZnO nitrocellulose membranes (blue) and nano-ZnO/CuO nitrocellulose membranes (red) with capture antibody ($n=3$) measured at the frequency of 100 Hz, – standard error bars are shown.

Table 5.2 shows the comparison of LoDs of nano-ZnO and nano-ZnO/CuO membranes with and without sonication. The LoD for the 1% nano-ZnO sonicated membranes with 200 ng anti-CRP was calculated to be 27 pg/mL, while the LoD for 1% nano-ZnO/CuO (1:2) sonicated membranes with 200 ng anti-CRP was 16 pg/mL. **Table 5.2** shows that the sonication has made a significant difference to the LoD on nano-ZnO/nitrocellulose membrane. The nano-ZnO/nitrocellulose membrane is a 92.6 times improvement, while nano-ZnO/CuO nitrocellulose membrane is a 1.25 times improvement. Both nano-ZnO/CuO nitrocellulose membranes with and without sonication show enhanced behaviours, i.e. lower limits of detection. It is hypothesised that the better detection limit and reduced enhancement due to sonication observed with the ZnO/CuO membranes is due to a decrease in the size to the voids in the nanoparticle structure compared with the ZnO membranes. This enhances the effect of nano-confinement, as described above, resulting in amplification of the signal and a smaller number of binding events being required to bring the signal above the noise threshold of the impedance instrument.

Table 5. 2 Limits of detection of the phase change calibration curve for non-sonicated and sonicated ZnO and ZnO/CuO membranes.

LoD	Nano-ZnO non-sonicated membrane	Nano-ZnO sonicated membrane	Nano-ZnO/CuO non-sonicated membrane	Nano-ZnO/CuO sonicated membrane
Blank mean+3× standard deviation	2.5 ng/mL	27 pg/mL	20 pg/mL	16 pg/mL

In many articles in the literature, CRP is utilised as the model analyte to characterise new types of biosensor. A number of examples of sensitive CRP biosensors are listed in the Appendix **Table S5.1**, and a selection is highlighted below. Dong *et al.* developed a paper-based microfluidic lateral flow immunoassay using gold nanoparticles to deliver a colorimetric output [63]. The key advancement presented related to the integration of the sensor with a

smartphone using a microlens [63]. The assay was able to detect the target protein up to 2 $\mu\text{g}/\text{mL}$, however the detection limit was only 54 ng/mL and thus substantially inferior to the value presented in this work [63]. Justino *et al.* adopted the approach of enhancing sensitivity with nanoparticles, using carbon nanotubes on the sensor surface of a field-effect transistor. This showed improved performance for CRP detection, with a LoD of 0.1 ng/mL [37].

Impedimetric biosensors for detection of CRP have been developed by a number of research groups. For example, Bryan *et al.* presented a sensitive and reusable biosensor, using a well-established technique of analysing the charge transfer resistance to determine the CRP level [52]. A LoD of approximately 19 ng/mL was presented [52]. Yagati *et al.* also developed a faradaic impedimetric biosensor. This research team realised the benefit of using nanoparticles, utilising graphene oxide to achieve an improved LoD of 0.08 ng/mL [57]. However, compared with all these previous studies, the non-faradaic impedimetric nano-ZnO and nano-ZnO/CuO membrane biosensors presented in our paper, show excellent limits of detection.

The advantages of the non-faradaic impedimetric methodology are reinforced by reports in the literature. Lin *et al.* developed a non-faradaic biosensor for CRP using a biogenic silica as the nanoporous template with the pore densities (40 pores of 40 nm diameter per 1 μm^2) integrated on to the microelectrode platform as the sensor surface, rather than ZnO/CuO nanoparticles within a 3D microporous membrane, as described in this paper. However, the approach also resulted in a low value for the LoD, i.e. 1 pg/mL . The advantages associated with the simplicity of measuring a change in capacitance were also highlighted [133]. Tanak *et al.* developed a non-faradaic electrochemical impedance spectroscopy-based biosensor for detection of CRP. In this case, 100 nm thin film of ZnO, deposited on the gold interdigitated electrodes was used and a LoD of 0.01 $\mu\text{g}/\text{mL}$ in serum was achieved [41]. Neither of these studies utilised, ZnO or CuO nanoparticles nor a nanoporous membrane and they did not include an insulating layer between the electrodes and the sensor surface. However, the low LoD values, evidence the promising nature of the non-faradaic approach.

5.4 Summary

Both nano-ZnO nitrocellulose membrane and nano-ZnO/CuO nitrocellulose membrane biosensors can be fabricated using a simple and inexpensive colloidal sonication technique. Following fabrication, the cross-section of nitrocellulose membrane contained increased densities of nanoparticles from the upper to the lower layers. The loading of ZnO and CuO nanoparticles within the membrane remained in proportion to the concentration of each type of nanoparticle within the original colloidal suspension. The sonication force is critical to assist the nanoparticles to be embedded into the lower layer of the membrane.

Figure S5.12, Appendix B compares phase change measured on both the nano-ZnO and the nano-ZnO/CuO nanoparticles-based PET (Chapter 4) at 138 Hz and nitrocellulose membranes (Chapter 5) at 100 Hz with the same concentration of CRP of 1, 5 10 ng/mL. It shows the similar enhanced impedance phase behaviour on nano-ZnO/CuO nanoparticles based on both PET and nitrocellulose membranes. However, Nano-ZnO membranes show an approximate 3-fold larger change than with PET, which is the reason why ZnO nanoparticles based sensors were kept for the following research.

The addition of CuO nanoparticles of nano-ZnO/CuO nitrocellulose membrane biosensors showed enhancement of performance on impedance spectroscopy at 100 Hz across a concentration range of 0.1 ng/mL to 15 ng/mL CRP. The nano-ZnO nitrocellulose membrane biosensors revealed dose dependent responses with saturation occurring at approximately 5 ng/ml. The sonicated nano-ZnO and nano-ZnO/CuO nitrocellulose membranes showed limits of detection of 27 and 16 $\mu\text{g/mL}$ respectively. Sonication during biosensor fabrication enhanced performance, with the nano-ZnO membrane showing an approximate 3-fold increase and the nano-ZnO/CuO nitrocellulose membrane showing an approximate 2-fold increase in phase change with sonication. The nano-ZnO/CuO nitrocellulose membrane with sonication showed the optimum results in terms of the highest gradient and broadest detection range. Further work is being carried out to fully evaluate the biosensor and improve reproducibility, particularly through automating the fabrication process.

In addition to the simple and inexpensive fabrication methodology, which is compatible with large scale manufacture, and the excellent limits of detection, other advantages of this

biosensor fabrication technique include the lack of contact between electrodes and measurement matrix and the fact that no redox active species are required. This biosensor fabrication methodology can be adapted to the measurement of any other analytes where an appropriate biological binding partner can be obtained and may be particularly suited to measurements, where high sensitivity or low sample volumes are required. These benefits make it a promising technique for adaption as a point-of-care diagnostic device.

The next chapter will describe the fabrication of a system by flow-based methodology on a nano-ZnO or ZnO/CuO composite 3D membrane. This will make the biosensor designable for point-of-care applications where monitoring over a period is required.

Chapter 6

Nano-membrane Based Biosensors for Detection of C-Reactive Protein by Flow-Based Methodology

Following from previous chapter, both ZnO and ZnO/CuO nano-membranes shows good characteristics for sensing CRP, with low limits of detection. In this last experimental chapter, nano-membrane, designed flow measurement, are fabricated and discussed. In order to optimise and compare the sensitivity of flow detection, two different electrodes are investigated. In contrast to the previous chapter, the sample containing the antigen is carried to the sensor at fixed time by capillary flow, facilitated by the arrangement of the sample and absorption pads. To demonstrate the capacitive changed due to accumulation of antibody-antigen in the 3D matrix, a mathematical model was used to confirm the impedance response over the time period. A discussion on flow rate is also presented.

6.1 Introduction

6.1.1 Background

Based on the previous three experimental chapters, it has been demonstrated that non-faradaic biosensing technology can be created using either nano-surfaces or nano-membranes. Using ZnO and ZnO/CuO nano-membranes on an insulating layer of glass above D-shape (1 mm gap) electrodes, measurement of CRP at low limits of detection has been shown.

In this chapter, new nano-membrane-based biosensors by flow-based methodology are presented. In order to develop a non-faradaic impedimetric biosensor for measurement of CRP over a broad detection range, ZnO/CuO nanomaterials and nitrocellulose membrane were utilised and the impedance responses obtained as immunoassays were performed. Non-faradaic impedance spectroscopy is known to be an effective technique to measure real time interfacial changes in the electrical double layer (EDL), as a time-sensitive biomarker tracking system [162]. Furthermore, it has been shown that increased roughness, for example by the addition of nanoparticles, can increase the capacitance in the EDL [163].

In contrast to the last chapter, the addition of antigen is carried out at fixed times, with the sample being moved to the sensor surface by capillary flow. The dynamics of the flow is dependent on the fabrication of flow set-up, i.e. the sample pad and the absorbent pad. Binding takes place within the porous structure. The advantage of porous material is the increase of the sensor surface area and thus the interaction between target molecule and receptor [120]. This arrangement has the potential to be integrated in to a lab-on-a-chip design, which offers great flexibility in application area in a similar way to other lab-on-a-chip impedimetric designs [119].

Preliminary investigations on nano-ZnO nitrocellulose membranes (n=3) with 200 ng antibody capture (blue) on 1 mm gap planar electrode after a 9 minute fluidic time with accumulative concentrations of CRP, measured at a frequency of 100 Hz showed the saturation at accumulative concentration after 1660 pg/mL (**Figure S6.1**). Therefore in this study the other two different electrodes were investigated and discussed in order to optimise and compare the sensitivity by flow-based detection. To demonstrate the capacitive change due to

accumulation of antibody-antigen in the 3D matrix, a mathematical model is introduced based on data analysis of the impedance magnitude to compare affinity in order to determine the numbers of binding molecules. This is introduced in the next section. A discussion on flow rate is subsequently presented.

6.1.2 Affinity

Antigen binding to an antibody is a dynamic process determined by the law of mass action. The strength of the antibody/antigen interaction gives the affinity (K) of the reaction with units being M^{-1} .



$$K = \frac{k_a}{k_d} \quad (6.2)$$

The affinity is the ratio of the association constant (k_a) and dissociation constant (k_d), when measured kinetically (these are often called the on-rate (k_{on}) and the off-rate (k_{off}) respectively). The association rate is a measure of how quickly an antibody binds to its target antigen which is related to diffusion and the probability that an antigen molecule will contact the antibody in the right orientation to enable binding. The dissociation rate is a measure how quickly the antibody/antigen complex dissociates and is related to the strength of the non-covalent bonds between the molecules. At equilibrium the rate of binding matches the rate of complex dissociation.

The units for the association rate are $M^{-1}s^{-1}$ and for the dissociation rate the units are s^{-1} . Antibody binding strength is often expressed as the equilibrium dissociation constant k_D with the units being expressed as Molarity (M). Lower k_D values equate to higher affinity antibody binding to the antigen, typical values for k_D are 10^{-10} to 10^{-5} M.

$$k_D = \frac{K_d}{k_a} \quad (6.3)$$

Antibodies with the same affinity may have quite different properties in how quickly they take up antigen or release antigen. Tajima *et al.* concluded that orientation-controlled antibodies had a lower equilibrium dissociation constant than randomly oriented ones [114].

Most antibodies will slightly increase association rates with increasing interaction temperature [34]. Hadzhieva *et al.* found that the antigen density qualitatively influenced the entropy change of the low affinity antibody [34]. For example, at low antigen density, the thermodynamic parameter value of CH103 (the lowest affinity antibody in five HIV-1 neutralizing antibodies) had a negative value, which was gradually transformed to positive as the antigen density increased [34].

6.1.3 Design Considerations and Flow Rate

There are two types of materials that are commonly used as sample pads: cellulose fibre filters and woven meshes. Woven meshes work well to distribute the sample volume evenly over the conjugate pad [65].

The ionic strength of the buffer should be reduced as much as possible [65]. Ions in solution can interfere with electrostatic interactions between the membrane and the capture reagents. In addition, physiological concentrations of buffer salts and sodium chloride promote the solubility of most proteins and reduce the hydrophobic attraction of the nitrocellulose membrane. Thus, the molarity of the buffer should be lowered to the minimum (< 10 mM) required to maintain a stable pH [65].

The definition of capillary flow is that a sample moves along a membrane strip when liquid is introduced at one end [65]. The alignments of strips will influence the flow rate, such as contact between the materials, degree of overlap, compression within the housing [164]. The liquid flow path is complex within a material or between materials [164]. The flow rate is not constant throughout the length of the strip; in fact it decays exponentially as the liquid progresses along the porous matrix [65]. The physical and chemical attributes of the membrane affect its capillary flow properties, which are important to test strip functionality [65].

Both the antibody fixed to the membrane and mobile antigen as well as the antibody-antigen complex are affected by the flow rate. The amount of complex formed, R , is equal to K , a rate

constant related to the affinity of the antibody for the antigen, times the concentrations of the reactants Ab and Ag [65]. At a flow rate:

$$R = K [Ab][Ag] \quad (6.4)$$

Gervais *et al.* developed a capillary-driven multiparametric microfluidic chips for detection of CRP in human serum [165]. There is an increased signal generated with increased incubation time due to slower flow rates and more time to interact [165]. Binding capacities depend on binding constant, protein concentration and the number of binding sites as well as non-specific binding for column chromatography [166].

6.2 Materials and Methods

6.2.1 Nanoparticles-Based Flow Test Strip Fabrication

The test strip consists of three components: (1) a sample pad made of glass fibre; (Glass Fibre Conjugate Pad Sheets (GFCP203000) was from EMD Millipore Corporation with thickness of 0.43 mm +/- 0.08 mm. The glass fibre sheet functioned as sample pad which was cut with the rectangle size of 20 × 15 mm.) (2) A nitrocellulose membrane; (from the Sartorius lab with 0.45 µm pore. The membranes were cut using Biodot guillotine in to squares of size of 15 × 15 mm.) The nano-ZnO and nano-ZnO/CuO nitrocellulose membranes were fabricated by methods mentioned in section 5.2.1 with sonication. (3) An absorbent pad made of cellulose fibre. (Cellulose fibre Sample Pad Sheets (CFSP223000) was from EMD Millipore Corporation with thickness of 0.825 +/- 0.0635 mm. The flow rate is 180 mL/min +/- 50. The cellulose fibre sheet functioned as absorbent pad which was cut with the rectangle size of 100 × 15 mm.)

In the flow system, two types of electrode were compared – planar electrodes and interdigitated. The importance of the electrode structure has been demonstrated in previous work. Zhang found that the EDL capacitance varies with the size of electrodes [105]. Hugo *et al.* presented a finite element analysis of coplanar electrodes, showing that the electrodes produce a non-homogeneous electric field. This resulted in impedance values which were very dependent on the relative positions of the electrodes [118]. In addition, interdigitated electrode designs have been shown to increase the overall capacitance due to increased surface area [120].

In this study, the nitrocellulose membranes were laid on a glass coverslip (from Deltalab, 22 mm × 22 mm and 0.13 - 0.16 mm thick), which was positioned on either a 23 mm × 23 mm electrode with 4 mm gap planar electrode or a 23 mm × 23 mm interdigitated electrode, line width and gap is 1 mm, as shown in **Figure 6.1**. The capacitance of electrodes compared with 1 mm gap D-shape electrode is shown in section 6.5 Appendix **Table S6.1**. The lower layer of nitrocellulose membrane with the highest density of nanoparticles faces towards the electrode, same as previous chapter. (The gradated porosity and associated variation in nanoparticle density will be described in section 6.3.1). There is no second coverslip placed on top of the membrane during the fluid flow and measurement.

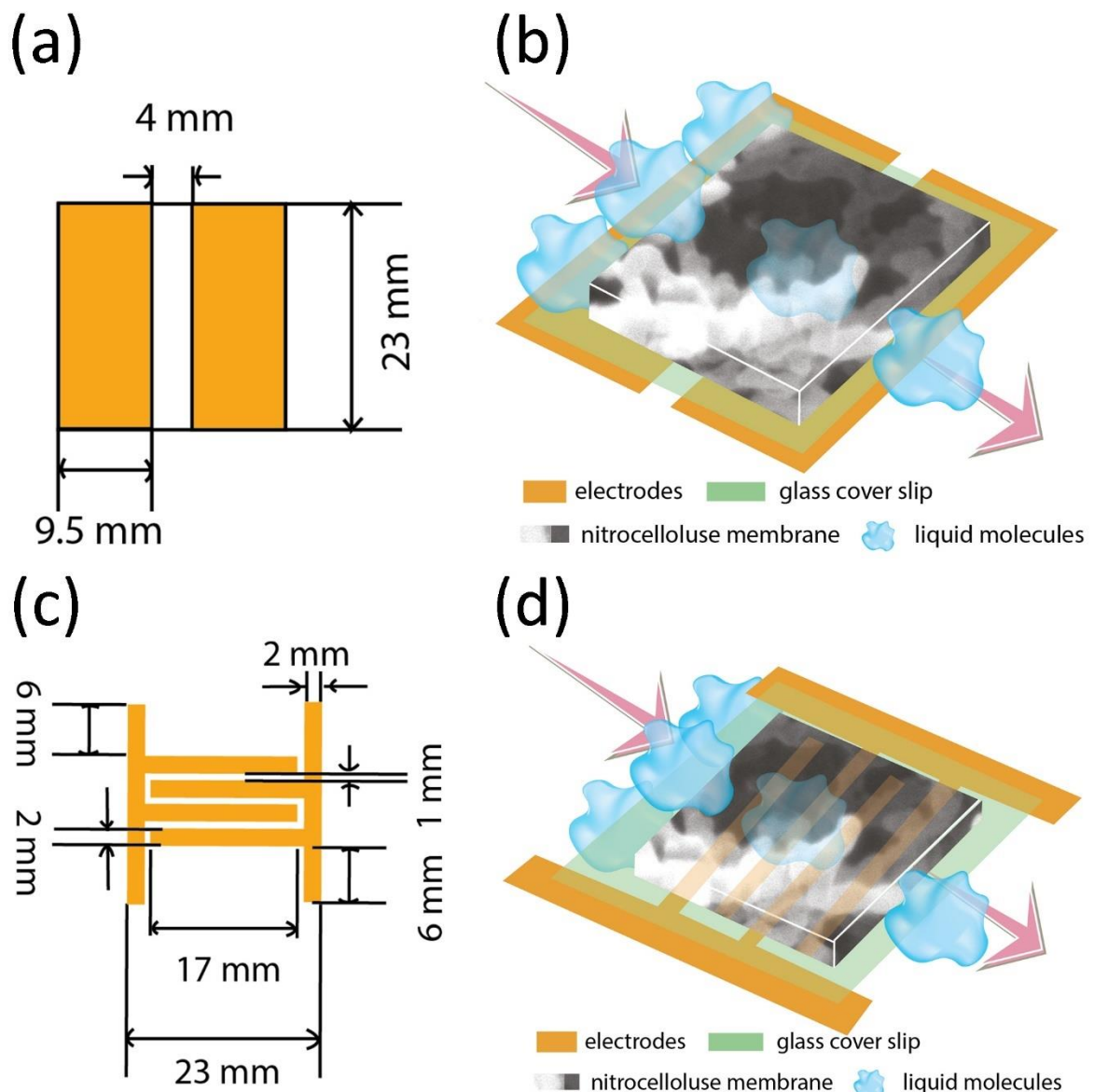


Figure 6. 1 The drawings of electrode design: (a,b) the design of planer electrode and (c,d) the interdigitated comb electrode. (a,c) the drawings of electrodes and (b,d) designed sensing area with coverslip as insulating material between nitrocellulose membranes and electrodes as non-direct contact. The liquid molecules (not scaled) shows the flow direction.

The flow-based system is illustrated in **Figure 6.2**. The overlap distance between the glass fibre and nitrocellulose membrane was defined as parameter $X=3$ mm and the overlap distance between the nitrocellulose membrane and cellulose fibre was defined as parameter $Y=3$ mm. It was important to keep the distance overlapped constant, because the flow speed

changes with different overlapping distances. Also, distances X and Y affects the overloading of liquid, influencing the reaction time and cause the errors of the impedance tests. The flow assembly was developed with an angle at 7.75 degree (measured by ImageJ shown on **Figure 6.2(b)**) created by two cover slips. Because the flow rate of glass fibre is much higher than nitrocellulose membrane, in order to avoid leaking, the 7.75-degree angle space between 2 cover slips was selected to allow the storage of liquid and help slow the release of liquid.

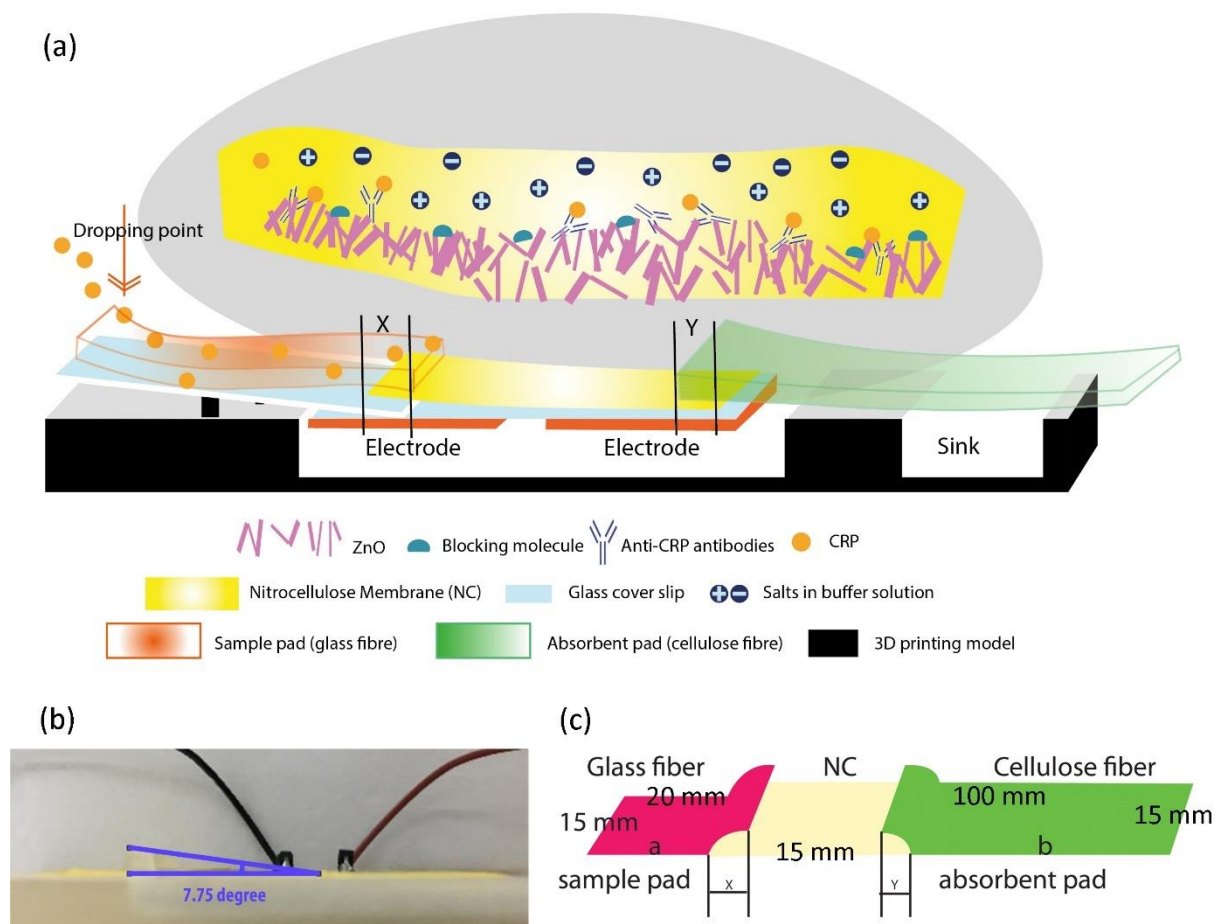


Figure 6. 2 Illustration of flow-based system: (a) Schematic diagram of strip by flow-based methodology; Illustration of flow-based system composed by components: glass fibre, nitrocellulose and cellulose fibre; (b) The photo of the flow-based biosensor system with angle shaped by two overlapped cover slips on electrodes and 3D printing model (seen Figure 6.3), and the degree was analysed by image J; (c) Dimensions of width and length of components arrangement with angle formed by two overlapped cover slips.

A 3D printed backing structure, shown in **Figure 6.3**, was used as a holder for the membranes and offers the advantage of easy handling and provides a high level of mechanical strength [65]. In a batch process, nitrocellulose membrane is cast onto a cover slip on specific electrode, the belt side (bottom layer) is masked, requiring that reagents be applied to the air side (upper side) shown in **Figure 6.3 (c)**.

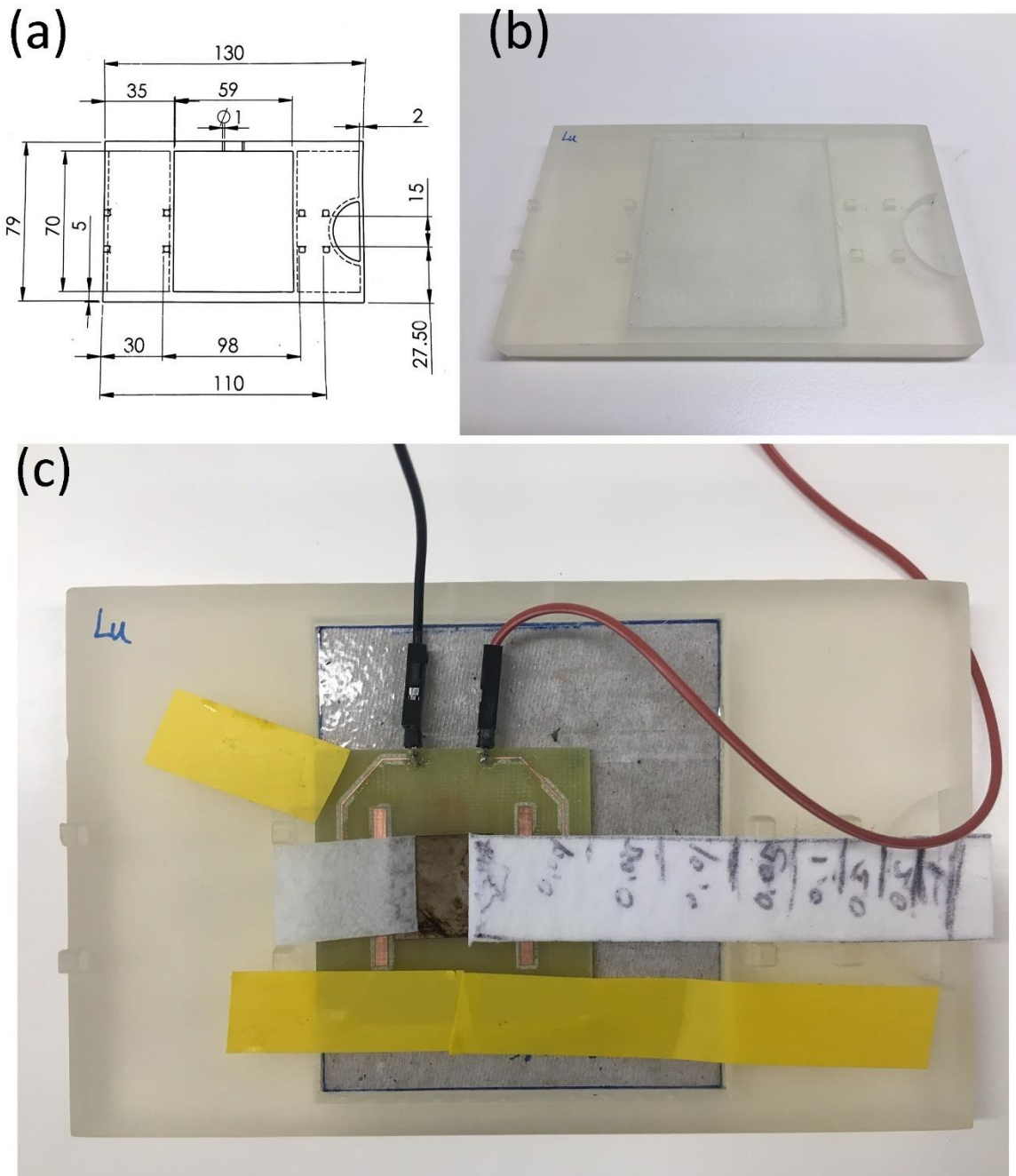


Figure 6. 3D printing design and assembly: (a) Drawing of 3D printed model design of sensor holder; (b) Photo of 3D printed structure; (The distance of the dots was designed to be the same width as sample pad and absorbent pad and was used to fix the pads of the strip. The electrode board was embedded above the sunken square to create the flow assembly almost at same horizontal level.) (c) Photo of complete flow system: materials (sample pad, nitrocellulose membrane and absorbent pad) alignment with angle formed by two overlapped cover slips on interdigitated electrode with flow rate calculation marks.

6.2.2 CRP Sensor Fabrication and CRP Assay

The developed nanoparticle-based flow assay was used for sensitive and rapid detection of CRP. To prepare the membranes for the assays, 40 μL of 5 $\mu\text{g}/\text{mL}$ monoclonal mouse anti-human C-reactive protein (4C28, from HyTest Ltd, Turku, Finland) was diluted in 5 mM PBS, purchased from OXOID Microbiology products, and was immobilised on to the nitrocellulose membranes (from the upper side to lower side) until it was fully wet. Based on the size of each nitrocellulose membrane (15 mm \times 15 mm \times 140 μm), it has a volume of 31.5 μL . If its porosity of air is 70%, the volume of air is referred as the bed volume of the membrane calculated ($0.7 \times 31.5 \mu\text{L}$) [65]. The total volume of liquid reagent required to wet it completely is 22.05 μL [65]. The anti-CRP antibody was easily immobilized in the membrane on the ZnO nanostructures, which were distributed thoroughly within the nitrocellulose membrane, as the ZnO nanostructures were positively charged, whereas the anti-CRP antibody is dominated by negative charge. Nitrocellulose membrane which also has binding abilities is normally used in the Western Blot, when proteins are separated in the electric field within the membrane after electrophoresis in polyacrylamide gel based on non-specific bindings [159].

The anti-CRP antibody was immobilised in the membrane with molecules adopting a random distribution and orientation; this has been discussed in previous chapter. In many reagent application protocols reported in the literature, the capture reagent ends up being evenly distributed throughout the thickness of the membrane [65]. In some cases, the antibody may be more concentrated on the side to which it is applied; but for the most part, no discernible gradient is observed [65]. Further experiments may need to be designed to explore this in further detail, beyond the experimental set-up described here. The number of antibody molecules on the sensor surface was based on 10 ng of the added antibody binding to the surface (further discussed in section 6.2.6). In experiments to investigate this value, it was found that the antibody number had little effect on the results at the CRP concentrations used, which means there is sufficient antibody to run the system by flow-based methodology, as shown in **Tables** S6.2 and S6.3. The antibody selected was monoclonal in order to provide good specificity.

The membranes were then dried in a desiccator with silica gel at 4 $^{\circ}\text{C}$ overnight. Under 18 hours of the overnight incubation, 200 ng anti-CRP antibody were immobilised in three

different membranes (blank nitrocellulose, nano-ZnO nitrocellulose and nano-ZnO/CuO nitrocellulose membranes). After the overnight incubation, the nano-particles/nitrocellulose membrane was washed in 15 mM PBS buffer by dipping in for 4 times and then blocked with 5% skimmed milk (Skimmed milk powder (SMP) was purchased from Tesco) for 1 h blocking at 4 °C in fridge. The blocking method using skimmed milk was improved from dip process used in the previous chapter to 1-hour solution-immersion process to provide enough time for covering the porous structure created by nanoparticles in nitrocellulose membrane. Afterwards the membranes were washed by dipping them into 15 mM PBS buffer and gently placing them on absorbent tissues to remove excess PBS buffer.

6.2.3 Valuation of Flow-Based Test Strip and CRP Assay

Robustness of whole system is achieved by the electrode board shown in **Figure 6.1** placed in a plastic holder shown in **Figure 6.3**. Sample pad (glass fibre), nitrocellulose membrane (after immobilisation of antibodies) and absorbent pad (cellulose fibre) were placed using double-side tape together with two glass cover slips forming the angle seen in **Figure 6.2**.

As mentioned in section 6.2.2, based on the size of nitrocellulose membranes (15 mm × 15 mm × 140 μm), the total volume of liquid reagent required to wet it out is 22.05 μL [65]. Based on the size of glass fibre pad (sample pad 20 mm × 15 mm × 0.43 mm +/- 0.08 mm), the total volume of liquid reagent required to wet it out is 90+/-16.8 μL [65]. The total volume of liquid of the CRP concentrations loaded into the pad was determined by the bed volume of the sample pad and the nitrocellulose membrane, at around 130 μL.

To start the flow-based technology, on the 4 mm gap planar electrode system, 150 μL of 5 mM PBS buffer was added to the edge of glass fibre. The glass fibre absorbed the liquid slowly to fully wet by wicking to activate the flow assay. Over the 9 minute fluidic period, the 150 μL solution of PBS buffer was completely absorbed and migrated along the strip. At 9 minutes, 80 μL of an increased concentration of CRP was added. Various concentrations of CRP (8C72) purchased from HyTest Ltd were diluted in 5 mM PBS (pH 7.3 ± 0.2 at 25 °C) from VWR supplier. The 80 μL of increasing concentrations of CRP (10, 50, 100, 500, 1000, 5000, 10000, 50000, 50000, 50000, 100000, 100000 pg/mL) were dropped onto the same sample pad area,

in a continuous manner every 9 minutes. The cumulative doses of CRP were calculated as shown in section 6.5 Appendix **Table S6.2**.

To start the flow-based technology, on the interdigitated electrode system, the immunoassay process is same as planar electrode system. Various concentrations of CRP (8C72) purchased from HyTest Ltd were diluted in 5 mM PBS. The 80 μ L of increasing concentrations of CRP (1, 5, 10, 50, 100, 500, 500, 1000, 1000 μ g/mL) were dropped onto the same sample pad area, in a continuous manner every 9 minutes. The cumulative doses of CRP were calculated as shown on section 6.5 Appendix **Table S6.3**. The reason for changing to a lower range of concentrations of CRP is due to the results of Preliminary experiments tried on the interdigitated electrode, shown in **Figure S6.2**. It shows that dose response on interdigitated electrode saturates when using the previous concentrations of CRP.

The sample was absorbed and migrated through the nitrocellulose membrane by capillary forces. Due to the flow rate through the glass fibre and nitrocellulose, the sample could not be absorbed by nitrocellulose instantly, the excess fluid accumulated in the angle space made by two glass slips, shown in **Figure 6.2**. After 9 minute measurement of an individual sample was complete, the extra liquid in the corner between the cover slips was all absorbed and this acted to prevent the nitrocellulose from drying out, ready to receive the next sample.

A Cypher Instruments C60 Impedance-Amplitude-Phase Analyser was used to measure the impedance of nanoparticle-based nitrocellulose membrane. As discussed in previous chapters, the double layer capacitance was dominant at frequencies below 1000 Hz. The frequency was scanned from 10 Hz to 1 KHz at a voltage of 2 Vpp with a DC offset of 0.9 mV, with 100 test points, in order to shorten the detection time to 3 minutes in contrast to full frequency sweep (10 Hz to 4 MHz with 300 test points) that takes around 5 minutes. The CRP could bind to the nanoparticles/antibody conjugates among the membranes via antigen and antibody interaction. The impedance amplitude and phase angle were measured every 3 minutes over 9 minutes (at 0, 3 and 6 minutes) and ready for adding next concentration, with 3 or 4 replicates of the nano-particles/nitrocellulose membranes, measured from 10 Hz to 1 KHz.

The calibration curve was plotted based on changes in impedance magnitude/phase value versus accumulative concentration of CRP. As in the previous chapter, the sensor impedance

responses at a single frequency of 100 Hz were analysed and compared with control, ZnO and ZnO/CuO (1:2) nanoparticle nitrocellulose membrane on both the 4 mm gap planar and interdigitated electrode. As a control, impedance and phase changes with ZnO and ZnO/CuO (1:2) nanoparticle nitrocellulose membrane were compared with or without CRP concentrations plus with or without anti-CRP antibodies under flow-based system. The changes in impedance magnitude/phase value were defined as the difference of the impedance magnitude/phase value of the biosensor after 9 minute fluidic time with accumulative CRP concentration and the impedance magnitude/phase value of the control (PBS buffer). The changes in impedance magnitude and phase value were plotted using a logarithmic scale on the x-axis. PBS buffer (acting as a blank) is defined as 0.1 pg/mL for plotting on a log axis on planar electrode. PBS buffer (acting as a blank) is defined as 0.01 pg/mL for plotting on a log axis on interdigitated electrode.

6.2.4 Statistical Analysis

A 4-parameter linear-log logistic curve, with the error bars, was created using R. The estimated limit of detection (LoD) was defined as the mean of the intercept on the y axis of the calibration curve, plus 3 times the standard deviation of the intercept. The mean value and Standard deviation of the “intercept” at the working zero was found using the 4-parameter logistic curve.

Two-sample Kolmogorov-Smirnov tests comparing differences on both curves, were performed using R.

6.2.5 Modelling the Response

The change in impedance magnitude over time, with the addition of increasing amounts of CRP was used to fit a model response that used a defined set of parameters associated with the antibody. The k_a and k_d values, numbers of antibody molecules on the surface and the dose of CRP at given time points were optimised to give the best fit to the experimental data.

This resulted in an estimate of the affinity of the antibody on the sensor surface expressed as the M^{-1} (k_A) or M (k_D).

The model used an iterative numerical approach to calculate the number of bound CRP molecules (B) on the sensor surface at one second intervals, based on the units of k_a and k_d , $M^{-1}s^{-1}$ and s^{-1} respectively. An initial condition of $B=0$ was used and each iteration resulted in an increase in B due to a given association rate and number of CRP molecules in the sample flowing across the sensor surface at the given time point of the iteration. Then B was modified by subtracting the number of CRP molecules leaving the sensor surface defined by the dissociation rate, the new value for B was then used as the starting point in the next iteration. Over time the concentration was modified according to the time points when the concentration of CRP in the sample was changed. Initial k_a , k_d values were chosen based on reports in the literature using the same antibody [27], the number of antibody molecules on the sensor surface was based on 10 ng of the added antibody binding to the surface. In experiments to investigate this value, it was found that the antibody number had little effect on the results at the CRP concentrations used. A scaling factor was used to relate the number of bound molecules on the sensor surface with the impedance value. The scaling factor used in all experiments was 290, in order to match experimental values with the fitted accumulative concentrations of binding complex by model.

$$\text{Impedance at time } T_n = \text{Impedance at } T_0 - \left(\frac{B}{290}\right) \quad (6.3)$$

Where time n refers to the time that each measurement was made. T_0 was the initial impedance reading put into the model.

Separate experimental data was fitted to the output of the model and the parameters modified until the best fit between the experimental and modelled data was achieved. The values of k_a and k_d were used in the model at this point was deemed to be the binding characteristics of the antibody and used to calculate the antibody affinity.

6.2.6 Validation of Flow Rate

Average flow rate was defined by the absorbent pad (cellulose fibre) flow distance (cm)/measurement time (min) in order to evaluate the capillary flow rate with concentrations of analyte, seen in handwriting on the pad in **Figure 6.3 (c)**. R software was used to plot the flow rate. An exponential model fitting was applied to data.

6.3. Results and Discussion

6.3.1 Characterisation of Membrane

The results of SEM imaging of the membranes used in this study produced identical results to those shown in Chapter 5 (see **Figures** S5.6 to S5.9 in the Appendix). As mentioned in section 5.3.1, there are three layers of nitrocellulose membrane: upper layer, middle layer and lower layer. The upper layer has the smallest pore sizes and the lower layer has a loose pore structure between the white support matrix with high density of columnar wurtzite structure of ZnO nanoparticles and the CuO nanoparticle flakes.

6.3.2 Calibration Curves

The nanoparticles-based nitrocellulose membranes were immobilised with anti-CRP antibodies, and mounted onto the flow assembly, ready for CRP detection by flow-based technology. As shown in previous experimental chapters, either impedance magnitude, $|Z|$, or phase value was used as the analysis method to plot the response, depending on which gives a better behaviour. Due to the fact that the measurement using the C60 were close to the manufacturer specified boundary limits when measuring below 10 KHz, the biosensor response had issues with measurement noise, seen as instabilities in the output trace. The data in the previous two chapters with measurement performed on the 1 mm D-shape electrode show a good response with a phase measurement because the electronic detection circuit and sensor are capacitively dominant, with changes affecting the phase angle. In the sensor arrangement used in this chapter, phase change responses, which were calculated with accumulative concentration of CRP, didn't show good response due to noise (**Appendix Figure** S6.3). It is speculated that this is because of the flow of liquid causes permittivity fluctuations in the capacitive sensor (further investigated with the control sensor, described in section 6.3.3.), as well as the influence of the accumulative concentration of CRP.

Figure 6.4 shows calibration curves of change in impedance magnitude in both nano-ZnO and nano-ZnO/CuO membranes on two different electrodes against the CRP concentrations, plotted by 4-parameter logistic curve method using R. The limits of detection were calculated and are shown in **Table** 6.1. As shown in **Figure** 6.4, the impedance change increased with

increasing accumulative concentration of CRP dose. It can be seen that this flow-based test using non-faradaic impedance measurement can be able to detect quantitatively CRP for around 2 hours. For the planar electrodes, the dynamic range is broad, from 10 pg/mL to beyond 366,660 pg/mL. For the interdigitated electrodes, the dynamic range is from 1 pg/mL to 3,166 pg/mL. Seen from Appendix **Figure S6.2** the impedance magnitude results saturate of nano-ZnO/CuO nitrocellulose membranes on interdigitated electrode after a 9 minute fluidic time with accumulative concentrations of CRP from 6660 to 266660 pg/mL.

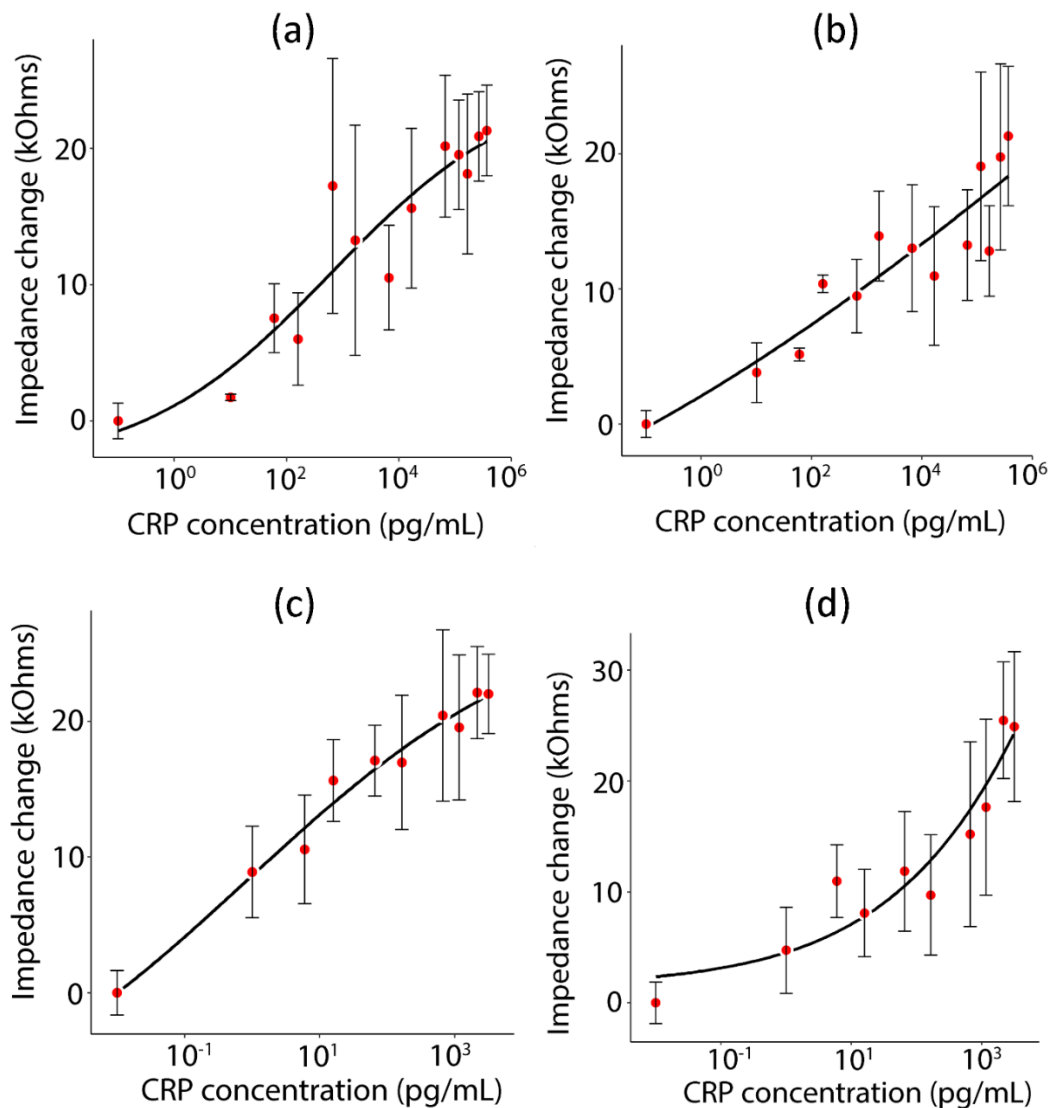


Figure 6. 4 Impedance change ($Z/kOhms$) on different nano-membranes on two separate electrodes: (a) nano-ZnO nitrocellulose membranes ($n=3$) and (b) nano-ZnO/CuO nitrocellulose membranes ($n=3$) on 4 mm gap planar electrode. (c) nano-ZnO nitrocellulose membranes ($n=4$) and (d) nano-ZnO/CuO nitrocellulose membranes ($n=3$) on interdigitated electrode after a 9 minute fluidic time with accumulative concentrations of CRP, measured at a frequency of 100 Hz.

Table 6. 1 limits of detection on 4 different sensing flow assembly

LoDs (pg/mL)	Nano-ZnO	Nano-ZnO/CuO
4 mm Planar	2.64	0.47
Interdigitated	0.02	4.10

For planar electrode, the limit of detections were calculated to be 2.64 pg/mL on nano-ZnO membranes and 0.47 pg/mL on nano-ZnO/CuO membranes. It shows the same behaviours as previous chapters, i.e. nano-ZnO/CuO membranes behave best on planar electrodes. But for interdigitated electrode, nano-ZnO membranes have a better response with the limit of detections calculated to be 0.02 pg/mL compared with 4.10 pg/mL on nano-ZnO/CuO membranes. ZnO/CuO membranes on interdigitated did not show the expected sensitivity due to lower affinity, which will be discussed in section 6.3.4. The limit of detections might be also related with error bars and reproducibility of each sample of nanoparticles-based membrane as well.

The capacitance of 4 mm gap planar electrodes is smaller, which results in a larger impedance compared with the interdigitated electrodes with same membrane. Referring to the capacitance values on **Table S6.1**, the 4 mm gap planar electrode has 1.905 pF while interdigitated electrode has capacitance of 9.15705 pF. It explained why **Figure 6.4** has larger change in impedance magnitude on (c,d) compared to (a,b) at similar accumulative concentration of CRP. As mentioned in previous chapters, the mixture ZnO/CuO nanoparticles can magnify the signal compared with purely ZnO. The impedance changes of nano-ZnO/CuO membranes are 0.2 larger than nano-ZnO on interdigitated electrode. From SEM on section 6.3.1, it shows rougher porous structures inside of nano-ZnO/CuO membranes. The depletion layer between the ZnO/CuO nanoparticles also decreased the capacitance which increases the impedance [167]. Meanwhile, the increased surface area in nano-ZnO/CuO membranes can increase the capacitance with binding events, due to charge accumulation, which is assumption why impedance magnified on nano-ZnO/CuO membranes with CRP binds. Consulted to capacitance on **Table S6.1**, higher capacitance of electrode board magnifies the impedance change. It didn't show much difference on 4 mm gap planar electrode due to lowest capacitance.

In summary, the impedance changes of both nanoparticles-based nitrocellulose membranes increased with increasing accumulative concentration of CRP on both planar and interdigitated electrodes with LoDs less than 5 pg/mL. Compared well with other research work published in the literature. For example, Kinnamon *et al.* [49] developed a non-faradaic label-free cortisol biosensor using molybdenum disulphide (MoS₂) nanosheets integrated into a nanoporous flexible electrode system. Their sensor was able to establish flow-based dosing studies between four cortisol concentration ranges (0.5, 5, 50, 500 ng/mL) for a 3+ hour duration with a limit of detection of 1 ng/mL [49]. Sensing was achieved by measuring impedance changes for electrochemical measurements by generating the 100 Hz sine wave and creating a 20 mV_{rms} signal [49]. The big difference is that Kinnamon *et al.* [49] used a vertically-aligned metal electrode sensor system in conjunction with confined semi-conductive MoS₂ nanosheets. The similarity is that impedance changes were determined to be primarily a result of capacitive reactance due to the modulation of the surface charge along the metal oxide nanoparticles-double layer interface [49].

6.3.3 Responses of Bare Nitrocellulose Membranes and PBS

Figure 6.5 shows the plot of impedance change (kOhms) on blank nitrocellulose membranes (n=3) without nanoparticles, but with 200 ng capture antibody and skimmed milk powder as a blocking agent. It shows there is dose dependent biological bindings between CRP molecules and the capture antibody directly linked to the membrane. However, compared with plots in **Figure 6.4**, the results in **Figure 6.5**, without nanoparticles, indicate saturation at much lower CRP concentrations (approximately 10³ pg/mL for the planar electrodes and 10¹ pg/mL for the interdigitated electrodes). This demonstrates that the capture antibody is less effective on the membrane substrate directly with only a proportion providing capture sites for the CRP molecules. This also shows the importance of the nano-crystalline structures in extending the dynamic range of the sensor and the increasing the potential for flow-based sensing methodology.

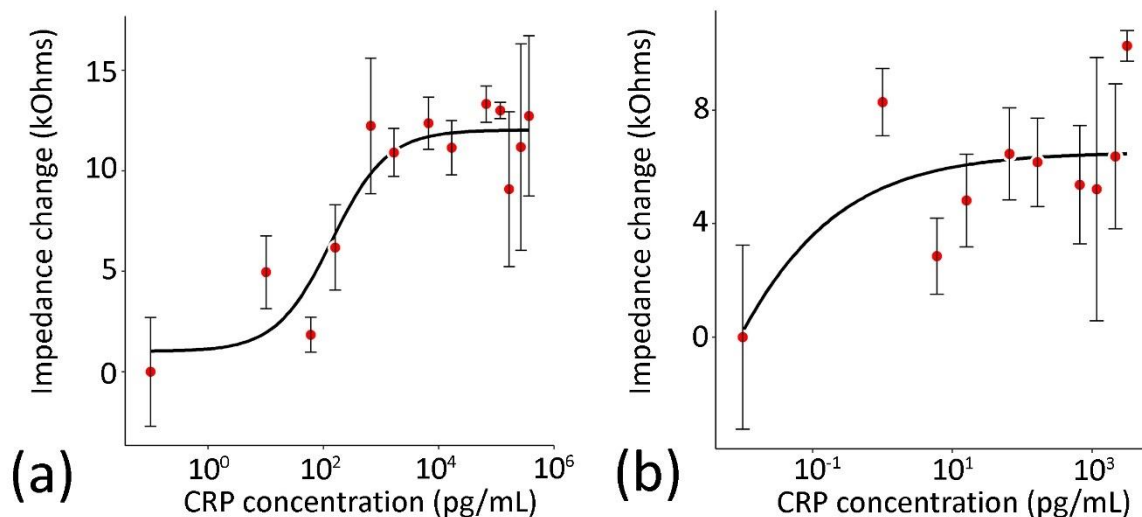


Figure 6. 5 Impedance change/kOhms on blank nitrocellulose membranes with 200 ng antibody capture on two separate electrodes: (a) blank nitrocellulose membranes (n=3) on 4 mm gap planar electrode; (b) blank nitrocellulose membranes (n=3) on interdigitated electrode after a 9 minute fluidic time with accumulative concentrations of CRP, measured at a frequency of 100 Hz.

Previous chapter section 5.3.3 **Figure 5.8** on 1 mm gap planar electrode showed the phase change of CRP concentrations placed on the membranes with and without antibodies on both nanoparticles-based membranes are significant different which indicates the charge interactions of antigen binding with antibody resulted in significantly larger output signals. **Figure S6.1** showed change comparison in phase values on nano-ZnO nitrocellulose membranes (n=3) without 200 ng antibody capture (red) and nano-ZnO nitrocellulose membranes (n=3) with 200 ng antibody capture (blue) on 1 mm gap planar electrode after a 9 minute fluidic time with accumulative concentrations of CRP, measured at a frequency of 100 Hz. There are 2 points at low concentration less significant, but the overall significance with a p-value of 0.0086 using the Two-sample Kolmogorov-Smirnov test. The control without antibodies has been done on 1 mm gap planar electrode with same flow-based system mentioned in this chapter.

Figure 6.6 (a) shows the plots of the impedance change (kOhms) on nano-ZnO/CuO nitrocellulose membranes (n=3) with 200 ng capture antibody with addition of accumulative CRP concentrations (black) and with only PBS (red) at the equivalent time points. **Figure 6.6(b)**

shows the equivalent plots but for the interdigitated rather than planar electrodes. Two-sample Kolmogorov-Smirnov tests show, there are highly significant differences on both curves. It shows in **Figure 6.6 (b)** on interdigitated electrode, there are 4 points at low concentration less significant, but the overall significance with a p-value of 0.0033. **Figure 6.6 (a)** shows significant differences all way through on planar electrode with a p-value of 0.0009.

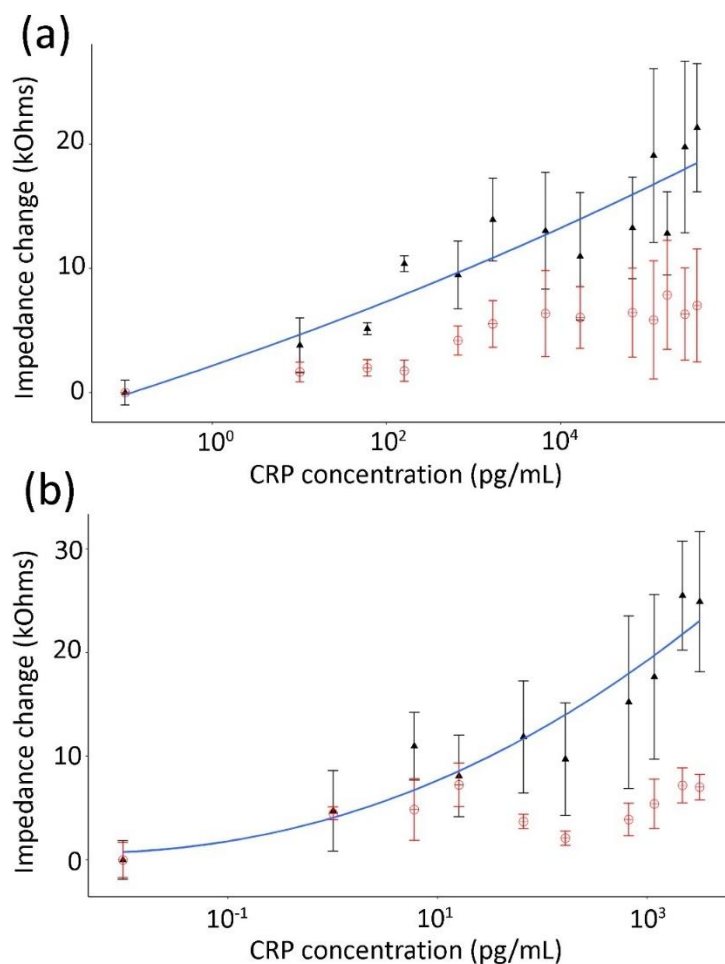


Figure 6. 6 Impedance change (Z/kOhms) Comparisons of nano-ZnO/CuO membranes (with 200 ng antibody capture) on two separate electrodes with addition of CRP concentrations (black) vs. pbs buffer only (red) with standard error bars: (a) nano-ZnO/CuO nitrocellulose membranes (n=3) on 4 mm gap planar electrode and (b) nano-ZnO/CuO nitrocellulose membranes (n=3) on interdigitated electrode after a 9 minute fluidic time with accumulative concentrations of CRP, measured at a frequency of 100 Hz.

In the absence of CRP (control PBS only), the output impedance values were significantly less than those observed when the analyte was present. This indicates that there was less charge

accumulation within the membrane with small changes observed caused by the impedance spectroscopy system or interruption of fluid flow.

6.3.4 Results by Flow-Based Methodology

Figure 6.7 shows the experimental data, together with modelled impedance, over the duration of the experiments, where (a) and (b) are on nano-ZnO membranes and (c) and (d) are on nano-ZnO/CuO membranes, and time = 0 represents the first addition of a given CRP concentration (10 pg/mL on planar electrode and 1 pg/mL on interdigitated electrode). Results are shown for both planar (**Figure 6.7 a,c**) and interdigitated electrode (**Figure 6.7 b,d**) on ZnO and ZnO/CuO nano-membranes. The figures show the experimental data (red points) and the modelled response (black line).

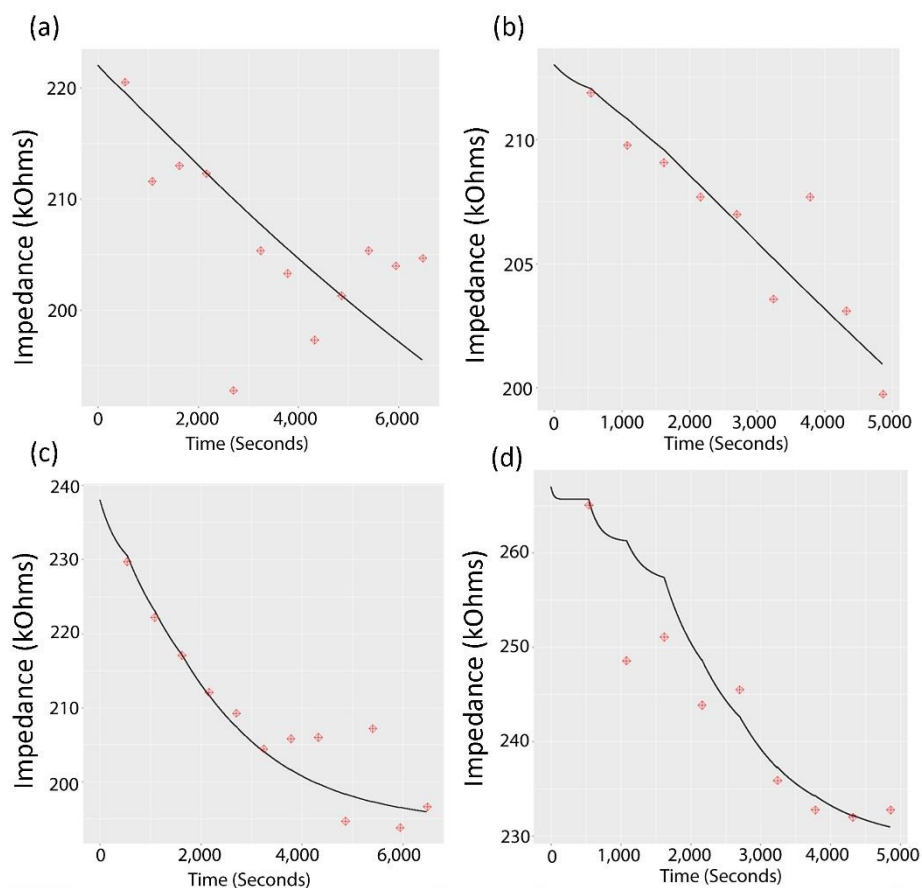


Figure 6. 7 Experimental results (red points), and modelled data, plotted versus time for (a) nano-ZnO on planar electrode; (b) nano-ZnO on interdigitated electrode; (c) nano-ZnO/CuO membranes on planar electrode and (d) nano-ZnO/CuO membranes on interdigitated electrode.

The average absorbance results in **Table 6.2** (taken from **Table 4.2** in Chapter 4) indicate that all the nano-surfaces were capable of capturing antibody on their surface using the simple drying technique used in this work. The ZnO/CuO surface, as described in Chapter 4, had a 7% greater protein uptake than ZnO. **Table 6.2** shows that although there were similar amounts of antibody captured on the surface the affinity of the antibody was different on the two surfaces.

Table 6. 2 Comparison of affinity and ELISA results on both nano-ZnO membranes and nano-ZnO/CuO membranes

	nano-ZnO membranes	nano-ZnO/CuO membranes
Average absorbance	0.5545	0.5955
k_D on planar electrode	4.00×10^{-8} M	7.69×10^{-8} M
Affinity K on planar electrode	2.50×10^7 M ⁻¹	1.30×10^7 M ⁻¹
k_D on interdigitated electrode	3.89×10^{-8} M	8.33×10^{-8} M
Affinity K on interdigitated electrode	2.57×10^7 M ⁻¹	1.20×10^7 M ⁻¹

Antibody on the nano-ZnO membranes demonstrated a greater affinity for CRP than the antibody on the nano-ZnO/CuO membranes with both electrode types giving a similar result – k_D for ZnO was 3.89×10^{-8} M on interdigitated electrodes and 4.00×10^{-8} M on planar electrodes. In contrast the k_D for the ZnO/CuO membranes was 8.33×10^{-8} M for the interdigitated electrodes and 7.69×10^{-8} M for the planar electrodes. An approximate two-fold difference.

The effect of the lower affinity of the antibody to CRP on the ZnO/CuO surfaces is seen by comparing the **Figure 6.7** upper (a,b) panels with the lower panels (c,d). It is seen that with the ZnO/CuO surface, with very low concentrations of CRP being added to the system (1 and 5 pg/mL shown in panels c and d in Figure 6.7) the signal quickly comes to an equilibrium with equilibrium being approached at higher concentration of CRP being added. Using a planar

electrode on the nano-ZnO/CuO membranes, higher concentrations of CRP were added to the system and in **Figure 6.7 (c)** it can be seen that the signal is starting to reach an equilibrium at accumulative concentration at 16,660 pg/mL (refer to 1,332.80 pg cumulative CRP does in section 6.5 Appendix **Table S6.2**). In comparison the results obtained using the nano-ZnO membranes in **Figure 6.7 (a,b)** show the signal does not show signs of reaching saturation for both planar and interdigitated electrodes.

As would be expected, the biological interactions on the sensor surface are not influenced by the electric field distribution within the sensor membranes, as seen by the very similar k_D values for the given membranes on the different electrode designs. The affinity difference that is observed when the CuO is added to the surface may be due to properties of CuO nanoparticles compared with biocompatible ZnO nanoparticles. It is known that the surface to which an antibody is immobilised will have an influence on the affinity of the antibody [114].

Metal ions environment can change antibody affinity. For example, Todorova-Balvay *et al.* utilised four different transition metal ions: copper(II), nickel(II), zinc(II) and cobalt(II) to modulate the affinity of the protein interactions in affinity chromatography for the purification of proteins [76]. Protein adsorption was different depending on the metals used.

6.3.5 Flow Rate

The product detail giving the flow rate of cellulose fibre is 180 mL/min +/- 50, which depends on the size/area of membrane used. It is assumed that 80 μ L is flowing through the cellulose fibre without loss or evaporation for 9 minutes on each addition. Therefore, the volumetric flow rate of liquid was 16.67 μ L/min in the experiments described in this chapter, far less than the 180 mL/min. It proved that there is enough time for all the liquid to flow through.

As seen from the **Figures** 6.8 and 6.9 with exponential model, with both ZnO and ZnO/CuO nano-membrane with antibody capture, the flow rate plots exponential line shift right to larger flow rate shown both on **Figures** 6.8 and 6.9, which corresponds to SEM results with larger voids created by nanoparticles in the membrane.

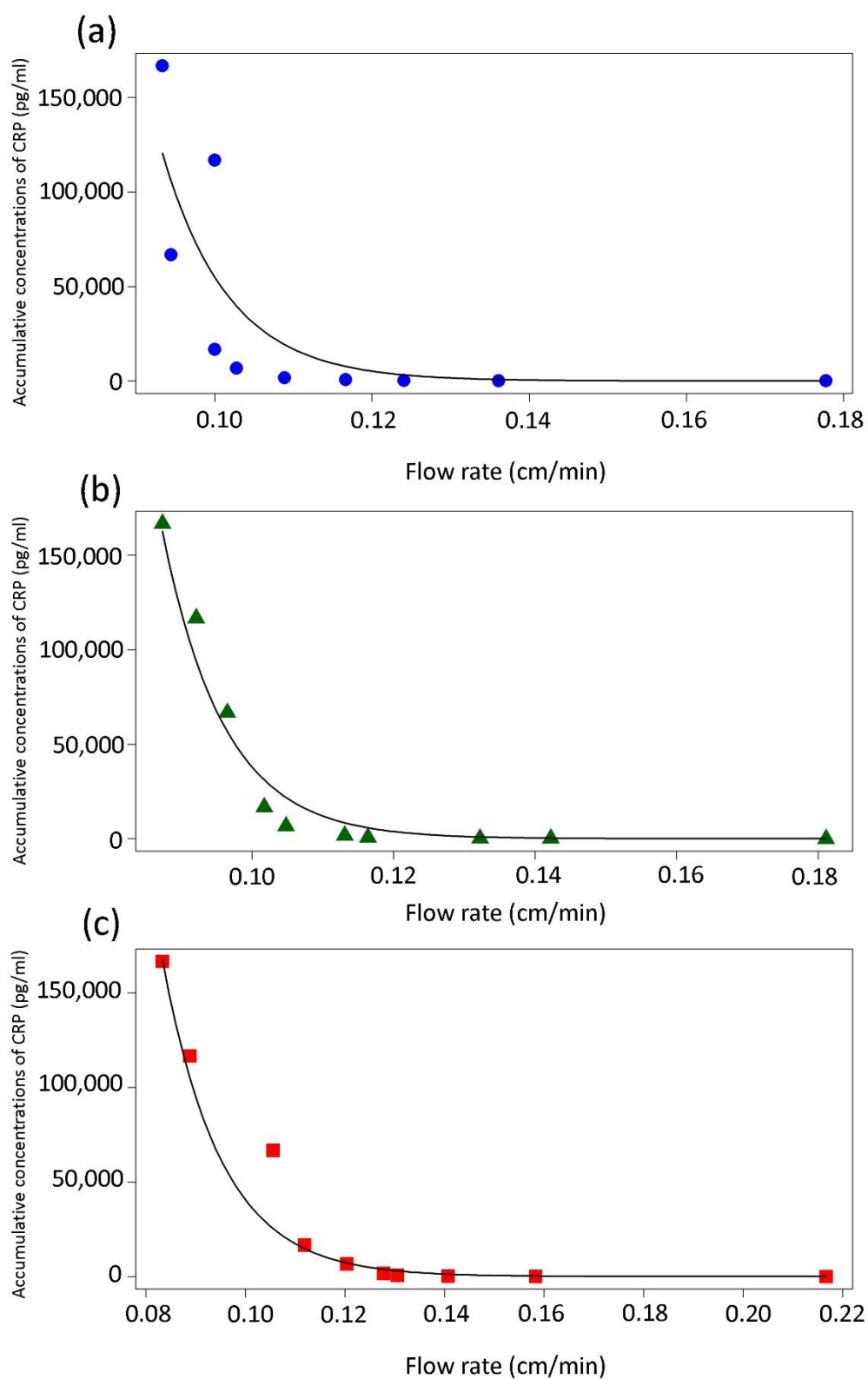


Figure 6. 8 Average flow rate (Black lines show regression fits with data points measured) on the planar electrode for CRP concentrations 10 - 166,660 pg/mL (Nitrocellulose membranes with 200 ng antibodies: (a) blue: blank; (b) green: ZnO; (c) red: ZnO/CuO).

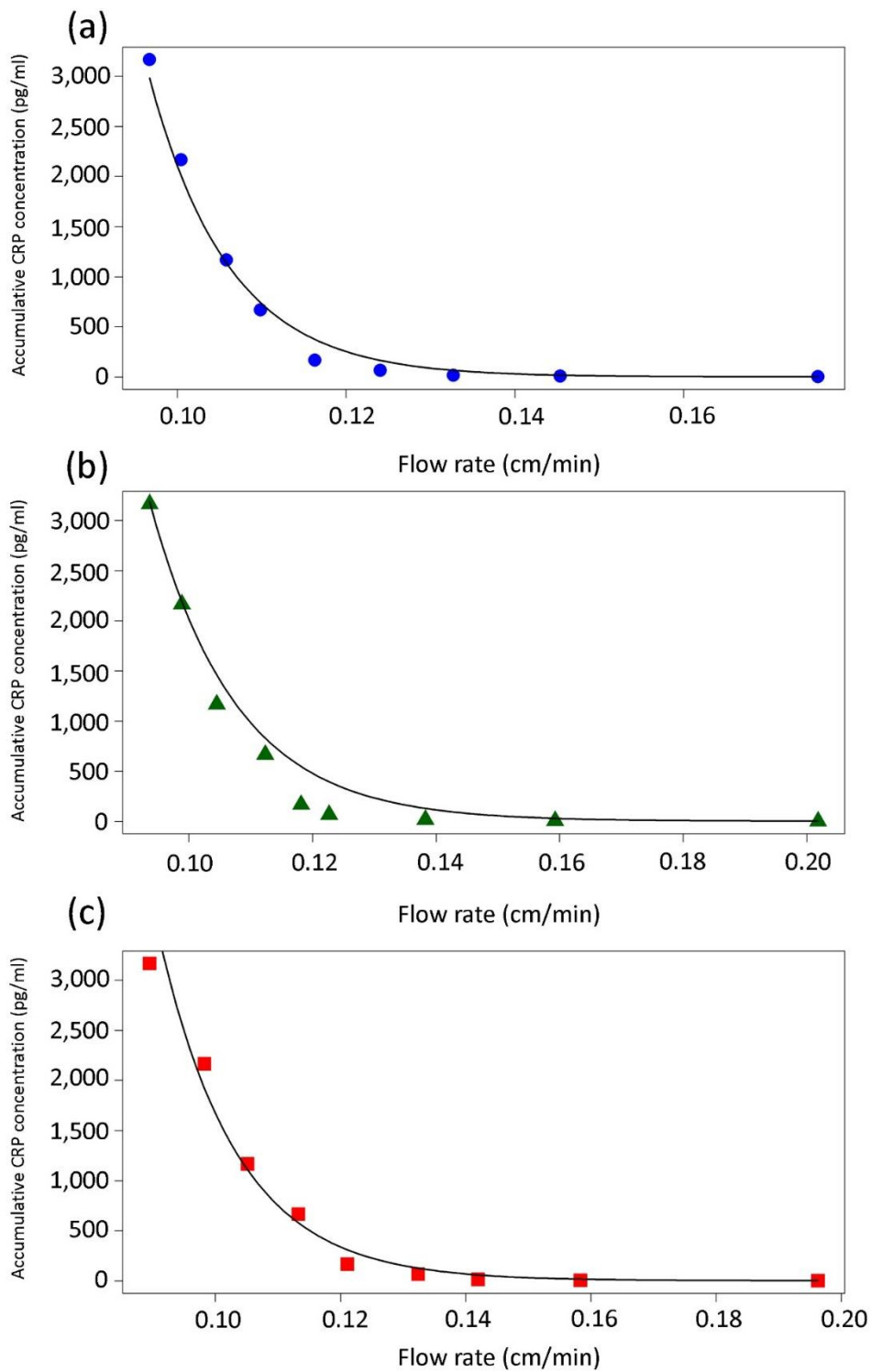


Figure 6. 9 Average flow rate (Black lines show regression fits with data points measured) on the interdigitated electrode with increasing concentrations of CRP, 1 - 3,166 pg/mL. (Nitrocellulose membranes with 200 ng antibodies: (a) blue: blank; (b) green: ZnO; (c) red: ZnO/CuO).

The flow rate can also be increased by increasing the overlap [164] between the sample pad and the nitrocellulose membrane, shown in Figure 6.2. Under the evaluation of the flow system, whether the complex of antibody-CRP can be detected is the key important issue. There are several issues that need to be considered in the future for development of flow-based assay. The biological complex may have the issues of stability and variability, caused by contamination of nature and activity [164]. Commonly, porous materials may fill with sample, but may have little or no active flow in some areas [164].

6.4 Summary

This chapter presents the development of a sensitive biosensor for CRP, based on nanoparticles/nitrocellulose membrane with limit of detection of less than 5 pg/mL. The sensors could provide flow-based measurements for up to 2 hours with additions of up to 100,000 pg/mL accumulative concentrations of sample every 9 minutes on planar electrodes.

For the flow-based sensor, the nanoparticles-based nitrocellulose membranes were assembled with glass fibre as sample pad and nitrocellulose fibre as absorbent pad in a 3D printed holder with an appropriate overlap. The affinity of the flowing system was modelled to prove the accumulative antibody-antigen complex increased during consequent addition of CRP samples.

The membrane with porous structures helps increase surface area and effective contact between antibody and antigen. The nitrocellulose membrane alone, with attached antibody, quickly saturates with addition of CRP samples. However, with the ZnO and ZnO/CuO nanoparticle coated membranes on two different electrodes, the dynamic range of the sensor can be increased. The antibody protein binds strongly and electrostatically to the ZnO and ZnO/CuO (with the electrostatic interactions reducing the process of sample preparation).

It can be found that the different electrodes are suitable for detection of different ranges in concentrations of CRP. The electrodes can be easily substituted without change of flowing assembly system.

This affinity model shows that the flow-based detection is feasible for the concentration of CRP added during the experiment. It can be seen from the experimental data that the sensor membranes do not become saturated.

The impedance change observed for both nano-ZnO and nano-ZnO/CuO membranes was similar for each electrode design. Despite the lower affinity of antibody to CRP on ZnO/CuO membranes, change in the impedance over the duration of the experiments was greater using the nano-ZnO/CuO membrane. This suggests strongly that, although the CuO has a negative effect on the antibody affinity, it has a positive effect on the signal, as shown in the previous chapter and this chapter where the mixture of ZnO and CuO nanoparticles helped enhance the signal.

In the future, an important area of work is to simulate the flow-based system. COMSOL simulation could be used to highlight the electrode features and fluidic wicking pattern of membrane in order to optimise fluid-based continuous detection platform [120]. For manufacture, the overlaps have to be consistent so that the flow dynamics are uniform and avoid the inconsistent flow arising on pad [65]. The optimised blocking agent is important to recognise against the processing speed and mechanical systems [65]. Automation machinery can assemble lateral flow test strips rapidly and accurately [164]. In the next chapter Conclusion, future work will mention manufacture considerations and future application in a little more detail.

Chapter 7

Conclusion

7.1 Key Findings

It is considered that the objectives of this research, as stated in Chapter 1, have been satisfied. The results are promising, with a new, sensitive and rapid immunoassay biosensor, fabricated from nano-particle metal oxide semiconductor materials integrated within a porous structure, for flow-based measurement of a biological target, being demonstrated. The salient points of the study are brought together below.

In Chapter 1 relevant literature was reviewed and each of the elements of the biosensors fabricated and evaluated in the experimental Chapters 3 to 6, was discussed. Comparison of approaches presented in the literature explained the methods adopted this research study. It was concluded that antibody-based impedimetric biosensors can offer high specificity and sensitivity, as well as being adaptable for detection of a wide range of analytes. Zinc oxide/Copper oxide (ZnO/CuO) nanoparticle biosensors showed enhanced performance (sensitivity and limit of detection) relative to sensors without nanostructures. Ultrasonication of the nanoparticles can result in enhanced performance and non-covalent antibody immobilisation could be used to effectively bind antibody on ZnO or ZnO/CuO. Nanoporous materials could be used to increase the sensor surface area and enhance charge screening through nanoconfinement, which affects electron transfer kinetics inside the nanopores.

Chapter 2 summarises the basic principles of non-faradaic impedance spectroscopy, from the literature. In the context of biosensors used in this research study, an approximation of the Debye length was calculated and related to the binding elements on the biosensor. The inclusion of the nanoparticles layers within the biosensor resulted in structure that had greater complexity than that represented by standard the Randles model. In order to create a more realistic representation an empirical approach was used, characterising the composition of each of the different layers of the sensing system: the interfacial surface, the

buffer solution, the nano-ZnO film, PET substrate, the electrodes and substrate. The limitations of the impedance measurement set-up were also defined.

In experimental Chapter 3, the fabrication of ZnO based nano-surfaces was presented. An important part of this chapter was the demonstration of a new colloidal dispersion technique, incorporating sonication, which allow sensor surfaces to be created simply and at low cost on an insulating layer. Raman spectra of the surface indicated the ZnO crystal surfaces was highly ordered and uniform. SEM analysis showed the variations in the roughness of the ZnO nano-surfaces formed from suspensions of various concentrations of ZnO nano-crystals; 1% showed the greatest surface roughness and the optimum biosensor characteristics. Impedance analysis of a biosensor formed from the nanosurfaces on an insulating layer positioned above the electrodes, confirmed that the ZnO surfaces were highly reproducible.

In experimental Chapter 4, to enhance sensitivity, copper oxide (CuO) nanoparticles were mixed with ZnO to form the suspension used to create the sensor surfaces. SEM and AFM images showed variations in the nano-surfaces with various ratios of ZnO to CuO. SEM images demonstrated that the CuO nanocrystals filled the deep voids between ZnO nanoparticles, laying flat on the ZnO nanocrystal and reducing the overall surface area. It was speculated that this was due to the fact that ZnO (n-type) and CuO (p-type) nanoparticles have opposite charges resulting in attraction between the two materials. Using impedance analysis of biosensors targeting CRP, 1:2 ZnO/CuO ratio suspension resulted in the sensor with the best sensitivity, even though the antibody loading was shown to be approximately equivalent on all samples. This suggests that the electrical interaction between ZnO and CuO nano-structures plays an important part in the generation of the enhanced signal. Importantly the new ZnO/CuO nano-surface, resulted in an improvement in biosensor performance compared with the ZnO nano-surface, with a limit of detection of 0.4 ng/mL being calculated for the biosensors formed from a 1:2 ZnO/CuO suspension of nanoparticles compared with 3.3 ng/mL (as shown in **Table 7.1**).

Table 7. 1 Summary of different types of nano-surfaces/nano-membranes

Biosensors with antibody capture	Contact electrodes/ Impedance Analysis	Frequency (Hz)	Experimental detection range (ng/mL)	LOD	Detection time (minutes)
0.5 % ZnO nanosurface (100 ng)	1 mm gap D-shape/ Impedance change	138	1-15	n.a	10
1% ZnO nanosurface (100 ng)				n.a	
1% ZnO nanosurface (200 ng)	1 mm gap D-shape With coverslip on the top/Phase change	138	1-100	3.3 ng/mL	10
1% ZnO: 1% CuO (1:2) nano-surface (200 ng)				0.4 ng/mL	
1% ZnO nanomembrane (200 ng)	1 mm gap D-shape/ Phase change	100	0.1-15	27 pg/mL	10
1% ZnO: 1% CuO (1:2) nanomembrane (200 ng)				16 pg/mL	
1% ZnO nanomembrane (200 ng)	4 mm gap planar electrode/Impedance change	100	0.01 - 366.66	2.64 pg/mL	9
1% ZnO: 1% CuO (1:2) nanomembrane (200 ng)				0.47 pg/mL	
1% ZnO nanomembrane (200 ng)	Interdigitated electrode/Impedance change	100	0.001 - 3.166	0.02 pg/mL	9
1% ZnO: 1% CuO (1:2) nanomembrane (200 ng)				4.10 pg/mL	

Chapter 5 analyses the benefits of the transition from a 2D to 3D sensor surface. Both nano-ZnO and nano-ZnO/CuO nitrocellulose membrane biosensors were evaluated. The colloidal sonication technique was again utilised and energy-dispersive spectroscopy (EDS) analysis showed that the loading of ZnO and CuO nanoparticles within the membrane remained in proportion to their concentrations in the original colloidal suspension. The sonication force was critical to assist the nanoparticles to be embedded into the lower layer of the membrane and enhanced performance, with the nano-ZnO and nano-ZnO/CuO nitrocellulose membranes showing an approximate 3 and 2-fold increase respectively in impedance compared with the non-sonicated membranes. The nano-ZnO and nano-ZnO/CuO nitrocellulose membrane-based biosensors (with sonication) showed limits of detection of 27 and 16 pg/mL respectively as presented in **Table 7.1**.

In Chapter 6 the progression to a flow-based measurement is described. The nanoparticles-based nitrocellulose membranes were assembled with glass fibre as the sample pad and nitrocellulose fibre as the absorbent pad in a 3D printed holder. A limit of detection of less than 5 pg/mL was demonstrated (see **Table 7.1**) with continuous addition of sample every 9 minutes over approximately a 2 hour testing period. Both ZnO and ZnO/CuO nanoparticle membranes were evaluated with the nano-ZnO/CuO membrane showing a broader detection range compared with nano-ZnO membrane. An affinity model concurred with the experimental data showing that for the concentration of CRP added during the experiments, the sensor membranes do not become saturated. The interdigitated electrode, with higher capacitance, showed larger impedance changes relative to the planar electrodes, but with a reduced dynamic range.

A summary of comparison of sensitivity with limit of detection on nano-surfaces and nano-membranes on electrodes is shown in **Table 7.1**.

The key attributes of the non-faradaic sensor systems investigated in this research work are the fact that the sensor preparation method is low-cost and simple, but biosensors with low limits of detection are delivered. The sensors can also be readily constructed to operate as a sensor permitting detection of analyte over an extended period with repeated addition of the sample by flow-based methodology. This work presented in this thesis has the potential for development in to a highly sensitive detection system for point-of-care use, particularly where flow-based measurement over a defined period is preferable. Areas of improvement to the system to work towards this goal are provided in the next section.

At the time of submission of this thesis, three related research papers have been published, one has been submitted for review and a further is in preparation.

7.2 Suggestions for Future Work

7.2.1 Targets

In this research C-reactive protein (CRP) was used as the target analyte in order to evaluate and compare the various sensor constructions. If CRP detection was the proposed future application, then additional optimisation of the sensor design, including quantity and distribution of antibody, would be required. However, the sensors could be adapted for a large variety of targets, including other proteins or nucleic acids. The system can easily be adapted for detection of other biomarkers due to principle of operation in which an antibody/antigen interaction results in a change in the capacitance at the sensor surface interface which is measured non-faradaic impedance spectroscopy. A second important area of investigation relates to non-specific binding in order to evaluate the selectivity of the system. For example, if a human sweat sample is proposed, the influence of the complex mixture of proteins, hormones, steroids and other molecules must be considered to establish how the sensors react with non-specific binding.

7.2.2 Fabrication and Design

Further investigation of the active region of the sensor could result in improved performance. It is well established that binding interactions that occur within a Debye length of electrode/electrolyte interface result in a larger change in the electrical double layer capacitance. Investigation of shorter binding partners may be an option. The dimensions, charge density and permittivity of electrodes will change electrical double layer capacitance, which needs to be considered.

Nitrocellulose membranes can also be replaced by other membranes, for example poly(vinylidene difluoride (PVDF), or nylon membranes with modified surface [159] which should result in improved performance. One limitation is that the mechanism of the electrical double layer within the porous membranes and the impact of the biological binding is unclear. Further empirical modelling of the sensor may help to gain greater understanding of the various components within the system.

It may be interesting to design a miniature system, and for this the size of electrodes and nanoparticles layers must be improved. Peng *et al.* fabricated a graphene-like hexagonal zinc oxide monolayer (g-ZnO) which showed good performance [168]. It is worth investigating the electrical properties of monolayer and also biological bindings on surface chemistry, but this would be constituting another PhD in itself.

The assembly of the substrate and electrodes function well for this research. The sensors presented in this thesis are based on insulating materials above the electrodes, which had benefits of ease of use and the reusability of the electrodes. However, the majority of the electrical field was dropped across the insulator and the gap between the electrodes. Investigation of alternative arrangements would be interesting, including nanoparticles-based substrates (insulating material) which could be embedded between the two electrodes [49], in order to increase the useful area of electrical field.

7.2.3 Antibody Immobilisation

To improve the sensitivity of sensor system, antibody affinities are an important aspect to research. A number of factors could be taken in to account. For example, orientation-controlled antibodies have low equilibrium dissociation constants [114] and three-dimensional substrates offer increased surface area for antibody binding, which can minimize steric hindrance that may prevent antigen capture [29]. However, these improvements must be weighed up against the importance of keeping the biosensor low cost particularly as currently, low concentrations (5 ng/ μL) of antibody are used with small volumes (40 μL). The optimised concentration of antibody can be established in the future according to the re-scaled sensing area.

7.2.4 Electrical Impedance Spectroscopy

Due to the fact that the capacitance of electrical double layer is small, the amplification approach of impedimetric signals is potentially beneficial [58]. The minimisation of noise contribution is essential to improve the system. Importantly the impedance analysis system must provide a highly stable impedance magnitude and/or phase change output across the

frequency range used. The coax connection is a significant parasitic contributor [117], resulting a more resistance behaviour at low frequency [115]. In order to remove parasitic capacitances of coax or BNC cables, an open calibration can be performed in the future [115]. Parasitic environmental effects can be minimised by reducing the length of cable or directly connecting the sensor electrode PCB to the BNC output [117].

7.2.5 Future Applications

In addition to the improvements discussed in the sections above, for the ideas presented in this thesis to have future commercial applications in, for example, in clinic settings, a number of steps are needed. The system needs to be optimised for the chosen target and careful control of the sensor manufacturing processes will be required to obtain good repeatability. The fluidic system will require re-designing to ensure consistent flow through the active sensor regions. Modelling will be important to validate results and ensure reliability of data. Substantial testing of the system with real samples and in clinical settings will be an essential step towards a useful, practical device. Although this is a long process, I am an advocate for the technology and hope one day that it will be used in a clinical application for real-time monitoring for diagnosis and to support treatment of disease.

References

- 1 Shanmugam NR, Muthukumar S, Prasad S. A review on ZnO-based electrical biosensors for cardiac biomarker detection. *Futur Sci OA*. 2017 Jun;3(4):FSO196-FSO196.
- 2 Justino CIL, Duarte AC, Rocha-Santos TAP. Critical overview on the application of sensors and biosensors for clinical analysis. *TrAC Trends Anal Chem*. 2016 Dec;85:36–60.
- 3 Bhalla N, Jolly P, Formisano N, Estrela P. Introduction to biosensors. *Essays Biochem*. 2016 Jun;60(1):1–8.
- 4 Mozaffari SA, Rahmanian R, Abedi M, Amoli HS. Urea impedimetric biosensor based on reactive RF magnetron sputtered zinc oxide nanoporous transducer. *Electrochim Acta*. 2014 Mar;146:538–47.
- 5 Matsumoto A, Miyahara Y. Current and emerging challenges of field effect transistor based bio-sensing. *Nanoscale*. 2013 Sep;5:10702.
- 6 Janovák L, Dékány I, Sebok D. The theoretical concept of polarization reflectometric interference spectroscopy (PRIFS): An optical method to monitor molecule adsorption and nanoparticle adhesion on the surface of thin films. *Photonics*. 2019;6(3). DOI: 10.3390/PHOTONICS6030076
- 7 Gu BX, Xu CX, Zhu GP, Liu SQ, Chen LY, Li XS. Tyrosinase immobilization on ZnO nanorods for phenol detection. *J Phys Chem B*. 2009;113(1):377–81.
- 8 Ibupoto ZH, Ali SM, Khun K, Chey CO, Nur O, Willander M. ZnO Nanorods Based Enzymatic Biosensor for Selective Determination of Penicillin. *Biosens*. 2011;1(4):153–63.
- 9 Ito Y, Okuda-Shimazaki J, Tsugawa W, Loew N, Shitanda I, Lin C-E, et al. Third generation impedimetric sensor employing direct electron transfer type glucose dehydrogenase. *Biosens Bioelectron*. 2019 Mar;129:189–97.
- 10 Han W, He H, Zhang L, Dong C, Zeng H, Dai Y, et al. A Self-Powered Wearable Noninvasive Electronic-Skin for Perspiration Analysis Based on Piezo-Biosensing Unit Matrix of Enzyme/ZnO Nanoarrays. *ACS Appl Mater Interfaces*. 2017;9(35):29526–37.

- 11 Yew C-HT, Azari P, Choi JR, Li F, Pingguan-Murphy B. Electrospin-coating of nitrocellulose membrane enhances sensitivity in nucleic acid-based lateral flow assay. *Anal Chim Acta*. 2018 Jun;1009:81–8.
- 12 Cao X, Cao X, Guo H, Li T, Jie Y, Wang N, et al. Piezotronic Effect Enhanced Label-Free Detection of DNA Using a Schottky-Contacted ZnO Nanowire Biosensor. *ACS Nano*. 2016;10(8):8038–44.
- 13 Chu C-H, Sarangadharan I, Regmi A, Chen Y-W, Hsu C-P, Chang W-H, et al. Beyond the Debye length in high ionic strength solution: direct protein detection with field-effect transistors (FETs) in human serum. *Sci Rep*. 2017;7(1):5256.
- 14 Lin K-C, Jagannath B, Muthukumar S, Prasad S. Sub-picomolar label-free detection of thrombin using electrochemical impedance spectroscopy of aptamer-functionalized MoS₂. *Analyst*. 2017;142(15):2770–80.
- 15 Singh NK, Thungon PD, Estrela P, Goswami P. Development of an aptamer-based field effect transistor biosensor for quantitative detection of *Plasmodium falciparum* glutamate dehydrogenase in serum samples. *Biosens Bioelectron*. 2019;123:30–5.
- 16 Shanmugam NR, Muthukumar S, Prasad S. Ultrasensitive and low-volume point-of-care diagnostics on flexible strips - a study with cardiac troponin biomarkers. *Sci Rep*. 2016;6. DOI: Artn 3342310.1038/Srep33423
- 17 Sharma A, Hong S, Singh R, Jang J. Single-walled carbon nanotube based transparent immunosensor for detection of a prostate cancer biomarker osteopontin. *Anal Chim Acta*. 2015 Apr;869:68–73.
- 18 Munje RD, Muthukumar S, Selvam AP, Prasad S. Flexible nanoporous tunable electrical double layer biosensors for sweat diagnostics. *Sci Rep*. 2015;5. DOI: Artn 1458610.1038/Srep14586
- 19 Shen YC, Yang CH, Chen SW, Wu SH, Yang TL, Huang JJ. IGZO thin film transistor biosensors functionalized with ZnO nanorods and antibodies. *Biosens Bioelectron*. 2014;54:306–10.
- 20 Selvam AP, Vattipalli KM, Prasad S. Design of a High Sensitive Non-Faradaic Impedimetric Sensor. 2012 Annu Int Conf Ieee Eng Med Biol Soc. 2012;3251–4.
- 21 Malkoc A, Probst D, Lin C, Khanwalker M, Beck C, Cook CB, et al. Enhancing Glycemic Control via Detection of Insulin Using Electrochemical Impedance Spectroscopy. *J Diabetes Sci Technol*. 2017 Sep;11(5):930–5.

- 22 Syahir A, Usui K, Tomizaki K-Y, Kajikawa K, Mihara H. Label and Label-Free Detection Techniques for Protein Microarrays. *Microarrays (Basel, Switzerland)*. 2015 Apr;4(2):228–44.
- 23 Poyton MF, Cremer PS. Electrophoretic measurements of lipid charges in supported bilayers. *Anal Chem*. 2013 Nov;85(22):10803–11.
- 24 Joung H-A, Oh YK, Kim M-G. An automatic enzyme immunoassay based on a chemiluminescent lateral flow immunosensor. *Biosens Bioelectron*. 2014;53:330–5.
- 25 Oh J, Joung H-A, Han HS, Kim JK, Kim M-G. A hook effect-free immunochromatographic assay (HEF-ICA) for measuring the C-reactive protein concentration in one drop of human serum. *Theranostics*. 2018;8(12):3189–97.
- 26 Yen Y-K, Lai Y-C, Hong W-T, Pheanpanitporn Y, Chen C-S, Huang L-S. Electrical detection of C-reactive protein using a single free-standing, thermally controlled piezoresistive microcantilever for highly reproducible and accurate measurements. *Sensors (Basel)*. 2013 Jul;13(8):9653–68.
- 27 Noi K, Iijima M, Kuroda S, Ogi H. Ultrahigh-sensitive wireless QCM with bio-nanocapsules. *Sensors Actuators B Chem*. 2019;293:59–62.
- 28 Choi HW, Sakata Y, Kurihara Y, Ooya T, Takeuchi T. Label-free detection of C-reactive protein using reflectometric interference spectroscopy-based sensing system. *Anal Chim Acta*. 2012 May;728:64–8.
- 29 Welch NG, Scoble JA, Muir BW, Pigram PJ. Orientation and characterization of immobilized antibodies for improved immunoassays (Review). *Biointerphases*. 2017;12 2:02D301.
- 30 Trilling AK, Beekwilder J, Zuillhof H. Antibody orientation on biosensor surfaces: a minireview. *Analyst*. 2013;138(6):1619–27.
- 31 Shafiee H, Asghar W, Inci F, Yuksekkaya M, Jahangir M, Zhang MH, et al. Paper and Flexible Substrates as Materials for Biosensing Platforms to Detect Multiple Biotargets. *Sci Rep*. 2015 Mar;5:8719.
- 32 Berggren C, Bjarnason B, Johansson G. An immunological Interleukine-6 capacitive biosensor using perturbation with a potentiostatic step. *Biosens Bioelectron*. 1998;13(10):1061–8.
- 33 Adamson TL, Eusebio FA, Cook CB, LaBelle JT. The promise of electrochemical impedance spectroscopy as novel technology for the management of patients with diabetes mellitus.

- Analyst. 2012;137(18):4179–87.
- 34 Hadzhieva M, Pashov AD, Kaveri S V, Lacroix-Desmazes S, Mouquet H, Dimitrov JD. Impact of Antigen Density on the Binding Mechanism of IgG Antibodies. *Sci Rep.* 2017;7:3767.
- 35 Wang C, Wang C, Feng B. Research progress on site-oriented and three-dimensional immobilization of protein. *Mol Biol (New York).* 2015;49(1):1–20.
- 36 Ghisellini P, Caiazza M, Alessandrini A, Eggenhöfner R, Vassalli M, Facci P. Direct electrical control of IgG conformation and functional activity at surfaces. *Sci Rep.* 2016 Nov;6:37779.
- 37 Justino CIL, Freitas AC, Amaral JP, Rocha-Santos TAP, Cardoso S, Duarte AC. Disposable immunosensors for C-reactive protein based on carbon nanotubes field effect transistors. *Talanta.* 2013 Apr;108:165–70.
- 38 Pradhan D, Niroui F, Leung KT. High-performance, flexible enzymatic glucose biosensor based on ZnO nanowires supported on a gold-coated polyester substrate. *ACS Appl Mater Interfaces.* 2010;2(8):2409–12.
- 39 Carvalho JT, Dubceac V, Grey P, Cunha I, Fortunato E, Martins R, et al. Fully Printed Zinc Oxide Electrolyte-Gated Transistors on Paper. *Nanomaterials.* 2019;9(2). DOI: 10.3390/nano9020169
- 40 Park HY, Go HY, Kalme S, Mane RS, Han SH, Yoon MY. Protective antigen detection using horizontally stacked hexagonal ZnO platelets. *Anal Chem.* 2009;81(11):4280–4.
- 41 Tanak AS, Jagannath B, Tamrakar Y, Muthukumar S, Prasad S. Non-faradaic electrochemical impedimetric profiling of procalcitonin and C-reactive protein as a dual marker biosensor for early sepsis detection. *Anal Chim Acta X.* 2019;3:100029.
- 42 Selvam AP, Muthukumar S, Kamakoti V, Prasad S. A wearable biochemical sensor for monitoring alcohol consumption lifestyle through Ethyl glucuronide (EtG) detection in human sweat. *Sci Rep.* 2016;6. DOI: Artn 2311110.1038/Srep23111
- 43 Ahmad M, Iqbal M, Kiely J, Luxton R, Jabeen M. Low temperature hydrothermal synthesis of ZnO nanowires for nanogenerator: Effect of gold electrode on the output voltage of nanogenerator. *Indian J Eng Mater Sci.* 2014 Dec;21(6):672–6.
- 44 Ahmad M, Iqbal MA, Kiely J, Luxton R, Jabeen M. Enhanced output voltage generation via ZnO nanowires (50 nm): Effect of diameter thinning on voltage enhancement. *J Phys Chem Solids.* 2017 May;104:281–5.

- 45 Bandodkar AJ, Jeang WJ, Ghaffari R, Rogers JA. Wearable Sensors for Biochemical Sweat Analysis. *Annu Rev Anal Chem.* 2019;12(1):1–22.
- 46 Wu R, Zhou S, Chen T, Li J, Shen H, Chai Y, et al. Quantitative and rapid detection of C-reactive protein using quantum dot-based lateral flow test strip. *Anal Chim Acta.* 2018 May;1008:1–7.
- 47 Cai Y, Kang K, Liu Y, Wang Y, He X. Development of a lateral flow immunoassay of C-reactive protein detection based on red fluorescent nanoparticles. *Anal Biochem.* 2018 Sep;556:129–35.
- 48 Hu J, Zhang Z-L, Wen C-Y, Tang M, Wu L-L, Liu C, et al. Sensitive and Quantitative Detection of C-Reaction Protein Based on Immunofluorescent Nanospheres Coupled with Lateral Flow Test Strip. *Anal Chem.* 2016 Jun;88(12):6577–84.
- 49 Kinnamon D, Ghanta R, Lin K-C, Muthukumar S, Prasad S. Portable biosensor for monitoring cortisol in low-volume perspired human sweat. *Sci Rep.* 2017;7(1):13312.
- 50 Munje RD, Muthukumar S, Prasad S. Lancet-free and label-free diagnostics of glucose in sweat using Zinc Oxide based flexible bioelectronics. *Sensors and Actuators B-Chemical.* 2017;238:482–90.
- 51 Ibupoto ZH, Jamal N, Khun K, Willander M. Development of a disposable potentiometric antibody immobilized ZnO nanotubes based sensor for the detection of C-reactive protein. *Sensors Actuators B Chem.* 2012 May;166–167:809–14.
- 52 Bryan T, Luo X, Bueno PR, Davis JJ. An optimised electrochemical biosensor for the label-free detection of C-reactive protein in blood. *Biosens Bioelectron.* 2013 Jan;39(1):94–8.
- 53 Okemefuna AI, Nan R, Miller A, Gor J, Perkins SJ. Complement factor H binds at two independent sites to C-reactive protein in acute phase concentrations. *J Biol Chem.* 2010 Jan;285(2):1053–65.
- 54 Zhao Z, Lei W, Zhang X, Wang B, Jiang H. ZnO-based amperometric enzyme biosensors. *Sensors (Basel).* 2010;10(2):1216–31.
- 55 Zhang L, Xiao X, Xu Y, Chen D, Chen J, Ma Y, et al. Electrochemical assay for continuous monitoring of dynamic DNA methylation process. *Biosens Bioelectron.* 2018 Feb;100:184–91.
- 56 Batra N, Tomar M, Gupta V. Realization of an efficient cholesterol biosensor using ZnO nanostructured thin film. *Analyst.* 2012;137(24):5854–9.

- 57 Yagati AK, Pyun JC, Min J, Cho S. Label-free and direct detection of C-reactive protein using reduced graphene oxide-nanoparticle hybrid impedimetric sensor. *Bioelectrochemistry*. 2016;107:37–44.
- 58 Lisdat F, Schäfer D. The use of electrochemical impedance spectroscopy for biosensing. *Anal Bioanal Chem*. 2008;391(5):1555.
- 59 Assaifan AK, Lloyd JS, Samavat S, Deganello D, Stanton RJ, Teng KS. Nanotextured Surface on Flexographic Printed ZnO Thin Films for Low-Cost Non-Faradaic Biosensors. *ACS Appl Mater Interfaces*. 2016 Dec;8(49):33802–10.
- 60 Qureshi A, Niazi JH, Kallempudi S, Gurbuz Y. Label-free capacitive biosensor for sensitive detection of multiple biomarkers using gold interdigitated capacitor arrays. *Biosens Bioelectron*. 2010 Jun;25(10):2318–23.
- 61 Santos A, Jason J D and, Paulo R B. Fundamentals and Applications of Impedimetric and Redox Capacitive Biosensors. *J Anal Bioanal Tech*. 2014 Jan;S7:016.
- 62 Bhide A, Muthukumar S, Prasad S. CLASP (Continuous lifestyle awareness through sweat platform): A novel sensor for simultaneous detection of alcohol and glucose from passive perspired sweat. *Biosens Bioelectron*. 2018 Oct;117:537–45.
- 63 Dong M, Wu J, Ma Z, Peretz-Soroka H, Zhang M, Komenda P, et al. Rapid and Low-Cost CRP Measurement by Integrating a Paper-Based Microfluidic Immunoassay with Smartphone (CRP-Chip). *Sensors (Basel)*. 2017 Apr;17(4):684.
- 64 Bothara M, Venkatraman V, Reddy RKK, Barrett T, Carruthers J, Prasad S. Nanomonitors: electrical immunoassays for protein biomarker profiling. *Nanomedicine*. 2008 Aug;3(4):423–36.
- 65 EMD Millipore Corporation, Billerica M. Rapid Lateral Flow Test Strips Considerations for Product Development. Brochure, Print USA. 2013;1–31.
- 66 Ragavendar MS, Anmol CM. A mathematical model to predict the optimal test line location and sample volume for lateral flow immunoassays. 2012 Annual International Conference of the IEEE Engineering in Medicine and Biology Society. 2012; pp 2408–11.
- 67 Li, H. and Han, D. and Pauletti, G. M. and Steckl AJ. Blood coagulation screening using a paper-based microfluidic lateral flow device. *Lab Chip*. 2014;14(20):4035–41.

- 68 Oh YK, Joung H-A, Han HS, Suk H-J, Kim M-G. A three-line lateral flow assay strip for the measurement of C-reactive protein covering a broad physiological concentration range in human sera. *Biosens Bioelectron.* 2014 Nov;61:285–9.
- 69 Hegener MA, Li H, Han D, Steckl AJ, Pauletti GM. Point-of-care coagulation monitoring: first clinical experience using a paper-based lateral flow diagnostic device. *Biomed Microdevices.* 2017;19(3):64.
- 70 Chin CD, Linder V, Sia SK. Commercialization of microfluidic point-of-care diagnostic devices. *Lab Chip.* 2012;12(12):2118–34.
- 71 Carrell C, Kava A, Nguyen M, Menger R, Munshi Z, Call Z, et al. Beyond the lateral flow assay: A review of paper-based microfluidics. *Microelectron Eng.* 2019 Feb;206:45–54.
- 72 Wang ZL. From nanogenerators to piezotronics-A decade-long study of ZnO nanostructures. *Mrs Bull.* 2012;37(9):814–27.
- 73 Janotti A, Van de Walle CG. Fundamentals of zinc oxide as a semiconductor. *Reports Prog Phys.* 2009;72(12). DOI: Artn 12650110.1088/0034-4885/72/12/126501
- 74 Meyer BK, Polity A, Reppin D, Becker M, Hering P, Klar PJ, et al. Binary copper oxide semiconductors: From materials towards devices. *Phys status solidi.* 2012 Aug;249(8):1487–509.
- 75 Vuong NM, Chinh ND, Huy BT, Lee Y-I. CuO-Decorated ZnO Hierarchical Nanostructures as Efficient and Established Sensing Materials for H₂S Gas Sensors. *Sci Rep.* 2016 May;6:26736.
- 76 Todorova-Balvay D, Pitiot O, Bourhim M, Srikrishnan T, Vijayalakshmi M. Immobilized metal-ion affinity chromatography of human antibodies and their proteolytic fragments. *J Chromatogr B.* 2004;808(1):57–62.
- 77 Widiarti N, Sae JK, Wahyuni S. Synthesis CuO-ZnO nanocomposite and its application as an antibacterial agent. *IOP Conf Ser Mater Sci Eng.* 2017;172(1):012036.
- 78 Zhou Y, Wang L, Ye ZZ, Zhao MG, Huang JY. Synthesis of ZnO micro-pompons by soft template-directed wet chemical method and their application in electrochemical biosensors. *Electrochim Acta.* 2014;115:277–82.
- 79 Sugunan A, Warad HC, Boman M, Dutta J. Zinc oxide nanowires in chemical bath on seeded substrates: Role of hexamine. *J Sol-Gel Sci Technol.* 2006;39(1):49–56.

- 80 Ahmad R, Tripathy N, Hahn YB. Wide linear-range detecting high sensitivity cholesterol biosensors based on aspect-ratio controlled ZnO nanorods grown on silver electrodes. *Sensors and Actuators B-Chemical*. 2012;169:382–6.
- 81 Chang C-J, Lee Y-H, Dai C-A, Hsiao C-C, Chen S-H, Nurmalasari NPD, et al. A large area bimaterial sheet of piezoelectric nanogenerators for energy harvesting: Effect of RF sputtering on ZnO nanorod. *Microelectron Eng*. 2011 Aug;88(8):2236–41.
- 82 Zhao MG, Zhou Y, Cai B, Ma Y, Cai H, Ye ZZ, et al. The application of porous ZnO 3D framework to assemble enzyme for rapid and ultrahigh sensitive biosensors. *Ceram Int*. 2013;39(8):9319–23.
- 83 Yang K, She GW, Wang H, Ou XM, Zhang XH, Lee CS, et al. ZnO Nanotube Arrays as Biosensors for Glucose. *J Phys Chem C*. 2009;113(47):20169–72.
- 84 Roza L, Rahman MYA, Umar AA, Salleh MM. Direct growth of oriented ZnO nanotubes by self-selective etching at lower temperature for photo-electrochemical (PEC) solar cell application. *J Alloys Compd*. 2015;618:153–8.
- 85 Yang RS, Qin Y, Dai LM, Wang ZL. Power generation with laterally packaged piezoelectric fine wires. *Nat Nanotechnol*. 2009;4(1):34–9.
- 86 Batra N, Tomar M, Gupta V. ZnO–CuO composite matrix based reagentless biosensor for detection of total cholesterol. *Biosens Bioelectron*. 2015 May;67:263–71.
- 87 Zheng X, Sun YH, Yan XQ, Chen X, Bai ZM, Lin P, et al. Tunable channel width of a UV-gate field effect transistor based on ZnO micro-nano wire. *Rsc Adv*. 2014;4(35):18378–81.
- 88 Cao X, Ning W, Li LD, Guo L. Synthesis and characterization of waxberry-like microstructures ZnO for biosensors. *Sensors and Actuators B-Chemical*. 2008;129(1):268–73.
- 89 Zhao M, Huang J, Zhou Y, Chen Q, Pan X, He H, et al. A single mesoporous ZnO/Chitosan hybrid nanostructure for a novel free nanoprobe type biosensor. *Biosens Bioelectron*. 2013;43(0):226–30.
- 90 Jeyarani WJ, Tenkyong T, Bachan N, Kumar DA, Shyla JM. An investigation on the tuning effect of glucose-capping on the size and bandgap of CuO nanoparticles. *Adv Powder Technol*. 2016 Mar;27(2):338–46.
- 91 Sanguino P, Monteiro T, Bhattacharyya SR, Dias CJ, Igreja R, Franco R. ZnO nanorods as

- immobilization layers for interdigitated capacitive immunosensors. *Sensors and Actuators B-Chemical*. 2014;204:211–7.
- 92 Anusha JR, Kim HJ, Fleming AT, Das SJ, Yu KH, Kim BC, et al. Simple fabrication of ZnO/Pt/chitosan electrode for enzymatic glucose biosensor. *Sensors and Actuators B-Chemical*. 2014;202:827–33.
- 93 Yang Z, Zong X, Ye Z, Zhao B, Wang Q, Wang P. The application of complex multiple forklike ZnO nanostructures to rapid and ultrahigh sensitive hydrogen peroxide biosensors. *Biomaterials*. 2010;31(29):7534–41.
- 94 Chung SJ, Leonard JP, Nettleship I, Lee JK, Soong Y, Martello DV, et al. Characterization of ZnO nanoparticle suspension in water: Effectiveness of ultrasonic dispersion. *Powder Technol*. 2009 Aug;194(1–2):75–80.
- 95 Chen C, Li Q, Nie M, Lin H, Li Y, Wu H, et al. An efficient room-temperature route to uniform ZnO nanorods with an ionic liquid. *Mater Res Bull*. 2011 Jun;46(6):888–93.
- 96 Lee KS, Kim CH, Jeong SW, Song Y, Bae NH, Lee SJ, et al. Ultrasonic fabrication of flexible antibacterial ZnO nanopillar array film. *Colloids Surfaces B Biointerfaces*. 2018 Oct;170:172–8.
- 97 Zhang YC, Yang T, Zhou N, Zhang W, Jiao K. Nano Au/TiO₂ hollow microsphere membranes for the improved sensitivity of detecting specific DNA sequences related to transgenes in transgenic plants. *Sci China Ser B-Chemistry*. 2008;51(11):1066–73.
- 98 Kivirand K, Mart M, Toonika R. Challenges and Applications of Impedance-Based Biosensors in Water Analysis. In: Min M, editor. Rijeka: IntechOpen; 2019; p Ch. 5.
- 99 Stevenson H, Radha Shanmugam N, Paneer Selvam A, Prasad S. The Anatomy of a Nonfaradaic Electrochemical Biosensor. *SLAS Technol Transl Life Sci Innov*. 2017 Nov;23(1):5–15.
- 100 Biesheuvel M, Dykstra J. The difference between Faradaic and Nonfaradaic processes in Electrochemistry. *arXiv.org*; 2018. DOI: <https://arxiv.org/abs/1809.02930>
- 101 Jacobs M, Muthukumar S, Selvam AP, Craven JE, Prasad S. Ultra-sensitive electrical immunoassay biosensors using nanotextured zinc oxide thin films on printed circuit board platforms. *Biosens Bioelectron*. 2014;55:7–13.
- 102 Park JS, Kim HJ, Lee J-H, Park JH, Kim J, Hwang KS, et al. Amyloid Beta Detection by Faradaic Electrochemical Impedance Spectroscopy Using Interdigitated Microelectrodes. *Sensors*

- (Basel). 2018 Feb;18(2):426.
- 103 Selvam P, Vattipalli A, Mohan K, Prasad S. Design of a high sensitive non-faradaic impedimetric sensor. Annual International Conference of the IEEE Engineering in Medicine and Biology Society. 2012; pp 3251–4.
- 104 Kao KC. Dielectric Phenomena in Solids. Elsevier Science; 2004. Available from: <https://books.google.co.uk/books?id=MxvRST5PT1cC>
- 105 Zhang G. Simulating the Electrical Double Layer Capacitance. COMSOL Conference 2010 Boston Simulating. 2010; p Excerpt from the Proceedings.
- 106 Dak P, Alam MA. Non-Faradaic Impedance Model of a Biochemical Sensor [Internet]. nanoHUB. 2015 DOI: doi:/10.4231/D3PR7MV7M
- 107 Shanmugam NR, Muthukumar S, Selvam AP, Prasad S. Electrochemical nanostructured ZnO biosensor for ultrasensitive detection of cardiac troponin-T. Nanomedicine. 2016 May;11(11):1345–58.
- 108 Palazzo G, De Tullio D, Magliulo M, Mallardi A, Intranuovo F, Mulla MY, et al. Detection Beyond Debye's Length with an Electrolyte-Gated Organic Field-Effect Transistor. Adv Mater. 2015;27(5):911–6.
- 109 Arnaut L, Formosinho S, Burrows H. 9 - Elementary Reactions in Solution. In: Arnaut L, Formosinho S, Burrows HBT-CK, editors. Amsterdam: Elsevier; 2007; pp 223–50.
- 110 Hatsuki R, Yujiro F, Yamamoto T. Direct measurement of electric double layer in a nanochannel by electrical impedance spectroscopy. Microfluid Nanofluidics. 2013;14(6):983–8.
- 111 Salmanzadeh A, Sano MB, Gallo-Villanueva RC, Roberts PC, Schmelz EM, Davalos R V. Investigating dielectric properties of different stages of syngeneic murine ovarian cancer cells. Biomicrofluidics. 2013 Jan;7(1):11809.
- 112 Zaccari I. Multiplexed label-free electronic biosensors for clinical diagnostics, PhD thesis, University of Leeds. 2013
- 113 Thiele JR, Habersberger J, Braig D, Schmidt Y, Goerendt K, Maurer V, et al. Dissociation of Pentameric to Monomeric C-Reactive Protein Localizes and Aggravates Inflammation. Circulation. 2014;130(1):35–50.
- 114 Tajima N, Takai M, Ishihara K. Significance of Antibody Orientation Unraveled: Well-Oriented

- Antibodies Recorded High Binding Affinity. *Anal Chem.* 2011 Mar;83(6):1969–76.
- 115 Couniot N, Afzalian A, Overstraeten-Schlögel N Van, Francis LA, Flandre D. Capacitive biosensing of bacterial cells: Analytical model and numerical simulations. *Sensors Actuators B Chem.* 2015;211:428–38.
- 116 Selvam AP, Wangzhou A, Jacobs M, Wu T, Mohan C, Prasad S. Development and validation of an impedance biosensor for point-of-care detection of vascular cell adhesion molecule-1 toward lupus diagnostics. *Futur Sci OA.* 2017 Jul;3(3):FSO224.
- 117 Eveness J, Cao L, Kiely J, Luxton R. Equivalent circuit model of a non-faradaic impedimetric ZnO nano-crystal biosensor. *J Electroanal Chem.* 2022;906:116003. DOI: <https://doi.org/10.1016/j.jelechem.2021.116003>
- 118 Daguette H, Solsona M, Cottet J, Gauthier M, Renaud P, Bolopion A. Positional dependence of particles and cells in microfluidic electrical impedance flow cytometry: origin, challenges and opportunities. *Lab Chip.* 2020;20(20):3665–89.
- 119 Kechadi M, Gamby J, Chaal L, Saidani B, Tribollet B. Free Contact Microchannel Impedance Through Two Antiparallel Planar Microelectrodes. *J Flow Chem.* 2013;3(3):81–6.
- 120 Upasham S, Bhide A, Lin K-C, Prasad S. Point-of-use sweat biosensor to track the endocrine–inflammation relationship for chronic disease monitoring. *Futur Sci OA.* 2020 Oct;10(2144):FSO628.
- 121 Cao L, Kiely J, Piano M, Luxton R. Facile and inexpensive fabrication of zinc oxide based bio-surfaces for C-reactive protein detection. *Sci Rep.* 2018;8(1):12687.
- 122 Rimbu C, Vranceanu N, Broasca G, Farima D, Ciocoiu M, Campagne C, et al. Zinc oxide application in the textile industry: surface tailoring and water barrier attributes as parameters with direct implication in comfort performance. *Text Res J.* 2013 Mar;83(20):2142–51.
- 123 Liu Y, Zhong M, Shan G, Li Y, Huang B, Yang G. Biocompatible ZnO/Au nanocomposites for ultrasensitive DNA detection using resonance Raman scattering. *J Phys Chem B.* 2008;112(20):6484–9.
- 124 Ng A, Tam WW, Zhang MW, Ho CS, Husain SF, McIntyre RS, et al. IL-1 β , IL-6, TNF- α and CRP in Elderly Patients with Depression or Alzheimer’s disease: Systematic Review and Meta-Analysis. *Sci Rep.* 2018;8(1):12050.

- 125 Panichi V, Migliori M, De Pietro S, Taccola D, Andreini B, Metelli MR, et al. The link of biocompatibility to cytokine production. *Kidney Int.* 2000;58:S96–103.
- 126 Lin KC, Kunduru V, Bothara M, Rege K, Prasad S, Ramakrishna BL. Biogenic nanoporous silica-based sensor for enhanced electrochemical detection of cardiovascular biomarkers proteins. *Biosens Bioelectron.* 2010;25(10):2336–42.
- 127 Hsu LA, Ko YL, Teng MS, Wu SM, Chou HH, Chang PY, et al. Effect of obesity on the association between common variations in the HNF1A gene region and C-reactive protein level in Taiwanese. *Clin Chim Acta.* 2011;412(9–10):725–9.
- 128 Rosenson RS, Fraser H, Goulder MA, Hislop C. Anti-Inflammatory Effects of Varespladib Methyl in Diabetic Patients with Acute Coronary Syndrome. *Cardiovasc Drugs Ther.* 2011;25(6):539–44.
- 129 Kim SJ, Choe YH, Bang OY, Collaborators C-B. Are Stroke Biomarkers Seeing Brain Vessels in Patients With Ischemic Stroke? A C-Reactive Protein and Homocysteine Study. *Stroke.* 2011;42(5):1464–8.
- 130 Shankar A, Sun LP, Klein BEK, Lee KE, Muntner P, Nieto FJ, et al. Markers of inflammation predict the long-term risk of developing chronic kidney disease: a population-based cohort study. *Kidney Int.* 2011;80(11):1231–8.
- 131 Chaturvedi AK, Caporaso NE, Katki HA, Wong HL, Chatterjee N, Pine SR, et al. C-Reactive Protein and Risk of Lung Cancer. *J Clin Oncol.* 2010;28(16):2719–26.
- 132 Ridker PM, Cook N. Clinical Usefulness of Very High and Very Low Levels of C-Reactive Protein Across the Full Range of Framingham Risk Scores. *Circulation.* 2004;109(16):1955–9.
- 133 Lin K-C, Kunduru V, Bothara M, Rege K, Prasad S, Ramakrishna BL. Biogenic nanoporous silica-based sensor for enhanced electrochemical detection of cardiovascular biomarkers proteins. *Biosens Bioelectron.* 2010 Jun;25(10):2336–42.
- 134 Gupta RK, Periyakaruppan A, Meyyappan M, Koehne JE. Label-free detection of C-reactive protein using a carbon nanofiber based biosensor. *Biosens Bioelectron.* 2014 Sep;59:112–9.
- 135 Jolly P, Batistuti MR, Miodek A, Zhurauski P, Mulato M, Lindsay MA, et al. Highly sensitive dual mode electrochemical platform for microRNA detection. *Sci Rep.* 2016;6(1):36719.
- 136 B. Radoičić M, V. Milošević M, Milicevic D, H. Suljovrujić E, Cirić-Marjanović G, Radetić M, et al.

- Influence of TiO₂ nanoparticles on formation mechanism of PANI/TiO₂ nanocomposite coating on PET fabric and its structural and electrical properties. *Surf Coatings Technol.* 2015 Aug;278(Supplement C):38–47.
- 137 Calleja JM, Cardona M. Resonant Raman scattering in ZnO. *Phys Rev B.* 1977 Oct;16(8):3753–61.
- 138 Zhang R, Yin P-G, Wang N, Guo L. Photoluminescence and Raman scattering of ZnO nanorods. *Solid State Sci.* 2009;11(4):865–9.
- 139 Umar A, Akhtar MS, Al-Assiri MS, Al-Hajry A, Algarni H, de Mendonca VR, et al. Highly porous ZnO nanosheets self-assembled in rosette-like morphologies for dye-sensitized solar cell application. *New J Chem.* 2015;39(10):7961–70.
- 140 Zhang S, Yin B, Jiang H, Qu F, Umar A, Wu X. Hybrid ZnO/ZnS nanoforests as the electrode materials for high performance supercapacitor application. *Dalt Trans.* 2015;44(5):2409–15.
- 141 Kengne-Momo RP, Daniel P, Lagarde F, Jeyachandran YL, Pilard JF, Durand-Thouand MJ, et al. Protein Interactions Investigated by the Raman Spectroscopy for Biosensor Applications. *Int J Spectrosc.* 2012 Jan;2012:462901.
- 142 Herrmann R, García-García FJ, Reller A. Rapid degradation of zinc oxide nanoparticles by phosphate ions. *Beilstein J Nanotechnol.* 2014;5:2007–15.
- 143 Liu C-F, Lu Y-J, Hu C-C. Effects of Anions and pH on the Stability of ZnO Nanorods for Photoelectrochemical Water Splitting. *ACS Omega.* 2018 Mar;3(3):3429–39.
- 144 Potempa LA, Yao Z-Y, Ji S-R, Filep JG, Wu Y. Solubilization and purification of recombinant modified C-reactive protein from inclusion bodies using reversible anhydride modification. *Biophys Reports.* 2015;1(1):18–33.
- 145 Cao L, Kiely J, Piano M, Luxton R. A Copper Oxide/Zinc Oxide Composite Nano-Surface for Use in a Biosensor. *Materials (Basel).* 2019;12(7). DOI: 10.3390/ma12071126
- 146 Karunakaran C, Vinayagamorthy P, Jayabharathi J. Nonquenching of Charge Carriers by Fe₃O₄ Core in Fe₃O₄/ZnO Nanosheet Photocatalyst. *Langmuir.* 2014 Dec;30(49):15031–9.
- 147 Li D, Zang J, Zhang J, Ao K, Wang Q, Dong Q, et al. Sol-Gel Synthesis of Carbon Xerogel-ZnO Composite for Detection of Catechol. *Mater.* 2016;9(4). DOI: 10.3390/ma9040282
- 148 Wang J, Sun X, Yang Y, Kyaw A, Huang X, Z Yin J, et al. Free-standing ZnO-CuO composite

- nanowire array films and their gas sensing properties. *Nanotechnology*. 2011 Aug;22:325704.
- 149 Zappa D, Dalola S, Faglia G, Comini E, Ferroni M, Soldano C, et al. Integration of ZnO and CuO nanowires into a thermoelectric module. *Beilstein J Nanotechnol*. 2014;5:927–36.
- 150 Rashad M, Rüsing M, Berth G, Lischka K, Pawlis A. CuO and Co₃O₄ Nanoparticles: Synthesis, Characterizations, and Raman Spectroscopy. *J Nanomater*. 2013;2013:6.
- 151 Chrzanowski J, Irwin JC. Raman scattering from cupric oxide. *Solid State Commun*. 1989;70(1):11–4.
- 152 Reichardt W, Gompf F, Ain M, Wanklyn BM. Lattice dynamics of cupric oxide. *Zeitschrift für Phys B Condens Matter*. 1990;81(1):19–24.
- 153 Wang X, Zhang J, Zheng Z. Label-Free Detection of C-Reactive Protein Using ZnO Tetrapods Modified Quartz Crystal Microbalance System. *Sens Lett*. 2013;11(9):1617–21.
- 154 Borse V, Srivastava R. Fluorescence lateral flow immunoassay based point-of-care nanodiagnostics for orthopedic implant-associated infection. *Sensors Actuators B Chem*. 2019 Feb;280:24–33.
- 155 Cao L, Kiely J, Piano M, Luxton R. Nanoparticle-based 3D membrane for impedimetric biosensor applications. *Bioelectrochemistry*. 2020;136:107593.
- 156 Al-Hinai MH, Sathe P, Al-Abri MZ, Dobretsov S, Al-Hinai AT, Dutta J. Antimicrobial Activity Enhancement of Poly(ether sulfone)Membranes by in Situ Growth of ZnO Nanorods. *ACS Omega*. 2017 Jul;2(7):3157–67.
- 157 Panneer Selvam A, Muthukumar S, Kamakoti V, Prasad S. A wearable biochemical sensor for monitoring alcohol consumption lifestyle through Ethyl glucuronide (EtG) detection in human sweat. *Sci Rep*. 2016 Mar;6:23111.
- 158 Edwards V. *Electron Theory*. EDTECH; 2018. Available from: <https://books.google.co.uk/books?id=GeTEDwAAQBAJ>
- 159 Kazmierczak B, Pijanowska DG, Baraniecka A, Dawgul M, Kruk J, Torbicz W. Immunosensors for human cardiac troponins and CRP, in particular amperometric cTnI immunosensor. *Biocybern Biomed Eng*. 2016 Jan;36(1):29–41.
- 160 Juntunen E. Lateral flow immunoassays with fluorescent reporter technologies, PhD thesis, University of Turku. 2017

- 161 Chatkaewsueb S, Saysunee N, Tamaekong N. The synthesis and characterization of p-CuO/n-ZnO nanoparticles synthesized by chemical method. *Mater Today Proc.* 2017 Jan;4(5):6111–7.
- 162 Mintah Churcher NK, Upasham S, Rice P, Bhadsavle S, Prasad S. Development of a flexible, sweat-based neuropeptide Y detection platform. *RSC Adv.* 2020;10(39):23173–86.
- 163 Lu P, Dai Q, Wu L, Liu X. Structure and Capacitance of Electrical Double Layers at the Graphene–Ionic Liquid Interface. *Appl Sci.* 2017;7(9). DOI: 10.3390/app7090939
- 164 Mansfield MA, Diagnostics O, Millipore E, Bedford M. Design Considerations for Lateral Flow Test Strips. Present EMD Millipore. 2015;1–32.
- 165 Gervais L, Hitzbleck M, Delamarche E. Capillary-driven multiparametric microfluidic chips for one-step immunoassays. *Biosens Bioelectron.* 2011;27(1):64–70.
- 166 Tsumoto K, Ejima D, Senczuk AM, Kita Y, Arakawa T. Effects of salts on protein–surface interactions: applications for column chromatography. *J Pharm Sci.* 2007;96(7):1677–90.
- 167 Smith L. Surface Characterization Of Thin Film Zno Capacitors By Capacitance-voltage Measurements. *Electron Theses Diss 2004-2019.* 2007;3356.
- 168 Peng Q, Liang C, Ji W, De S. A first principles investigation of the mechanical properties of g-ZnO: The graphene-like hexagonal zinc oxide monolayer. *Comput Mater Sci.* 2013;68:320–4.

Appendix A

Chapter 4 Supplementary

Information

Figure S4. 1 The different combinations of ZnO:CuO (5%:5%; 5%:1%; 1%:5%; 1%:1%) nano-surfaces with volume ratio 1:1.....	176
Figure S4. 2 The break of flatter 5% CuO nano-surfaces during the process of protein immobilization.	177
Figure S4. 3 SEM images of nano-surfaces: (a,b) 1% pure ZnO (c,d) 1% ZnO and CuO suspensions with the ratio of 1:2 (e,f) 1:1 (g,h) 2:1.	178
Figure S4. 4 AFM 3D images of 1 μm by 1 μm area of the nano-surfaces: 1% pure ZnO; 1% ZnO and CuO suspensions with the ratio of 2:1 and 1:2.....	179
Figure S4. 5 AFM 3D images of 10 μm by 10 μm area of the nano-surfaces: 1% pure ZnO; 1% pure CuO; 1% ZnO and CuO suspensions with the ratio of 2:1 and 1:2.....	179
Figure S4. 6 Comparisons in change of impedance magnitude of anti-CRP loading (100 ng and 200 ng) on different surfaces for the detection of 1, 10 and 100 ng/mL CRP (n=3) with standard error bars. (Exception: pure 1% ZnO nano-surfaces with 200 ng capture antibody (n=4)).....	180
Table S4. 1 Phase value comparisons based on 100 ng anti-CRP antibody loading 1% ZnO nano-surfaces (n=2).....	176

The nano-surfaces were stable in storage for CRP assay stored in a dry atmosphere with silica gel for up to one year shown in **Table S4.1**. A Mann-Whitney test between group comparisons proved no significant differences with p value at 0.574. It shows the same batch of nano-surfaces showed the similar behaviours as biosensors for CRP detection.

Table S4. 1 Phase value comparisons based on 100 ng anti-CRP antibody loading 1% ZnO nano-surfaces (n=2)

Concentration of CRP (ng/mL)	1	10	100
Average degree of phase change taken on 30/06/2016	0.13	0.31	0.26
Average degree of phase change taken on 28/07/2017	0.09	0.22	0.26

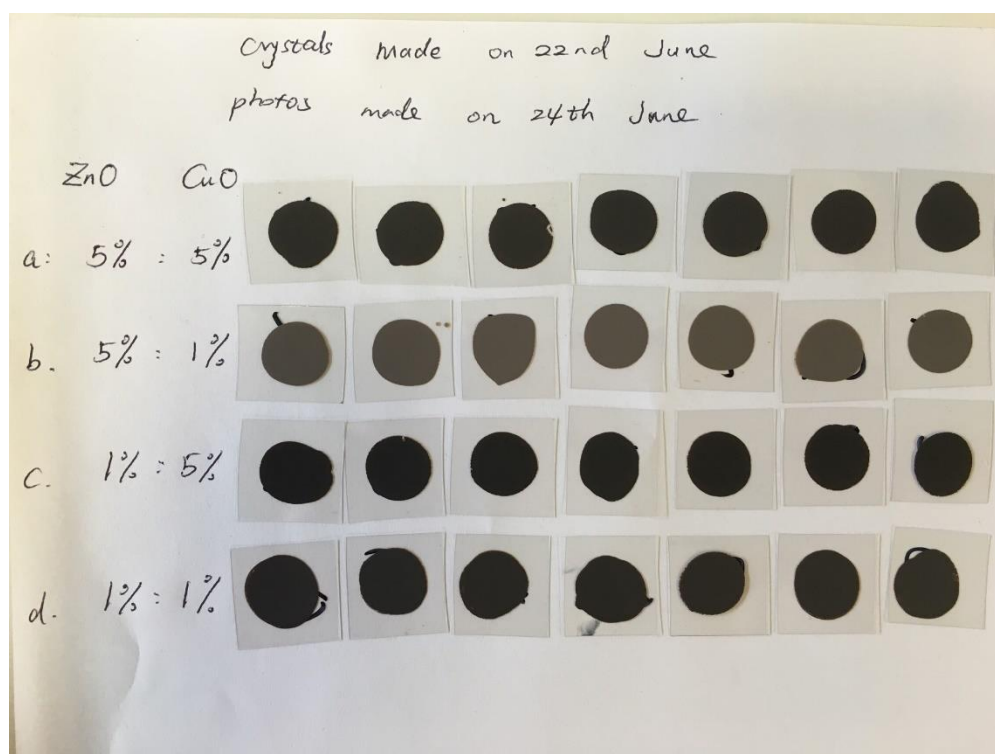


Figure S4. 1 The different combinations of ZnO:CuO (5%:5%; 5%:1%; 1%:5%; 1%:1%) nano-surfaces with volume ratio 1:1.

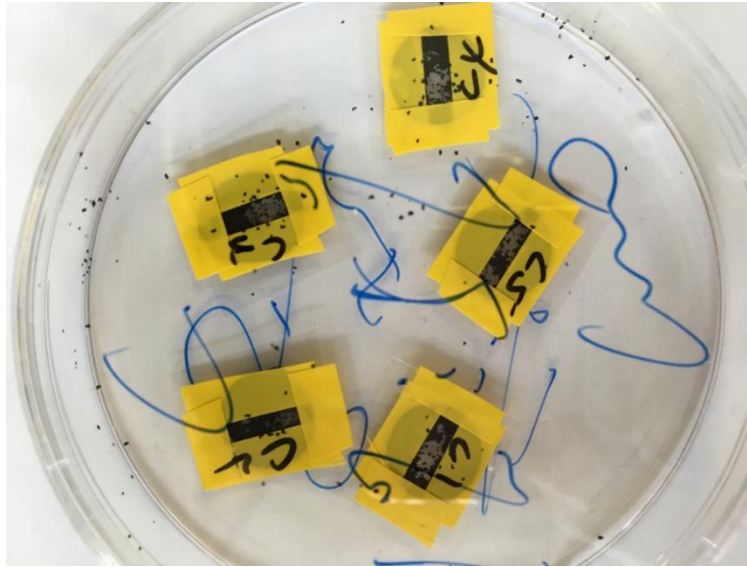


Figure S4. 2 The break of flatter 5% CuO nano-surfaces during the process of protein immobilization.

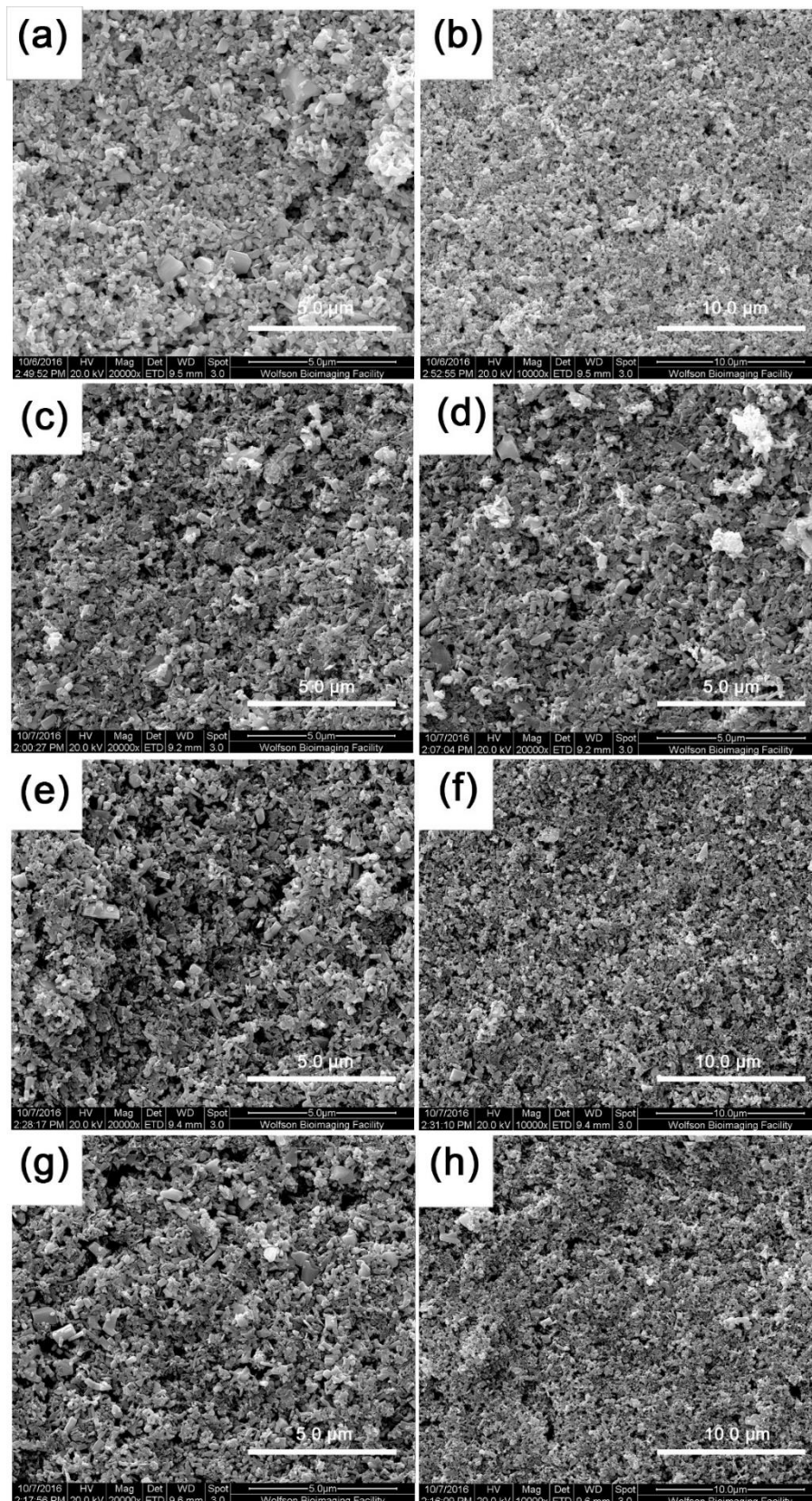


Figure S4. 3 SEM images of nano-surfaces: (a,b) 1% pure ZnO (c,d) 1% ZnO and CuO suspensions with the ratio of 1:2 (e,f) 1:1 (g,h) 2:1.

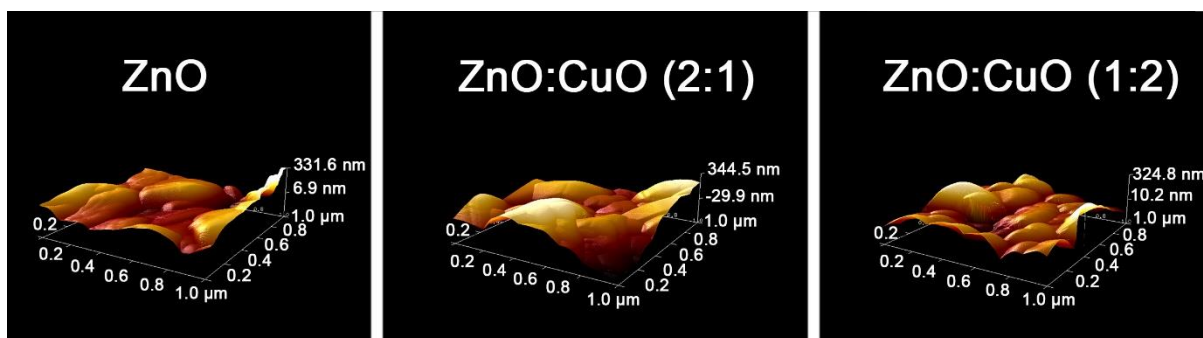


Figure S4. 4 AFM 3D images of 1 μm by 1 μm area of the nano-surfaces: 1% pure ZnO; 1% ZnO and CuO suspensions with the ratio of 2:1 and 1:2.

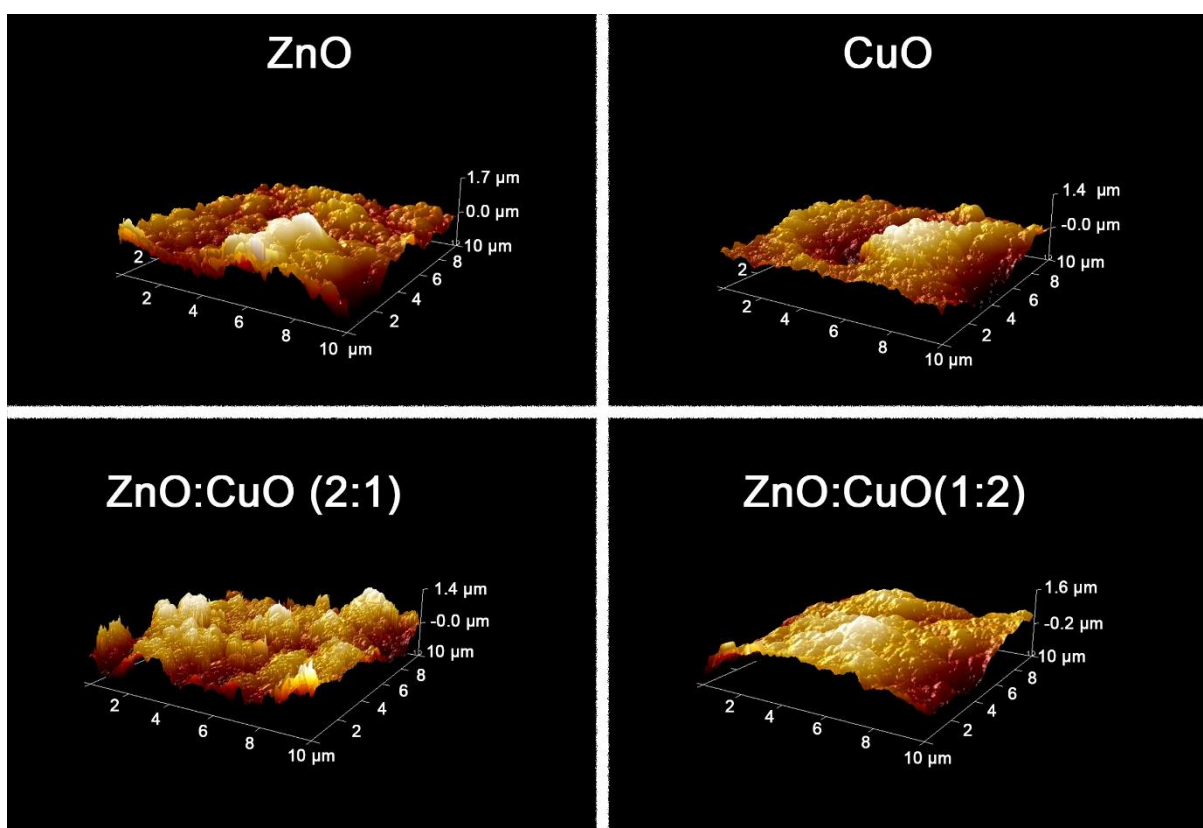


Figure S4. 5 AFM 3D images of 10 μm by 10 μm area of the nano-surfaces: 1% pure ZnO; 1% pure CuO; 1% ZnO and CuO suspensions with the ratio of 2:1 and 1:2.

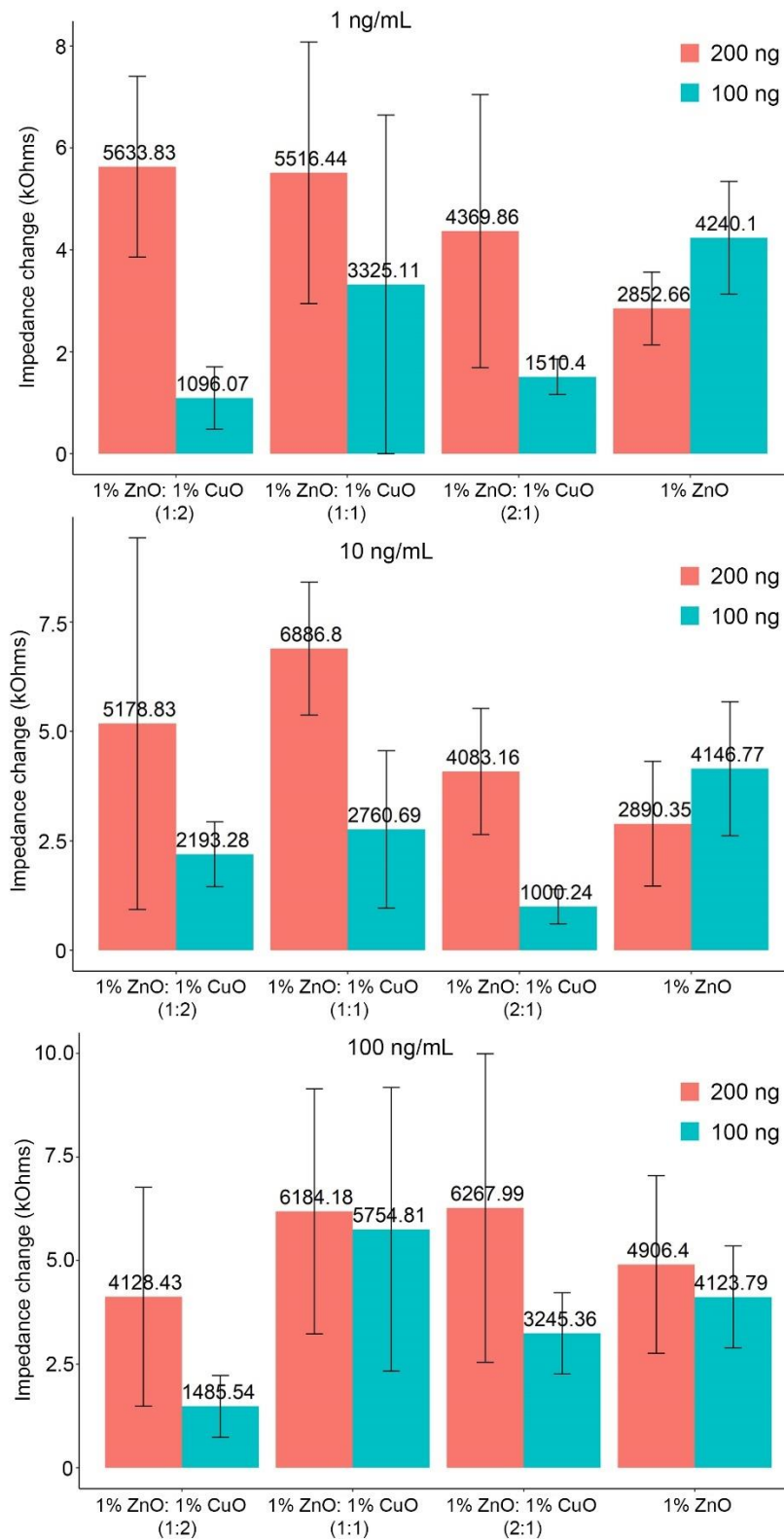


Figure S4. 6 Comparisons in change of impedance magnitude of anti-CRP loading (100 ng and 200 ng) on different surfaces for the detection of 1, 10 and 100 ng/mL CRP (n=3) with standard error bars. (Exception: pure 1% ZnO nano-surfaces with 200 ng capture antibody (n=4))

Appendix B

Chapter 5 Supplementary

Information

Figure S5. 1 Scanning electron micrograph of nano-ZnO nitrocellulose membrane cross-section at 120,000× magnification, with labels of diameter measurement by ImageJ. 183

Figure S5. 2 Scanning electron micrograph of nano-ZnO/CuO nitrocellulose membrane cross-section at 80,000× magnification, with labels of diameter of CuO nanoparticles measurement by ImageJ. 184

Figure S5. 3 Scanning electron micrograph of nano-ZnO/CuO nitrocellulose membrane cross-section at 80,000× magnification, with labels of length of CuO nanoparticles measurement by ImageJ. 184

Figure S5. 4 Scanning electron micrograph of nano-ZnO/CuO nitrocellulose membrane cross-section at 20,000× magnification, with labels of voids size measurement by ImageJ. 185

Figure S5. 5 Scanning electron micrograph of nano-ZnO nitrocellulose membrane cross-section at 80,000× magnification, with labels of voids size measurement by ImageJ. 185

Figure S5. 6 Scanning electron micrographs of the nitrocellulose membrane cross-section: (a) 600× magnification of nano-ZnO nitrocellulose membrane (whole view); (b) lower layer of nano-ZnO nitrocellulose membrane (full of ZnO nanoparticles) at 120,000× magnification; (c) 1,000× magnification of nano-ZnO/CuO nitrocellulose membrane (whole view); (d) lower layer of nano-ZnO/CuO nitrocellulose membrane (full of ZnO/CuO nanoparticles) at 160,000× magnification. 186

Figure S5. 7 Scanning electron micrographs of the nitrocellulose membrane cross-section: (a) upper layer of nitrocellulose membrane at 30,000× magnification; (b) upper layer of nitrocellulose membrane at 8,000× magnification; (c,e) middle layer of nitrocellulose membrane at 30,000× magnification; (d,f) middle layer of nitrocellulose membrane at 8,000× magnification; (g) lower layer of nano-ZnO/nitrocellulose membrane at 30,000× magnification; (h) lower layer of nano-ZnO/nitrocellulose membrane at 30,000× magnification. 187

Figure S5. 8 Scanning electron micrographs of nano-ZnO nitrocellulose membrane cross-section: (a) upper layer at 15,000× magnification; (b) middle layer at 30,000× magnification; (c) lower layer at 120,000× magnification. 188

Figure S5. 9 Scanning electron micrographs of nano-ZnO/CuO nitrocellulose membrane cross-section: (a) whole middle-lower cross-section at 2,400× magnification; (b) upper layer of nano-ZnO/CuO nitrocellulose membrane at 40,000× magnification; (c) middle layer of nano-ZnO/CuO nitrocellulose membrane at 20,000× magnification; (d) middle layer of nano-ZnO/CuO nitrocellulose membrane at 80,000× magnification; (e) middle layer of nano-ZnO/CuO nitrocellulose membrane at 160,000× magnification; (f) middle-lower layer of nano-ZnO/CuO nitrocellulose membrane at 160,000×

magnification; (g,h,i) lower layer of nano-ZnO/CuO nitrocellulose membrane at 80,000× magnification. 189

Figure S5. 10 Bode plots of nano-ZnO/nitrocellulose membranes (n=3) with and without anti-CRP antibodies on detection of 0 ng/mL (blue) and 10 ng/mL (red) CRP: (a) ZnO nano-membranes with anti-CRP antibodies; (b) ZnO nano-membranes with anti-CRP antibodies at frequency of 10 and 1000 Hz; (c) ZnO nano-membranes without anti-CRP antibodies; (d) ZnO nano-membranes without anti-CRP antibodies at frequency of 10 and 1000 Hz. 190

Figure S5. 11 Bode plots of nano-ZnO/CuO/nitrocellulose membranes (n=3) with and without anti-CRP antibodies on detection of 0 ng/mL (blue) and 10 ng/mL (red) CRP: (a) ZnO/CuO nano-membranes with anti-CRP antibodies; (b) ZnO/CuO nano-membranes with anti-CRP antibodies at frequency of 10 and 1000 Hz; (c) ZnO/CuO nano-membranes without anti-CRP antibodies; (d) ZnO/CuO nano-membranes without anti-CRP antibodies at frequency of 10 and 1000 Hz. 191

Figure S5. 12 Comparison of phase change measured on both the nano-ZnO and the nano-ZnO/CuO nanoparticles-based PET (Chapter 4) at 138 Hz and nitrocellulose membranes (Chapter 5) at 100 Hz with the same concentration of CRP of 1, 5 10 ng/mL. 192

Table S5. 1 Comparisons of antibody-based sensors on CRP detection..... 193

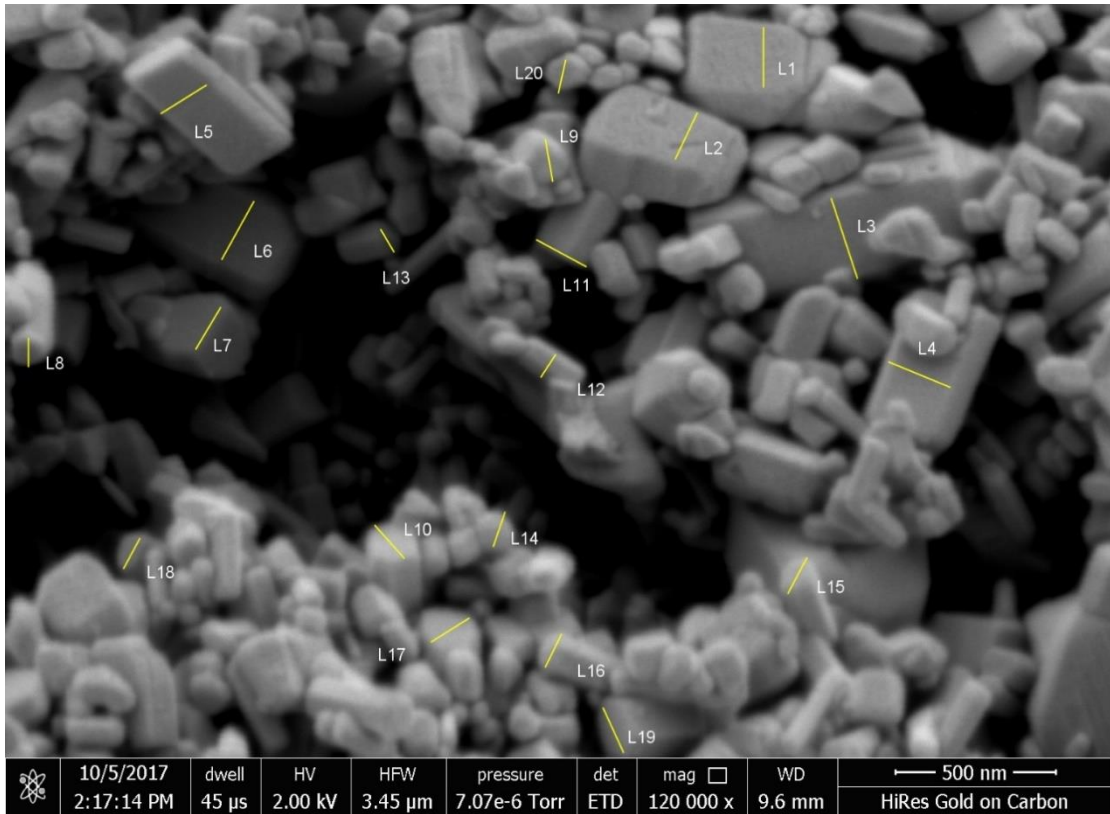


Figure S5. 1 Scanning electron micrograph of nano-ZnO nitrocellulose membrane cross-section at 120,000 \times magnification, with labels of diameter measurement by ImageJ.

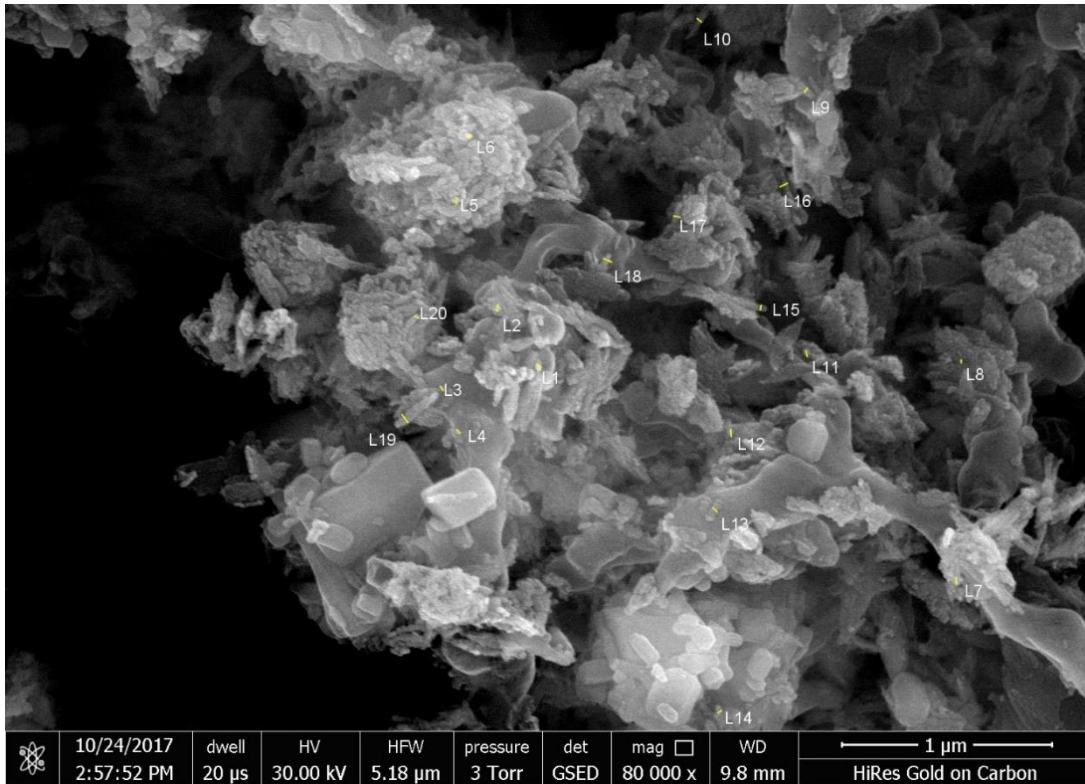


Figure S5. 2 Scanning electron micrograph of nano-ZnO/CuO nitrocellulose membrane cross-section at 80,000× magnification, with labels of diameter of CuO nanoparticles measurement by ImageJ.

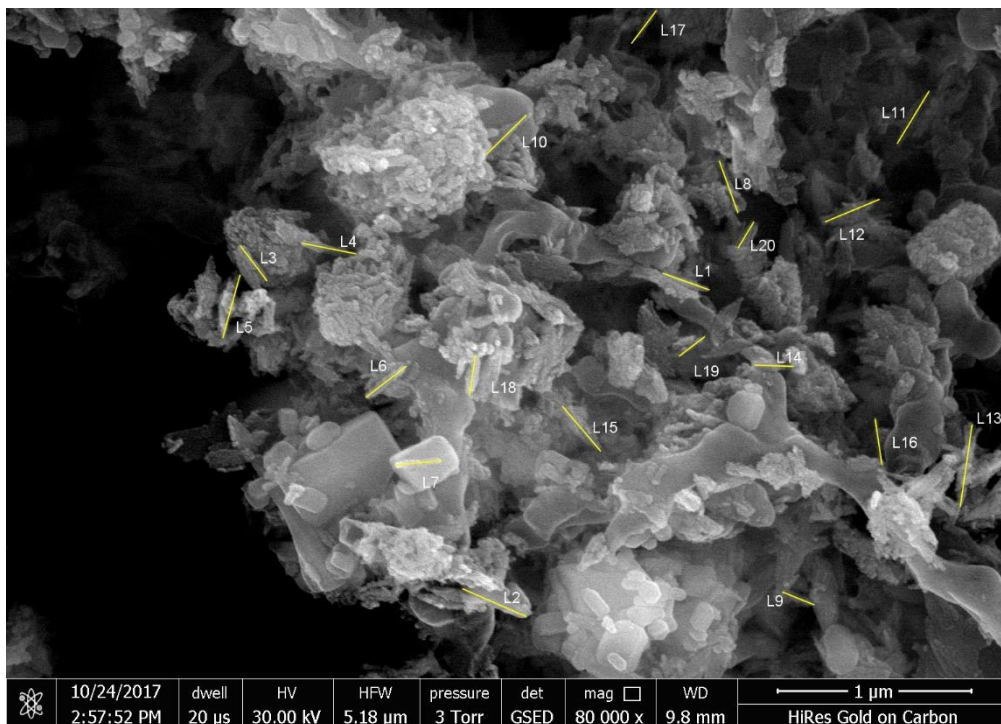


Figure S5. 3 Scanning electron micrograph of nano-ZnO/CuO nitrocellulose membrane cross-section at 80,000× magnification, with labels of length of CuO nanoparticles measurement by ImageJ.

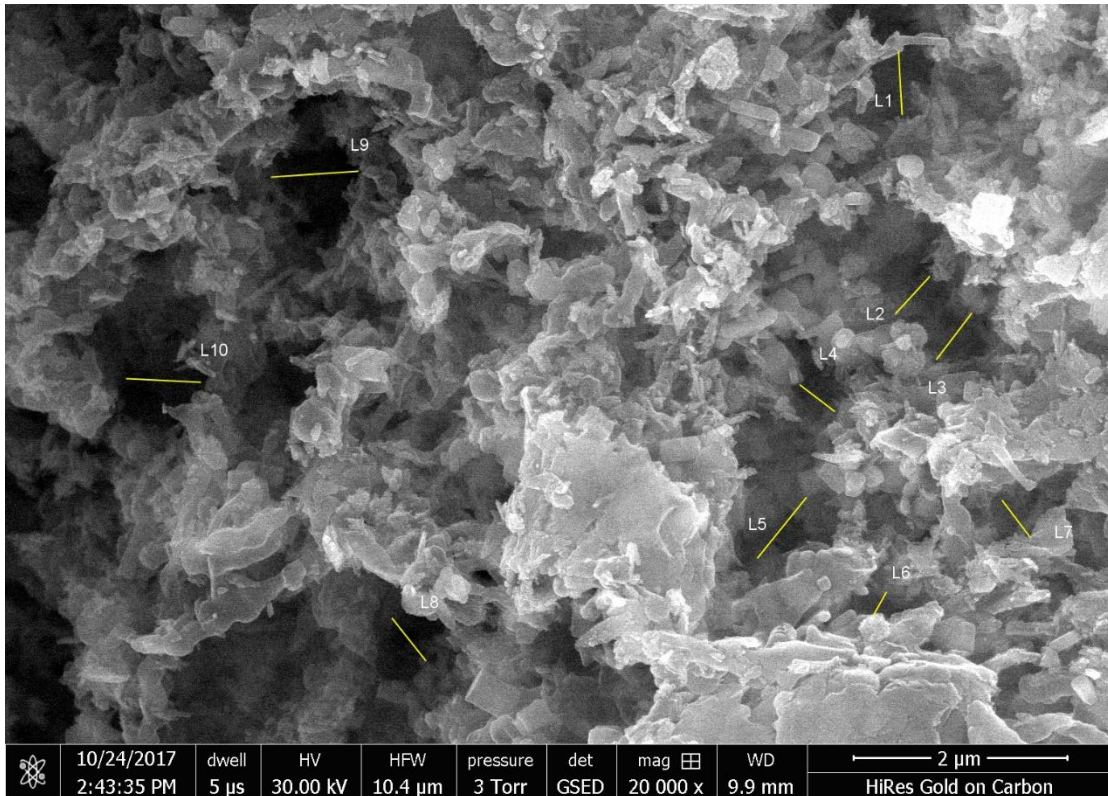


Figure S5. 4 Scanning electron micrograph of nano-ZnO/CuO nitrocellulose membrane cross-section at 20,000× magnification, with labels of voids size measurement by ImageJ.

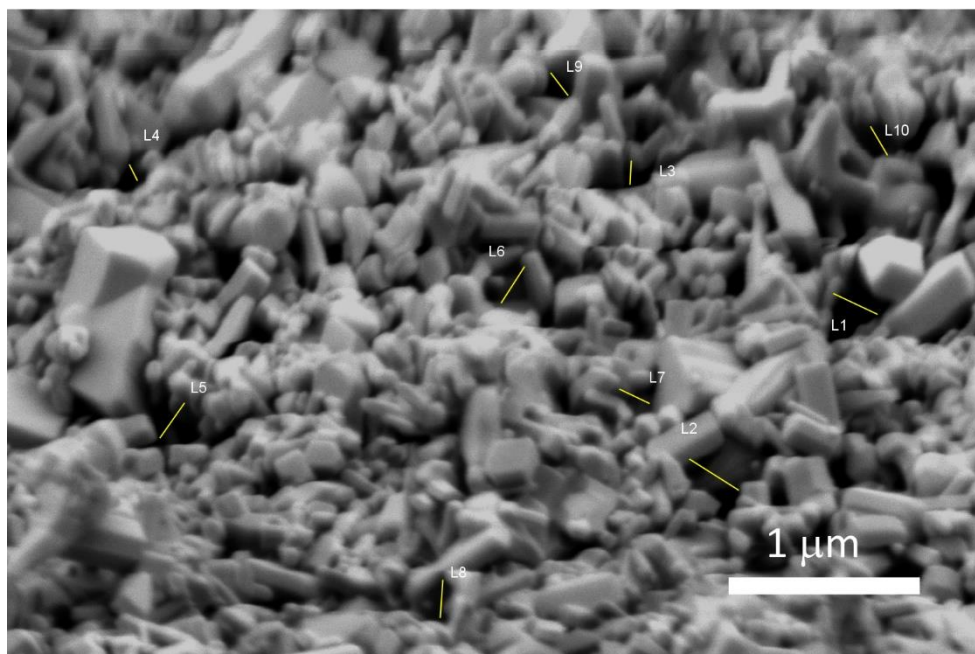


Figure S5. 5 Scanning electron micrograph of nano-ZnO nitrocellulose membrane cross-section at 80,000× magnification, with labels of voids size measurement by ImageJ.

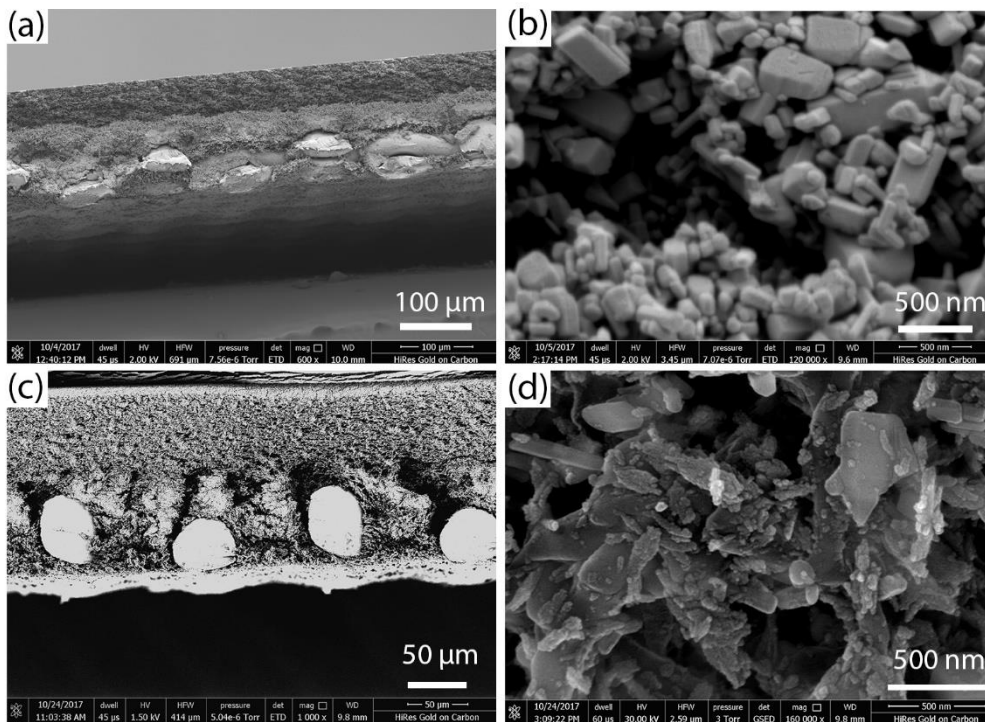


Figure S5. 6 Scanning electron micrographs of the nitrocellulose membrane cross-section: (a) 600 \times magnification of nano-ZnO nitrocellulose membrane (whole view); (b) lower layer of nano-ZnO nitrocellulose membrane (full of ZnO nanoparticles) at 120,000 \times magnification; (c) 1,000 \times magnification of nano-ZnO/CuO nitrocellulose membrane (whole view); (d) lower layer of nano-ZnO/CuO nitrocellulose membrane (full of ZnO/CuO nanoparticles) at 160,000 \times magnification.

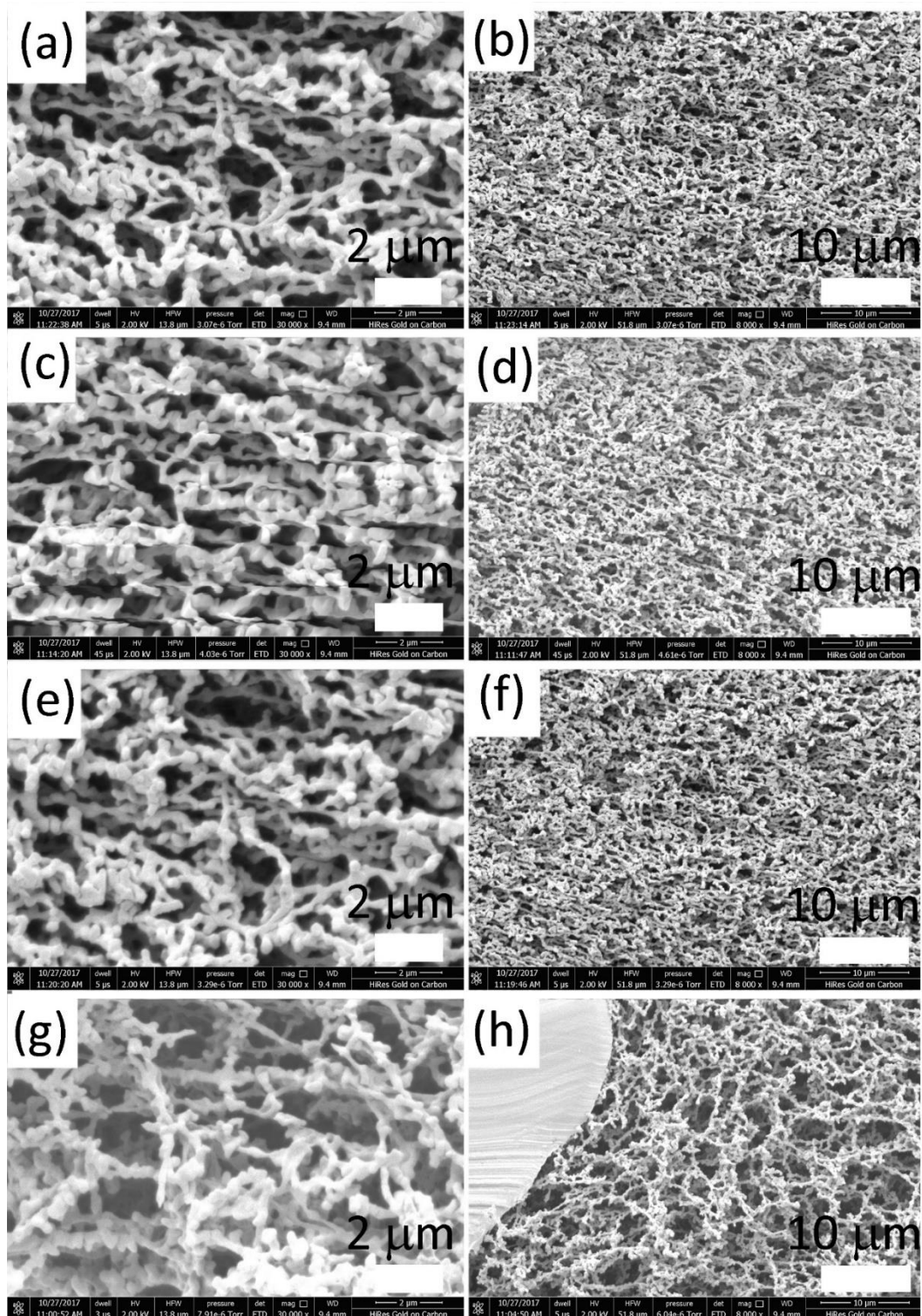


Figure S5. 7 Scanning electron micrographs of the nitrocellulose membrane cross-section: (a) upper layer of nitrocellulose membrane at 30,000× magnification; (b) upper layer of nitrocellulose membrane at 8,000× magnification; (c,e) middle layer of nitrocellulose membrane at 30,000× magnification; (d,f) middle layer of nitrocellulose membrane at 8,000× magnification; (g) lower layer of nano-ZnO/nitrocellulose membrane at 30,000× magnification; (h) lower layer of nano-ZnO/nitrocellulose membrane at 30,000× magnification.

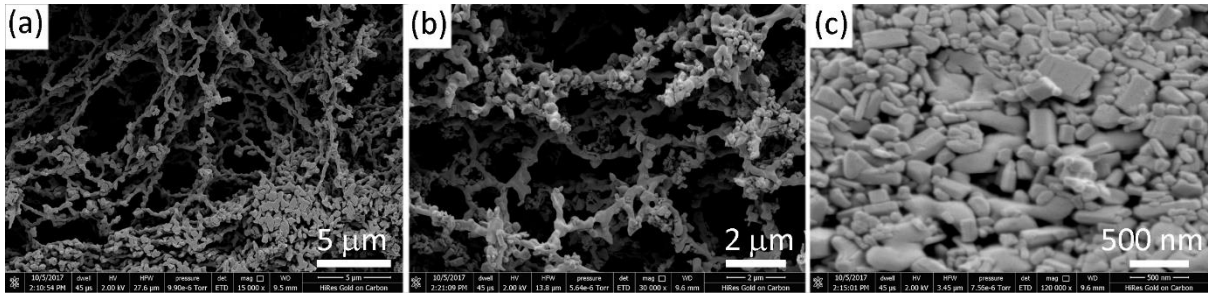


Figure S5. 8 Scanning electron micrographs of nano-ZnO nitrocellulose membrane cross-section: (a) upper layer at 15,000× magnification; (b) middle layer at 30,000× magnification; (c) lower layer at 120,000× magnification.

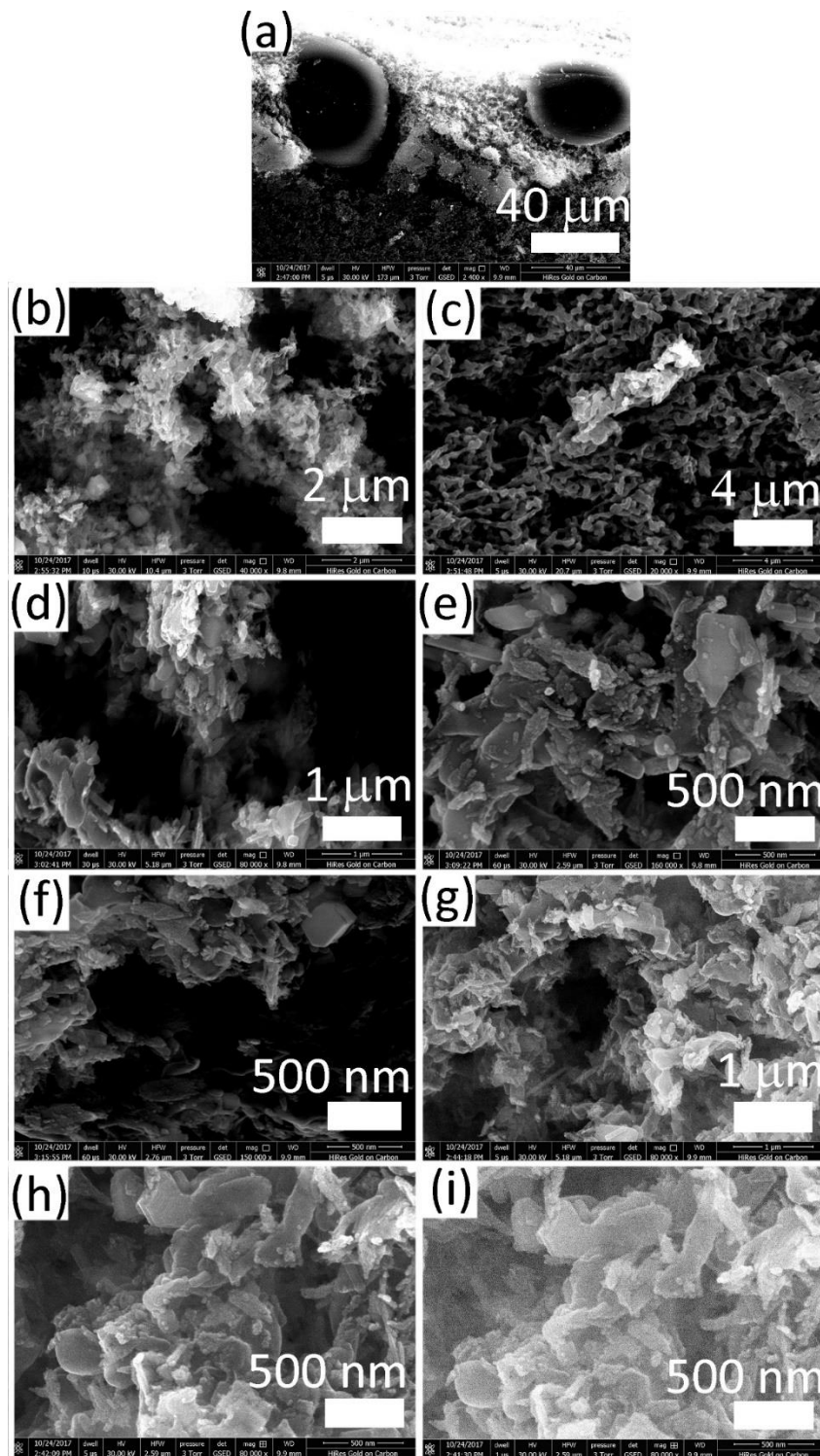


Figure S5. 9 Scanning electron micrographs of nano-ZnO/CuO nitrocellulose membrane cross-section: (a) whole middle-lower cross-section at 2,400 \times magnification; (b) upper layer of nano-ZnO/CuO nitrocellulose membrane at 40,000 \times magnification; (c) middle layer of nano-ZnO/CuO nitrocellulose membrane at 20,000 \times magnification; (d) middle layer of nano-ZnO/CuO nitrocellulose membrane at 80,000 \times magnification; (e) middle layer of nano-ZnO/CuO nitrocellulose membrane at 160,000 \times magnification; (f) middle-lower layer of nano-ZnO/CuO nitrocellulose membrane at 160,000 \times magnification; (g,h,i) lower layer of nano-ZnO/CuO nitrocellulose membrane at 80,000 \times magnification.

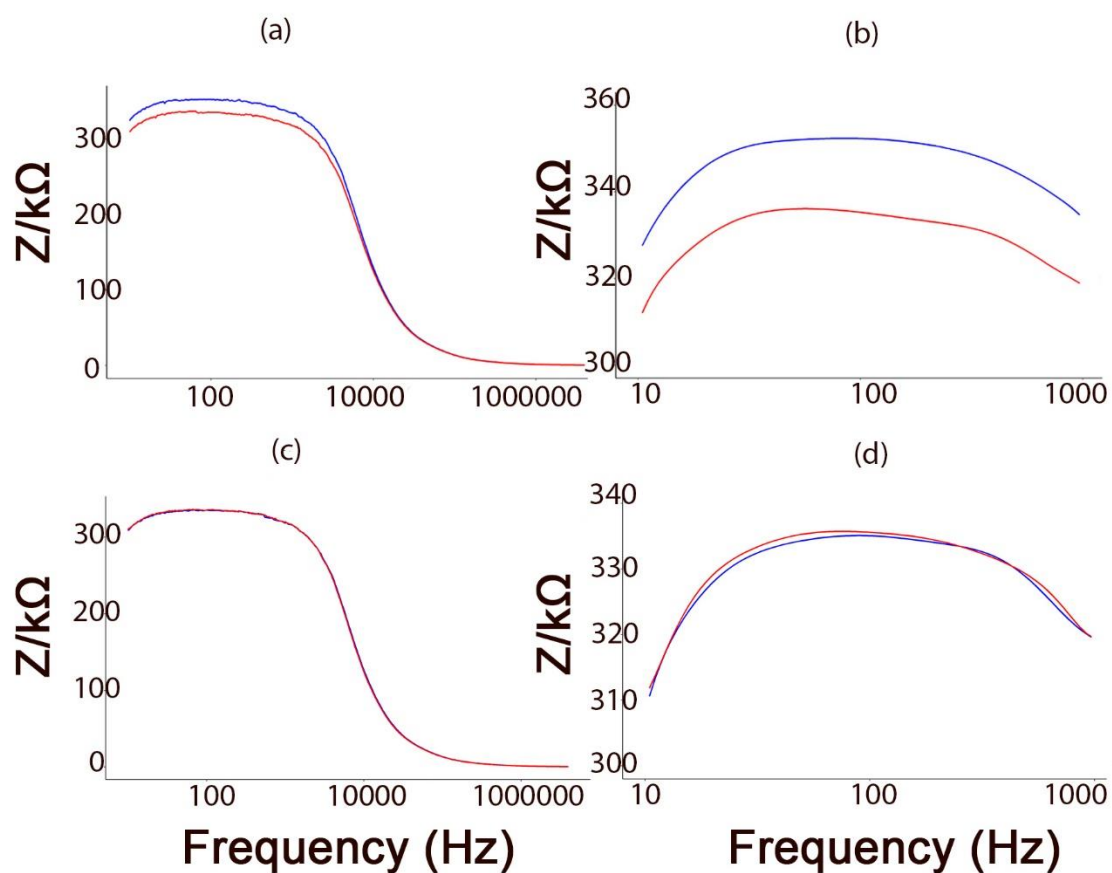


Figure S5. 10 Bode plots of nano-ZnO/nitrocellulose membranes ($n=3$) with and without anti-CRP antibodies on detection of 0 ng/mL (blue) and 10 ng/mL (red) CRP: (a) ZnO nano-membranes with anti-CRP antibodies; (b) ZnO nano-membranes with anti-CRP antibodies at frequency of 10 and 1000 Hz; (c) ZnO nano-membranes without anti-CRP antibodies; (d) ZnO nano-membranes without anti-CRP antibodies at frequency of 10 and 1000 Hz.

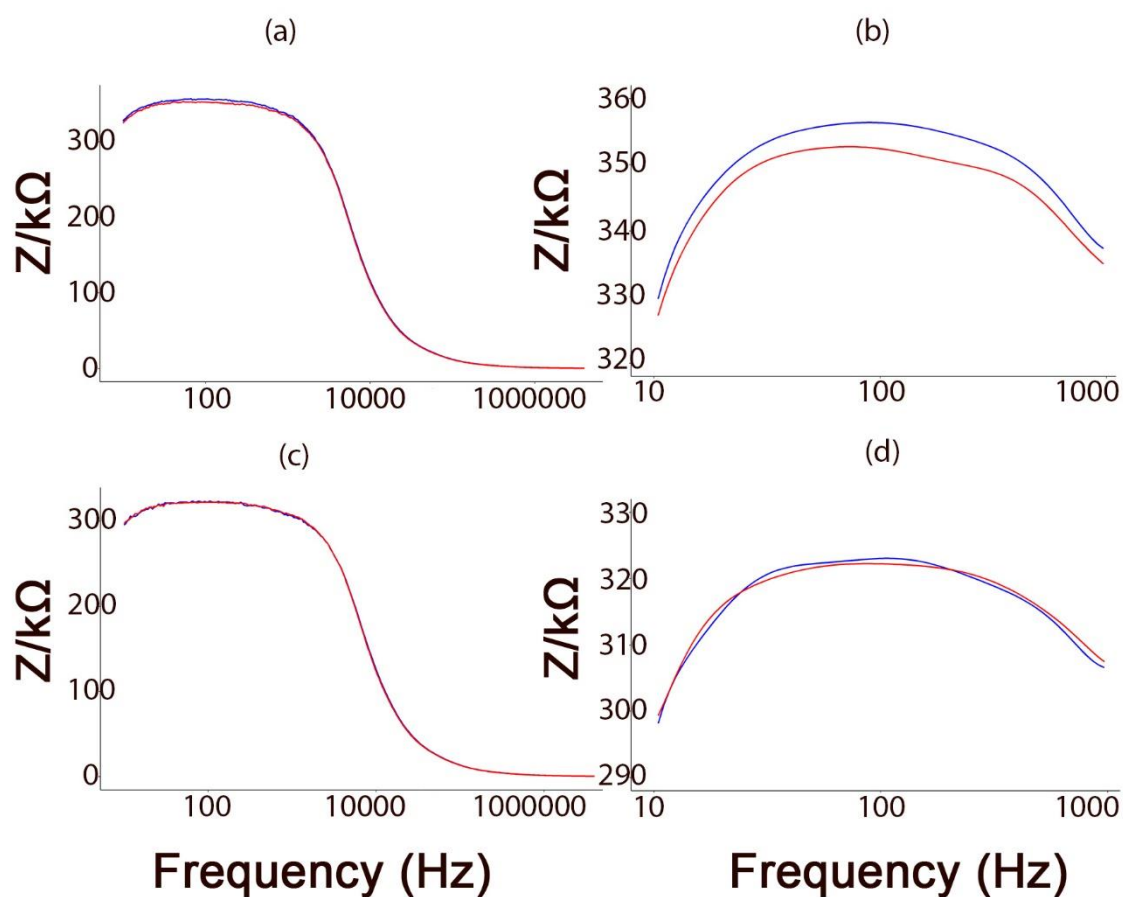


Figure S5. 11 Bode plots of nano-ZnO/CuO/nitrocellulose membranes ($n=3$) with and without anti-CRP antibodies on detection of 0 ng/mL (blue) and 10 ng/mL (red) CRP: (a) ZnO/CuO nano-membranes with anti-CRP antibodies; (b) ZnO/CuO nano-membranes with anti-CRP antibodies at frequency of 10 and 1000 Hz; (c) ZnO/CuO nano-membranes without anti-CRP antibodies; (d) ZnO/CuO nano-membranes without anti-CRP antibodies at frequency of 10 and 1000 Hz.

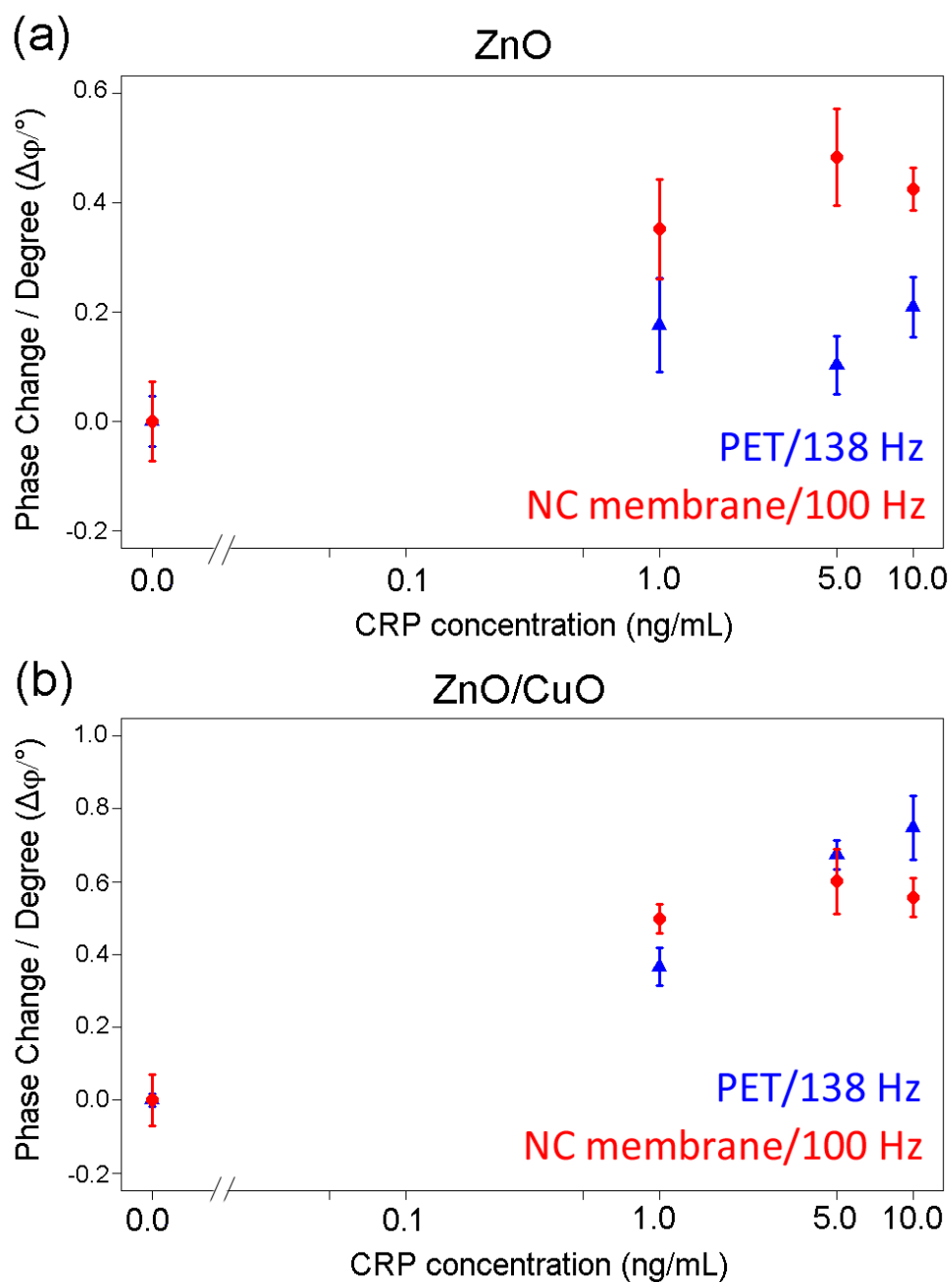


Figure S5. 12 Comparison of phase change measured on both the nano-ZnO and the nano-ZnO/CuO nanoparticles-based PET (Chapter 4) at 138 Hz and nitrocellulose membranes (Chapter 5) at 100 Hz with the same concentration of CRP of 1, 5 10 ng/mL.

Table S5. 1 Comparisons of antibody-based sensors on CRP detection

Biosensors	Principle	Antibodies volumes and concentrations in solution	Total amounts immobilised / Incubation time and storage time	Antigen/ Target detection range and separate concentrations	Incubation time	Sensitivity/ Linear range	Refs
A Paper-Based Microfluidic Immunoassay with Smartphone (CRP-Chip) under polydimethylsiloxane (PDMS) Microlens	The colorimetric CRP test signal in the CRP-Chip is imaged using the smartphone module	0.1 μL of anti-CRP antibody (200 $\text{ng}/\mu\text{L}$) on the nitrocellulose membrane	20 ng anti-CRP/ N.A.	0–2 $\mu\text{g}/\text{mL}$ CRP in standard, plasma and serum (0, 0.5, 1.0, 1.5, 2.0 $\mu\text{g}/\text{mL}$)	Within 15 minutes	The linear detection range of the CRP-Chip is up to 2 $\mu\text{g}/\text{mL}$ and the detection limit is 54 ng/mL	[63]
Carbon nanotubes based disposable immunosensors on field effect transistors	The drain current reduced with the exposure of antibody molecules because the amine groups of antibodies provide electrons for nanotubes, which reduced the number of	A droplet of 1 mL stock solution of anti-CRP (1 g/L) in PBS	1 μg by the non-covalent adsorption/ stored overnight at 4 $^{\circ}\text{C}$	Between 0.1 ng/mL to 100 $\mu\text{g}/\text{mL}$ CRP in PBS	15 minutes at room temperature	10^{-4} to 10^2 $\mu\text{g}/\text{mL}$	[37]

	major charge carriers						
A sensitive and reusable faradaic electrochemical impedimetric biosensor	The resistance of the interface responds in a calibratable manner to target protein binding	10 mM CRP antibody solution	1 hour	Across a 0.5–50 nM range CRP	10-15 minutes	LOD around 19 ng/mL in buffer solution/60 µg/L–6.0 mg/L Linear range	[52]
A reduced graphene oxide-nanoparticle hybrid impedimetric sensor	The normalized impedance magnitude clearly changed with increasing CRP.	20 µL of anti-CRP (10 µg/mL) solution in PBS (10 mM)	200 ng of anti-CRP/ kept in a humid chamber for 2 h	0.1 ng/mL - 10,000 ng/mL of CRP in human serum. (control, 0.1, 1, 10, 100, 500, 1000, 5000 and 10,000 ng/mL)	3 hours	Detection limits of 0.06 and 0.08 ng/mL in PBS and human serum	[57]
Biogenic nanoporous silica-based biosensor using EIS	The electrical double layer formed when the biomolecules are added, resulting	10 µL of 5 µg/mL of anti-CRP antibodies in 0.15 M PBS	50 ng of anti-CRP antibodies/ N.A.	1 pg/mL to 1 µg/mL of CRP in 0.15 M PBS The 0 dose, 0.001, 0.01, 0.1,	15 minutes	The sensitivity is ~1 pg/mL and the linear dose response range from 1	[133]

	in a change in capacitance.			1, 10, 100, 1000 ng/mL		pg/mL to 1 µg/mL.	
A non-faradaic electrochemical impedimetric biosensor for procalcitonin and C-reactive detection	ZnO thin film on gold electrodes. Measure binding interaction on sensor surface without needing a redox molecule. The imaginary part of impedance is inversely proportional to the electrical double layer capacitance.	10 µL of 10 µg/mL PCT antibody and 20 µg/mL CRP antibody	100 ng PCT and 200 ng CRP antibody/ incubated for 90 minutes	In the range of 0.01 ng/mL to 10 ng/mL PCT in whole blood/ from 0.01 µg/mL to 20 µg/mL CRP in human serum and 0.01 µg/mL to 10 µg/mL CRP in whole blood.	15 minutes	0.10 µg/mL of CRP in human serum and whole blood	[41]

Appendix C

Chapter 6 Supplementary

Information

Figure S6. 1 Impedance phase change/degree ($\phi/^\circ$) on nano-ZnO nitrocellulose membranes (n=3) with 200 ng antibody capture (red) and nano-ZnO nitrocellulose membranes (n=3) without 200 ng antibody capture (blue) on 1 mm gap planar electrode after a 9 minute fluidic time with accumulative concentrations of CRP, measured at a frequency of 100 Hz. 197

Figure S6. 2 Impedance magnitude (Z/kOhms) on nano-ZnO/CuO nitrocellulose membranes (n=2) on interdigitated electrode after a 9 minute fluidic time with accumulative concentrations of CRP (preliminary experiments with addition of same concentrations as on planar electrode), measured at a frequency of 100 Hz. 201

Figure S6. 3 Impedance phase change/degree ($\phi/^\circ$) on different nano-membranes on two separate electrodes: (a) nano-ZnO nitrocellulose membranes (n=3) and (b) nano-ZnO/CuO nitrocellulose membranes (n=3) on 4 mm gap planar electrode. (c) nano-ZnO nitrocellulose membranes (n=4) and (d) nano-ZnO/CuO nitrocellulose membranes (n=3) on interdigitated electrode after a 9 minute fluidic time with accumulative concentrations of CRP, measured at a frequency of 100 Hz. 202

Table S6. 1 Capacitance results of three different types on electrodes used 198

Table S6. 2 Concentration and molarity of CRP added concentration calculation on nano-ZnO and nano-ZnO/CuO membrane on planar electrode (10 ng antibody calculated molecule number is 40,200,000,000) 199

Table S6. 3 Concentration and molarity of CRP added concentration calculation on nano-ZnO and nano-ZnO/CuO membrane on interdigitated electrode (10 ng antibody calculated molecule number is 40,200,000,000) 200

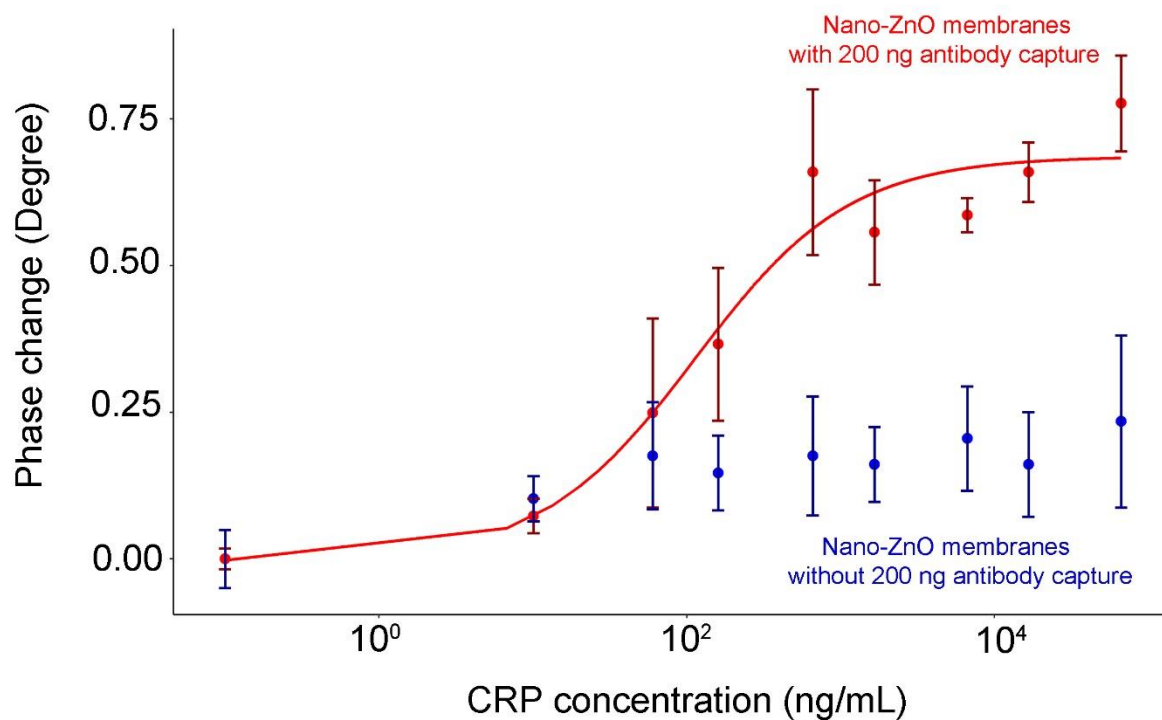


Figure S6.1 Impedance phase change/degree ($\varphi/^\circ$) on nano-ZnO nitrocellulose membranes ($n=3$) with 200 ng antibody capture (red) and nano-ZnO nitrocellulose membranes ($n=3$) without 200 ng antibody capture (blue) on 1 mm gap planar electrode after a 9 minute fluidic time with accumulative concentrations of CRP, measured at a frequency of 100 Hz.

The capacitance of a 23 mm × 23 mm electrode with 4 mm gap planar electrode and a 23 mm × 23 mm D-shape electrode with 1 mm gap planar electrode is calculated from website: <https://www.emissoftware.com/calculator/coplanar-capacitance/>. The capacitance of a 23 mm × 23 mm interdigitated electrode is calculated from website: <https://www.rfwireless-world.com/calculators/interdigital-capacitor-calculator.html>. Capacitance was calculated using 4.7 as dielectric constant. The results of capacitance are listed shown in Table S6.1.

Table S6. 1 Capacitance results of three different types on electrodes used

Electrodes Types	1 mm gap D-shape planar	4 mm gap planar	Interdigitated
Capacitance (pF)	2.753	1.905	9.15705

Table S6. 2 Concentration and molarity of CRP added concentration calculation on nano-ZnO and nano-ZnO/CuO membrane on planar electrode (10 ng antibody calculated molecule number is 40,200,000,000)

Fluidic Time (min)	0	9	18	27	36	45	54	63	72	81	90	99	108
Concentrations of adding CRP (pg/mL)	PBS	10	50	100	500	1,000	5,000	10,000	50,000	50,000	50,000	100,000	100,000
Cumulative concentration of adding CRP (pg/mL)	0	10	60	160	660	1,660	6,660	16,660	66,660	116,660	166,660	266,660	366,660
Cumulative Antigen dose /pg	0.0	0.8	4.8	12.8	52.8	132.8	532.8	1,332.8	5,332.8	9,332.8	13,332.8	21,332.8	29,332.8
Molarity of cumulative CRP (pM)	0.000000	0.000007	0.000041	0.000108	0.000447	0.001125	0.004515	0.011295	0.045193	0.079092	0.112990	0.180786	0.248583
The number of molecules (agn) of cumulative CRP does added	0	4,088,136	24,528,814	65,410,169	269,816,949	678,630,508	2,722,698,305	6,810,833,898	27,251,511,864	47,692,189,831	68,132,867,797	109,014,223,729	149,895,579,661

Table S6. 3 Concentration and molarity of CRP added concentration calculation on nano-ZnO and nano-ZnO/CuO membrane on interdigitated electrode (10 ng antibody calculated molecule number is 40,200,000,000)

Fluidic Time (min)	0	9	18	27	36	45	54	63	72	81
Concentrations of adding CRP (pg/mL)	PBS	1	5	10	50	100	500	500	1,000	1,000
Cumulative concentration of adding CRP (pg/mL)	0	1	6	16	66	166	666	1,166	2,166	3,166
Cumulative Antigen dose /pg	0.00	0.08	0.48	1.28	5.28	13.28	53.28	93.28	173.28	253.28
Molarity of cumulative CRP (pM)	0.0000000	0.0000007	0.0000041	0.0000108	0.0000447	0.0001125	0.0004515	0.0007905	0.0014685	0.0021464
The number of molecules (agn) of cumulative CRP does added	0	408,814	2,452,881	6,541,017	26,981,695	67,863,051	272,269,831	476,676,610	885,490,169	1,294,303,729

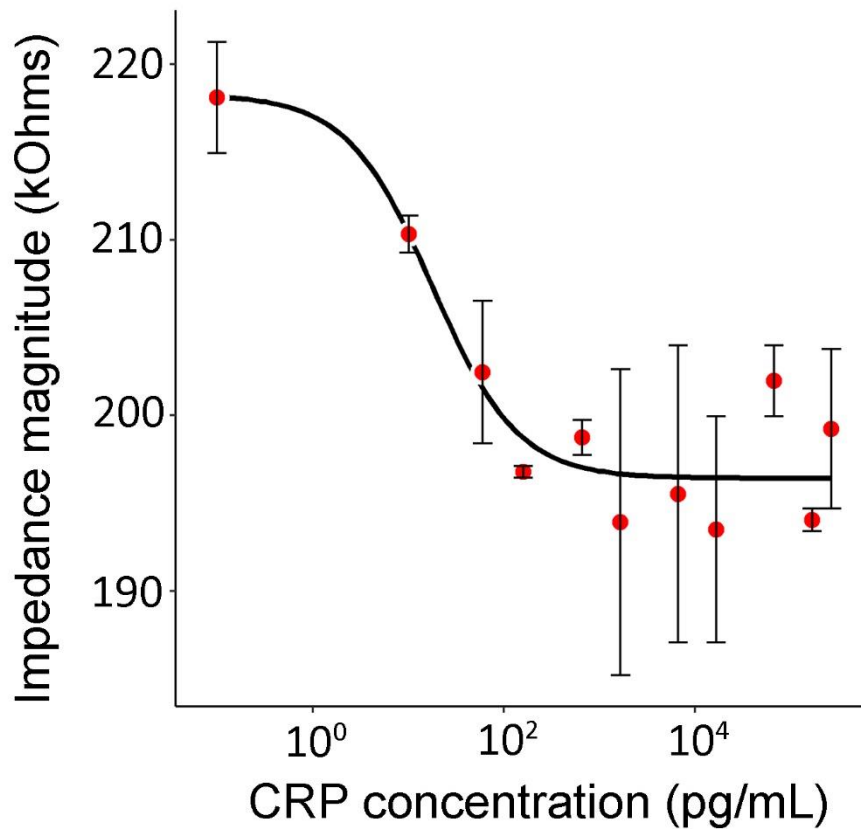


Figure S6. 2 Impedance magnitude (Z/kOhms) on nano-ZnO/CuO nitrocellulose membranes (n=2) on interdigitated electrode after a 9 minute fluidic time with accumulative concentrations of CRP (preliminary experiments with addition of same concentrations as on planar electrode), measured at a frequency of 100 Hz.

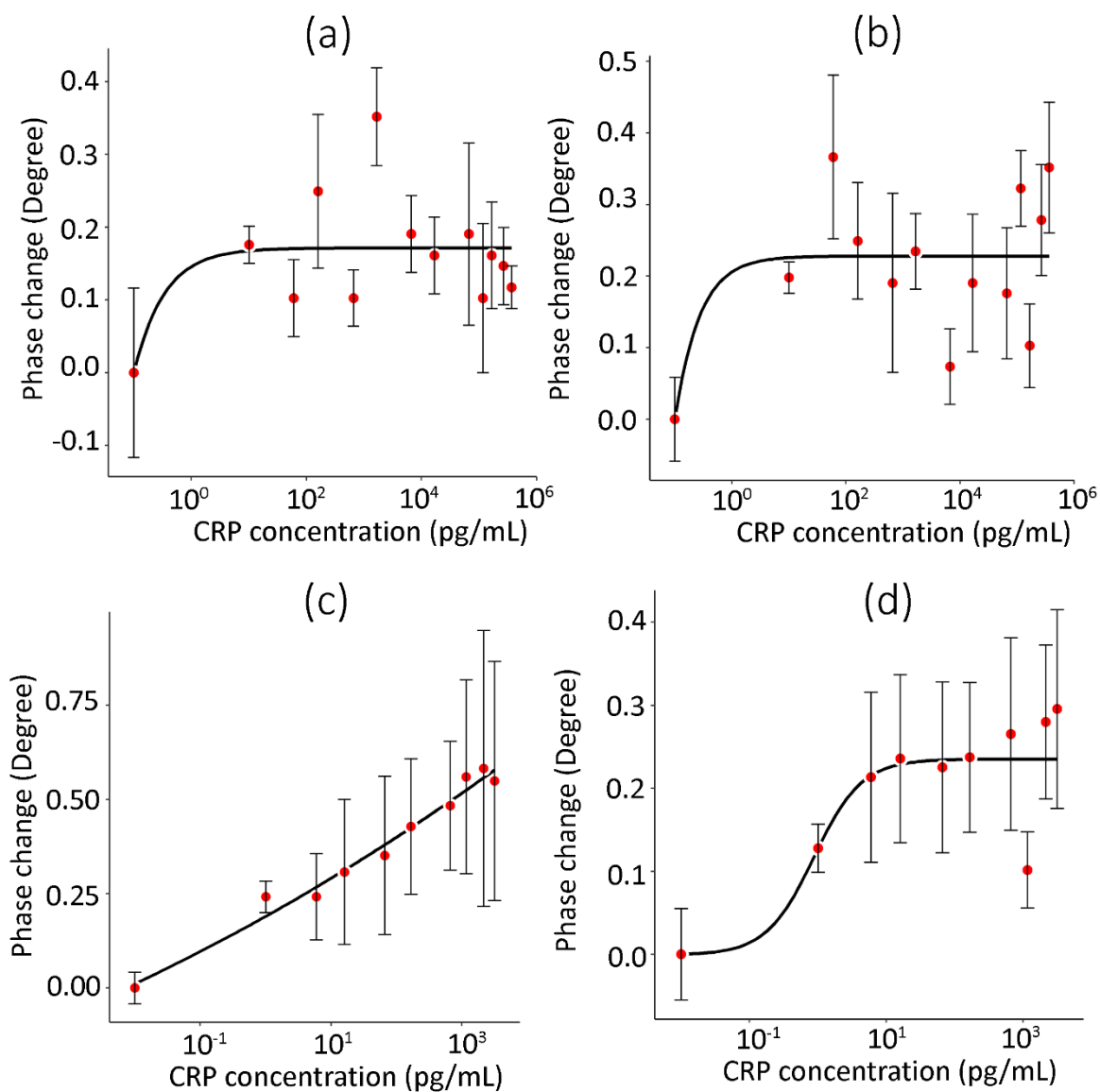


Figure S6. 3 Impedance phase change/degree ($\varphi/^\circ$) on different nano-membranes on two separate electrodes: (a) nano-ZnO nitrocellulose membranes ($n=3$) and (b) nano-ZnO/CuO nitrocellulose membranes ($n=3$) on 4 mm gap planar electrode. (c) nano-ZnO nitrocellulose membranes ($n=4$) and (d) nano-ZnO/CuO nitrocellulose membranes ($n=3$) on interdigitated electrode after a 9 minute fluidic time with accumulative concentrations of CRP, measured at a frequency of 100 Hz.

Appendix D

Copyright Permissions

ELSEVIER LICENSE
TERMS AND CONDITIONS

Oct 14, 2021

This Agreement between University of the West of England -- Lu Cao ("You") and Elsevier ("Elsevier") consists of your license details and the terms and conditions provided by Elsevier and Copyright Clearance Center.

License Number	5167720215473
License date	Oct 14, 2021
Licensed Content Publisher	Elsevier
Licensed Content Publication	Electrochimica Acta
Licensed Content Title	Urea impedimetric biosensor based on reactive RF magnetron sputtered zinc oxide nanoporous transducer
Licensed Content Author	Sayed Ahmad Mozaffari, Reza Rahmanian, Mohammad Abedi, Hossein Salar Amoli
Licensed Content Date	Nov 10, 2014
Licensed Content Volume	146
Licensed Content Issue	n/a
Licensed Content Pages	10
Start Page	538
End Page	547
Type of Use	reuse in a thesis/dissertation
Portion	figures/tables/illustrations
Number of figures/tables/illustrations	1

Format	both print and electronic
Are you the author of this Elsevier article?	No
Will you be translating?	No
Title	Investigation of nanocrystalline zinc oxide and zinc oxide/copper oxide composites for use in a continuous flow biosensor
Institution name	University of the West of England, Bristol
Expected presentation date	Jan 2022
Portions	Figure 9
Requestor Location	University of the West of England Health Technology Hub Frenchay Bristol, BS34 8QZ United Kingdom Attn: University of the West of England
Publisher Tax ID	GB 494 6272 12
Total	0.00 GBP
Terms and Conditions	

INTRODUCTION

1. The publisher for this copyrighted material is Elsevier. By clicking "accept" in connection with completing this licensing transaction, you agree that the following terms and conditions apply to this transaction (along with the Billing and Payment terms and conditions established by Copyright Clearance Center, Inc. ("CCC"), at the time that you opened your Rightslink account and that are available at any time at <http://myaccount.copyright.com>).

GENERAL TERMS

2. Elsevier hereby grants you permission to reproduce the aforementioned material subject to the terms and conditions indicated.

3. Acknowledgement: If any part of the material to be used (for example, figures) has appeared in our publication with credit or acknowledgement to another source, permission must also be sought from that source. If such permission is not obtained then that material may not be included in your publication/copies. Suitable acknowledgement to the source must be made, either as a footnote or in a reference list at the end of your publication, as follows:

"Reprinted from Publication title, Vol /edition number, Author(s), Title of article / title of chapter, Pages No., Copyright (Year), with permission from Elsevier [OR APPLICABLE SOCIETY COPYRIGHT OWNER]." Also Lancet special credit - "Reprinted from The

Lancet, Vol. number, Author(s), Title of article, Pages No., Copyright (Year), with permission from Elsevier."

4. Reproduction of this material is confined to the purpose and/or media for which permission is hereby given.

5. Altering/Modifying Material: Not Permitted. However figures and illustrations may be altered/adapted minimally to serve your work. Any other abbreviations, additions, deletions and/or any other alterations shall be made only with prior written authorization of Elsevier Ltd. (Please contact Elsevier's permissions helpdesk [here](#)). No modifications can be made to any Lancet figures/tables and they must be reproduced in full.

6. If the permission fee for the requested use of our material is waived in this instance, please be advised that your future requests for Elsevier materials may attract a fee.

7. Reservation of Rights: Publisher reserves all rights not specifically granted in the combination of (i) the license details provided by you and accepted in the course of this licensing transaction, (ii) these terms and conditions and (iii) CCC's Billing and Payment terms and conditions.

8. License Contingent Upon Payment: While you may exercise the rights licensed immediately upon issuance of the license at the end of the licensing process for the transaction, provided that you have disclosed complete and accurate details of your proposed use, no license is finally effective unless and until full payment is received from you (either by publisher or by CCC) as provided in CCC's Billing and Payment terms and conditions. If full payment is not received on a timely basis, then any license preliminarily granted shall be deemed automatically revoked and shall be void as if never granted. Further, in the event that you breach any of these terms and conditions or any of CCC's Billing and Payment terms and conditions, the license is automatically revoked and shall be void as if never granted. Use of materials as described in a revoked license, as well as any use of the materials beyond the scope of an unrevoked license, may constitute copyright infringement and publisher reserves the right to take any and all action to protect its copyright in the materials.

9. Warranties: Publisher makes no representations or warranties with respect to the licensed material.

10. Indemnity: You hereby indemnify and agree to hold harmless publisher and CCC, and their respective officers, directors, employees and agents, from and against any and all claims arising out of your use of the licensed material other than as specifically authorized pursuant to this license.

11. No Transfer of License: This license is personal to you and may not be sublicensed, assigned, or transferred by you to any other person without publisher's written permission.

12. No Amendment Except in Writing: This license may not be amended except in a writing signed by both parties (or, in the case of publisher, by CCC on publisher's behalf).

13. Objection to Contrary Terms: Publisher hereby objects to any terms contained in any purchase order, acknowledgment, check endorsement or other writing prepared by you, which terms are inconsistent with these terms and conditions or CCC's Billing and Payment terms and conditions. These terms and conditions, together with CCC's Billing and Payment terms and conditions (which are incorporated herein), comprise the entire agreement between you and publisher (and CCC) concerning this licensing transaction. In the event of any conflict between your obligations established by these terms and conditions and those established by CCC's Billing and Payment terms and conditions, these terms and conditions shall control.

14. Revocation: Elsevier or Copyright Clearance Center may deny the permissions described in this License at their sole discretion, for any reason or no reason, with a full refund payable to you. Notice of such denial will be made using the contact information provided by you. Failure to receive such notice will not alter or invalidate the denial. In no event will Elsevier or Copyright Clearance Center be responsible or liable for any costs, expenses or damage incurred by you as a result of a denial of your permission request, other than a refund of the amount(s) paid by you to Elsevier and/or Copyright Clearance Center for denied permissions.

LIMITED LICENSE

The following terms and conditions apply only to specific license types:

15. Translation: This permission is granted for non-exclusive world **English** rights only unless your license was granted for translation rights. If you licensed translation rights you may only translate this content into the languages you requested. A professional translator must perform all translations and reproduce the content word for word preserving the integrity of the article.

16. Posting licensed content on any Website: The following terms and conditions apply as follows: Licensing material from an Elsevier journal: All content posted to the web site must maintain the copyright information line on the bottom of each image; A hyper-text must be included to the Homepage of the journal from which you are licensing at <http://www.sciencedirect.com/science/journal/xxxxx> or the Elsevier homepage for books at <http://www.elsevier.com>; Central Storage: This license does not include permission for a scanned version of the material to be stored in a central repository such as that provided by Heron/XanEdu.

Licensing material from an Elsevier book: A hyper-text link must be included to the Elsevier homepage at <http://www.elsevier.com>. All content posted to the web site must maintain the copyright information line on the bottom of each image.

Posting licensed content on Electronic reserve: In addition to the above the following clauses are applicable: The web site must be password-protected and made available only to bona fide students registered on a relevant course. This permission is granted for 1 year only. You may obtain a new license for future website posting.

17. For journal authors: the following clauses are applicable in addition to the above:

Preprints:

A preprint is an author's own write-up of research results and analysis, it has not been peer-reviewed, nor has it had any other value added to it by a publisher (such as formatting, copyright, technical enhancement etc.).

Authors can share their preprints anywhere at any time. Preprints should not be added to or enhanced in any way in order to appear more like, or to substitute for, the final versions of articles however authors can update their preprints on arXiv or RePEc with their Accepted Author Manuscript (see below).

If accepted for publication, we encourage authors to link from the preprint to their formal publication via its DOI. Millions of researchers have access to the formal publications on ScienceDirect, and so links will help users to find, access, cite and use the best available version. Please note that Cell Press, The Lancet and some society-owned have different preprint policies. Information on these policies is available on the journal homepage.

Accepted Author Manuscripts: An accepted author manuscript is the manuscript of an article that has been accepted for publication and which typically includes author-incorporated changes suggested during submission, peer review and editor-author communications.

Authors can share their accepted author manuscript:

- immediately
 - via their non-commercial person homepage or blog
 - by updating a preprint in arXiv or RePEc with the accepted manuscript
 - via their research institute or institutional repository for internal institutional uses or as part of an invitation-only research collaboration work-group
 - directly by providing copies to their students or to research collaborators for their personal use
 - for private scholarly sharing as part of an invitation-only work group on commercial sites with which Elsevier has an agreement
- After the embargo period
 - via non-commercial hosting platforms such as their institutional repository
 - via commercial sites with which Elsevier has an agreement

In all cases accepted manuscripts should:

- link to the formal publication via its DOI
- bear a CC-BY-NC-ND license - this is easy to do
- if aggregated with other manuscripts, for example in a repository or other site, be shared in alignment with our hosting policy not be added to or enhanced in any way to appear more like, or to substitute for, the published journal article.

Published journal article (JPA): A published journal article (PJA) is the definitive final record of published research that appears or will appear in the journal and embodies all value-adding publishing activities including peer review co-ordination, copy-editing, formatting, (if relevant) pagination and online enrichment.

Policies for sharing publishing journal articles differ for subscription and gold open access articles:

Subscription Articles: If you are an author, please share a link to your article rather than the full-text. Millions of researchers have access to the formal publications on ScienceDirect, and so links will help your users to find, access, cite, and use the best available version.

Theses and dissertations which contain embedded PJAs as part of the formal submission can be posted publicly by the awarding institution with DOI links back to the formal publications on ScienceDirect.

If you are affiliated with a library that subscribes to ScienceDirect you have additional private sharing rights for others' research accessed under that agreement. This includes use for classroom teaching and internal training at the institution (including use in course packs and courseware programs), and inclusion of the article for grant funding purposes.

Gold Open Access Articles: May be shared according to the author-selected end-user license and should contain a [CrossMark logo](#), the end user license, and a DOI link to the formal publication on ScienceDirect.

Please refer to Elsevier's [posting policy](#) for further information.

18. **For book authors** the following clauses are applicable in addition to the above: Authors are permitted to place a brief summary of their work online only. You are not allowed to download and post the published electronic version of your chapter, nor may you scan the printed edition to create an electronic version. **Posting to a repository:** Authors are permitted to post a summary of their chapter only in their institution's repository.

19. **Thesis/Dissertation:** If your license is for use in a thesis/dissertation your thesis may be submitted to your institution in either print or electronic form. Should your thesis be published commercially, please reapply for permission. These requirements include permission for the Library and Archives of Canada to supply single copies, on demand, of the complete thesis and include permission for Proquest/UMI to supply single copies, on demand, of the complete thesis. Should your thesis be published commercially, please reapply for permission. Theses and dissertations which contain embedded PJAs as part of the formal submission can be posted publicly by the awarding institution with DOI links back to the formal publications on ScienceDirect.

Elsevier Open Access Terms and Conditions

You can publish open access with Elsevier in hundreds of open access journals or in nearly 2000 established subscription journals that support open access publishing. Permitted third party re-use of these open access articles is defined by the author's choice of Creative Commons user license. See our [open access license policy](#) for more information.

Terms & Conditions applicable to all Open Access articles published with Elsevier:

Any reuse of the article must not represent the author as endorsing the adaptation of the article nor should the article be modified in such a way as to damage the author's honour or reputation. If any changes have been made, such changes must be clearly indicated.

The author(s) must be appropriately credited and we ask that you include the end user license and a DOI link to the formal publication on ScienceDirect.

If any part of the material to be used (for example, figures) has appeared in our publication with credit or acknowledgement to another source it is the responsibility of the user to ensure their reuse complies with the terms and conditions determined by the rights holder.

Additional Terms & Conditions applicable to each Creative Commons user license:

CC BY: The CC-BY license allows users to copy, to create extracts, abstracts and new works from the Article, to alter and revise the Article and to make commercial use of the Article (including reuse and/or resale of the Article by commercial entities), provided the user gives appropriate credit (with a link to the formal publication through the relevant DOI), provides a link to the license, indicates if changes were made and the licensor is not represented as endorsing the use made of the work. The full details of the license are available at <http://creativecommons.org/licenses/by/4.0>.

CC BY NC SA: The CC BY-NC-SA license allows users to copy, to create extracts, abstracts and new works from the Article, to alter and revise the Article, provided this is not done for commercial purposes, and that the user gives appropriate credit (with a link to the formal publication through the relevant DOI), provides a link to the license, indicates if changes were made and the licensor is not represented as endorsing the use made of the work. Further, any new works must be made available on the same conditions. The full details of the license are available at <http://creativecommons.org/licenses/by-nc-sa/4.0>.

CC BY NC ND: The CC BY-NC-ND license allows users to copy and distribute the Article, provided this is not done for commercial purposes and further does not permit distribution of the Article if it is changed or edited in any way, and provided the user gives appropriate credit (with a link to the formal publication through the relevant DOI), provides a link to the license, and that the licensor is not represented as endorsing the use made of the work. The full details of the license are available at <http://creativecommons.org/licenses/by-nc-nd/4.0>. Any commercial reuse of Open Access articles published with a CC BY NC SA or CC BY NC ND license requires permission from Elsevier and will be subject to a fee.

Commercial reuse includes:

- Associating advertising with the full text of the Article
- Charging fees for document delivery or access
- Article aggregation
- Systematic distribution via e-mail lists or share buttons

Posting or linking by commercial companies for use by customers of those companies.

20. Other Conditions:

v1.10

Questions? customercare@copyright.com or +1-855-239-3415 (toll free in the US) or +1-978-646-2777.

This is a License Agreement between Lu Cao /University of the West of England, Bristol ("User") and Copyright Clearance Center, Inc. ("CCC") on behalf of the Rightsholder identified in the order details below. The license consists of the order details, the CCC Terms and Conditions below, and any Rightsholder Terms and Conditions which are included below.

All payments must be made in full to CCC in accordance with the CCC Terms and Conditions below.

Order Date	14-Oct-2021	Type of Use	Republish in a thesis/dissertation
Order License ID	1154445-1	Publisher Portion	RSC Pub Chart/graph/table/figure
ISSN	2040-3372		

LICENSED CONTENT

Publication Title	Nanoscale	Rightsholder	Royal Society of Chemistry
Article Title	Current and emerging challenges of field effect transistor based bio-sensing.	Publication Type	e-Journal
Author/Editor	National Center for Nanoscience and Technology., Royal Society of Chemistry (Great Britain)	Start Page	10702
Date	01/01/2009	Issue	22
Language	English	Volume	5
Country	United Kingdom of Great Britain and Northern Ireland	URL	http://www.rsc.org/Publishing/Journals/NR/index.asp

REQUEST DETAILS

Portion Type	Chart/graph/table/figure	Distribution	Worldwide
Number of charts / graphs / tables / figures requested	1	Translation	Original language of publication
Format (select all that apply)	Print, Electronic	Copies for the disabled?	Yes
Who will republish the content?	Academic institution	Minor editing privileges?	Yes
Duration of Use	Life of current edition	Incidental promotional use?	No
Lifetime Unit Quantity	Up to 500,000	Currency	GBP
Rights Requested	Main product		

NEW WORK DETAILS

Title	Investigation of nanocrystalline zinc oxide and zinc oxide/copper oxide composites for use in a continuous flow biosensor	Institution name	Institution of Bio-sensing Technology
Instructor name	Janice Kiely, Richard Luxton & Martina Piano	Expected presentation date	2021-10-14

ADDITIONAL DETAILS

Order reference number	N/A	The requesting person / organization to appear on the license	Lu Cao /University of the West of England, Bristol
-------------------------------	-----	--	--

REUSE CONTENT DETAILS

Title, description or numeric reference of the portion(s)	Figure 7
--	----------

Editor of portion(s)	Matsumoto, Akira; Miyahara, Yuji	Title of the article/chapter the portion is from	Current and emerging challenges of field effect transistor based bio-sensing.
Volume of serial or monograph	5	Author of portion(s)	Matsumoto, Akira; Miyahara, Yuji
Page or page range of portion	10702	Issue, if republishing an article from a serial	22
		Publication date of portion	2013-10-24

CCC Terms and Conditions

1. Description of Service; Defined Terms. This Republication License enables the User to obtain licenses for republication of one or more copyrighted works as described in detail on the relevant Order Confirmation (the "Work(s)"). Copyright Clearance Center, Inc. ("CCC") grants licenses through the Service on behalf of the rightsholder identified on the Order Confirmation (the "Rightsholder"). "Republication", as used herein, generally means the inclusion of a Work, in whole or in part, in a new work or works, also as described on the Order Confirmation. "User", as used herein, means the person or entity making such republication.
2. The terms set forth in the relevant Order Confirmation, and any terms set by the Rightsholder with respect to a particular Work, govern the terms of use of Works in connection with the Service. By using the Service, the person transacting for a republication license on behalf of the User represents and warrants that he/she/it (a) has been duly authorized by the User to accept, and hereby does accept, all such terms and conditions on behalf of User, and (b) shall inform User of all such terms and conditions. In the event such person is a "freelancer" or other third party independent of User and CCC, such party shall be deemed jointly a "User" for purposes of these terms and conditions. In any event, User shall be deemed to have accepted and agreed to all such terms and conditions if User republishes the Work in any fashion.
3. Scope of License; Limitations and Obligations.
 - 3.1. All Works and all rights therein, including copyright rights, remain the sole and exclusive property of the Rightsholder. The license created by the exchange of an Order Confirmation (and/or any invoice) and payment by User of the full amount set forth on that document includes only those rights expressly set forth in the Order Confirmation and in these terms and conditions, and conveys no other rights in the Work(s) to User. All rights not expressly granted are hereby reserved.
 - 3.2. General Payment Terms: You may pay by credit card or through an account with us payable at the end of the month. If you and we agree that you may establish a standing account with CCC, then the following terms apply: Remit Payment to: Copyright Clearance Center, 29118 Network Place, Chicago, IL 60673-1291. Payments Due: Invoices are payable upon their delivery to you (or upon our notice to you that they are available to you for downloading). After 30 days, outstanding amounts will be subject to a service charge of 1-1/2% per month or, if less, the maximum rate allowed by applicable law. Unless otherwise specifically set forth in the Order Confirmation or in a separate written agreement signed by CCC, invoices are due and payable on "net 30" terms. While User may exercise the rights licensed immediately upon issuance of the Order Confirmation, the license is automatically revoked and is null and void, as if it had never been issued, if complete payment for the license is not received on a timely basis either from User directly or through a payment agent, such as a credit card company.
 - 3.3. Unless otherwise provided in the Order Confirmation, any grant of rights to User (i) is "one-time" (including the editions and product family specified in the license), (ii) is non-exclusive and non-transferable and (iii) is subject to any and all limitations and restrictions (such as, but not limited to, limitations on duration of use or circulation) included in the Order Confirmation or invoice and/or in these terms and conditions. Upon completion of the licensed use, User shall either secure a new permission for further use of the Work(s) or immediately cease any new use of the Work(s) and shall render inaccessible (such as by deleting or by removing or severing links or other locators) any further copies of the Work (except for copies printed on paper in accordance with this license and still in User's stock at the end of such period).
 - 3.4. In the event that the material for which a republication license is sought includes third party materials (such as photographs, illustrations, graphs, inserts and similar materials) which are identified in such material as having been used by permission, User is responsible for identifying, and seeking separate licenses (under this Service or otherwise) for, any of such third party materials; without a separate license, such third party materials may not be used.
 - 3.5. Use of proper copyright notice for a Work is required as a condition of any license granted under the Service. Unless otherwise provided in the Order Confirmation, a proper copyright notice will read substantially as follows: "Republished with permission of [Rightsholder's name], from [Work's title, author, volume, edition number and year of copyright]; permission conveyed through Copyright Clearance Center, Inc." Such notice must be provided in a reasonably legible font size and must be placed either immediately adjacent to the Work as used (for example, as part of a by-line or footnote but not as a separate electronic link) or in the place where substantially all other credits or

notices for the new work containing the republished Work are located. Failure to include the required notice results in loss to the Rightsholder and CCC, and the User shall be liable to pay liquidated damages for each such failure equal to twice the use fee specified in the Order Confirmation, in addition to the use fee itself and any other fees and charges specified.

- 3.6. User may only make alterations to the Work if and as expressly set forth in the Order Confirmation. No Work may be used in any way that is defamatory, violates the rights of third parties (including such third parties' rights of copyright, privacy, publicity, or other tangible or intangible property), or is otherwise illegal, sexually explicit or obscene. In addition, User may not conjoin a Work with any other material that may result in damage to the reputation of the Rightsholder. User agrees to inform CCC if it becomes aware of any infringement of any rights in a Work and to cooperate with any reasonable request of CCC or the Rightsholder in connection therewith.
4. Indemnity. User hereby indemnifies and agrees to defend the Rightsholder and CCC, and their respective employees and directors, against all claims, liability, damages, costs and expenses, including legal fees and expenses, arising out of any use of a Work beyond the scope of the rights granted herein, or any use of a Work which has been altered in any unauthorized way by User, including claims of defamation or infringement of rights of copyright, publicity, privacy or other tangible or intangible property.
5. Limitation of Liability. UNDER NO CIRCUMSTANCES WILL CCC OR THE RIGHTSHOLDER BE LIABLE FOR ANY DIRECT, INDIRECT, CONSEQUENTIAL OR INCIDENTAL DAMAGES (INCLUDING WITHOUT LIMITATION DAMAGES FOR LOSS OF BUSINESS PROFITS OR INFORMATION, OR FOR BUSINESS INTERRUPTION) ARISING OUT OF THE USE OR INABILITY TO USE A WORK, EVEN IF ONE OF THEM HAS BEEN ADVISED OF THE POSSIBILITY OF SUCH DAMAGES. In any event, the total liability of the Rightsholder and CCC (including their respective employees and directors) shall not exceed the total amount actually paid by User for this license. User assumes full liability for the actions and omissions of its principals, employees, agents, affiliates, successors and assigns.
6. Limited Warranties. THE WORK(S) AND RIGHT(S) ARE PROVIDED "AS IS". CCC HAS THE RIGHT TO GRANT TO USER THE RIGHTS GRANTED IN THE ORDER CONFIRMATION DOCUMENT. CCC AND THE RIGHTSHOLDER DISCLAIM ALL OTHER WARRANTIES RELATING TO THE WORK(S) AND RIGHT(S), EITHER EXPRESS OR IMPLIED, INCLUDING WITHOUT LIMITATION IMPLIED WARRANTIES OF MERCHANTABILITY OR FITNESS FOR A PARTICULAR PURPOSE. ADDITIONAL RIGHTS MAY BE REQUIRED TO USE ILLUSTRATIONS, GRAPHS, PHOTOGRAPHS, ABSTRACTS, INSERTS OR OTHER PORTIONS OF THE WORK (AS OPPOSED TO THE ENTIRE WORK) IN A MANNER CONTEMPLATED BY USER; USER UNDERSTANDS AND AGREES THAT NEITHER CCC NOR THE RIGHTSHOLDER MAY HAVE SUCH ADDITIONAL RIGHTS TO GRANT.
7. Effect of Breach. Any failure by User to pay any amount when due, or any use by User of a Work beyond the scope of the license set forth in the Order Confirmation and/or these terms and conditions, shall be a material breach of the license created by the Order Confirmation and these terms and conditions. Any breach not cured within 30 days of written notice thereof shall result in immediate termination of such license without further notice. Any unauthorized (but licensable) use of a Work that is terminated immediately upon notice thereof may be liquidated by payment of the Rightsholder's ordinary license price therefor; any unauthorized (and unlicensable) use that is not terminated immediately for any reason (including, for example, because materials containing the Work cannot reasonably be recalled) will be subject to all remedies available at law or in equity, but in no event to a payment of less than three times the Rightsholder's ordinary license price for the most closely analogous licensable use plus Rightsholder's and/or CCC's costs and expenses incurred in collecting such payment.
8. Miscellaneous.
 - 8.1. User acknowledges that CCC may, from time to time, make changes or additions to the Service or to these terms and conditions, and CCC reserves the right to send notice to the User by electronic mail or otherwise for the purposes of notifying User of such changes or additions; provided that any such changes or additions shall not apply to permissions already secured and paid for.
 - 8.2. Use of User-related information collected through the Service is governed by CCC's privacy policy, available online here:<https://marketplace.copyright.com/frs-ui-web/mp/privacy-policy>
 - 8.3. The licensing transaction described in the Order Confirmation is personal to User. Therefore, User may not assign or transfer to any other person (whether a natural person or an organization of any kind) the license created by the Order Confirmation and these terms and conditions or any rights granted hereunder; provided, however, that User may assign such license in its entirety on written notice to CCC in the event of a transfer of all or substantially all of User's rights in the new material which includes the Work(s) licensed under this Service.
 - 8.4. No amendment or waiver of any terms is binding unless set forth in writing and signed by the parties. The Rightsholder and CCC hereby object to any terms contained in any writing prepared by the User or its principals, employees, agents or affiliates and purporting to govern or otherwise relate to the licensing transaction described in the Order Confirmation, which terms are in any way inconsistent with any terms set forth in the Order Confirmation and/or in these terms and conditions or CCC's standard operating procedures, whether such writing is prepared prior to,

simultaneously with or subsequent to the Order Confirmation, and whether such writing appears on a copy of the Order Confirmation or in a separate instrument.

- 8.5. The licensing transaction described in the Order Confirmation document shall be governed by and construed under the law of the State of New York, USA, without regard to the principles thereof of conflicts of law. Any case, controversy, suit, action, or proceeding arising out of, in connection with, or related to such licensing transaction shall be brought, at CCC's sole discretion, in any federal or state court located in the County of New York, State of New York, USA, or in any federal or state court whose geographical jurisdiction covers the location of the Rightsholder set forth in the Order Confirmation. The parties expressly submit to the personal jurisdiction and venue of each such federal or state court. If you have any comments or questions about the Service or Copyright Clearance Center, please contact us at 978-750-8400 or send an e-mail to tsupport@copyright.com

v 1.1

Search for Articles:

All Journals

All Article Types

About

[For Authors](#)[For Reviewers](#)[For Editors](#)[For Librarians](#)[For Publishers](#)[For Societies](#)[Article Processing Charges](#)

Open Access Policy

- Permissions
- External Open Access Resources
- Open Access Explained!
- Meaning of Open Access
- Advantages of Open Access for Authors

MDPI Open Access Information and Policy

All articles published by MDPI are made immediately available worldwide under an open access license. This means:

- everyone has free and unlimited access to the full-text of all articles published in MDPI journals;
- everyone is free to re-use the published material if proper accreditation/citation of the original publication is given;
- open access publication is supported by the authors' institutes or research funding agencies by payment of a comparatively low [Article Processing Charge \(APC\)](#) for accepted articles.

Permissions

No special permission is required to reuse all or part of article published by MDPI, including figures and tables. For articles published under an open access Creative Common CC BY license, any part of the article may be reused without permission provided that the original article is clearly cited. Reuse of an article does not imply endorsement by the authors or MDPI.

External Open Access Resources

MDPI is a [RoMEO green publisher](#) — RoMEO is a database of Publishers' copyright and self-archiving policies hosted by the [University of Nottingham](#)

Those who are new to the concept of open access might find the following websites or 'Open Access 101' video informative:

[Wikipedia article on 'Open Access'](#)

We use cookies on our website to ensure you get the best experience.
[Read more about our cookies here.](#)

From the journal:
Analyst

Antibody orientation on biosensor surfaces: a minireview

[Anke K. Trilling](#)^{ab}, [Jules Beekwilder](#)^a and [Han Zuilhof](#)^{†bc}[+](#) Author affiliations

Abstract

Detection elements play a key role in analyte recognition in biosensors. Therefore, detection elements with high analyte specificity and binding strength are required. While antibodies (Abs) have been increasingly used as detection elements in biosensors, a key challenge remains – the immobilization on the biosensor surface. This minireview highlights recent approaches to immobilize and study Abs on surfaces. We first introduce Ab species used as detection elements, and discuss techniques recently used to elucidate Ab orientation by determination of layer thickness or surface topology. Then, several immobilization methods will be presented: non-covalent and covalent surface attachment, yielding oriented or random coupled Abs. Finally, protein modification methods applicable for oriented Ab immobilization are reviewed with an eye to future application.

Antibody orientation on biosensor surfaces: a minireview

A. K. Trilling, J. Beekwilder and H. Zuilhof, *Analyst*, 2013, **138**, 1619 DOI: 10.1039/C2AN36787D

This article is licensed under a [Creative Commons Attribution 3.0 Unported Licence](#). You can use material from this article in other publications without requesting further permissions from the RSC, provided that the correct acknowledgement is given.

Read more about [how to correctly acknowledge RSC content](#).

This page is available in the following languages:



Creative Commons License Deed

Attribution 3.0 Unported (CC BY 3.0)



This is a human-readable summary of (and not a substitute for) the [license](#).

You are free to:

Share — copy and redistribute the material in any medium or format

Adapt — remix, transform, and build upon the material

for any purpose, even commercially.

The licensor cannot revoke these freedoms as long as you follow the license terms.

Under the following terms:

Attribution — You must give appropriate credit, provide a link to the license, and indicate if changes were made. You may do so in any reasonable manner, but not in any way that suggests the licensor endorses you or your use.

No additional restrictions — You may not apply legal terms or technological measures that legally restrict others from doing anything the license permits.

Notices:

You do not have to comply with the license for elements of the material in the public domain or where your use is permitted by an applicable exception or limitation.

No warranties are given. The license may not give you all of the permissions necessary for your intended use. For example, other rights such as publicity, privacy, or moral rights may limit how you use the material.

SPRINGER NATURE LICENSE
TERMS AND CONDITIONS

Oct 14, 2021

This Agreement between University of the West of England -- Lu Cao ("You") and Springer Nature ("Springer Nature") consists of your license details and the terms and conditions provided by Springer Nature and Copyright Clearance Center.

License Number	5167740454300
License date	Oct 14, 2021
Licensed Content Publisher	Springer Nature
Licensed Content Publication	Molecular Biology
Licensed Content Title	Research progress on site-oriented and three-dimensional immobilization of protein
Licensed Content Author	C. Wang et al
Licensed Content Date	Feb 14, 2015
Type of Use	Thesis/Dissertation
Requestor type	academic/university or research institute
Format	print and electronic
Portion	figures/tables/illustrations
Number of figures/tables/illustrations	1
Will you be translating?	no
Circulation/distribution	50000 or greater
Author of this Springer Nature content	no

Title	Investigation of nanocrystalline zinc oxide and zinc oxide/copper oxide composites for use in a continuous flow biosensor
Institution name	University of the West of England, Bristol
Expected presentation date	Jan 2022
Portions	Figure 2
Requestor Location	University of the West of England Health Technology Hub Frenchay Bristol, BS34 8QZ United Kingdom Attn: University of the West of England
Total	0.00 GBP

Terms and Conditions

Springer Nature Customer Service Centre GmbH Terms and Conditions

This agreement sets out the terms and conditions of the licence (the **Licence**) between you and **Springer Nature Customer Service Centre GmbH** (the **Licensor**). By clicking 'accept' and completing the transaction for the material (**Licensed Material**), you also confirm your acceptance of these terms and conditions.

1. Grant of License

1. 1. The Licensor grants you a personal, non-exclusive, non-transferable, world-wide licence to reproduce the Licensed Material for the purpose specified in your order only. Licences are granted for the specific use requested in the order and for no other use, subject to the conditions below.

1. 2. The Licensor warrants that it has, to the best of its knowledge, the rights to license reuse of the Licensed Material. However, you should ensure that the material you are requesting is original to the Licensor and does not carry the copyright of another entity (as credited in the published version).

1. 3. If the credit line on any part of the material you have requested indicates that it was reprinted or adapted with permission from another source, then you should also seek permission from that source to reuse the material.

2. Scope of Licence

2. 1. You may only use the Licensed Content in the manner and to the extent permitted by these Ts&Cs and any applicable laws.

2. 2. A separate licence may be required for any additional use of the Licensed Material, e.g. where a licence has been purchased for print only use, separate permission must be obtained for electronic re-use. Similarly, a licence is only valid in the language selected and does not apply for editions in other languages unless additional translation rights have been granted separately in the licence. Any content owned by third parties are expressly excluded from the licence.

2. 3. Similarly, rights for additional components such as custom editions and derivatives require additional permission and may be subject to an additional fee. Please apply to Journalpermissions@springernature.com/bookpermissions@springernature.com for these rights.

2. 4. Where permission has been granted **free of charge** for material in print, permission may also be granted for any electronic version of that work, provided that the material is incidental to your work as a whole and that the electronic version is essentially equivalent to, or substitutes for, the print version.

2. 5. An alternative scope of licence may apply to signatories of the [STM Permissions Guidelines](#), as amended from time to time.

3. Duration of Licence

3. 1. A licence for is valid from the date of purchase ('Licence Date') at the end of the relevant period in the below table:

Scope of Licence	Duration of Licence
Post on a website	12 months
Presentations	12 months
Books and journals	Lifetime of the edition in the language purchased

4. Acknowledgement

4. 1. The Licensor's permission must be acknowledged next to the Licenced Material in print. In electronic form, this acknowledgement must be visible at the same time as the figures/tables/illustrations or abstract, and must be hyperlinked to the journal/book's homepage. Our required acknowledgement format is in the Appendix below.

5. Restrictions on use

5. 1. Use of the Licensed Material may be permitted for incidental promotional use and minor editing privileges e.g. minor adaptations of single figures, changes of format, colour and/or style where the adaptation is credited as set out in Appendix 1 below. Any other changes including but not limited to, cropping, adapting, omitting material that affect the meaning, intention or moral rights of the author are strictly prohibited.

5. 2. You must not use any Licensed Material as part of any design or trademark.

5. 3. Licensed Material may be used in Open Access Publications (OAP) before publication by Springer Nature, but any Licensed Material must be removed from OAP sites prior to final publication.

6. Ownership of Rights

6. 1. Licensed Material remains the property of either Licensor or the relevant third party and any rights not explicitly granted herein are expressly reserved.

7. Warranty

IN NO EVENT SHALL LICENSOR BE LIABLE TO YOU OR ANY OTHER PARTY OR ANY OTHER PERSON OR FOR ANY SPECIAL, CONSEQUENTIAL, INCIDENTAL OR INDIRECT DAMAGES, HOWEVER CAUSED, ARISING OUT OF OR IN

CONNECTION WITH THE DOWNLOADING, VIEWING OR USE OF THE MATERIALS REGARDLESS OF THE FORM OF ACTION, WHETHER FOR BREACH OF CONTRACT, BREACH OF WARRANTY, TORT, NEGLIGENCE, INFRINGEMENT OR OTHERWISE (INCLUDING, WITHOUT LIMITATION, DAMAGES BASED ON LOSS OF PROFITS, DATA, FILES, USE, BUSINESS OPPORTUNITY OR CLAIMS OF THIRD PARTIES), AND WHETHER OR NOT THE PARTY HAS BEEN ADVISED OF THE POSSIBILITY OF SUCH DAMAGES. THIS LIMITATION SHALL APPLY NOTWITHSTANDING ANY FAILURE OF ESSENTIAL PURPOSE OF ANY LIMITED REMEDY PROVIDED HEREIN.

8. Limitations

8. 1. **BOOKS ONLY**: Where 'reuse in a dissertation/thesis' has been selected the following terms apply: Print rights of the final author's accepted manuscript (for clarity, NOT the published version) for up to 100 copies, electronic rights for use only on a personal website or institutional repository as defined by the Sherpa guideline (www.sherpa.ac.uk/romeo/).

8. 2. For content reuse requests that qualify for permission under the [STM Permissions Guidelines](#), which may be updated from time to time, the STM Permissions Guidelines supersede the terms and conditions contained in this licence.

9. Termination and Cancellation

9. 1. Licences will expire after the period shown in Clause 3 (above).

9. 2. Licensee reserves the right to terminate the Licence in the event that payment is not received in full or if there has been a breach of this agreement by you.

Appendix 1 — Acknowledgements:

For Journal Content:

Reprinted by permission from [the Licensor]: [Journal Publisher (e.g. Nature/Springer/Palgrave)] [JOURNAL NAME] [REFERENCE CITATION (Article name, Author(s) Name), [COPYRIGHT] (year of publication)

For Advance Online Publication papers:

Reprinted by permission from [the Licensor]: [Journal Publisher (e.g. Nature/Springer/Palgrave)] [JOURNAL NAME] [REFERENCE CITATION (Article name, Author(s) Name), [COPYRIGHT] (year of publication), advance online publication, day month year (doi: 10.1038/sj.[JOURNAL ACRONYM].)

For Adaptations/Translations:

Adapted/Translated by permission from [the Licensor]: [Journal Publisher (e.g. Nature/Springer/Palgrave)] [JOURNAL NAME] [REFERENCE CITATION (Article name, Author(s) Name), [COPYRIGHT] (year of publication)

Note: For any republication from the British Journal of Cancer, the following credit line style applies:

Reprinted/adapted/translated by permission from [the Licensor]: on behalf of Cancer Research UK: : [Journal Publisher (e.g. Nature/Springer/Palgrave)] [JOURNAL NAME] [REFERENCE CITATION (Article name, Author(s) Name), [COPYRIGHT] (year of publication)

For Advance Online Publication papers:

Reprinted by permission from The [the Licensor]: on behalf of Cancer Research UK: [Journal Publisher (e.g. Nature/Springer/Palgrave)] [JOURNAL NAME] [REFERENCE CITATION (Article name, Author(s) Name), [COPYRIGHT] (year

of publication), advance online publication, day month year (doi: 10.1038/sj.
[JOURNAL ACRONYM])

For Book content:

Reprinted/adapted by permission from [the Licensor]: [Book Publisher (e.g.
Palgrave Macmillan, Springer etc) [Book Title] by [Book author(s)]
[COPYRIGHT] (year of publication)

Other Conditions:

Version 1.3

Questions? customercare@copyright.com or +1-855-239-3415 (toll free in the US) or
+1-978-646-2777.



A mathematical model to predict the optimal test line location and sample volume for lateral flow immunoassays

Conference Proceedings:
2012 Annual International Conference of the IEEE Engineering in Medicine and Biology Society
Author: M. S. Ragavendar
Publisher: IEEE
Date: Aug. 2012

Copyright © 2012, IEEE

Thesis / Dissertation Reuse

The IEEE does not require individuals working on a thesis to obtain a formal reuse license, however, you may print out this statement to be used as a permission grant:

Requirements to be followed when using any portion (e.g., figure, graph, table, or textual material) of an IEEE copyrighted paper in a thesis:

- 1) In the case of textual material (e.g., using short quotes or referring to the work within these papers) users must give full credit to the original source (author, paper, publication) followed by the IEEE copyright line © 2011 IEEE.
- 2) In the case of illustrations or tabular material, we require that the copyright line [year of original publication] IEEE appear prominently with each reprinted figure and/or table.
- 3) If a substantial portion of the original paper is to be used, and if you are not the senior author, also obtain the senior author's approval.

Requirements to be followed when using an entire IEEE copyrighted paper in a thesis:

- 1) The following IEEE copyright/ credit notice should be placed prominently in the reference [year of original publication] IEEE. Reprinted, with permission, from [author names, paper title, IEEE publication title, and month/year of publication]
- 2) Only the accepted version of an IEEE copyrighted paper can be used when posting the paper or your thesis online.
- 3) In placing the thesis on the author's university website, please display the following message in a prominent place on the website: In reference to IEEE copyrighted material which is used with permission in this thesis, the IEEE does not endorse any of [university/educational entity's name goes here]'s products or services. Internal or personal use of this material is permitted. If interested in reprinting/republishing IEEE copyrighted material for advertising or promotional purposes or for creating new collective works for resale or redistribution, please go to http://www.ieee.org/publications_standards/publications/rights/rights_link.htm to learn how to obtain a License from RightsLink.

If applicable, University Microfilms and/or ProQuest Library, or the Archives of Canada may supply single copies of the dissertation.

BACK

CLOSE WINDOW

A review on ZnO-based electrical biosensors for cardiac biomarker detection

Nandhinee R Shanmugam, Sriram Muthukumar & Shalini Prasad 

Published Online: 7 Jun 2017 | <https://doi.org/10.4155/fsoa-2017-0006>

 Sections  PDF/EPUB

 Tools  Share

Over the past few decades zinc oxide (ZnO)-based thin films and nanostructures have shown unprecedented performance in a wide range of applications. In particular, owing to high isoelectric point, biocompatibility and other multifunctional characteristics, ZnO has extensively been studied as a transduction material for biosensor development. The fascinating properties of ZnO help retain biological activity of the immobilized biomolecule and help in achieving enhanced sensing performance. As a consequence of recent advancements in this multidisciplinary field, diagnostic biosensors are expanding beyond traditional clinical labs to point-of-care and home settings. Label-free electrical detection of biomarkers has been demonstrated using ZnO-sensing platforms. In this review we highlight the characteristics of ZnO that enable realization of its use in development of point-of-care biosensors toward disease diagnosis, in particular cardiovascular diseases.

Lay abstract

The goal of this review is to discuss the features of ZnO in enhancing the sensitivity and selectivity of biomarker detection toward the development of point-of-care diagnostic devices. Basic biosensor design features and fabrication of ZnO

conceptualized the idea. N R Shanmugam wrote the manuscript, S Muthukumar and S Prasad read and commented on the manuscript.

Acknowledgements

The authors thank David Kinnamon for his efforts in proofreading this manuscript.

Financial & competing interests disclosure

The authors have no relevant affiliations or financial involvement with any organization or entity with a financial interest in or financial conflict with the subject matter or materials discussed in the manuscript. This includes employment, consultancies, honoraria, stock ownership or options, expert testimony, grants or patents received or pending, or royalties.

No writing assistance was utilized in the production of this manuscript.

Open access

This work is licensed under the Creative Commons Attribution 4.0 License. To view a copy of this license, visit <http://creativecommons.org/licenses/by/4.0/>.

PDF

Help

Rights and permissions

This work is licensed under a Creative Commons Attribution 4.0 International License. The images or other third party material in this article are included in the article's Creative Commons license, unless indicated otherwise in the credit line; if the material is not included under the Creative Commons license, users will need to obtain permission from the license holder to reproduce the material. To view a copy of this license, visit

<http://creativecommons.org/licenses/by/4.0/>

[Reprints and Permissions](#)

About this article



Check for updates

Cite this article

Panneer Selvam, A., Muthukumar, S., Kamakoti, V. et al. A wearable biochemical sensor for monitoring alcohol consumption lifestyle through Ethyl glucuronide (EtG) detection in human sweat. *Sci Rep* **6**, 23111 (2016). <https://doi.org/10.1038/srep23111>

[Download citation](#) ↓

Received	Accepted	Published
01 December 2015	29 February 2016	21 March 2016

DOI

<https://doi.org/10.1038/srep23111>

Share this article

Anyone you share the following link with will be able to read this content:

[Get shareable link](#)

Sections

Figures

References

[Abstract](#)

[Introduction](#)

[Results and Discussion](#)

[Conclusions](#)

[Experimental Section](#)

[Additional Information](#)

[References](#)

[Acknowledgements](#)

[Author information](#)

[Ethics declarations](#)

[Rights and permissions](#)

[About this article](#)

[Further reading](#)

[Comments](#)

Advertisement

This page is available in the following languages:



Creative Commons License Deed

Attribution 4.0 International (CC BY 4.0)



This is a human-readable summary of (and not a substitute for) the [license](#).

You are free to:

Share — copy and redistribute the material in any medium or format

Adapt — remix, transform, and build upon the material

for any purpose, even commercially.

The licensor cannot revoke these freedoms as long as you follow the license terms.

Under the following terms:

Attribution — You must give appropriate credit, provide a link to the license, and indicate if changes were made. You may do so in any reasonable manner, but not in any way that suggests the licensor endorses you or your use.

No additional restrictions — You may not apply legal terms or technological measures that legally restrict others from doing anything the license permits.

Notices:

You do not have to comply with the license for elements of the material in the public domain or where your use is permitted by an applicable exception or limitation.

No warranties are given. The license may not give you all of the permissions necessary for your intended use. For example, other rights such as publicity, privacy, or moral rights may limit how you use the material.

Multiplexed label-free electronic biosensors for clinical diagnostics

Zaccari, Irene (2013) *Multiplexed label-free electronic biosensors for clinical diagnostics*. PhD thesis, University of Leeds.

Abstract

The development of a highly sensitive, label-free, multiplexed biosensor platform for point-of-care diagnostics is presented. The sensor surface of a non-faradaic electrochemical impedance spectroscopy (EIS) immunosensor platform was developed and fully characterised. Optimisation of the binding of monoclonal antibodies (mAb) towards the model target human chorionic gonadotropin (hCG) to the OEG self-assembled monolayers (SAMs) was carried out. Optimal conditions for immobilisation were found for buffer pH approximately one unit below the pI of the antibody. The same condition resulted in both higher antibody density on the sensor surface as well as higher response to the antigen. At the same time the surface showed good resistance to non-specific adsorption of proteins. Based on these principles, a biosensor to detect hCG in full serum was demonstrated. By using the phase of the impedance at 100 mHz as the sensor response, a linear relationship of the phase shift vs the logarithm of hCG concentration was established between 2.6×10^{-14} M and 2.6×10^{-10} M with a sensitivity of 0.6 degree per decade, which is a significant improvement over current state-of-the-art biosensor systems. Finally, The dielectric properties of COOH-terminated hexa(ethylene glycol)undecanethiol (OEG) and 11-mercaptoundecanol (MUD) and mixed MUD:OEG SAMs, at different ratios, were studied by means of EIS. The study demonstrates that small amounts of MUD in the mixed MUD:OEG SAMs lead to a considerable decrease of the phase of the impedance as well as a significant increase in the resistivity of the SAM at low frequencies, indicating a significant improvement of the dielectric properties. Furthermore, a considerable change in the formation of clusters of OEG molecules for mixed MUD:OEG SAMs with increasing MUD content was shown by AFM imaging.

Metadata

ISBN:	978-0-85731-814-5
Awarding institution:	University of Leeds
Academic Units:	The University of Leeds > Faculty of Engineering (Leeds) > School of Electronic & Electrical Engineering (Leeds)

Download

Final eThesis - complete (pdf)

Filename: [Irene Zaccari - Multiplexed label-free electronic biosensors for clinical diagnostics.pdf](#)

[CLICK TO DOWNLOAD](#)

Licence: Creative Commons Attribution Non-commercial Share Alike (UK)

Share / Export



RDF+XML

Export

This page is available in the following languages:



Creative Commons License Deed

Attribution-NonCommercial-ShareAlike 2.0 UK: England & Wales (CC BY-NC-SA 2.0 UK)

This is a human-readable summary of (and not a substitute for) the [license](#).



You are free to:

Share — copy and redistribute the material in any medium or format

Adapt — remix, transform, and build upon the material

The licensor cannot revoke these freedoms as long as you follow the license terms.

Under the following terms:

Attribution — You must give appropriate credit, provide a link to the license, and indicate if changes were made. You may do so in any reasonable manner, but not in any way that suggests the licensor endorses you or your use.

Non-Commercial — You may not use the material for commercial purposes.

ShareAlike — If you remix, transform, or build upon the material, you must distribute your contributions under the same license as the original.

No additional restrictions — You may not apply legal terms or technological measures that legally restrict others from doing anything the license permits.

Notices:

You do not have to comply with the license for elements of the material in the public domain or where your use is permitted by an applicable exception or limitation.

No warranties are given. The license may not give you all of the permissions necessary for your intended use. For example, other rights such as publicity, privacy, or moral rights may limit how you use the material.



Equivalent circuit model of a non-faradaic impedimetric ZnO nano-crystal biosensor

Author: John Eveness, Lu Cao, Janice Kiely, Richard Luxton

Publication: Journal of Electroanalytical Chemistry

Publisher: Elsevier

Date: 1 February 2022

© 2022 Elsevier B.V. All rights reserved.

Journal Author Rights

Please note that, as the author of this Elsevier article, you retain the right to include it in a thesis or dissertation, provided it is not published commercially. Permission is not required, but please ensure that you reference the journal as the original source. For more information on this and on your other retained rights, please visit: <https://www.elsevier.com/about/our-business/policies/copyright#Author-rights>

BACK

CLOSE WINDOW

Facile and inexpensive fabrication of zinc oxide based bio-surfaces for C-reactive protein detection

SPRINGER NATURE

Author: Lu Cao et al

Publication: Scientific Reports

Publisher: Springer Nature

Date: Aug 23, 2018

Copyright © 2018, The Author(s)

Creative Commons

This is an open access article distributed under the terms of the [Creative Commons CC BY](#) license, which permits unrestricted use, distribution, and reproduction in any medium, provided the original work is properly cited.

You are not required to obtain permission to reuse this article.

To request permission for a type of use not listed, please contact [Springer Nature](#)

Materials (Basel), 2019 Apr; 12(7): 1126.
Published online 2019 Apr 6. doi: [10.3390/ma12071126](https://doi.org/10.3390/ma12071126)

PMCID: PMC6480568
PMID: [30959878](https://pubmed.ncbi.nlm.nih.gov/30959878/)

A Copper Oxide/Zinc Oxide Composite Nano-Surface for Use in a Biosensor

Lu Cao,* Janice Kiehl, Martina Piano, and Richard Luxton

Author information Article notes Copyright and License information Disclaimer

Copyright © 2019 by the authors.

Licensee MDPI, Basel, Switzerland. This article is an open access article distributed under the terms and conditions of the Creative Commons Attribution (CC BY) license (<http://creativecommons.org/licenses/by/4.0/>).

This article has been cited by other articles in PMC.

Abstract

Go to: 

In this study, biosensors based on zinc oxide–copper oxide composite nano-surfaces were prepared using a simple and inexpensive distributed colloidal technique. Combinations of mixed dispersions with volume ratios of 1:1, 1:2 and 2:1 ZnO:CuO were compared. The uniform nano-crystalline sensor surfaces on polyethylene terephthalate (PET) were analysed using scanning electron microscopy (SEM), Atomic Force Microscopy (AFM) and Raman Spectroscopy. The ZnO–CuO composite biosensor nano-surfaces showed a significantly increased impedimetric signal compared with pure ZnO nanocrystals, and the maximum output was achieved with a volume ratio of 1:2 ZnO:CuO. The antibody capture of C-reactive protein (CRP) on the nano-surfaces was used to demonstrate the enhanced signal generated with increasing amounts of CuO in the nano-surface.

Keywords: biosensor, impedance, ZnO–CuO, CRP



Formats:

Article | [PubReader](#) | [PDF \(4.5M\)](#) | [Cite](#)

Share

 Facebook  Twitter  Google+

Save Items

 Add to Favorites 

Similar articles in PubMed

Nanoparticle-based 3D membrane for impedimetric biosensor applications. [Bioelectrochemistry. 2020]

Facile and inexpensive fabrication of zinc oxide based bio-surfaces for C-reactive protein detection. [Sci Rep. 2018]

A novel impedimetric glucose biosensor based on immobilized glucose oxidase on a CuO-Chitosan ns [Int J Biol Macromol. 2018]

ZnO-CuO composite matrix based reagentless biosensor for detection of total cholesterol. [Biosens Bioelectron. 2015]

Disposable urea biosensor based on nanoporous ZnO film fabricated from ommissible polyr [Mater Sci Eng C Mater Biol App...]

[See reviews...](#)

[See all...](#)

Cited by other articles in PMC

Editorial for the Special Issue on Nanomaterials in Health Care Diagnostics [Materials. 2021]

Nanoplatfoms for Sepsis Management: Rapid Detection/Warning, Pathogen Elimination and Restoring Im [Nano-Micro Letters. 2021]

Flexible ZnO-mAb nanoplatfoms for selective peripheral blood mononuclear cell immobilization [Scientific Reports. 2020]

* Review of Materials Synthesis of The Oxide Nanomaterials



Nanoparticle-based 3D membrane for impedimetric biosensor applications

Author: Lu Cao, Janice Kiely, Martina Piano, Richard Luxton

Publication: Bioelectrochemistry

Publisher: Elsevier

Date: December 2020

© 2020 Elsevier B.V. All rights reserved.

Journal Author Rights

Please note that, as the author of this Elsevier article, you retain the right to include it in a thesis or dissertation, provided it is not published commercially. Permission is not required, but please ensure that you reference the journal as the original source. For more information on this and on your other retained rights, please visit: <https://www.elsevier.com/about/our-business/policies/copyright#Author-rights>

BACK

CLOSE WINDOW